

Integrated microseismic analysis: From relocation to advanced geomechanical interpretation

by

Himanshu Barthwal

A thesis submitted in partial fulfillment of the requirements for the degree of

Doctor of Philosophy

in

Geophysics

Department of Physics

University of Alberta

© Himanshu Barthwal, 2017

# Abstract

Microseismic events are often recorded during hydraulic fracturing stimulations of unconventional hydrocarbon reservoirs like tight sands and shales, Enhanced Geothermal Systems, mine development and carbon dioxide sequestration. Most applications involve locating and tracking these events over time to monitor subsurface deformation. However, event locations give information only in the seismically active regions. One of the objectives of this thesis is to use the microseismic data for imaging the medium through which the seismic waves propagate.

We first test the feasibility of seismic tomography using microseismic data. The data were recorded during an underground mine development in January 2011 by a network of 7 boreholes each having 4 three-component geophones. We perform P-wave double-difference tomography using the waveform cross-correlation derived differential arrival times. The relocated events tightly cluster in the space near the main working level and the access shaft and show preferential alignment along a planar surface such as a geological fault. The 3D velocity model obtained from tomographic inversion correlates well with the known geotechnical zones in the mine. Some of the mapped geological faults appear to delineate the high and low-velocity regions in the velocity model. Thus, passive seismic tomography gives information beyond the excavation damaged zones in terms of the seismic velocity which can be an effective tool in complimenting geological and geotechnical interpretations.

Next, we try to understand the origin of the microseismic events recorded during an underground mine development. We compare the spatiotemporal distribution of microseismicity with various mining activities like blasting and rock removal to identify the main cause of seismicity.

The microseismic events do not occur immediately following the mine blasts but show some correlation with the daily rate of rock volume removed. Furthermore, the events are located far from the actual construction sites at the main working level. Therefore, the large stress concentrations near the walls of the newly excavated cavities are not responsible for triggering microseismicity. We then model the stress perturbations due to the extensive horizontal tunnel network at the main working level and the vertical shafts. Based on the geometry of the microseismic event cluster, we propose a hypothesis that the events are triggered due to fault reactivation. Using the Coulomb stress change, we investigate the likelihood of fault reactivation based on their orientations and spatial locations with respect to the mine layout. Furthermore, we show that the dynamic stresses generated by the vibrations due to a rock crusher near the access shaft may be responsible for triggering the observed microseismicity along an unmapped fault.

We then focus on the origin of the microseismic events observed during hydraulic fracturing of unconventional hydrocarbon reservoirs like tight sands and shales. We model the effect of the opening of the fracture cavity on the in-situ elastic stresses and the pore pressure diffusion profiles. We show that for a fixed length of a hydraulic fracture cavity, the first events in time occur near the crack tip region where the Coulomb stress changes are positive due to the elastic stress perturbations. The pore pressure diffusion subsequently leads to microseismic events near the fracture face where elastic stress perturbations have a stabilizing effect. Furthermore, the shape of the pore pressure diffusion front depends upon the shape of the hydraulic fracture cavity. Thus, the elastic stress changes ahead of the crack tip due to fracture opening facilitate failure and this process affects the spatiotemporal distributions of microseismicity.

Finally, we study the effect of stress changes on seismic velocities and anisotropy of rocks in a hydraulic fracturing environment. We propose a forward model to compute the stress-induced seismic anisotropy due to hydraulic fracturing using third-order elasticity. We present a methodology to model the shear wave splitting delay times by simulating a real hydraulic fracturing job and acquisition set up. We then compare the measured and the modeled splitting delay times for the microseismic data acquired during a single stage of the hydraulic fracturing stimulation. Thus,

forward modeling of stress-dependent stiffness tensors and splitting delay times combined with other information such as lithology and well-constrained stress measurements can be used to get insights into the potential source of anisotropy.

# Preface

This dissertation is submitted for the degree of Doctor of Philosophy in Geophysics at the University of Alberta. The research described herein is original, and neither this nor any substantially similar dissertation was or is being submitted for any other degree or other qualification at any other university.

A manuscript including parts of **chapter 2** and **chapter 3** of this thesis is in preparation for submission to *Bulletin of the Seismological Society of America*. I am responsible for code development, data analysis, figure preparation, and manuscript writing.

A manuscript including a version of **chapter 4** of this thesis is in preparation for submission to *Geomechanics for Energy and the Environment*. I am responsible for code development, data analysis, figure preparation, and manuscript writing.

A manuscript including a version of **chapter 5** of this thesis is in preparation for submission to *Geophysics*. I am responsible for code development, data analysis, figure preparation, and manuscript writing.

**To my parents and wife, Sai**

# Acknowledgements

I would like to express my profound gratitude to my supervisor, Dr. Mirko van der Baan, for his continued guidance and support during my Ph.D. He has always motivated me to explore new scientific frontiers. I have been inspired by his vast knowledge and have greatly benefitted by his insightful comments and suggestions. I highly appreciate him for investing his time and efforts in my Ph.D.

Special thanks to the members of my supervisory and candidacy committee, Dr. David Potter, Dr. Moritz Heimpel, Dr. Lawrence Le, and Dr. Juliana Leung for their feedback which helped in improving the overall quality of my thesis. I would also like to thank Dr. Giovanni Grasselli and Dr. Bruce Sutherland for accepting to be a part of the examination committee for my Ph.D. defense.

I would like to thank all my past and present colleagues at the Microseismic Industry Consortium for their direct or indirect support. Fernando's efforts in the processing of the microseismic data recorded in an underground mine are duly acknowledged. Siwen Wei, Zhenhua Li, and Hung Dinh have been my great friends and made my stay at the University of Alberta a truly memorable one.

I would like to thank an anonymous company for the permission to use and show the microseismic data acquired during an underground mining development. I am grateful to the Lightstream resources for permitting the use of the microseismic data recorded during a hydraulic fracturing stimulation. I am also thankful to the sponsors of the Microseismic Industry Consortium for the financial support during my Ph.D.

Big thanks to Ruby, Mirko's wife, for organizing wonderful parties at their home for our entire group and making us feel at home away from home.

Above all, I am indebted to my family, my parents, and sisters for their unconditional love and support, and the numerous sacrifices they made to help me succeed in my academic career. This whole journey was possible only because of my beautiful wife, Sai, by my side. She constantly motivated me and made sure that all my energies were channeled towards my research while she took care of the worldly affairs. Thank you, Sai, for everything.

# Contents

<b>1</b>	<b>Introduction</b>	<b>1</b>
1.1	Background . . . . .	1
1.1.1	Microseismic data analysis . . . . .	1
1.1.2	Geomechanics and microseismic triggering . . . . .	5
1.1.3	Integrated analysis: Relating velocity and anisotropy derived from microseismic data with stress changes triggering microseismicity . . . . .	7
1.2	Motivation and contribution . . . . .	8
1.3	Thesis overview . . . . .	9
<b>2</b>	<b>Case studies: Data background and geological setting</b>	<b>11</b>
2.1	Case study 1: Microseismic data recorded during underground mine development . . . . .	12
2.1.1	Introduction . . . . .	12
2.1.2	Geological setting and mine layout . . . . .	12
2.1.3	Mining operations . . . . .	21
2.1.4	Microseismic data . . . . .	23
2.1.5	Objectives . . . . .	26
2.2	Case study 2: Microseismic data recorded during hydraulic fracturing . . . . .	27
2.2.1	Introduction . . . . .	27
2.2.2	Geological setting . . . . .	27
2.2.3	Hydraulic fracturing operations . . . . .	28

2.2.4	Microseismic data . . . . .	28
2.2.5	Objectives . . . . .	29
2.3	Miscellaneous data . . . . .	31
<b>3</b>	<b>Passive seismic tomography using recorded microseismicity: Application to mining-induced seismicity</b>	<b>32</b>
3.1	Introduction . . . . .	33
3.2	Theory . . . . .	35
3.3	Synthetic example . . . . .	40
3.3.1	Methodology . . . . .	40
3.3.2	Results . . . . .	43
3.3.3	Discussion . . . . .	45
3.4	Real microseismic data . . . . .	48
3.4.1	Methodology . . . . .	48
3.4.2	Results . . . . .	49
3.4.3	Discussion . . . . .	57
3.5	Conclusions . . . . .	64
<b>4</b>	<b>Induced seismicity during underground mine development: Causes and mechanisms</b>	<b>66</b>
4.1	Introduction . . . . .	67
4.2	Potential causes of microseismicity . . . . .	69
4.2.1	Man made seismic signals due to mining activity . . . . .	69
4.2.2	Dynamic triggering due to blasting or vibrations from rock crusher . . . . .	72
4.2.3	Microseismicity due to local stress concentrations around newly excavated cavities . . . . .	75
4.2.4	Microseismicity caused by stress perturbations due to the horizontal tunnel network and the vertical shafts . . . . .	77
4.3	Stress modeling . . . . .	78

4.3.1	Model geometry and parameters . . . . .	78
4.3.2	Boundary conditions . . . . .	81
4.3.3	Eshelby's equivalent inclusion method . . . . .	82
4.3.4	Stress concentration around vertical cylindrical cavities . . . . .	83
4.3.5	Coulomb failure function . . . . .	85
4.4	Results . . . . .	86
4.4.1	Static stress changes due to shaft and tunnel network . . . . .	86
4.4.2	Coulomb stress change . . . . .	90
4.5	Discussion . . . . .	95
4.5.1	Static stress transfer due to the horizontal tunnel network: Modeling as- sumptions and role in triggering microseismicity . . . . .	95
4.5.2	Dynamic triggering due to the vibrations generated by the rock crusher . .	102
4.5.3	Implications for fluid injection-induced seismicity . . . . .	107
4.6	Conclusions . . . . .	108
<b>5</b>	<b>Dynamics of hydraulic fracturing induced microseismicity: Effect of fracture opening on elastic stresses and pore pressure distribution</b>	<b>110</b>
5.1	Introduction . . . . .	111
5.2	Methods . . . . .	113
5.2.1	Model geometry and boundary conditions . . . . .	113
5.2.2	Eshelby's equivalent inclusion method . . . . .	114
5.2.3	Pore pressure diffusion . . . . .	114
5.2.4	Reactivation potential of faults/fractures . . . . .	117
5.2.5	Crack tip propagation . . . . .	118
5.3	Results . . . . .	119
5.4	Discussion . . . . .	130
5.4.1	Implications for seismicity based reservoir characterization . . . . .	135

5.4.2	Evolution of the microseismic cloud in the case of a planar hydraulic fracture	137
5.5	Conclusions	139
<b>6</b>	<b>Modeling shear wave splitting due to stress-induced seismic anisotropy: Application to hydraulic fracturing induced microseismicity</b>	<b>141</b>
6.1	Introduction	142
6.2	Methods	143
6.2.1	Model set up	144
6.2.2	Event location and seismic ray tracing	147
6.2.3	Elastic Stress changes due to hydraulic fracturing	149
6.2.4	Anisotropy calculation using third-order elasticity	149
6.2.5	Modeling shear wave splitting delay time	152
6.2.6	Splitting delay time measurements on microseismic data	154
6.3	Results	154
6.4	Discussion	162
6.5	Conclusions	163
<b>7</b>	<b>Conclusions and suggested directions for future research</b>	<b>165</b>
7.1	Conclusions	165
7.2	Suggested directions for future research	168

# List of Tables

2.1	Geotechnical zones within the mine based on the rock quality . . . . .	15
3.1	Distance and absolute differences between true and inverted event locations for the largest multiplet group (Group 1) obtained with two sets of damping parameters namely large=0.1, and small=0.002. . . . .	45
3.2	Distance and absolute differences between true and inverted event locations for the largest multiplet group (Group 1) obtained with and without distance weighting. . .	48
4.1	Parameters for computing stress perturbations around the cylindrical cavity and the oblate spheroidal inclusion . . . . .	80
5.1	Material and fluid transport properties, geometrical parameters of the hydraulic fracture, and the far-field stresses and pore pressure . . . . .	113
5.2	Parameters used for modeling the triggering front due to fluid diffusion from a point injector . . . . .	124
5.3	Material and fluid transport properties used for the Carthage Cotton Valley gas field	127
6.1	Material properties, Fracture dimensions, pore pressure, fracture pressure and regional stress state . . . . .	146
6.2	Model 2 and Model 3 with different fracture dimensions used to compute the elastic stress changes . . . . .	147
6.3	Third-order elastic constants reported for different rocks in the published literature.	159

# List of Figures

2.1	Schematic geological map and cross-section of the mining region showing major faults, lithologies and zones of mineralization. . . . .	14
2.2	Schematic North-South cross-section through the mine . . . . .	17
2.3	Schematic North-South cross-section through the mine . . . . .	18
2.4	Map view of the geotechnical zones in the mine at a depth of 480 m. . . . .	19
2.5	3D distribution of faults in the study region. . . . .	20
2.6	A composite plot showing N-S cross-sections and map view of the mine overlain with the fault traces and the geotechnical zones based on most updated and accurate technical information provided by the mining company. . . . .	22
2.7	Acquisition setup used for microseismic data recording along with the recorded seismogram of a typical microseismic event. . . . .	24
2.8	Microseismic data analysis showing the amplitude spectrum of a typical event and the waveform similarity of multiple recorded events. . . . .	25
2.9	Acquisition setup for microseismic monitoring in the case of hydraulic fracture stimulation of a low permeability hydrocarbon reservoir. . . . .	29
2.10	A typical microseismic event recorded during a single stage of the hydraulic fracture stimulation. . . . .	30
3.1	True velocity model, event locations, and the receiver positions used to generate the synthetic arrival time data. . . . .	41

3.2	Results of the 1D tomographic inversion using the synthetic data along with the corresponding trade-off curves. . . . .	44
3.3	Results of double-difference tomography using synthetic data with different damping parameters. . . . .	46
3.4	Results of the 1D tomographic inversion of field data along with the corresponding trade-off curves. . . . .	50
3.5	Event locations of the two largest multiplet groups (group 1 and 3) obtained from double-difference tomography of field data. Locations of Castellanos and Van der Baan (2015a) are also shown for comparison. . . . .	52
3.6	3D velocity model obtained from double-difference tomography of field data overlain with the shafts and tunnel network. . . . .	53
3.7	Synthetic characteristic tests comparing the true velocity models used to generate the synthetic data and the recovered velocity models using the same methodology and parametrization as used in the case of field data. . . . .	55
3.8	3D view of the microseismic event locations and the mapped faults. . . . .	58
3.9	A comparison of the velocity map obtained from double-difference tomography and the density map at 0.45 km depth. . . . .	60
3.10	A comparison of the velocity model obtained from passive seismic tomography with the geotechnical domains and the mapped geological faults. . . . .	62
4.1	Waveforms of a mine blast signal, a microseismic event and the vibrations due to a rock crusher recorded at a common receiver. . . . .	71
4.2	Temporal distribution of blasting, volume of rock removed per day, and the microseismic event count per day during January 2011. . . . .	72
4.3	Temporal distribution of recorded seismograms and blasting activity on daily basis during January 2011. . . . .	74

4.4	Map view of the horizontal tunnel network at 480 m depth overlain with the micro-seismic event locations and the spatial location of the construction sites. . . . .	76
4.5	Map view of the tunnel layout at depths of 0.420 km, 0.460 km, 0.480 km, and 0.500 km. . . . .	79
4.6	Stress perturbations due to an oblate spheroidal inclusion for different volume fractions of rock and void space. . . . .	88
4.7	Map view of stress distribution around the vertical cylindrical cavity. . . . .	89
4.8	Stereonet plots of the Coulomb failure function in the regional stress state and the Coulomb stress change due to the introduction of the horizontal tunnel network. . .	91
4.9	Coulomb stress changes computed for two fault planes as a function of their spatial position. . . . .	94
4.10	Event locations for the two largest multiplet groups, Group 1 and Group 3 projected on top of the computed Coulomb stress changes. . . . .	96
4.11	Stress perturbations due to a single tunnel modeled as a horizontal cylindrical cavity.	98
4.12	Schematic diagram of the Mohr-Coulomb failure criterion showing the positions of some of the geological faults. . . . .	103
4.13	Peak ground velocity of the vibrations due to a rock crusher as a function of the receiver distance from the rock crusher. . . . .	105
5.1	Elastic stress perturbations induced by a penny-shaped hydraulic fracture. . . . .	120
5.2	Evolution of pore pressure distribution with time due to a uniformly pressurized penny shaped crack. . . . .	121
5.3	Evolution of Coulomb failure function with time and triggering of the micro-seismic events due to a uniformly pressurized penny-shaped crack. . . . .	122
5.4	Distance of hydraulic fracture tip and pore pressure diffusion front from a point injector as a function of time. . . . .	124

5.5	Distance of hydraulic fracture tip from the injection point as a function of time for different values of the fracture toughness, $K_{ic}$ , the volume injection rate, $Q_i$ , the fluid leak-off coefficient, $C_l$ , and the elastic constants of the medium. . . . .	125
5.6	Microseismicity induced in Barnett Shale due to hydraulic fracturing (data are taken from Shapiro and Dinske (2009)) showing the borehole pressure, fluid flow rate, and the time-distance plots of the microseismic events. . . . .	128
5.7	Hydraulic fracturing induced microseismicity at the Carthage Cotton valley gas field (data are taken from Shapiro and Dinske (2009)) showing the borehole pressure, fluid flow rate, and the time-distance plots of the microseismic events. . . . .	129
5.8	Coulomb stress changes computed for faults of all orientations in 3D near the tip of the fracture cavity and near the wall of the cavity directly above its center. . . . .	132
5.9	Event locations of the Carthage Cotton valley gas field microseismic data taken from Rutledge and Phillips (2003). . . . .	134
5.10	Schematic diagram showing the evolution of a planar hydraulic fracture and the associated microseismicity over time. . . . .	138
6.1	Treatment plot of stage 7 of the hydraulic fracturing stimulation of the Cardium formation in the Pembina oil field. . . . .	145
6.2	P and S velocity models obtained by averaging sonic logs using 5 m blocking. . . . .	148
6.3	A typical microseismic event recorded during stage 7 at well 2 showing manual time picks. . . . .	153
6.4	Microseismic event locations of stage 7. Geophones are shown by black triangles. . . . .	154
6.5	Modeled ray paths from microseismic events identified in stage 7 to the receivers in the two monitoring wells. . . . .	156
6.6	Elastic stress perturbations induced by a penny-shaped hydraulic fracture. . . . .	157

6.7 Velocities around a hydraulic fracture for a vertically propagating wave by superimposing the elastic stress perturbations due to the opening of the fracture on the effective stresses before hydraulic fracturing (far-field stresses minus the hydrostatic pore pressure). . . . . 158

6.8 A comparison of the measured and the modeled splitting delay times at the two monitoring wells. . . . . 159

6.9 A comparison of the measured and the modeled delay times at the well 1 and well 2 by varying the stress magnitudes and the third-order elastic constants. . . . . 161

# Chapter 1

## Introduction

### 1.1 Background

#### 1.1.1 Microseismic data analysis

Microseismic events are earthquakes with negative moment magnitudes and are not noticeable to humans on the earth's surface. These events are recorded using a highly sensitive network of geophones/seismometers preferably close to the source locations. The geophones can be placed downhole in monitoring wells or on the ground surface. The data recorded downhole generally have high signal-to-noise ratio as compared to those recorded near the ground surface. A continuous recording of microseismic events can help in understanding subsurface deformations in the case of hydraulic fracturing stimulations of unconventional hydrocarbon reservoirs (Rutledge and Phillips, 2003; Maxwell *et al.*, 2002), mine developments (McGarr *et al.*, 2002), Enhanced Geothermal Systems (Moeck *et al.*, 2009), and carbon dioxide sequestration (Verdon *et al.*, 2013; Goertz-Allmann *et al.*, 2014).

Since microseismic events are low magnitude earthquakes, the standard methods used in seismology for processing earthquake data can be applied to microseismic data analysis. However, these methods should be modified to account for the poor signal-to-noise ratio and inadequate

acquisition geometry often encountered in the case of microseismic monitoring. For example, microseismic monitoring is mostly carried out with geophones in a single observation well. Therefore event location is performed by combining polarization (back azimuth) information with travel times. These event locations can provide information about the subsurface region undergoing deformation. In the case of hydraulic fracturing of hydrocarbon-bearing shales and tight sands, microseismic event locations help in identifying the fracture geometry. The fracture dimensions estimated from microseismic event locations are used to compute stimulated reservoir volume which has implications for subsequent production. The event locations can be further used to detect out-of-zone fracture growth in real time and the hydraulic fracturing treatment parameters can be adjusted accordingly. However microseismic event locations give information about the seismically active region only. In this thesis, we intend to explore the possibility of obtaining medium properties like seismic velocity and anisotropy using microseismic data.

In global seismology, seismic tomography has been instrumental in exploring the Earth's heterogeneity with the 3-dimensional velocity models obtained from geophysical inversion of recorded seismograms. The pioneering work on seismic tomography revealed velocity images of local crustal structure (Aki and Lee, 1976; Aki *et al.*, 1977) as well as that of the Earth's mantle (Dziewonski *et al.*, 1977). Aki and Lee (1976) performed simultaneous inversion for event locations and crustal velocity structure using local earthquake arrival time data. This simultaneous inversion method was further developed by Thurber (1983) and is commonly known as local earthquake tomography.

The application of local earthquake tomography in case of microseismic recordings in exploration settings is challenging due to two reasons, (1) the low signal-to-noise ratio due to the small magnitude of the microseismic events cause considerable uncertainty in arrival time picks, and (2) the events are tightly clustered in space which combined with poor recording geometry do not constrain the 3D velocity model. The first problem can be tackled by computing the highly accurate differential arrival times using the events with similar waveforms (Poupinet *et al.*, 1984; Got *et al.*, 1994; Waldhauser and Ellsworth, 2000; Castellanos and Van der Baan, 2013). These differ-

ential arrival times can be used for tomographic inversion under the condition that the receivers provide sufficient azimuthal coverage. The second problem of poor ray path coverage due to poor acquisition setup does not allow seismic tomography for a 3D velocity model, yet we can get useful information about the seismic anisotropy using shear wave splitting data. Since microseismic events are mostly dominated by shear waves, reliable shear wave splitting data can be obtained. We give a brief overview of double-difference tomography and shear wave splitting in the next subsections.

#### **1.1.1.1 Double-difference tomography**

The accuracy of estimated velocities from tomographic inversion of arrival times depends strongly on the picking quality. The waveform cross-correlation techniques (Poupinet *et al.*, 1984; Got *et al.*, 1994) provide reliable differential arrival times which are at least an order of magnitude more accurate as compared to the picked absolute arrival times. The differential arrival time here refers to the difference between the arrival times of two events at a common receiver but is computed using waveform cross-correlation and not simple subtraction. Waldhauser and Ellsworth (2000) use these differential arrival times to obtain high-resolution event locations. Zhang and Thurber (2003) developed double-difference tomography algorithm for simultaneous inversion of event locations and velocity parameters using differential arrival times.

The double-difference tomography method (Zhang and Thurber, 2003) solves a non-linear inverse problem iteratively by linearizing it around an initial solution and minimizing the data misfit in the least squares sense. Zhang and Thurber (2003) apply a relative weighting between differential and absolute arrival times starting with a higher weight on the absolute times for first few iterations and then down-weighting the absolute times and increasing weight on the differential times. However, Monteiller *et al.* (2005) show that it is not strictly necessary to solve both absolute and double-difference equations simultaneously to resolve the absolute locations. In fact, Menke and Schaff (2004) show that double-difference equations can constrain absolute locations better than

purely absolute approaches owing to the high accuracy of differential arrival times, provided the events form dense, continuous and extended correlated sets. Since microseismic data often contain many events with similar waveforms, double-difference tomography can provide high-resolution event locations and velocity models.

The tomographic inversion is generally ill-conditioned and is stabilized by applying damping and smoothing regularizations. First order smoothing constraints are commonly applied to the slowness perturbations between neighbor grid nodes. Zhang and Thurber (2003) penalize the model roughness defined as the difference of the slowness perturbations at neighbor grid points divided by the distance between the grid nodes. The smoothing and damping parameters are selected on the basis of trade-off curves between model norm and data misfit.

### **1.1.1.2 Shear wave splitting**

Shear wave splitting refers to the break down of a shear wave on entering an anisotropic medium into fast and slow shear waves which are polarized orthogonally to each other (Crampin, 1981). The shear wave splitting along a ray path is characterized by two parameters namely the polarization of the fast shear wave ( $\psi$ ), and the time lag ( $\delta t$ ) between the fast and the slow shear waves (Silver and Chan, 1991; Teanby *et al.*, 2004b). The seismic anisotropy of a medium can be characterized by measurements of the shear wave splitting parameters along various ray paths.

Seismic anisotropy can originate due to three processes (Savage, 1999), (1) thin layers of otherwise isotropic material with different velocities, or aligned heterogeneities, (2) presence of aligned discontinuities like preferential crack orientation, and (3) preferred alignment of anisotropic minerals. Shear wave splitting has been successfully used to study crustal and mantle anisotropy. Teanby *et al.* (2004a) measured shear wave splitting from microseismic events recorded at the Valhall oil reservoir in the North Sea and suggested that the temporal variations in splitting parameters can be stress induced. The temporal variations in splitting parameters measured from microseismic data recorded during hydraulic fracturing of unconventional hydrocarbon reservoirs have been used to

infer fracture evolution (Wuestefeld *et al.*, 2011).

### **1.1.2 Geomechanics and microseismic triggering**

It is important to understand the geomechanical context in which microseismic events occur. For example, hydraulic fracturing results in the pore pressure changes in surrounding rocks due to fluid diffusion and/or leak-off which trigger the microseismic events. The spatiotemporal evolution of microseismic events has been well described by the pore pressure diffusion process (Shapiro *et al.*, 2002; Rothert and Shapiro, 2003). Poroelastic stresses have also been invoked to explain the observed microseismicity (Rozhko, 2010; Segall and Lu, 2015). All these studies try to explain the physical processes responsible for triggering seismicity by modeling the spatiotemporal distribution based on the injection parameters and the material and fluid transport properties of the stimulated rocks. Understanding the physical processes triggering microseismicity has important implications for (1) optimizing hydraulic fracturing for efficient well completions by changing the treatment parameters, and (2) mitigating the risks associated with induced seismicity due to anthropogenic activities like hydraulic fracturing and wastewater disposal.

Earthquakes occur due to brittle failure of rocks along a fault when the shear stresses become large enough to overcome the normal stresses that combined with friction prevent a locked fault from slipping (Freed, 2005). This is mathematically formulated in terms of the Coulomb failure criterion. In the case of static triggering the stress perturbations which promote or inhibit earthquakes leave a permanent imprint on the in situ stress field. King *et al.* (1994) computed the static Coulomb stress changes due to the 1992 M=7.4 magnitude Landers earthquake on the surrounding faults. The aftershocks were mostly located in the region of increase in the Coulomb stress due to the main shock. On the other hand, dynamic triggering refers to the earthquake occurrence due to the transient stress changes caused by the passage of the seismic waves through the medium (Hill *et al.*, 1993; Kilb *et al.*, 2000). It has been invoked to explain the increase in seismic activity due to large earthquakes such as 1992 M=7.4 Landers and 2002 M=7.9 Denali, Alaska earthquake at

distances beyond 1000 km from the epicenter (Hill *et al.*, 1993; Husen *et al.*, 2004). At these distances, the static Coulomb stress changes drop below the daily lunar tidal stress change magnitudes whereas the dynamic stress changes due to the passage of seismic waves are at least two order of magnitudes greater than the tidal stresses (Freed, 2005). The remotely triggered seismicity occur immediately or within few minutes of passage of seismic waves, however, aftershocks last between several hours to days.

The stress changes can also be caused by anthropogenic activities like underground mine development, hydraulic fracturing, wastewater disposal and reservoir impoundment. The earthquakes resulting from these activities are termed as induced seismic events. Sometimes these events may be classified as "induced" if the stress changes due to the anthropogenic activity are comparable in magnitude to the ambient stresses or "triggered" if the stress changes are only a small fraction of the ambient level (McGarr *et al.*, 2002). However, in this thesis, we use the term "induced" to include both the "triggered" and "induced" seismicity. Induced seismicity is often characterized by their close spatial and temporal correlations with the anthropogenic activities. Davis and Frohlich (1993) provide a set of criteria for proper assessment of induced seismicity.

The main cause of induced seismicity due to a specific industrial activity can be established by continuously monitoring the operational parameters used during that activity. For example, in the case of underground mining, the volume of rock removed, the mining technique, and the spatial location and geometry of excavation front are important factors affecting induced seismicity (McGarr *et al.*, 2002). Similarly, fluid injection rate, the volume of fluid injected and injection pressure are important for fluid injection-induced seismicity as observed in the case of hydraulic fracturing and wastewater disposal. A temporal correlation of these operational parameters with the recorded seismicity can help in identifying the root cause of seismicity.

### **1.1.3 Integrated analysis: Relating velocity and anisotropy derived from microseismic data with stress changes triggering microseismicity**

The elastic properties of rocks depend upon the applied stresses and pore pressure. Laboratory experiments have confirmed that seismic P- and S-wave velocities tend to increase with increasing confining pressure (Nur and Simmons, 1969a). With the increase in confining pressure the compliant parts of the pore spaces including microcracks and compliant grain boundaries close thereby making the rock more stiffer. This results in the observed increase in the seismic velocities with increasing confining pressure (Nur and Simmons, 1969a).

In the case of non-hydrostatic stresses, there is a similar increase in seismic velocities. However, due to the preferential closure of cracks perpendicular to the maximum compressive stress, the resulting velocity field is anisotropic (Nur and Simmons, 1969a). Thus field measurements of velocity variations and anisotropy can be used to constrain in-situ stresses (Nur, 1976; Crampin, 1978) and pore pressure changes (Nur and Simmons, 1969b; Nur, 1987). However, a correct interpretation of velocity variations and anisotropy requires theoretical tools to quantify velocity changes in terms of applied stresses and pore pressure changes.

There are several approaches to quantify the stress-velocity relationship which can be classified into two groups, (1) models based on the micromechanics of the rocks taking into account the various crack parameters, and (2) phenomenological models which ignore the actual micromechanics of the rock. The approach of Mavko *et al.* (1995) and Sayers and Kachanov (1995) falls under the first category. These approaches are related to the effective medium theory of fractured media (Kachanov, 1993). However, these methods rely on experimental observations to get stress dependence of crack density or compliance. Gurevich *et al.* (2011) compute the effective compliance by assuming that the cracks specific area have an exponential normal stress dependency. Thus Gurevich *et al.* (2011) model does not require laboratory measurements of the crack compliances as a function of the applied stresses.

Third order elasticity theory (Thurston and Brugger, 1965; Thurston, 1965; Sinha, 1982; Nor-

ris *et al.*, 1994) is an example of the phenomenological approach since it is not related to any crack geometry. This theory gives analytical expressions for the stress-dependent effective elastic constants of the medium in terms of the elastic constants in a reference state (initial state before application of the stress), the third-order elastic constants and the finite strains due to applied stress. The potential energy in linear elasticity is a quadratic function of strains, but it includes cubic terms in third-order elasticity which accounts for stress-dependent elastic properties. Non-linear elasticity has been used for explaining stress-induced anisotropy in laboratory experiments (Johnson and Rasolofosaon, 1996; Winkler *et al.*, 1998) and boreholes (Sinha and Kostek, 1996).

## 1.2 Motivation and contribution

Microseismic data recorded in exploration settings are mainly processed to yield event locations. These event locations are interpreted in terms of the subsurface deformations, eg, fracture development in the case of hydraulic fracturing or excavation damaged zone during underground mining. However, the recorded data contain a lot more information about the medium through which the seismic waves have traveled. One of the motivations for this thesis is to extract information from microseismic data about the surrounding medium in terms of velocity. The velocity models thus obtained can give insights into local geology beyond the seismically active regions.

Microseismic events are essentially very low magnitude earthquakes; studying their triggering mechanisms can have implications for understanding large magnitude earthquakes of tectonic origins. Furthermore, it has direct consequences for understanding the triggering mechanisms of felt earthquakes due to hydraulic fracturing and wastewater disposal. In this thesis, we are motivated to understand the role of elastic stress perturbations and/or pore pressure diffusion in triggering of microseismicity due to different anthropogenic activities namely underground mine development and hydraulic fracturing.

Elastic stress and pore pressure perturbations are important in triggering of seismicity. The stress perturbations affect seismic velocity but the interpretation is not straightforward. One of our

objectives in this thesis is to provide a framework for mapping the stress perturbations directly into velocity changes in a hydraulic fracturing environment.

The major contributions of this thesis are listed below.

1. We analyze various causes and mechanisms which trigger microseismicity during underground mine development.

2. We present a workflow for application of double-difference tomography to the microseismic dataset and interpretation of inverted velocity model in terms of geological structures and geotechnical zones.

3. We develop an analytical framework for computing elastic stress perturbations due to mining and hydraulic fracture cavities using Eshelby's equivalent inclusion method.

4. We show that the elastic stress changes ahead of the crack tip due to hydraulic fracture opening facilitate failure and this process affects the spatiotemporal distributions of microseismicity.

5. We demonstrate that the shape of the pore pressure diffusion front depends upon the shape of the hydraulic fracture cavity. Therefore, elongated microseismic clouds can be obtained even with an isotropic diffusivity.

6. We propose a forward model to compute stress-induced seismic anisotropy due to hydraulic fracturing using third-order elasticity. This stress-induced seismic anisotropy is subsequently used to model the shear wave splitting parameters.

## **1.3 Thesis overview**

**Chapter 2** gives an overview of the case studies examined in this thesis. Case study 1 corresponds to the microseismic data acquired during an underground mine development. Case study 2 corresponds to the microseismic data acquired during hydraulic fracturing of an unconventional hydrocarbon reservoir. The geological and operational settings in which the microseismic data have been acquired are discussed. The microseismic data examples are provided and the rationale for the choice of data analysis and modeling methodologies is explained with respect to individual

case studies.

**Chapter 3** shows the application of double-difference tomography on a microseismic dataset acquired during an underground mining development (Case study 1). Based on the geometry of the microseismic event clusters and a comparison with the mapped faults, we present a hypothesis that the events occur on an unmapped geological fault. The inverted 3D velocity model shows lateral velocity contrasts which correlate well with the known geotechnical zones in the mine.

**Chapter 4** analyzes the causes and mechanisms that induce seismicity during underground mining development. Using Case study 1 as an example, the spatiotemporal distribution of microseismicity is compared with various mining activities to identify the main cause of microseismicity. The perturbations in regional stresses due to the horizontal tunnel network and vertical shafts are then computed to investigate the likelihood of fault reactivation based on their orientations and spatial locations with respect to the mine layout.

**Chapter 5** highlights the role of the opening of the hydraulic fracture cavity in triggering microseismicity. The fracture opening affects the in situ elastic stresses and the pore pressure diffusion profiles, and subsequently potential of shear slippages along pre-existing fault planes. The elastic stress changes thus affect the spatiotemporal distributions of microseismicity.

**Chapter 6** proposes a quantitative forward model for mapping induced stresses due to hydraulic fracturing into seismic anisotropy based on third-order elasticity. The shear wave splitting parameters are subsequently modeled by simulating a real hydraulic fracturing job and acquisition set up (Case study 2). A comparison of the modeled and measured delay times provides insights into the possible source of the observed anisotropy.

**Chapter 7** presents the conclusions of the thesis and suggests possible directions for future research.

## Chapter 2

# Case studies: Data background and geological setting<sup>1</sup>

### Summary

The microseismic data used in this thesis are acquired in two very different operational settings, (1) microseismic data recorded during an underground mining development, and (2) microseismic data recorded during the hydraulic fracturing stimulation. The geological settings, the acquisition setup, and the recording duration vary widely for these microseismic datasets. We give an overview of the microseismic data and the geological settings for each case. We also highlight the rationale for our choice of data analysis and modeling methodologies based on the specific case study.

---

<sup>1</sup>A manuscript including parts of this chapter is in preparation for submission to *Bulletin of the Seismological Society of America*.

## **2.1 Case study 1: Microseismic data recorded during underground mine development**

### **2.1.1 Introduction**

This case study involves the microseismicity recorded during the development of an underground uranium mine located 660 km north of Saskatoon in Saskatchewan, Canada. It is the world's highest grade known uranium mine with grades over 100 times of the world average for uranium deposits. The uranium deposit was first discovered in 1981 by diamond drill testing of the geophysical anomalies detected by a geophysical reconnaissance survey. The uranium mineralization is along an unconformity contact which separates the overlying sandstone containing water at a significant pressure from the highly altered basement rock. Therefore, the construction of shafts and access tunnels is very challenging and the mine development program has been delayed due to three water inflow incidents between the period of 2006 to 2008. A microseismic monitoring system is installed to detect subsurface deformation. We use the data recorded during January 2011 in this case study. We give the details of the geological setting and the mining operations, the microseismic data, and our objectives in the next subsections.

### **2.1.2 Geological setting and mine layout**

The underground uranium mine is located in the eastern part of the Athabasca Basin of northern Saskatchewan, Canada at the unconformity contact separating Helikian sandstones of the Athabasca Group from Aphebian metasedimentary gneisses and plutonic rocks of the Wollaston Domain. The sandstone overlying the basement rock contains large volumes of water at significant pressure. The uranium deposit has a shape of a flat-lying lens with an average thickness of about 5.4 m and shows remarkable lateral geological continuity. Uranium mineralization processes are generally associated with complex hydrothermal systems that involve repeated fault slip and fluid flow along major lithospheric structural features. Uranium deposits occur where faults in

the crystalline basement rocks cut into the overlying sediments, creating fluid paths allowing the interaction of the ore-forming fluids with the host rocks (Fayek, 2013).

A high-resolution seismic survey in the Athabasca basin (Hajnal *et al.*, 1997) outlined a number of steeply dipping imbricate fault zones. Some of these fracture zones intersect the overlying sandstones and extend several thousand meters into the basement. The dominant fault system is striking NE-SW as shown in Figure 2.1a (Bruneton, 1993). The faults are dipping SE with dips greater than 45 degrees. Li *et al.* (2013) found three dominant systems of sub-vertical basement faults in the Southeastern Athabasca basin trending NE, N-NW, and NW. The most frequently occurring faults are NE-trending with strikes ranging from 030° to 075° (average 050°). The second most encountered faults are N-NW-trending having strikes ranging from 340° to 360° (average of 352°). The least frequently occurring fault system is trending NW with strikes ranging from 300° to 330° (average 315°). The existence of various basement faults cross-cutting into the overlying sediments which acted as known fluid pathways provides ample opportunity for fault reactivation and thus induced microseismicity.

This study focuses on the microseismic data acquired during an underground mine development in January 2011. However, the mine development continued after that and the mining company added more details to their geological models in terms of the number of faults, their spatial locations, and orientations. The mining company provided geological cross-sections through the mine in 2012 and updated them in 2016. Here, we first show a North-South cross-section through the mine based on the technical information available in the year 2012 (Figure 2.1b). Red bold lines mark the boundaries of the eight geotechnical zones (I-VIII) classified by the mine operating company based on the rock quality inferred from the drilling and development during test mining and rock mechanics studies. Table 2.1 lists the rock type, quality, and classification based on the Rock Mass Rating (RMR) system for all eight geotechnical zones. The study region extends 600 m laterally along Easting and Northing and up to a depth of 600 m from the mine surface (reference datum with depth equal to 0 m). The unconformity is around 450 m depth from the surface and hosts the high-grade mineralization. The crescent-shaped cross-sectional outline of the uranium

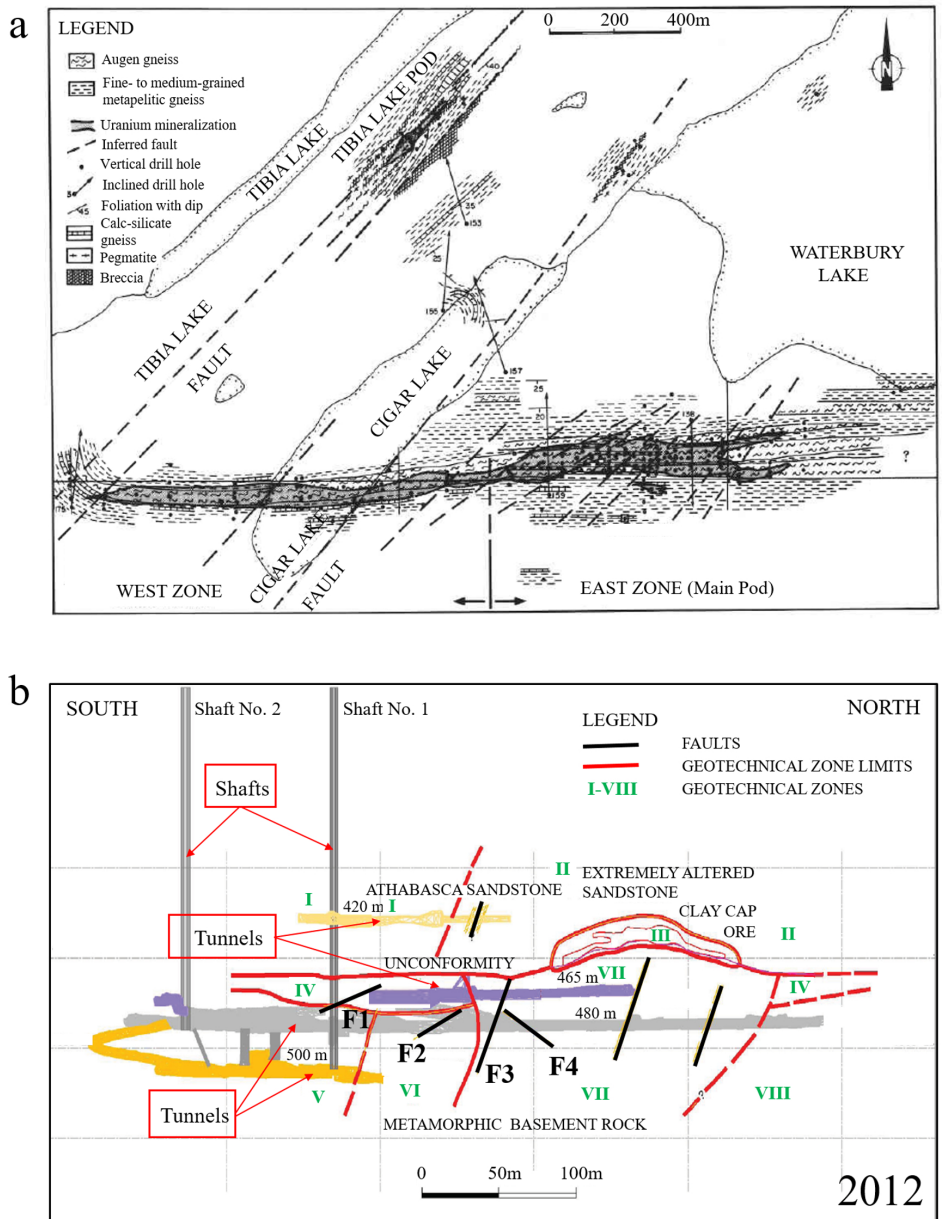


Figure 2.1: (a) Schematic geological map of the area around the study region showing major inferred faults, various lithologies and zone of uranium mineralization taken from Bruneton (1993), ©2008 Canadian Science Publishing or its licensors and reproduced with permission. The major faults are striking NE-SW. (b) Schematic North-South cross-section through the mine showing vertical shafts, horizontal tunnels and inferred faults based on the technical information available in the year 2012 (Courtesy: anonymous company). We have annotated four fault traces as **F1**, **F2**, **F3** and **F4**.

Table 2.1: Geotechnical zones within the mine based on the rock quality

Geotechnical Zone	Name	Rock quality	Rock mass classification (RMR)
I	Sandstone-unaltered	Good to excellent	60-70
II	Sandstone-altered	Poor to extremely poor	<30
III	Ore zone and Clay Cap	Fair to poor	Not determined
IV	Regolith	Fair to good	<40
V	Biotite Metapelite	Good to excellent	41-70
VI	Meta-Arkose	Fair to very good	65-70
VII	Graphitic Metapelite-Altered	Extremely poor to good	5-50
VIII	Graphitic Metapelite-weakly altered	Fair to good	about 50

deposit closely reflects the topography of the unconformity. There are various tunnels at depths of 420 m, 465 m, 480 m and 500 m. There are two vertical shafts to access the tunnel networks at different depths. Shaft No. 1 extends from surface to a depth of 500 m and provides direct access to the 480 m level. It has a circular cross-section with an internal diameter of 4.9 m. Shaft No. 2 is located approximately 90 m south of Shaft No. 1 and has an internal diameter of 6.1 m. Shaft No. 2 extends from surface to a depth of 480 m. Shaft No. 1 acts as the main service and access shaft.

Figures 2.2 and 2.3 show the North-South cross-sections through the mine provided by the mine operating company in their technical report updated in the year 2016. The crescent-shaped outline of the ore-deposit and the various clay altered zones around the ore are clearly highlighted in Figures 2.2 and 2.3. As compared to Figure 2.1b, Figures 2.2 and 2.3 show a large number of faults cutting through the 480 m level towards North close to the ore deposit. Moreover the fault **F4** annotated in Figure 2.1b is dipping in opposite direction when compared to the faults visible in Figures 2.2 and 2.3. Fault **F1** near shaft 1 in Figure 2.1b is absent in Figure 2.2. The differences in the geological fault traces between the 2012 and 2016 cross-sections can be attributed to the fact that continued mine development over the years (from 2012 to 2016) provided direct access to the previously inaccessible regions thereby enabling detailed fault mapping and resulting in a more

complex mapped fault network in the 2016 cross-sections. As for the cross-sections available from the 2016 technical report, Figure 2.3 shows more faults near the 480 m mine level towards South as compared to that in Figure 2.2. This may be attributed to the fact that the two N-S cross-sections (Figures 2.2 and 2.3) are taken at different values of Easting.

Another visible difference between the 2012 and 2016 cross-sections (Figures 2.1b-2.3) is in the defined geotechnical zones. Figure 2.1b shows eight geotechnical zones classified on the basis of lithology, degree of alteration, rock quality and a modified rock mass rating. This classification is based on the drilling and development during test mining and rock mechanics studies. On the other hand, Figure 2.3 shows only three geotechnical zones namely RM1 with RMR between 0-20, RM2 with RMR between 20-40 and RM3 with RMR greater than 40. In Figure 2.3 both the unaltered sandstone and unaltered basement rock are classified into the RM3 domain because of weak to no clay alteration and weak to moderate fracturing. In Figure 2.1b, the geotechnical zones I, V, VI, and VIII have RMR values greater than 40 (Table 2.1) so they can be grouped together as the RM3 domain according to the classification shown in Figure 2.3. This is despite the fact that they have different lithologies and a different degree of alteration. Similarly, the zones RM1 and RM2 above the unconformity contact in Figure 2.3 corresponds to zones III and II respectively in Figure 2.1b, whereas those below the unconformity are grouped together as zone VII (RMR 5-50) in Figure 2.1b. Thus, the geotechnical evaluations in Figures 2.1b-2.3 are consistent and the visible differences are mainly due to the fact that the classification in Figure 2.1b is much more detailed based on multiple factors such as the lithologies and rock quality.

Figure 2.4 shows the map view of the mine at a depth of 480 m provided by the mining company in the technical report updated in the year 2016. The geotechnical classification is as shown in the N-S cross-section in Figure 2.3 with three zones defined as RM1, RM2 and RM3 with RMR values in the range 0-20, 20-45 and >45 respectively. Fault traces are shown by black dashed lines. A large number of fault traces can be observed striking in the E-W, NE-SW, N-S, NNW-SSE and NW-SE directions. The dominant fault strike is in the E-W direction. The position of shaft 1 is shown by a black arrow. The region near the shaft 1 is delineated by a number of faults; however,

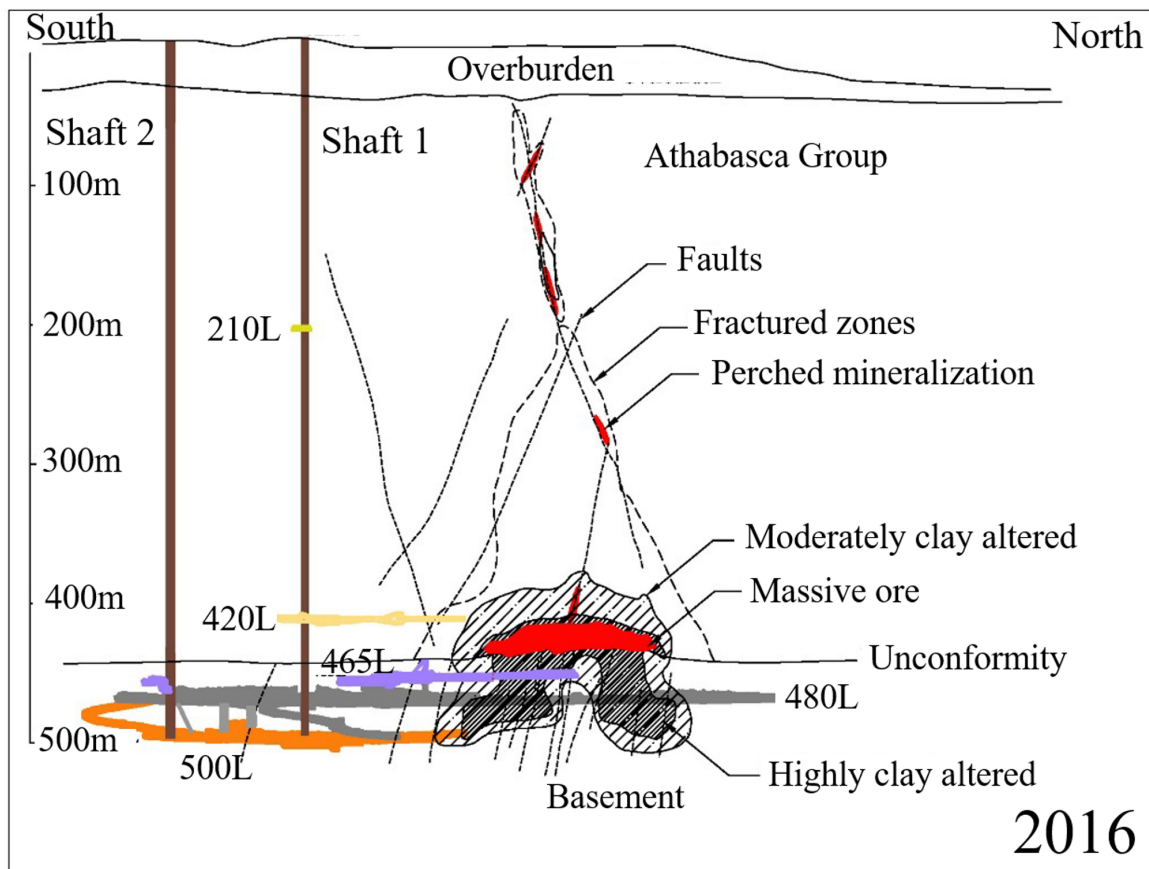


Figure 2.2: Schematic North-South cross-section through the mine showing vertical shafts, horizontal tunnels, inferred faults and the ore deposit based on the technical information available in the year 2016 (year marked in the lower right corner) (Courtesy: anonymous company).

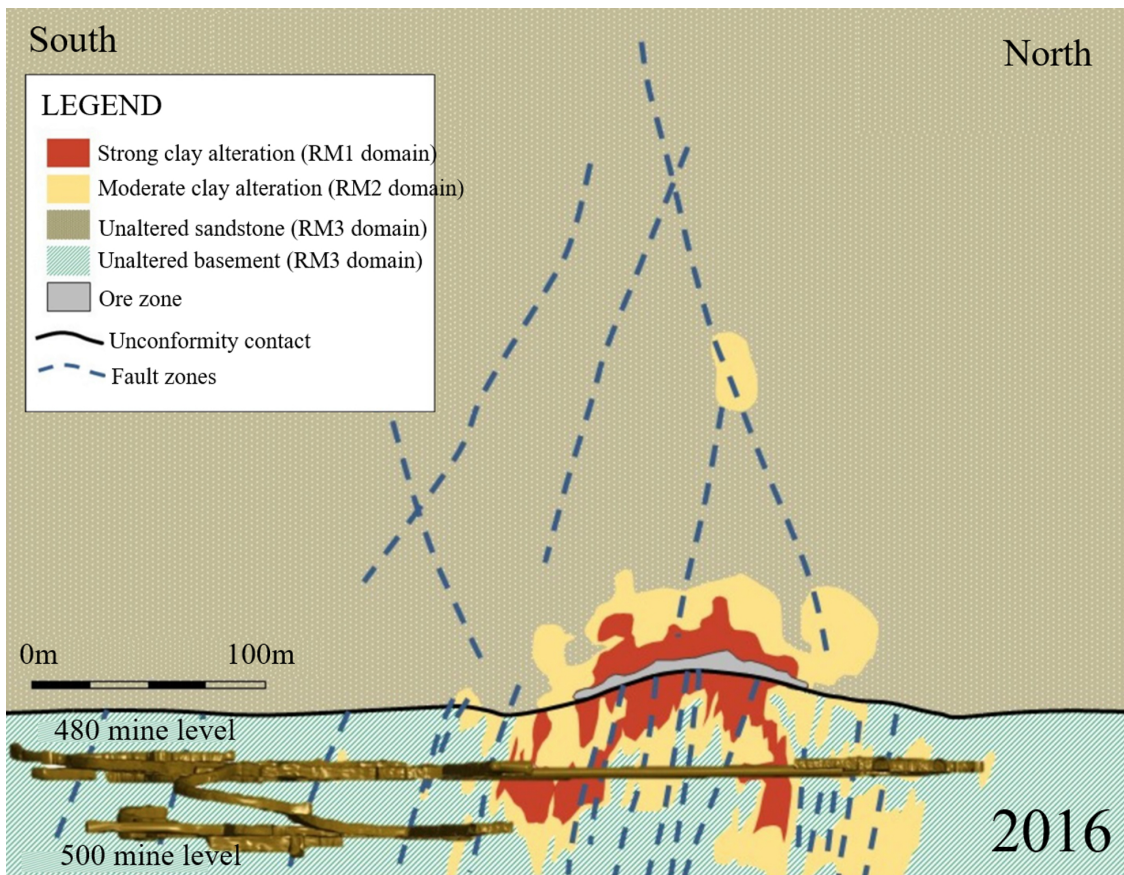


Figure 2.3: Schematic North-South cross-section through the mine showing the horizontal tunnels, inferred faults and the ore deposit based on the technical information available in the year 2016 (year marked in the lower right corner) (Courtesy: anonymous company).

there is no fault passing through the location of the shaft 1.

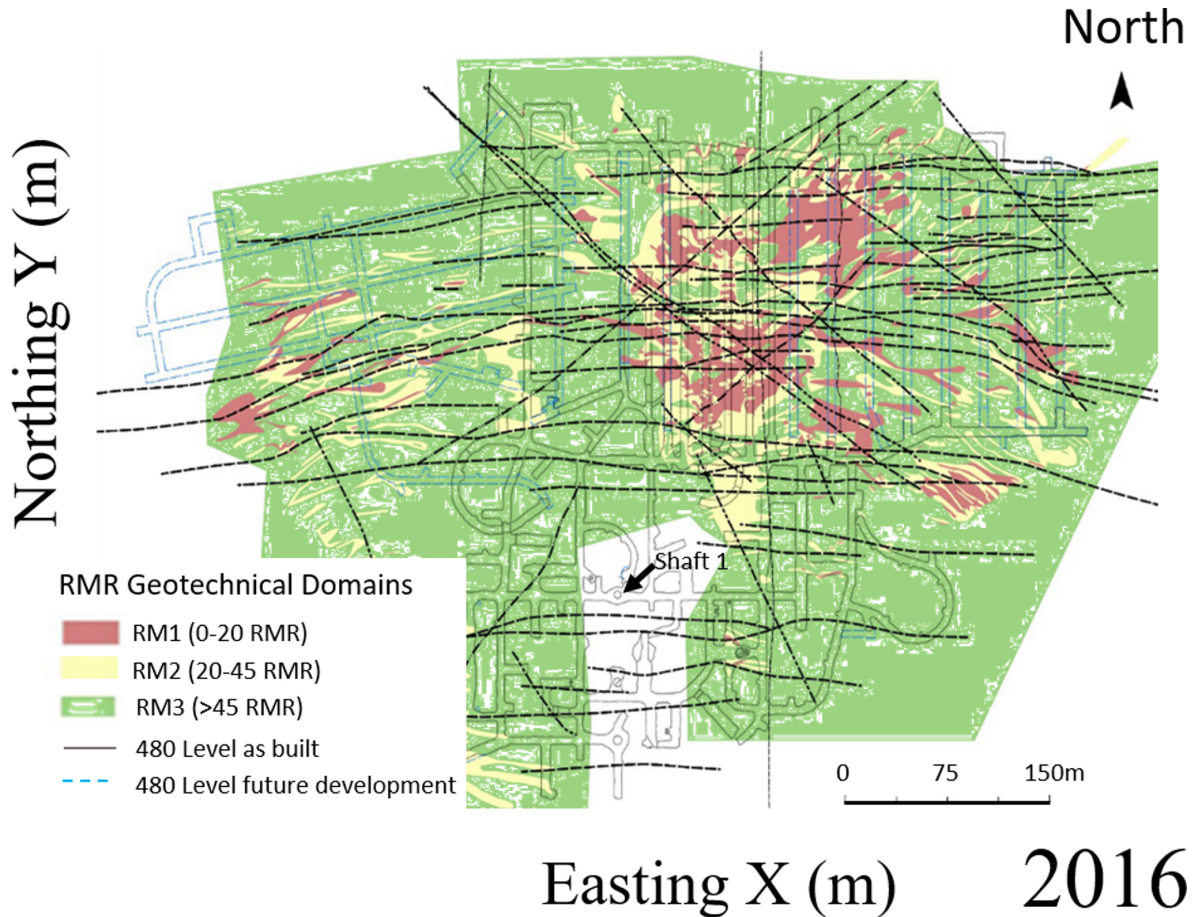


Figure 2.4: Map view of the geotechnical zones classified on the basis of the RMR values overlain with the horizontal tunnel network at 480 m depth taken from the 2016 technical report of the mining company (year marked in the lower right corner). Fault traces are projected on top of the map. The location of shaft 1 is shown by black arrow.

As noted earlier, the geological complexity in terms of the mapped fault network increased in the 2016 cross-sections (Figures 2.2 and 2.3) as compared to that in 2012 cross-section (Figure 2.1b) due to extensive mining development post 2012 thereby allowing direct outcrop access. However, in Figures 2.2 and 2.3, the Easting values at which these North-South cross-sections are taken are not specified. Therefore, we look at the 3D distribution of the faults mapped in the region by the mining company as per the information available until 2016. Figure 2.5 shows the 3D distribution of faults along with the vertical shafts and the horizontal tunnel network. For visual

clarity, only some faults close to the shafts and the horizontal tunnel network are shown as colored surfaces. We use the complete 3D distribution of faults to get their intersections along various vertical and horizontal cross-sections.

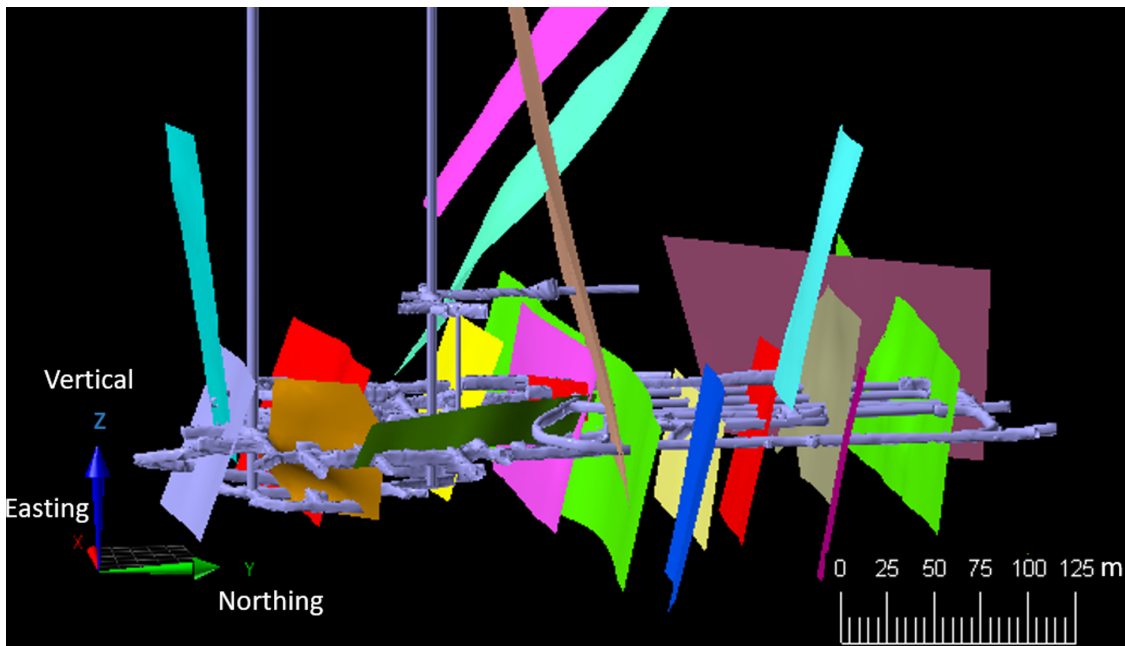


Figure 2.5: 3D distribution of faults in the study region shown as colored surfaces. The shafts and the tunnel network are shown by solid blue color.

Figure 2.6 is a composite plot showing the N-S cross-sections and the map view of the mine with the most detailed and accurate information about the geotechnical zones and the faults available as of 2016. Figures 2.6a and 2.6b show the N-S cross-sections at Easting,  $X=0.2$  and  $0.25$  km respectively with the geotechnical zone limits highlighted by bold red lines and the zones numbered from I-VIII. These geotechnical zones are taken from Figure 2.1b since that classification is most detailed as discussed earlier. The fault traces are shown by black dashed lines and are obtained from the actual 3D fault distribution. The filled blue circles show the projection of the vertical shafts and the horizontal tunnel network on the cross-sections. Figure 2.6c shows the map view at a depth of  $0.48$  km showing the various geotechnical zones overlain with the fault traces. This is the only available map showing the geotechnical zones. The geotechnical classification

in Figure 2.6c is less detailed as compared to that shown in Figures 2.6a and 2.6b, yet the two classifications are mutually consistent as discussed earlier when comparing Figures 2.1b and 2.3. Figure 2.6d shows a map view of the fault traces at a depth of 0.45 km obtained from the actual 3D distribution of faults. The fault orientations are similar to that shown in Figure 2.6c (which is at 0.48 km depth) with the dominant faults striking in the E-W direction. Other fault strikes are in the NW-SE, NNW-SSE, N-S and NE-SW directions. This composite plot (Figure 2.6) serves as a reference for the geotechnical zones and the fault distribution to be used ahead in this study.

### **2.1.3 Mining operations**

There are two main levels in the mine, the 480 m and 500 m levels, both located in the basement rock below the unconformity. There are two other levels at 420 m and 465 m which suffered major water inflow incidents during the period of 2006 to 2008. Therefore, the 420 m level, located in the sandstone above the basement rock, and the 465 m level are not in use and have been backfilled to reduce the likelihood of ground failure or water inflow. At the time of data recording, the Uranium production has not started and the access tunnels at 480 m depth are being extended in the North and South sides of the ore body. The future plan is to produce the ore from the 480 m level which is 25 m below the orebody using a non-entry mining method to mitigate the risks associated with radiation, and water inflows.

The development of access tunnels uses two different approaches, the drill and blast method using conventional ground support, and the mine development system (MDS). The mine development system (MDS) consists of a tunnel boring machine with a full face diameter of 5.1 m and the installation of pre-cast concrete tunnel lining for ground support. The mine development system method is best suited to regions of poor ground conditions. With the exception of MDS headings, the access tunnels are being developed using the conventional drill and blast mining method. The mine development is planned to take place away from known groundwater sources wherever possible.

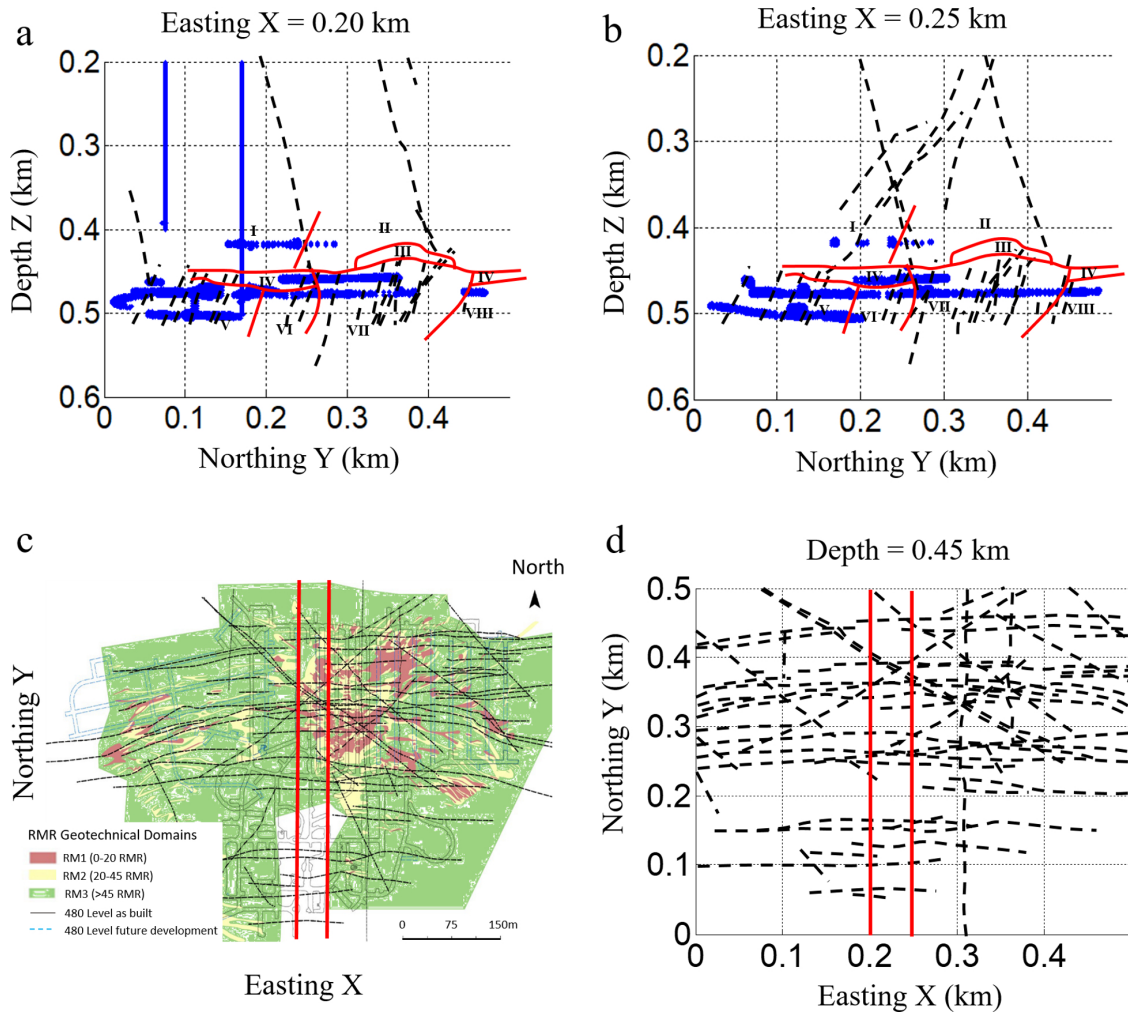


Figure 2.6: (a-b) N-S cross-sections showing the geotechnical zones (I-VIII), their boundaries (bold red lines), fault traces (black dashed lines), and the projection of the shaft and tunnel network (blue filled circles) at (a) Easting, X=0.2 km, and (b) X=0.25 km. (c) Map view at a depth of 0.48 km showing the geotechnical zones (RM1-RM3), the horizontal tunnel network (solid black and dashed blue line) and the fault traces (black dashed lines). (d) Map view of the fault traces (black dashed lines) at a depth of 0.45 km. The solid red lines in (c) and (d) mark the locations of the N-S cross-sections at X=0.2 and 0.25 km on the map views.

## 2.1.4 Microseismic data

In order to monitor zones of potential instabilities and possible water inflow incidents, a microseismic system was installed in the underground mine. A network of 7 monitoring wells each with 4 active three-components geophones recorded the microseismic events (shown by colored triangles in Figures 2.7a-2.7c). The monitoring wells provide good azimuthal coverage around the shaft and tunnel network. Figure 2.7d shows a typical microseismic event recorded by the 28 geophones. The geophones in borehole CL-272 were inactive during most of the recording period as shown by the dead traces in Figure 2.7d. We use the data recorded in January 2011. This data was also used by Castellanos and Van der Baan (2013) who identified 488 events each having at least 12 P-arrival time picks. The data were recorded with a sampling rate of 500 samples/s. All recorded events have maximum amplitudes less than those of the underground blasts. Thus their moment magnitudes are all likely to be negative.

Figure 2.8a shows the amplitude spectrum of the 3 components of the microseismic event shown in Figure 2.7d recorded at one of the receivers. The dominant frequency ranges from 100 to 150 Hz. Figure 2.8b shows the vertical components of 4 events recorded at a common receiver. The waveforms of these 4 events are highly similar which is quantified using waveform cross-correlation. Unlike Castellanos and Van der Baan (2015a) we performed cross-correlation analysis by using a window of 150 ms after the picked P-arrival times. This large window includes both the P and S- arrival phases. It seems more reasonable than a smaller window including only P arrival as used by Castellanos and Van der Baan (2013) since the onset of the S-arrival is not very clear and P and S phases are not well separated. Also, weak P-wave arrivals are difficult to identify as they may be masked due to high background noise. The events in Figure 2.8b have normalized cross-correlation values greater than 0.8. Following Castellanos and Van der Baan (2013) we define our multiplet group such that each event is connected with at least one other event in the group with mutual normalized cross-correlation coefficient greater than 0.8. We identify 277 doublets and the two largest multiplet groups (Group 1 and 3) contain 179 and 38 events respectively.

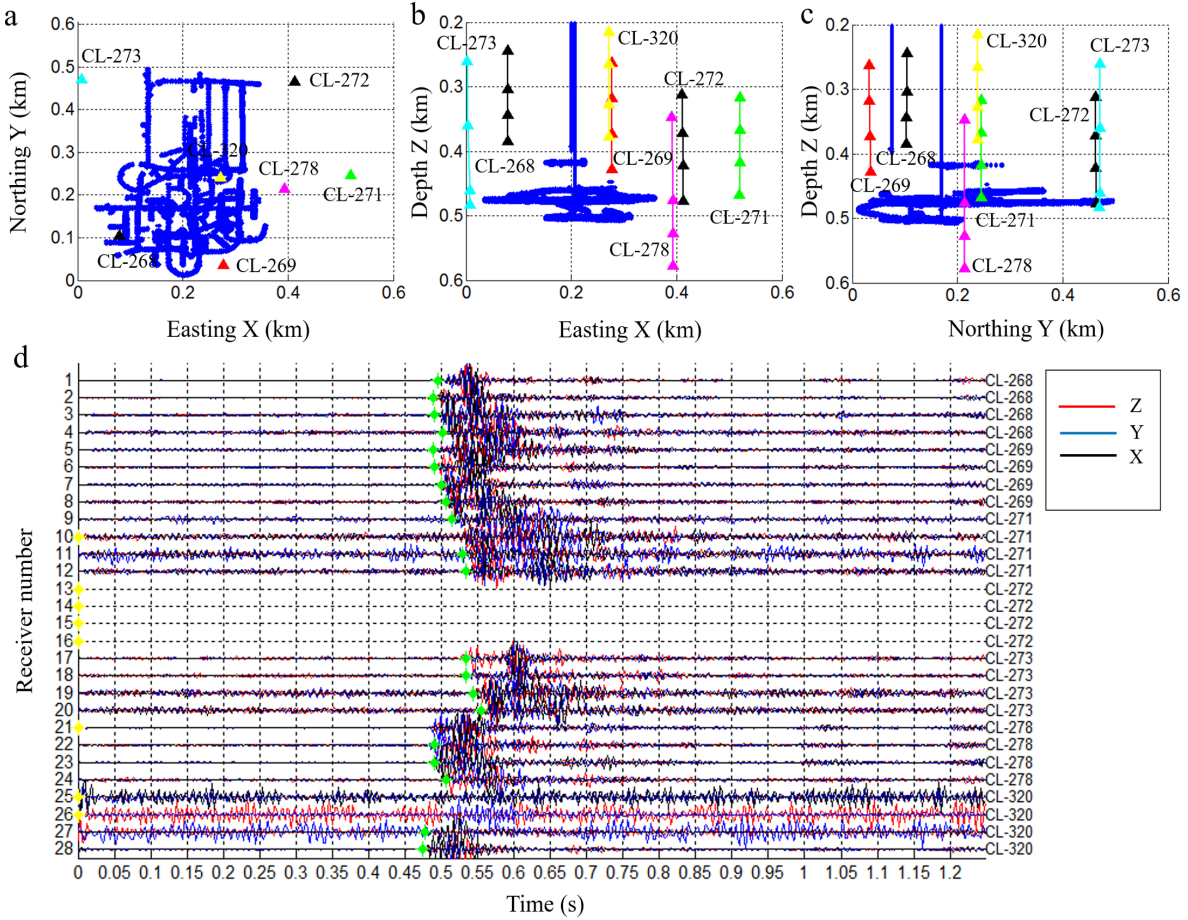


Figure 2.7: (a-c) Acquisition setup with geophones shown by colored triangles and shafts and tunnel layout shown by blue filled circles. (a) Map view. (b) East-West cross-section. (c) North-South cross-section. (d) A typical microseismic event recorded at the 28 receivers. Green points: receivers with arrival times picked. Yellow points: receivers with no picks due to dead traces or low signal to noise ratio.

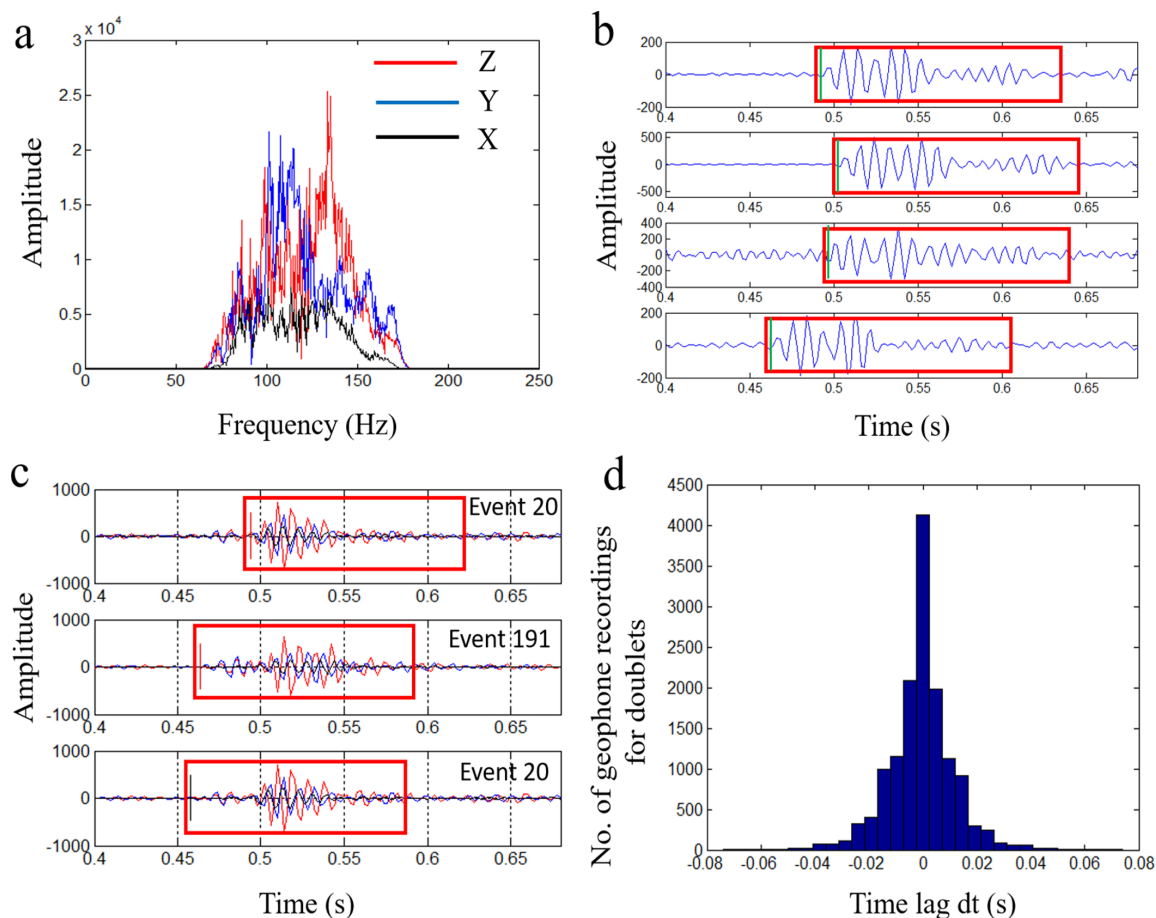


Figure 2.8: (a) Amplitude spectrum of 3 components of the event shown in Figure 2.7 at a receiver after applying a [60 80 170 180] Hz bandpass filter. (b) Vertical components of 4 microseismic events recorded at a common receiver. A large window of 150 ms (red rectangle) after the P-arrival time is used to compute cross-correlation. (c) Doublets event 20 and 191 at top and middle with manual P-phase picks shown by red lines. Event 20 with the corrected P-phase pick (black line) at the bottom shifted by the time lag (-36 ms) computed from waveform cross-correlation using 150 ms window (red rectangle). (d) Histogram of time lags between identified doublets in the data. A zero lag represents time picks at the same onset.

Figure 2.8c shows the computation of the time lag using waveform cross-correlation of events with normalized cross-correlation greater than 0.8. In Figure 2.8c two doublets namely events 20 and 191 recorded at a common receiver are shown with the manual picks (top and middle panel) shown by red color. The bottom panel in Figure 2.8c shows event 20 with the corrected P-phase pick (black line) shifted by the time lag (-36 ms) computed from waveform cross-correlation using 150 ms window (red rectangle). Figure 2.8d shows the histogram of the time lags between the identified doublets in the data. A zero lag represents two events with time picks at the same onset. A time lag of 10 ms means that the P picking is not consistent and one of the picks needs to be shifted by 10 ms to align the waveforms so that we have maximum cross-correlation at zero lag. This histogram provides a quality control on the range of likely picking errors in the dataset. Figure 2.8d indicates that for most recordings of the doublets the time lag is zero, ie, the picking quality is good. The maximum lag is up to  $\pm 76$  ms. The time lags obtained from waveform cross-correlation are then used to compute the differential arrival times. These differential arrival times have much greater accuracy than the picked absolute arrival times.

### **2.1.5 Objectives**

As mentioned in Chapter 1, the main motivation of this thesis is to extract information about the medium properties in terms of seismic velocity using microseismic data and understand the origin of the microseismic events. This mining induced microseismic data offer an opportunity to perform seismic tomography owing to the good azimuthal coverage provided by the acquisition setup, thereby obtaining a high-resolution 3D velocity model. Since the signal-to-noise ratio is low, we obtain differential arrival times using waveform cross-correlation. These reliable differential arrival times are incorporated in the double-difference tomography which involves joint inversion for event locations and a P-wave velocity model. Furthermore, we integrate the event locations, velocity model and known geological and geotechnical information to present our interpretation. The methodology, results, and interpretation are discussed in Chapter 3.

In Chapter 4, we analyze the spatial and temporal distribution of the microseismic events and identify the potential cause triggering the microseismic events. We further perform stress modeling to understand why these events are observed at specific locations, and then try to develop a triggering mechanism for these events.

## **2.2 Case study 2: Microseismic data recorded during hydraulic fracturing**

### **2.2.1 Introduction**

This case study involves the microseismic data acquired during hydraulic fracturing of low permeability hydrocarbon formations. The data were recorded on 13<sup>th</sup> and 14<sup>th</sup> January 2012 during hydraulic fracturing stimulation of Cardium formation of West Pembina field of central Alberta, WSW of Edmonton. The Pembina oil field is one of the largest conventional oil fields in the province of Alberta, Canada. It was discovered in 1953 by Mobil oil and consists of 20 individual pools that have produced nearly 1.1 billion bbls from an original oil in place of 7.46 billion bbls (Duhault, 2012). The main hydrocarbon-bearing formation is the Cardium formation of the Western Canada Sedimentary Basin which is late Cretaceous in age. We give details of the geological settings, hydraulic fracturing operations, and the recorded microseismic data used in this study in following subsections.

### **2.2.2 Geological setting**

The Cardium formation is a late Cretaceous, marine clastic containing repeated and stacked coarsening upward successions of silty mudstones through siltstones to very fine to fine-grained sandstones. The Cardium formation overlies the mudstones of the Blackstone formation. The Cardium formation is overlain unconformably by chert-pebble conglomerates which in turn are overlain by

the marine mudstones of the Colorado (Wapiabi) formation. The mudstones of Blackstone formations act as good source rocks, whereas the sandstones of Cardium formation act as reservoir rocks and the mudstones of the overlying Wapiabi formation act as a seal thereby forming stratigraphic traps.

The conventional hydrocarbon reservoirs in the Cardium formation are highly permeable and porous but they have been exploited since 1950's. With the advances in horizontal drilling and hydraulic fracturing, the focus is now on the tight oil Cardium play on the margins of these conventional fields. These tight oil plays have gross reservoir thickness up to 12 meters with a net sandstone thickness between 3 to 7 meters.

### **2.2.3 Hydraulic fracturing operations**

Hydraulic fracturing stimulation was performed on 13<sup>th</sup> and 14<sup>th</sup> January 2012 in a horizontal treatment well located in the Cardium formation of the Pembina field in central Alberta. The hydraulic fracturing is carried out using a slickwater stimulation fluid containing sand proppant. Hydraulic fracturing was performed in 18 stages along the open-hole section of the treatment well using external packers for zonal isolation with ball actuated frac sleeves. This completion strategy significantly reduces operational time by eliminating wireline perforations and post job coiled tubing operations.

### **2.2.4 Microseismic data**

Microseismic data were acquired with two vertical monitoring wells each having 12 3C geophones (Figure 2.9). The azimuthal coverage provided by the receivers is relatively poor due to only two monitoring wells and the azimuthal gap is approx 180 degrees. The geophones are separated by 30 m interval. The data were recorded with a sampling rate of 2000 samples/s. All 18 treatment stages are recorded but in this thesis, we focus on the data recorded during stage 7.

Figure 2.10 shows a typical microseismic event recorded during stage 7 at the 12 geophones

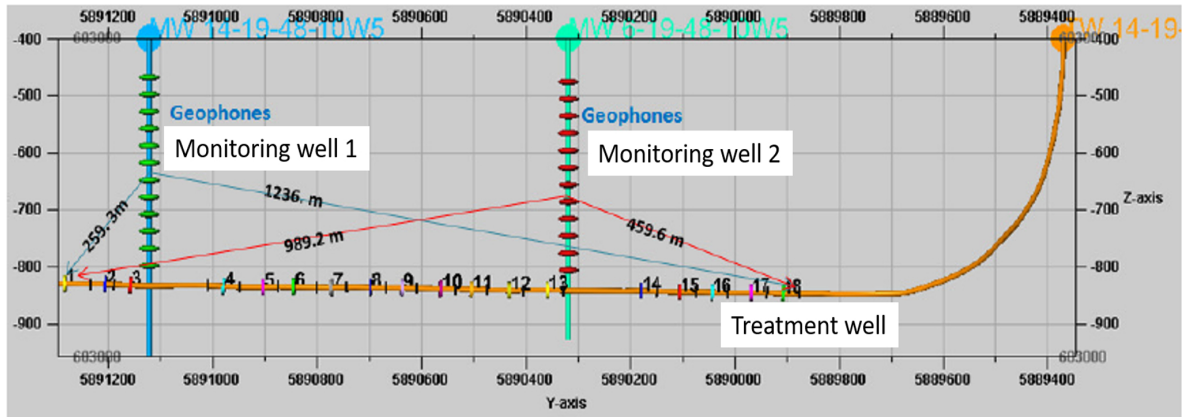


Figure 2.9: Acquisition setup: Horizontal treatment well and two vertical monitoring wells with 12 geophones each. The treatment stages are numbered from 1 to 18. Ports are shown as colored disks and packers are shown as small black disks. Distances from some ports to the center of the geophone arrays are shown for reference. (From PetroBakken Pembina 14-19-48-10W5 microseismic processing report).

in both monitoring well 1 and well 2. Both P- and S-arrivals are identified on the recorded seismograms with green points showing P-arrivals and magenta points showing S-arrivals. The fast and slow shear waves are clearly separated indicating the presence of shear wave splitting.

### 2.2.5 Objectives

Since there are only two monitoring wells and the azimuthal coverage is not good, double-difference tomography cannot be applied to these data. However, the high signal-to-noise ratio makes it possible to pick both P- and S- phases on the recorded seismograms. Also, S-wave splitting can be easily identified on most of the events. So these data allow for shear wave splitting analysis which can provide important information about anisotropy of the medium. Since the events are tightly clustered and occur over a period of time, such data can be used to identify stress-induced anisotropy which can have implications for better understanding of stress evolution. However, interpretation of observed shear wave splitting in terms of stress evolution is not straightforward. Therefore, we use the acquisition setup of this dataset for forward modeling of shear wave splitting parameters due to stress-induced anisotropy. We employ nonlinear elasticity theory to model the anisotropy

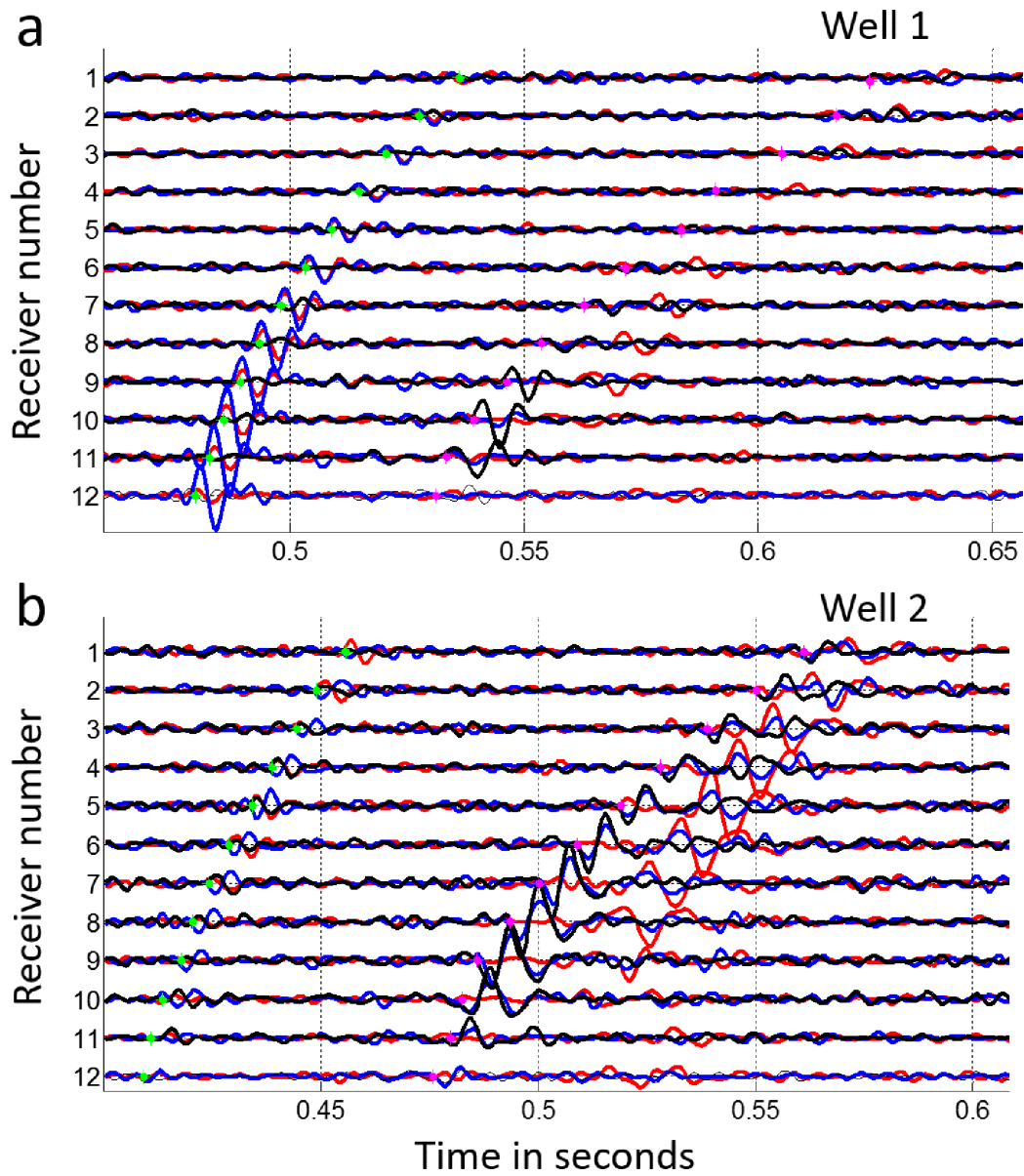


Figure 2.10: A typical microseismic event recorded during stage 7. For the traces, red=Z, blue=Y, and black=X. Green points: P-arrival times picks. Magenta points: S-arrival times picks.

resulting from the induced stresses during hydraulic fracturing. This study is presented in detail in Chapter 6.

## **2.3 Miscellaneous data**

Besides the two case studies mentioned in the previous sections, we have also used induced micro-seismicity data acquired during the hydraulic fracturing stimulation in the Barnett shale, and the Carthage Cotton Valley gas field. The data are taken from Shapiro and Dinske (2009). The details of the Carthage Cotton Valley gas field data are given in Rutledge and Phillips (2003). These data have been used in Chapter 5 to validate our modeling study of the evolution of seismic cloud during hydraulic fracturing.

# Chapter 3

## Passive seismic tomography using recorded microseismicity: Application to mining-induced seismicity<sup>1</sup>

### Summary

Microseismicity is recorded during an underground mine development by a network of 7 boreholes each having 4 geophones in the month of January 2011. After initial preprocessing 488 events are identified with a minimum of 12 P-arrival time picks per event. We adopt a three-steps approach for P-wave passive seismic tomography: (1) a probabilistic grid search algorithm for locating the events, (2) joint inversion for 1D velocity model and event locations using absolute arrival times, and (3) double-difference tomography using reliable differential arrival times obtained from waveform cross-correlation. The originally diffused microseismic event cloud tightens after tomography between depths of 0.45 and 0.5 km towards the center of the tunnel network. The geometry of the event clusters suggests their occurrence on a planar surface such as a geological fault. The

---

<sup>1</sup>A manuscript including parts of this chapter is in preparation for submission to *Bulletin of the Seismological Society of America*.

plane which best fits the largest event cluster in the least squares sense has a strike of 164.7 deg North and dip angle of 55.0 deg towards West. The study region has known faults striking in the NNW-SSE direction with dip angle of 60 deg. However, the relocated event clusters do not fall along any mapped fault. We hypothesize that the microseismic events occur due to slips along an unmapped fault facilitated by the mining activity. The 3D velocity model obtained from double-difference tomography shows lateral velocity contrasts between the depths of 0.4 to 0.5 km. We interpret the lateral velocity contrasts in terms of the altered rock types due to ore deposition. The known geotechnical zones in the mine show good correlation with the inverted velocities. Thus, passive seismic tomography using microseismic data provides information beyond the excavation damaged zones and can act as an effective tool to complement geotechnical evaluations.

### **3.1 Introduction**

Underground mining operations are often accompanied by a very small energy release in the form of microseismic events caused by the brittle failure of the surrounding rocks (McGarr *et al.*, 1975; Gibowicz *et al.*, 1991; Martin, 1997). The real-time monitoring of microseismic events in terms of source location is a useful tool in assessing possible damage zones around underground excavations (Cai *et al.*, 2001; Young *et al.*, 2004). Microseismic monitoring also finds applications in studying subsurface deformations during hydraulic fracturing of unconventional hydrocarbon reservoirs like shales and tight sands (Rutledge and Phillips, 2003; Maxwell *et al.*, 2002), Enhanced Geothermal Systems (Majer *et al.*, 2007), and carbon dioxide sequestration (Verdon *et al.*, 2013; Goertz-Allmann *et al.*, 2014). Most applications are limited to locating and tracking these events over time to monitor subsurface deformation. However, event locations give information only in the seismically active regions of the mine. The microseismic data contain information about the velocity of the medium through which the seismic waves propagate. However, the low signal-to-noise ratio resulting from the small magnitude of the microseismic events cause considerable uncertainty in arrival time picks making it challenging to extract reliable seismic velocities.

Microseismic data in exploration settings usually contain many events with similar waveforms. Waveform cross-correlation techniques have been used to compute highly accurate differential arrival times and accurate relative relocations (Poupinet *et al.*, 1984; Got *et al.*, 1994; Waldhauser and Ellsworth, 2000; Castellanos and Van der Baan, 2013). The differential arrival times obtained from waveform cross-correlation can be incorporated in a joint inversion for both the velocity field and relative event locations using the double-difference tomography method (Zhang and Thurber, 2003). Zhang *et al.* (2009) apply double-difference tomography to a petroleum field thereby mapping faults and velocity changes within the reservoir. Calo *et al.* (2011) identify a large scale aseismic region in an enhanced geothermal system by using time-lapse double-difference tomography. Westman *et al.* (2012) use double-difference tomography to generate time-lapse images for monitoring underground mining operations.

The interpretation of 3D velocity model obtained from tomographic inversion can be complicated since the seismic velocity depends upon a number of factors such as lithology, in situ stresses, pore pressure, fluid contents and saturation, and temperature (Nur, 1987). If other factors remain more or less unchanged, lithological variations have the dominant effect on the seismic velocity changes. Thus, the inverted velocity model can be correlated with the lithology of the known geological units in a given area. In mining regions, the ore deposition often leads to the alteration of the host rock which can impact the seismic velocity of the rock. At the same time, this alteration renders the rock weak which makes it necessary to carry out the geotechnical evaluation of the rock strength. Such geotechnical evaluation helps in identifying zones where the shafts and access tunnels can be constructed as well as the reinforcement required for their safe operations. Interpretation of the 3D velocity model obtained from tomographic inversion in terms of geotechnical zones can have important implications for underground mining development.

In this chapter, we use the microseismic data acquired during underground mining development corresponding to Case study 1. The details of the microseismic data, geological and operational settings are given chapter 2. Here we present the general theory of double-difference tomography, the methodology used in this study, the results, and the interpretation of the inverted velocity

models in terms of the known geotechnical zones.

## 3.2 Theory

Tomographic algorithms invert observed arrival times into a velocity profile (Thurber, 1983). However, the accuracy of estimated velocities depends strongly on the picking quality. With the advent of waveform cross-correlation techniques (Poupinet *et al.*, 1984), it has become clear that differential arrival times between two events can produce more accurate inversion results than those obtained using individual (absolute) arrival time picks. Therefore, we use the double-difference tomography method (Zhang and Thurber, 2003) to obtain high-resolution velocity model and event locations.

Suppose  $T_k^i$  is the body wave arrival time from an event  $i$  to a seismic station  $k$ , then using ray theory  $T_k^i$  can be expressed as a path integral:

$$T_k^i = \tau_0^i + \int_i^k u ds, \quad (3.1)$$

where  $\tau_0^i$  is the origin time of event  $i$ ,  $u$  is the slowness field,  $ds$  is an element of path length and integral from  $i$  to  $k$  represents integral over ray path from  $i^{th}$  event coordinates  $(x_1^i, x_2^i, x_3^i)$  to  $k^{th}$  station coordinates. Using a truncated Taylor series expansion the misfit between the observed and predicted arrival time  $\Delta T_k^i = T_k^{i(obs)} - T_k^{i(cal)}$  is related to the perturbations in the hypocenter and velocity parameters as:

$$\Delta T_k^i = T_k^{i(obs)} - T_k^{i(cal)} = \sum_{l=1}^3 \frac{\partial T_k^i}{\partial x_l^i} \Delta x_l^i + \Delta \tau_0^i + \int_i^k \delta u ds, \quad (3.2)$$

where  $(\Delta x_1^i, \Delta x_2^i, \Delta x_3^i, \Delta \tau_0^i)$  are perturbations in hypocentral parameters and  $\delta u$  is the perturbation in the slowness field.

Suppose there is another event  $j$  observed at the same station  $k$ , we have a similar equation for its misfit between observed and predicted arrival time  $\Delta T_k^j = T_k^{j(obs)} - T_k^{j(cal)}$ . Subtracting the

equation for the  $j^{th}$  event with the equation for the  $i^{th}$  event we get:

$$\begin{aligned} \Delta T_k^i - \Delta T_k^j &= \sum_{l=1}^3 \frac{\partial T_k^i}{\partial x_l^i} \Delta x_l^i + \Delta \tau_0^i + \int_i^k \delta u ds \\ &\quad - \sum_{l=1}^3 \frac{\partial T_k^j}{\partial x_l^j} \Delta x_l^j - \Delta \tau_0^j - \int_j^k \delta u ds , \end{aligned} \quad (3.3)$$

where

$$\Delta T_k^i - \Delta T_k^j = [T_k^{i(obs)} - T_k^{j(obs)}] - [T_k^{i(cal)} - T_k^{j(cal)}] , \quad (3.4)$$

is the difference between the observed and calculated differential arrival times for the two events and is called the double-difference.

Let us consider  $p = 1, 2, \dots, P$  seismic events with  $N_p$  arrival times for each event. For an individual event, eq. 3.2 can be written in matrix form as

$$\mathbf{A}_p \Delta \mathbf{x}_p + \mathbf{C}_p \Delta \mathbf{u} = \Delta \mathbf{t}_p , \quad (3.5)$$

where  $\mathbf{A}_p (N_p \times 4)$  is the partial derivative matrix corresponding to hypocenter and origin time,  $\Delta \mathbf{x}_p (4 \times 1)$  is the perturbation vector of the event location and origin time,  $\mathbf{C}_p (N \times L)$  is the model derivative matrix corresponding to the slowness model,  $\Delta \mathbf{u} (L \times 1)$  is the vector of slowness perturbations, and  $\Delta \mathbf{t}_p (N_p \times 1)$  is the vector of arrival time residuals.

Let  $N_T (= \sum_{p=1}^P N_p)$  be the total number of arrival time data,  $M_T$  be the total number of unknown hypocenter and origin parameters ( $= 4 \times P$ ). Then combining the equations for  $P$  events into one linear system, we get

$$\mathbf{A} \Delta \mathbf{x} + \mathbf{C} \Delta \mathbf{u} = \Delta \mathbf{t} , \quad (3.6)$$

where

$$\mathbf{A} = \begin{bmatrix} \mathbf{A}_1 & \mathbf{0} & \dots & \mathbf{0} \\ \mathbf{0} & \mathbf{A}_2 & \dots & \mathbf{0} \\ \cdot & \cdot & \dots & \cdot \\ \cdot & \cdot & \dots & \cdot \\ \mathbf{0} & \mathbf{0} & \dots & \mathbf{A}_p \end{bmatrix}; N_T \times M_T, \quad (3.7)$$

$$\Delta \mathbf{t} = \begin{bmatrix} \Delta t_1 \\ \Delta t_2 \\ \cdot \\ \cdot \\ \Delta t_p \end{bmatrix}; N_T \times 1, \quad (3.8)$$

$$\mathbf{C} = \begin{bmatrix} \mathbf{C}_1 & \mathbf{0} & \dots & \mathbf{0} \\ \mathbf{0} & \mathbf{C}_2 & \dots & \mathbf{0} \\ \cdot & \cdot & \dots & \cdot \\ \cdot & \cdot & \dots & \cdot \\ \mathbf{0} & \mathbf{0} & \dots & \mathbf{C}_p \end{bmatrix}; N_T \times , \quad (3.9)$$

$$\Delta \mathbf{u} = \begin{bmatrix} \Delta u_1 \\ \Delta u_2 \\ \cdot \\ \cdot \\ \Delta u_L \end{bmatrix}; L \times 1, \quad (3.10)$$

The double-difference tomography equation 3.3 is equivalent to the application of a difference operator  $\mathbf{Q}_{DD}$  to equation 3.6, where

$$\mathbf{Q}_{\text{DD}} = \begin{bmatrix} 1 & -1 & . & . & 0 \\ 1 & . & . & -1 & 0 \\ . & . & . & . & . \\ . & . & . & . & . \\ 0 & . & 1 & . & -1 \end{bmatrix} . \quad (3.11)$$

Let  $w_k$  equal the number of events observed at station  $k$ , then matrix  $\mathbf{Q}_{\text{DD}}$  has the dimension of  $\sum_{k=1}^{N_T} \frac{w_k(w_k-1)}{2} \times N_T$ , corresponding to the possible combinations of differences of event arrival times at station  $k$ ,  $\Delta T_k^i - \Delta T_k^j$  (for  $i \neq j$  and  $i < j$ ), excluding the terms  $\Delta T_k^i - \Delta T_k^i$  and removing the redundancy associated with  $\Delta T_k^i - \Delta T_k^j = -1(\Delta T_k^i - \Delta T_k^j)$ .

The matrix form of double-difference tomography is

$$\mathbf{Q}_{\text{DD}}\mathbf{A}\Delta\mathbf{x} + \mathbf{Q}_{\text{DD}}\mathbf{C}\Delta\mathbf{u} = \mathbf{Q}_{\text{DD}}\Delta\mathbf{t} . \quad (3.12)$$

Equation 3.12 can be written in a tighter matrix form as:

$$\mathbf{Q}_{\text{DD}}\mathbf{E}\mathbf{y} = \mathbf{Q}_{\text{DD}}\Delta\mathbf{t} , \quad (3.13)$$

where  $\mathbf{E} = \begin{bmatrix} \mathbf{A} & \mathbf{C} \end{bmatrix}$  has the dimension of  $N_T \times (M_T + L)$  and  $\mathbf{y} = \begin{bmatrix} \Delta\mathbf{x} \\ \Delta\mathbf{u} \end{bmatrix}$  has the dimension of  $(M_T + L) \times 1$ .

The complete double-difference tomography system of equations for joint inversion of velocity structure and event locations using both absolute and differential arrival data is given as

$$\begin{pmatrix} \mathbf{W}\mathbf{Q}_{\text{DD}}\mathbf{E} \\ w\mathbf{E} \end{pmatrix} \mathbf{y} = \begin{pmatrix} \mathbf{W}\mathbf{Q}_{\text{DD}} \\ w\mathbf{I} \end{pmatrix} \Delta\mathbf{t} , \quad (3.14)$$

where  $w$  is a scalar which gives the relative weighting between absolute and differential arrival times,  $\mathbf{I}$  is the identity matrix, and  $\mathbf{W}$  is a diagonal matrix to weight each equation based on inter

event distances and is often known as the distance weighting matrix

Waldhauser and Ellsworth (2000) apply a distance-based weighting in their double-difference relocation algorithm to put more weight on closer events and downweight event pairs with large separation distance. This is done to ensure that the differencing process removes path anomalies among event pairs at common stations. Zhang and Thurber (2003) also apply distance weighting in the double-difference tomography code (matrix  $\mathbf{W}$  in equation 3.14). The distance weighting function is given by

$$W = \max\left(0, 1 - \left(\frac{s_i}{d_{max}}\right)^a\right)^b, \quad (3.15)$$

where  $s_i$  is the interevent distance between  $i^{th}$  event pair,  $d_{max}$  is the maximum cutoff distance to discard event pairs with interevent separation larger than  $d_{max}$ , and  $a$  and  $b$  are the exponents which govern the shape of the weighting function. The cutoff distance  $d_{max}$  is selected on the basis of expected velocity heterogeneity. The decay rate of the weighting function from maximum value of one to minimum value of zero at the cutoff distance depends upon the exponents  $a$  and  $b$ .

The tomographic system of equations (equation 3.14) is generally ill-conditioned and is stabilized by applying damping and smoothing regularizations. We apply first-order smoothing constraints to the slowness perturbations between neighbor grid nodes. We penalize the model roughness defined as the difference of the slowness perturbations at neighbor grid points divided by the distance between the grid nodes (Zhang and Thurber, 2003). The smoothing and damping parameters are selected on the basis of trade-off curves between model norm and data misfit. We also apply preconditioning to the derivative matrix by normalizing each column of the derivative matrix with its  $L^2$  norm.

### 3.3 Synthetic example

We generate synthetic arrival and differential arrival times using the real acquisition setup and the total number of events identified in the microseismic data recorded during mining operations. The true velocity model used to generate the data consists of a 1D background velocity model with velocities increasing with depth (Figure 3.1a). The true model contains two blocks of high and low velocities of 4.2 km/s and 3.8 km/s respectively between depths of 0.4 to 0.5 km and  $X=0.1$  km to  $X=0.3$  km. The two blocks are separated by a boundary at  $Y=0.2$  km (Figure 3.1b). The event locations obtained by grid search on the real data using a homogeneous velocity model of 3700 km/s are taken as true event locations for generating synthetic data (Figures 3.1d-3.1f). The true receiver locations are used for generating synthetic data. Synthetic travel times are computed using the finite difference solution of the Eikonal equations (Podvin and Lecomte, 1991). The arrival times are obtained by adding the true origin times to the computed travel times. Differential arrival times are calculated by subtracting the noise-free arrival times of event pairs at common receivers. The number of observations for arrival times and differential arrival times is same as that for the real data. Finally, we add random Gaussian noise with zero mean and standard deviations of 10 ms and 2 ms to the synthetic arrival and differential arrival times respectively. The standard deviation of the noise added to the differential arrival times is smaller than that added to absolute arrival times to simulate the real world scenario where the differential arrival times obtained from waveform cross-correlation are usually an order of magnitude more accurate than the absolute arrival times.

#### 3.3.1 Methodology

Our microseismic location and tomographic inversion scheme consists of three main steps: (1) obtain absolute event locations using a probabilistic grid search location algorithm (Lomax *et al.*, 2000), (2) perform 1D tomographic inversion for event locations and 1D velocity model using absolute arrival times, and (3) double-difference tomographic inversion for 3D velocity model and

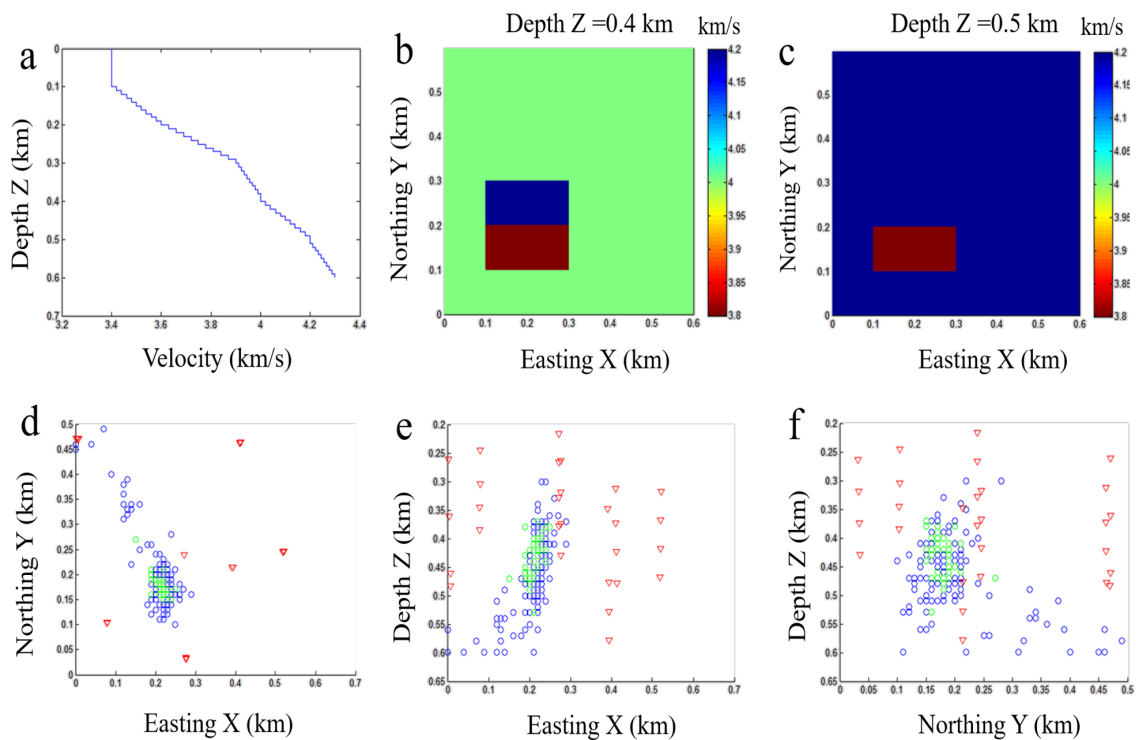


Figure 3.1: True velocity model (a-c) used to generate the synthetic data: (a) background 1D velocity model, (b) map view at 0.4 km depth, and (c) map view at 0.5 km depth. The true model has a high and low-velocity anomaly of 4.2 and 3.8 km/s respectively towards the center with a sharp interface. True event locations (d-f) of the two largest multiplet groups having 179 and 38 events shown with blue and green circles respectively. These locations are obtained by a grid search assuming a constant velocity model of 3.7 km/s. The red triangles are the receivers locations. (d) Map view of the events, (e) projection of events on East-West cross-section, and (f) projection of events on North-South cross-section.

event locations using differential arrival times.

To start we need an initial guess solution for the velocity model and event locations. We consider two substantially different 1D velocity models, both in magnitude and trend, as compared to the true background 1D velocity model. From our initial 1D velocity models, the average velocity of the target area can be approximated as 4.0 km/sec. We find the initial locations with a probabilistic grid search location algorithm (Lomax *et al.*, 2000) using the homogeneous velocity model of 4.0 km/sec and a grid spacing of 40 m along all three axes. We employ a homogeneous velocity model for the grid search as it uses an analytical expression to compute arrival times and hence is much faster than a 1D velocity model which involves ray tracing.

Next, we perform a 1D tomographic inversion where we invert for event locations and 1D velocity model using absolute arrival times. Since our two starting 1D velocity models have large differences in velocities, we must do a 1D tomographic inversion to obtain a best fitting 1D velocity model to be used as an initial guess for 3D inversion. In the first iteration, we invert only for hypocentral parameters since the initial event locations are obtained by grid search assuming a homogeneous velocity model of 4.0 km/s which is quite different from our starting 1D velocity model. In the second iteration, we invert simultaneously for hypocentral and velocity parameters. We stop after two iterations as there is no further improvement in residual arrival times.

Then we apply our double-difference tomography code with the updated hypocentral parameters and best fitting 1D velocity model obtained from the 1D tomographic inversion. The code applies a relative weighting between differential and absolute data of 1:0.01 (equation 3.14). In the first iteration, we invert only for hypocentral parameters, whereas in the second iteration we invert simultaneously for hypocentral and velocity parameters. We stop after two iterations as there is no further improvement in residual differential arrival times.

We analyze the impact of distance weighting and damping on tomographic inversion results by using different parameters. We perform double-difference tomography with (1) a sharp distance weighting using  $a = 1$ ,  $b = 5$  and cutoff distance  $d_{max} = 0.7$  km in equation 3.15, and (2) no distance weighting. A sharp distance weighting applies more weight to closely spaced events and

promotes clustering. We also test the impact of a smaller damping parameter on our tomographic inversion. We select optimal damping value of 0.1 and 0.005 for first and second iteration respectively using tradeoff curves. To test the effect of a lower damping parameter we do inversion with a damping parameter of 0.002. We use a smoothing parameter of 0.05 in both cases (selected on the basis of tradeoff curves).

### 3.3.2 Results

Figures 3.2a and 3.2b show respectively the tradeoff curves for the first and second iteration of the 1D tomographic inversion. We select a damping parameter of 0.03 and 0.01 for the first and second iteration respectively. Figure 3.2c shows the tradeoff curve for the smoothing parameters for the optimal damping parameter of 0.01 in the second iteration. We select the optimal smoothing parameter of 1. Figure 3.2d shows the two different starting velocity models (red and green curves) and the true 1D background velocity model (blue curve). Figure 3.2e shows the inverted velocity model with damping=0.1 and smoothing=0.01. The inverted velocity models for optimal damping and smoothing parameters obtained from the tradeoff curves are shown in Figure 3.2f. The inverted velocity models with optimal damping parameters are quite similar and close to the true 1D background velocity model especially between 0.25 to 0.5 km depths where ray coverage is good.

Figures 3.3a, 3.3b, and 3.3c show the map view of the true and inverted velocity models at different depths when inversion was performed with the suggested optimal damping (=0.1) and smoothing (=0.05) parameters obtained from tradeoff curves. The low-velocity anomaly is poorly recovered at depths of 0.4 and 0.5 km while the high-velocity anomaly is overestimated at depths of 0.45 and 0.5 km. In general, the shape of the low-velocity anomaly is not preserved and the high and low-velocity anomalies are respectively over- and under-estimated. On the other hand, the shape and amplitudes of anomalies are better recovered with a low damping parameter(=0.002) as shown in Figures 3.3d, 3.3e and 3.3f.

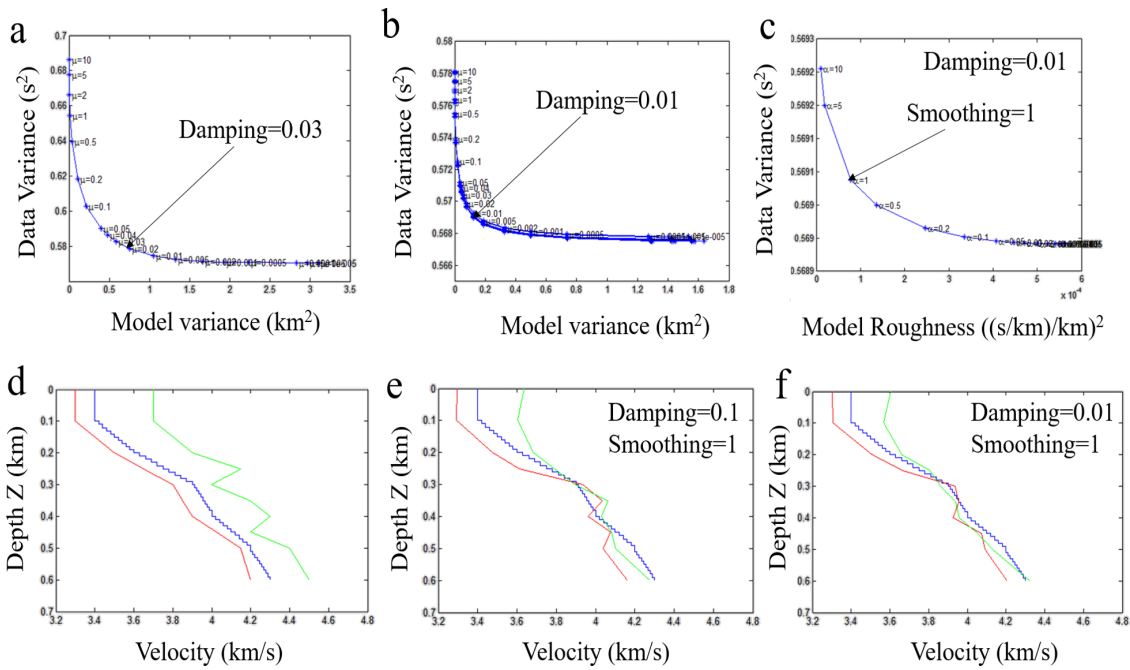


Figure 3.2: 1D tomographic inversion: tradeoff curves (a-c) for selecting optimal damping and smoothing parameters. (a) Optimal damping parameter when inverting for event locations only (1st iteration). (b) Optimal damping parameter for joint inversion of event locations and 1D velocity model. Multiple tradeoff curves are obtained by varying damping parameter ( $\mu$ ) for different fixed values of smoothing parameter ( $\alpha$ ). (c) Optimal smoothing parameter for optimal damping parameter=0.01. (d) True background 1D velocity model (blue curve), and two different starting 1D velocity models (red and green), (e) after 1D tomography with damping parameter=0.1, and (f) after 1D tomography with damping parameter=0.01. The final 1D velocity models with the optimal damping parameter (0.01) are similar and close to the true 1D background velocity model despite large differences in the starting 1D velocity models.

Table 3.1: Distance and absolute differences between true and inverted event locations for the largest multiplet group (Group 1) obtained with two sets of damping parameters namely large=0.1, and small=0.002.

Damping	Distance (m)			$\Delta x$ (m)			$\Delta y$ (m)			$\Delta z$ (m)		
	Mean	Median	Std	Mean	Median	Std	Mean	Median	Std	Mean	Median	Std
Large	22.9	7.8	48.5	8.8	2.7	24.2	15.8	4.5	39.7	10.4	4.7	16.5
Small	12.7	6.7	33.5	5.4	2.3	17.7	8.4	3.1	26.3	5.9	3.5	12.1

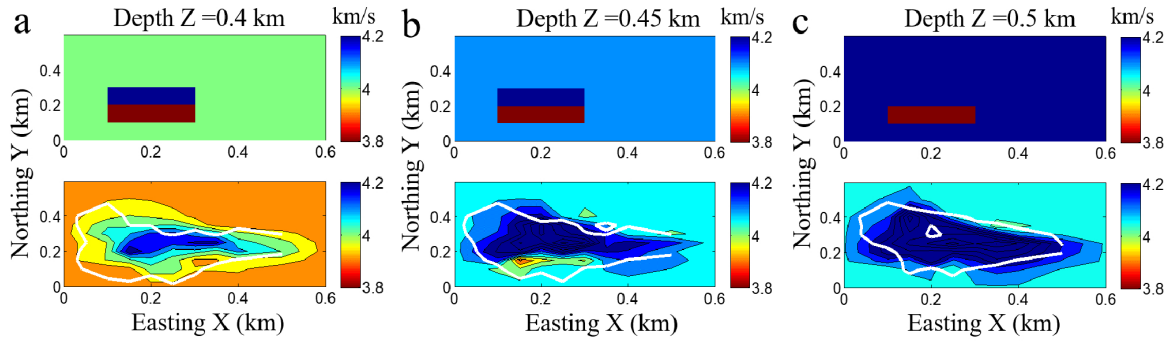
We also compute full resolution matrices for both cases and plot the contours corresponding to the diagonal elements of the resolution matrix with values 0.1 on top of the velocity maps (white lines in Figure 3.3). The region enclosed by the white contour line in Figure 3.3 has larger diagonal resolution elements than 0.1. However, the amplitudes and shape of the velocity anomalies are better recovered in the case of the lower damping parameter (Bottom panel in Figure 3.3). This synthetic example suggests that for the given acquisition geometry and recorded data in our mining environment, the velocities of nodes with diagonal element greater than 0.1 have a proper recovery of velocities for interpretation purpose provided the damping parameter is properly selected.

We also compare the inverted event locations for the largest multiplet group (Group 1) obtained with the two sets of damping parameters. Table 3.1 summarizes the comparison of the inverted locations with respect to the true event locations. We compute the distance between true and inverted event locations and also the absolute differences between location coordinates in X, Y and Z directions. We tabulate the mean, median and standard deviation of the distances and the absolute differences for all the events belonging to Group 1 in Table 3.1. The distances and absolute differences are smaller when the events are located close to their true positions. We find that a lower damping parameter of 0.002 helps in a better recovery of the absolute locations.

### 3.3.3 Discussion

We adopt a three steps scheme for passive seismic tomography which involves (1) a probabilistic grid search location algorithm (Lomax *et al.*, 2000) to obtain absolute event locations, (2) a 1D tomographic inversion for event locations and 1D velocity model using absolute arrival times, and

Larger damping



Smaller damping

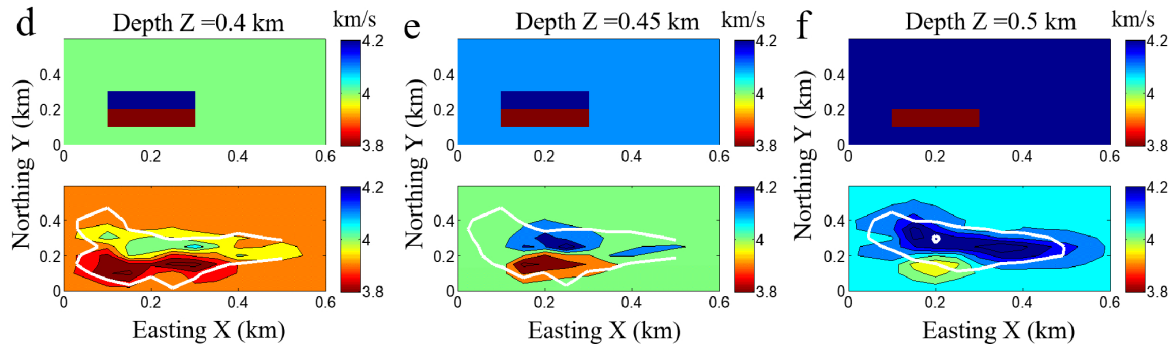


Figure 3.3: Map view of the true and inverted velocity model obtained from 3D tomographic inversion. Top panel: Results obtained with a larger damping parameter ( $=0.1$ ) at depth of (a)  $Z=0.4$  km, (b)  $Z=0.45$  km, and (c)  $Z=0.5$  km. Bottom panel: Results obtained with a smaller damping parameter ( $=0.002$ ) at depth of (d)  $Z=0.4$  km, (e)  $Z=0.45$  km, and (f)  $Z=0.5$  km. Counters corresponding to the diagonal element of the resolution matrix with values of 0.1 are plotted as white lines on top of the velocity maps.

(3) a double-difference tomographic inversion for 3D velocity model and event locations using differential arrival times. The 1D velocity model obtained from step 2 is essentially the minimum 1D velocity model described by Kissling *et al.* (1994) which provides better recovery of the true velocity model when used as an initial velocity model in the 3D tomographic inversion. The double-difference tomography yields higher resolution near the source region (Zhang and Thurber, 2003), however outside the source region the absolute arrival times can give better resolution. In exploration settings like underground mine development or hydraulic fracturing, the microseismic source locations are tightly clustered in space. Thus the velocity parameters outside the source region may not be well resolved. Therefore, it is important to perform 1D inversion using absolute arrival times to get a 1D velocity model and use it as an initial model in 3D inversion in order to get fewer artifacts in the final 3D velocity images (Kissling *et al.*, 1994). Furthermore, the velocity parameters outside the source region which are not well resolved by double-difference tomographic inversion may represent average velocities in that region as they have been obtained from 1D tomographic inversion.

The choice of damping parameter used in double-difference relocation significantly affects the inversion results (Castellanos and Van der Baan, 2013). In earlier studies, the relocations using differential arrival times were believed to improve only the relative positions and not the absolute positions. In the double-difference relocation algorithm, Waldhauser and Ellsworth (2000) restrict the mean shift of all seismic events during relocation to zero by applying the explicit constraint. They downweight this constraint during inversion to allow the cluster centroid to move slightly and correct for possible errors in initial absolute locations. Menke and Schaff (2004) show that absolute locations can be better constrained by the double-difference equations than the absolute equations owing to the high accuracy of differential data. This is even more important in the case of microseismic data where the picked absolute arrival times can have much larger relative errors due to low signal-to-noise ratio as compared to the cross-correlation derived differential arrival times. The damping parameter constrains the shift in the cluster centroid, therefore a large damping parameter may introduce bias in the estimate of absolute position and noise in the relative position

Table 3.2: Distance and absolute differences between true and inverted event locations for the largest multiplet group (Group 1) obtained with and without distance weighting.

Distance weighting	Distance (m)			$\Delta x$ (m)			$\Delta y$ (m)			$\Delta z$ (m)		
	Mean	Median	Std	Mean	Median	Std	Mean	Median	Std	Mean	Median	Std
Yes	23.3	7.0	56.9	9.2	2.4	27.1	17.0	3.6	48.3	8.9	4.2	16.0
No	12.7	6.7	33.5	5.4	2.3	17.7	8.4	3.1	26.3	5.9	3.5	12.1

computation. In our synthetic example, we find that inversion with a smaller damping parameter gives better absolute locations as compared to those obtained with a larger damping parameter (Table 3.1). Furthermore, Scales *et al.* (1990) show that damping is potentially disastrous in multiparameter inversions since the small singular values may control long spatial wavelength features in the solution. In settings where events are highly localized in space, it is important to include the velocity parameters associated with small singular values near the noise level to get a more detailed velocity model. We get a better recovery of the true velocity model in our synthetic example with a lower damping parameter (Figure 3.3).

Monteiller *et al.* (2005) suggest that a sharp distance weighting is detrimental in providing a reliable solution for the geometric center of the event cluster. In our synthetic example, the inversion performed with no distance weighting gives a better result as shown in Table 3.2. This may be due to the fact that the initial event locations obtained from absolute arrival times have large errors. A sharper distance weighting removes these event pairs from inversion while no distance weighting includes them in inversion and they get relocated with the more accurate differential arrival times.

## 3.4 Real microseismic data

### 3.4.1 Methodology

We follow the same three steps passive seismic tomography scheme which we use in the case of the synthetic example. Firstly we perform a probabilistic grid search for event locations (Lomax

*et al.*, 2000) assuming a constant velocity model of 3.7 km/s and a grid spacing of 5 m along all three axes. This constant velocity model represents the average velocity of the medium obtained from calibration shot analysis and was used by Castellanos and Van der Baan (2015a) for double-difference relocation. The event locations obtained from grid search are used as initial locations for 1D tomographic inversion. The starting 1D velocity models used are obtained from VSP data and calibration shot analysis. The inverted event locations and 1D velocity model obtained from 1D tomographic inversion are used as input for double difference tomography. The double-difference tomographic inversion using the waveform-crosscorrelation derived differential arrival times gives us the final microseismic event locations and 3D velocity model.

Finally to assess the solution quality of our inverted 3D velocity model we perform synthetic characteristic tests (Haslinger *et al.*, 1999; Husen *et al.*, 2000). In this test, we use a specifically designed synthetic velocity model for generating synthetic data. We add Gaussian noise to this synthetic data. The noisy data are then inverted using the same parametrization and regularization parameters as used for inversion of real data. A comparison of the synthetic and the inverted velocity models helps in identifying well-recovered regions. We also compute the full resolution matrix and the spread function (Michellini and McEvelly, 1991) to identify well-resolved regions in the model. Each row of the resolution matrix acts as an averaging vector for a model parameter. The velocity parameter estimate at a node depends not only on its true value but also on velocities at other nodes. This information is quantified using the spread function which describes how strong and peaked the resolution is for each node (Michellini and McEvelly, 1991).

### **3.4.2 Results**

Figure 3.4 shows the tradeoff curves and the 1D velocity models before and after 1D tomographic inversion. The two 1D velocity models used as initial models in the 1D tomographic inversion are shown in Figure 3.4d. The red and blue curves represent the 1D velocities obtained from VSP data and calibration shot analysis respectively. The two velocity models have a large difference in

velocities. Figure 3.4e shows the inverted velocity models with a larger damping parameter of 0.1. The two models approach similar velocity values. With optimal damping parameter of 0.02, the two velocity models are nearly identical (Figure 3.4f). We take the inverted event locations and 1D velocity model (blue curve in Figure 3.4f) obtained from 1D inversion with optimal damping parameters as input for double-difference tomography.

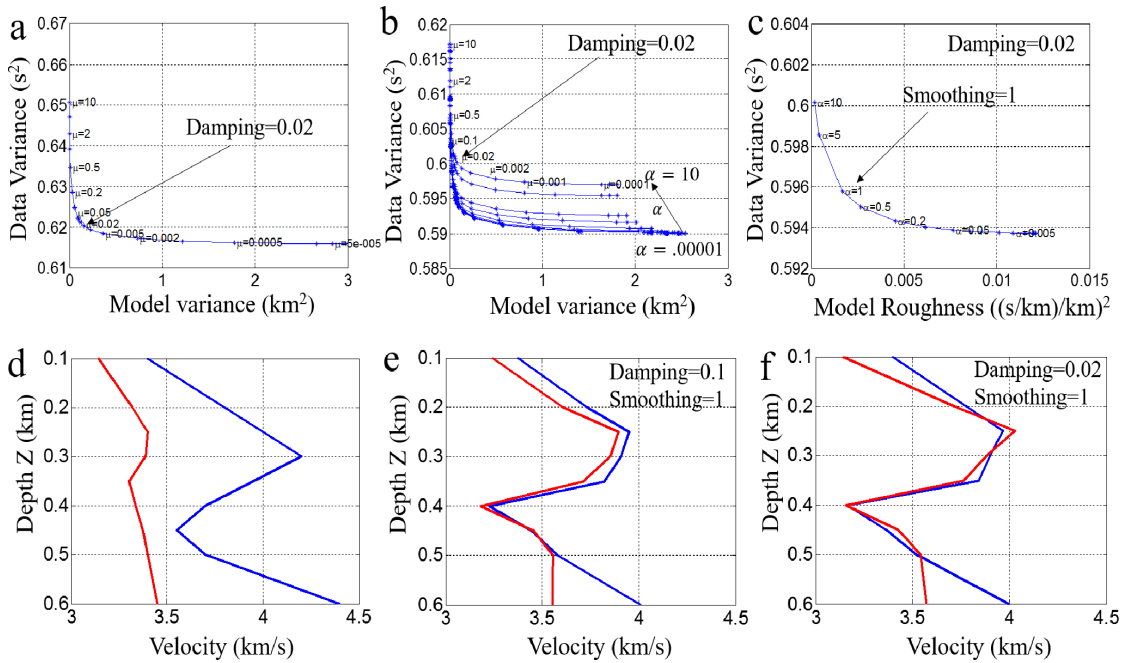


Figure 3.4: 1D tomographic inversion of field data: tradeoff curves (a-c) for selecting optimal damping and smoothing parameters. (a) Optimal damping parameter when inverting for event locations only (1st iteration). (b) Optimal damping parameter for joint inversion of event locations and 1D velocity model. Multiple tradeoff curves are obtained by varying damping parameter ( $\mu$ ) for different fixed values of smoothing parameter ( $\alpha$ ). (c) Optimal smoothing parameter for damping =0.02. (d) Two different starting 1D velocity models, the blue curve is the velocity model obtained from calibration shot analysis and the red curve is the velocity model obtained by averaging the VSP velocities. Inverted velocity models: (e) after 1D tomography with damping parameter=0.1, and (f) after 1D tomography with damping parameter=0.02. The final 1D velocity models show similar trends between depths of 0.2 to 0.5 km even though the initial velocity models from average VSP and calibration shot analysis had large differences in velocities.

Figure 3.5 shows the inverted event locations of Castellanos and Van der Baan (2015a) for the two largest multiplet groups (group 1 and 3) and those obtained from double-difference tomography of the field data. The event locations of Castellanos and Van der Baan (2015a) (Figures

3.5a-3.5c) are more spread out between 0.4 to 0.52 km depth. The new locations tightly cluster between depths of 0.45 to 0.5 km towards the center of the tunnel network at 480 m depth close to shaft 1 (Figures 3.5d-3.5f). The largest multiplet group containing 179 events (gray circles in Figure 3.5) is located above and below the tunnel network at 480 m depth (Figures 3.5d and 3.5e). The event locations show distinct trends and appear to originate from one or more planar surfaces. Figures 3.5c and 3.5f show the event locations for multiplet group 1 in 3D, together with the best fitting planes in the least squares sense (shown by pink color). The event locations of Castellanos and Van der Baan (2015a) are spread out in the direction normal to the plane and the apparent thickness (computed as twice the median of the perpendicular distances of event locations from the best fitting plane) is 21.8 m. However, the apparent thickness in the case of locations obtained by double-difference tomography is 5.6 m, so these event locations appear to occur on a fault. The dip and strike of the plane shown in Figure 3.5f are 55.0 deg towards West and 164.7 deg North respectively. Similarly, we find the best fitting plane to multiplet group 3 with dip and strike as 62.0 deg towards West and 161.5 deg North respectively. We also fit a plane simultaneously to both the multiplet groups (group 1 and 3) whose dip and strike are 56.6 deg towards West and 162.6 deg North respectively. The three best fitting planes have similar dips and strikes.

Figures 3.6a-3.6f show the various cross-sections through the final 3D velocity model obtained from double-difference tomography of the field data overlain with the shafts and tunnel network and the inverted event locations of the largest multiplet group. The velocity cross-sections show lateral velocity gradient between depths of 0.45 km and 0.5 km. The North-South velocity cross-section at  $X=0.25$  km shows sharp contact between the high and low velocities between depths of 0.45 km and 0.5 km, and  $Y=0.2$  km and  $Y=0.3$  km. The velocities between depths of 0.4 to 0.5 km and 0.2 to 0.3 km along East and North are considered reliable as suggested by the synthetic characteristic tests described in the following subsection.

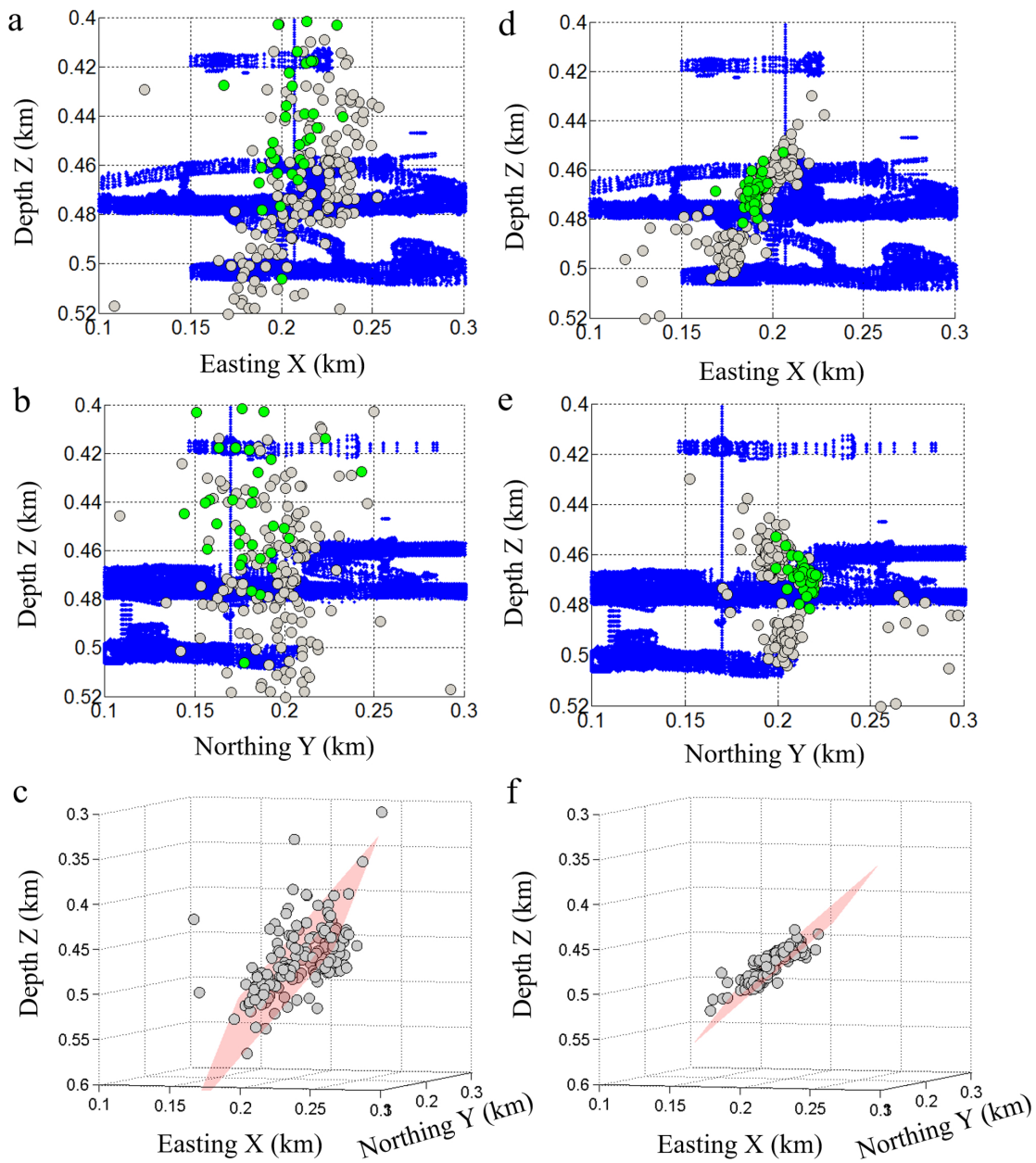


Figure 3.5: (a,b,d,e) Event locations of multiplet group 1 (gray circles) and group 3 (green circles) projected on top of the tunnel and shaft layout (blue filled circles). Castellanos and Van der Baan (2015a) locations projected on (a) East-West cross-section. (b) North-South cross-section. Locations obtained from double-difference tomography projected on (d) East-West cross-section. (e) North-South cross-section. 3D view of multiplet group 1 locations obtained by (c) Castellanos and Van der Baan (2015a), and (f) double-difference tomography with the best fitting planes shown by pink color.

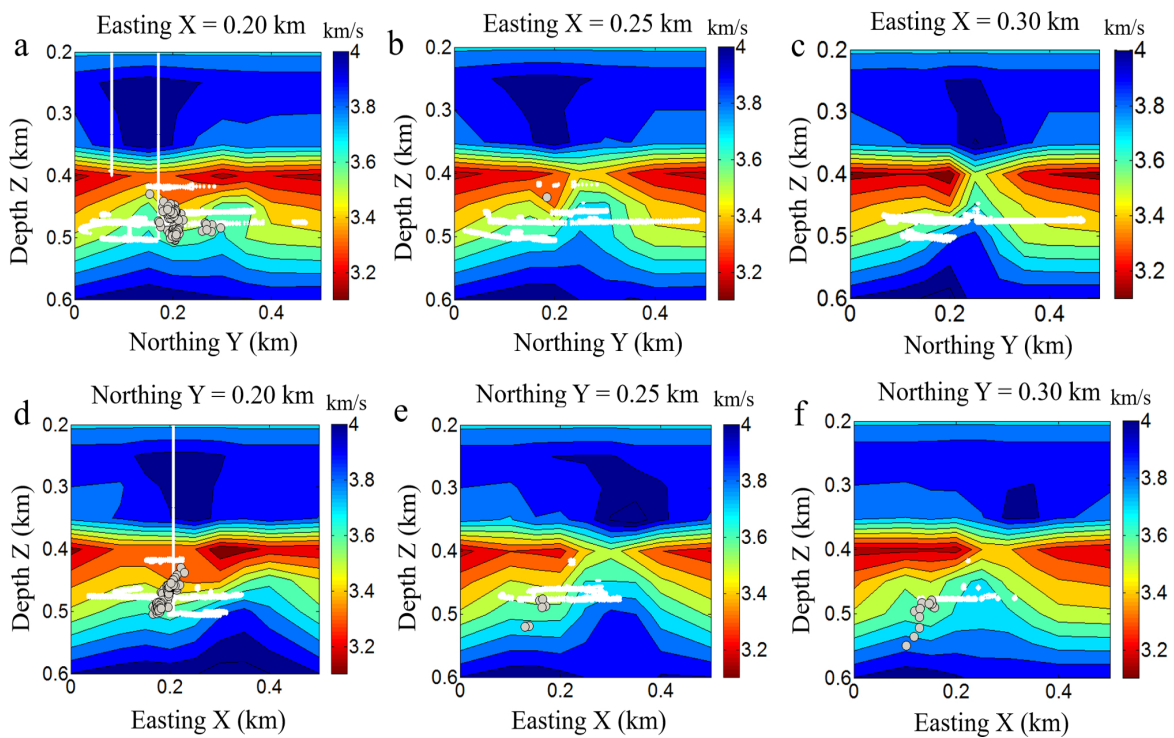


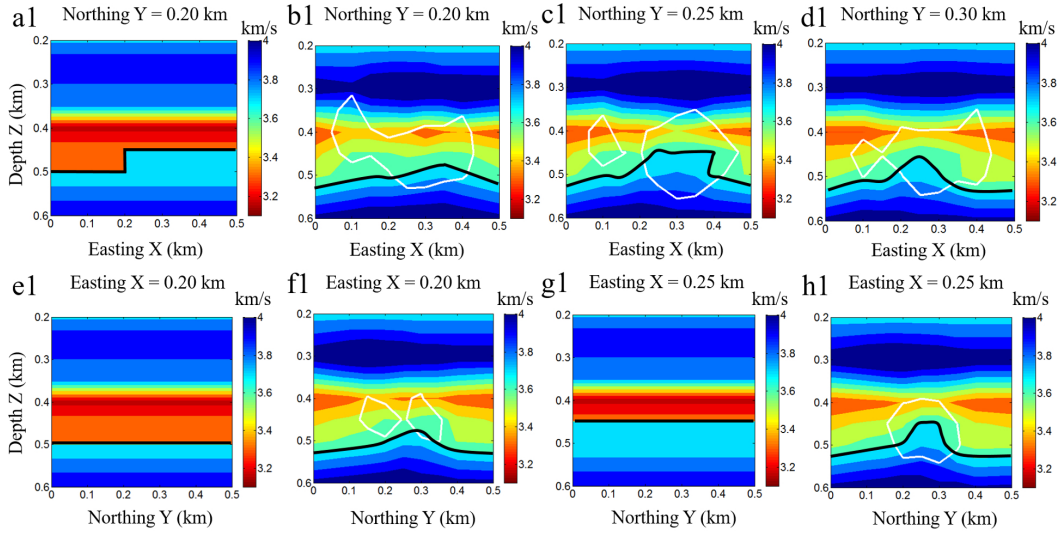
Figure 3.6: 3D velocity model obtained from double-difference tomography of field data overlain with the shafts and tunnel network (white dots) and the inverted event locations of multiplet group 1 (gray dots). North-South cross-sections at (a)  $X=0.20$  km, (b)  $X=0.25$  km, and (c)  $X=0.30$  km. East-West cross-sections at (d)  $Y=0.20$  km, (e)  $Y=0.25$  km, and (f)  $Y=0.30$  km.

### 3.4.2.1 Synthetic characteristic test

We assess the solution quality of our final velocity model using synthetic characteristic tests [Haslinger *et al.*, 1999; Husen *et al.*, 2000] by considering two different velocity models for generating synthetic data. Model 1 has a N-S striking vertical fault separating a low velocity block (3.4 km/s) from a high velocity block (3.7 km/s) at  $X=0.2$  km between depths of 0.45 to 0.5 km (Figures 3.7a1, 3.7e1 and 3.7g1). Model 2 has a constant velocity block between depths of 0.45 and 0.5 km which is in contact with the lower velocities above it along a sharp interface at depth of 0.45 km (Figures 3.7a2 and 3.7e2). Both the fault interface and the contact at 0.45 km depth are very sharp boundaries defined on a fine grid so that these features cannot be obtained exactly. The test inversions enable us to understand how well these features are resolved. We generate the synthetic data with the inverted event locations obtained from double-difference tomography of the field data as the true positions and the two synthetic velocity models as true velocity models using a finite difference solution to the Eikonal equations (Podvin and Lecomte, 1991). We add random Gaussian noise with standard deviation of 10 ms to the absolute arrival times and 3.5 ms to the differential arrival times. We perform 1D inversion followed by 3D inversion and use the same parametrization and damping and smoothing parameters as those used for tomography with the field data.

Figure 3.7 shows the vertical cross-sections through the true velocity models (Model 1 and 2) and the recovered velocity models. Figures 3.7b1 to 3.7d1 are the East-West cross-sections through the inverted velocity model on which the velocity contour of 3.7 km/s has been shown by the bold black curve. The Fault interface is marked by bold black lines on the true velocity model. In Figure 3.7c1 the velocity is well recovered between  $X=0.2$  km to 0.4 km and  $Z=0.45$  to 0.5 km. This higher velocity is in contact with relatively low velocity at  $X=0.2$  km along a slanted interface. The lower velocity block between  $X=0.1$  to 0.2 km (left of the fault interface) is smoothed and the velocities are higher compared to the true model, yet the sharp fault interface may be identified in this cross-section at  $X=0.2$  km. However, we see another interface at  $X=0.4$

### MODEL 1



### MODEL 2

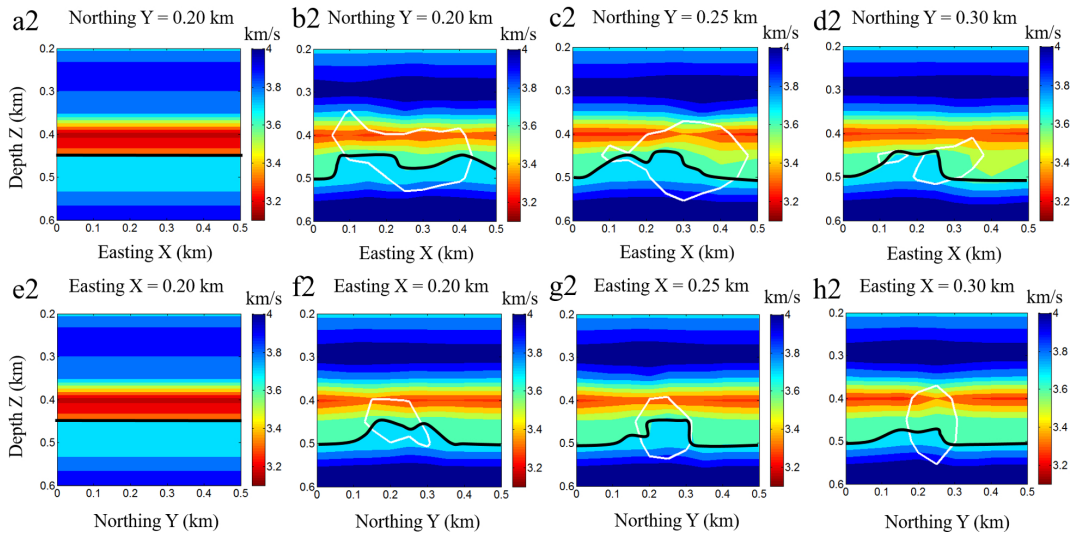


Figure 3.7: Synthetic characteristic tests: (a1) East-West cross-section through true velocity model (Model 1). (b1-d1) East-West cross-sections through inverted velocity model at  $Y=0.2, 0.25$  and  $0.3$  km respectively. (e1) North-South cross-section through Model 1 at  $X=0.2$  km. (f1) North-South cross-section through inverted velocity model at  $X=0.2$  km. (g1) North-South cross-section through Model 1 at  $X=0.25$  km. (h1) North-South cross-section through inverted velocity model at  $X=0.25$  km. (a2) East-West cross-section through true velocity model (Model 2). (b2-d2) East-West cross-sections through inverted velocity model at  $Y=0.2, 0.25$  and  $0.3$  km respectively. (e2) North-South cross-section through Model 2. (f2-h2) North-South cross-sections through inverted velocity model at  $X=0.2$  km,  $0.25$  and  $0.3$  km respectively. The velocity cross-sections are overlain by white contour for spread function  $SF = -1$ .

km which is an artifact due to poor ray coverage towards East of  $X=0.4$  km. We have similar observations for East-West cross-section at  $Y=0.3$  km. On comparing Figures 3.7e1 and 3.7f1 we observe averaging of the lower velocity block between  $Z=0.45$  to  $0.5$  km and the sharp interfaces are smoothed out. Comparing Figures 3.7g1 and 3.7h1 the higher velocities between  $X=0.2$  to  $0.3$  km are well recovered between  $Z=0.45$  to  $0.5$  km. However, the shape of the block is not recovered due to poor ray coverage and larger averaging outside this region as indicated by the spread function contour ( $SF=-1$ ) shown by the white curve. The spread function is computed as defined by *Michelini and McEvilly* [1991].

In Model 2 we have a higher velocity block between  $Z=0.45$  to  $0.5$  km and there is no lateral velocity variation. Comparing the East-West cross-sections through the inverted velocity model (Figures 3.7b2-3.7d2) with the true velocity model (Figure 3.7a2), the higher velocity block is well recovered between  $X=0.1$  to  $X=0.3$  km. The interface is also flat as compared to the fault interface recovered for Model 1. However artificial interfaces are introduced around  $X=0.3$  km on  $Y=0.25$  and  $0.3$  km which may be the result of poor ray coverage as we move towards East of  $X=0.3$  km. Comparing the North-South cross-sections through the inverted velocity model (Figures 3.7f2-3.7h2) with the true velocity model (Figure 3.7e2), the higher velocities between  $Y=0.2$  and  $Y=0.3$  km are well recovered and the interface is also relatively flat. However artificial interfaces are introduced outside  $Y=0.2$  and  $Y=0.3$  km.

These synthetic characteristic tests suggest that the higher velocities are well recovered in magnitude whereas the lower velocities are averaged and may be overestimated. The sharp interfaces are smoothed out and artificial interfaces may be introduced especially between  $0.3$  to  $0.5$  km along East or North in all the vertical cross-sections. The inverted velocities at grid nodes with spread function values smaller than  $-1$  can be considered reliable for interpretation.

### 3.4.3 Discussion

The underground mine is located in Saskatchewan, Canada which has a very low ambient rate of seismicity with only 59 earthquakes recorded between Jan 1985 and Dec 2016 with magnitudes ranging from 2.3 to 4.0 (Earthquakes Canada, <http://www.earthquakescanada.nrcan.gc.ca/>). The epicenters of the two nearest earthquakes are at distances of approximately 41 km and 275 km from our study area. All other earthquakes occur at distances greater than 600 km from the study region. Thus, the study region is nearly devoid of background seismicity. The microseismic events recorded during the underground mine development in January 2011 tightly cluster around the 480 m tunnel network near shaft 1 after double-difference tomography (Figure 3.5). Furthermore, during the month of January 2011, the access tunnels were being constructed in the 480 m and 500 m levels. The close spatiotemporal association of the microseismic events with the mining activities and lack of background seismicity confirms that these events are induced due to mining activity.

Figure 3.8 shows the event locations of the multiplet groups 1 and 3 and the 3D distribution of the mapped faults in the mine. The vertical shafts and the horizontal tunnel network are shown by solid blue color. For proper visualization, we have only shown the faults which are close to the shaft 1 and the 480 m horizontal tunnel network. The events do not lie along any mapped fault. However, as shown in Figure 3.5 in the results section, the event cluster geometry suggests that they may occur along a planar surface with dip and strike of 55.0 deg towards West and 164.7 deg North respectively. Such fault orientations are present in the study region as shown in the map view in Figures 2.6c and 2.6d; however, no such fault is mapped along the event locations. The mapped fault nearest to the main cluster is oriented in the NW-SE direction (shown by red color in Figure 3.8). This fault has a small area and cuts only through the 465 m level. Thus, it is possible that the event clusters occur along faults which have not been mapped due to their small areal extent with orientations as suggested by the cluster geometry.

The recorded microseismic events show a high degree of waveform similarity with the different

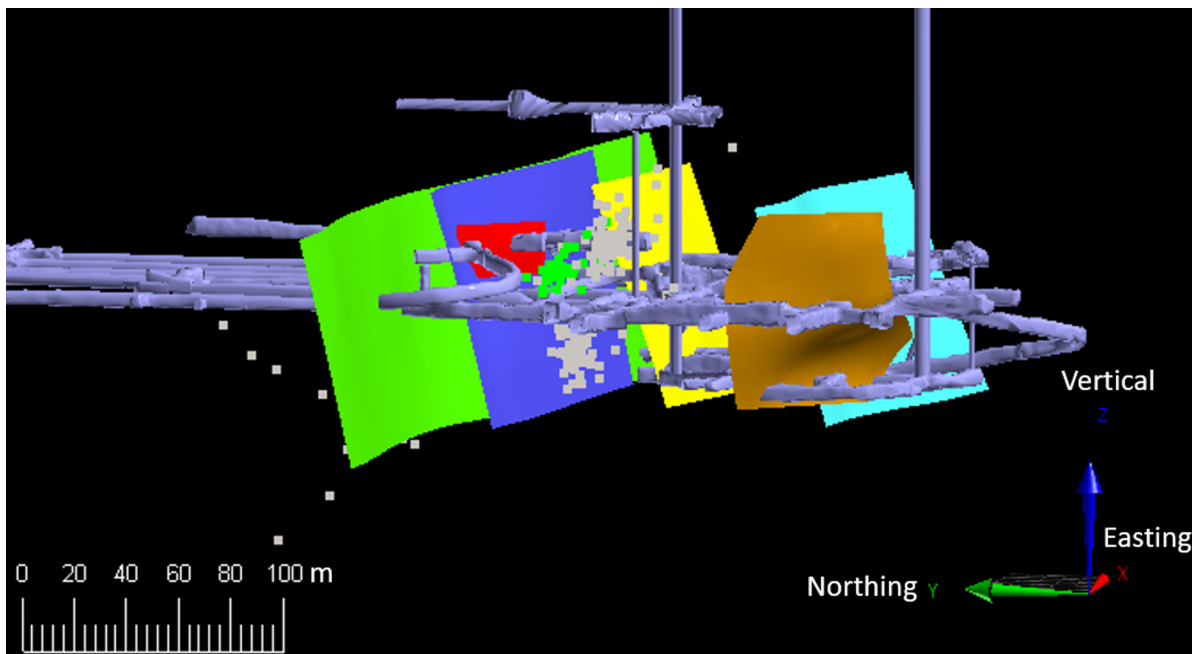


Figure 3.8: 3D view of the microseismic event locations and the mapped faults. Event locations belonging to multiplet groups 1 and 3 are shown as gray and green squares respectively. Faults are shown as colored surfaces. The shafts and tunnels are shown by solid blue color. For visual clarity, only faults close to shaft 1 and the 480 m tunnel network are shown.

multiplet groups containing doublets with normalized cross-correlation coefficients greater than 0.8. Therefore, these events should occur close to each other and should have similar source mechanisms (Castellanos and Van der Baan, 2015b). Also, the microseismic events have significant shear wave components visible in their waveforms recorded at different monitoring wells. Only S-wave/P-wave amplitude ratios less than 5 are indicative of tensile failure (Eaton *et al.*, 2014) for instance due to fluid injection. Therefore, we expect these events to have shear slip source mechanisms. Furthermore, based on the geometry of the microseismic event clusters and the presence of the numerous small faults in the mining area, we hypothesize that the microseismicity occurs due to repeated slips on an unmapped pre-existing fault due to mining activity.

Next, we compare the 3D velocity model obtained from tomography with the 3D density model provided by the mine operating company. The 3D density model is obtained from the inversion of the gravity data performed by the mine operating company. The 3D density model is very smooth which may be due to a number of factors like the grid used for inversion of the gravity data and the regularization parameters used. Therefore, we cannot expect a one-to-one correlation between the velocity and the density model. In Figure 3.9, we compare the map view of the velocity and the density model at a depth of 0.45 km. The white contour on top of the velocity map (Figure 3.9a) corresponds to spread function value of -1 and the velocities inside this contour are reliable and well constrained by the double-difference tomography. The velocity map in Figure 3.9a shows a low-velocity zone near  $Y=0.2$  km and  $X=0.2$  to  $0.3$  km surrounded by relatively higher velocities. In the density map, we have a low-density zone near  $Y=0.2$  to  $0.3$  km and  $X=0.2$  to  $0.3$  km with relatively higher densities surrounding it. Thus, the low (-high) density seems to correlate with the low (-high) velocity but the correlation is not one-to-one and the density map is much smoother than the velocity map.

Figures 3.10a and 3.10b show the North-South cross-sections through the final 3D velocity model obtained from double-difference tomography of the field data overlain with the shafts and tunnel network and the inverted event locations of the largest multiplet group. We have projected the fault traces and the geotechnical zone limits from Figures 2.6a and 2.6b on top of the N-S

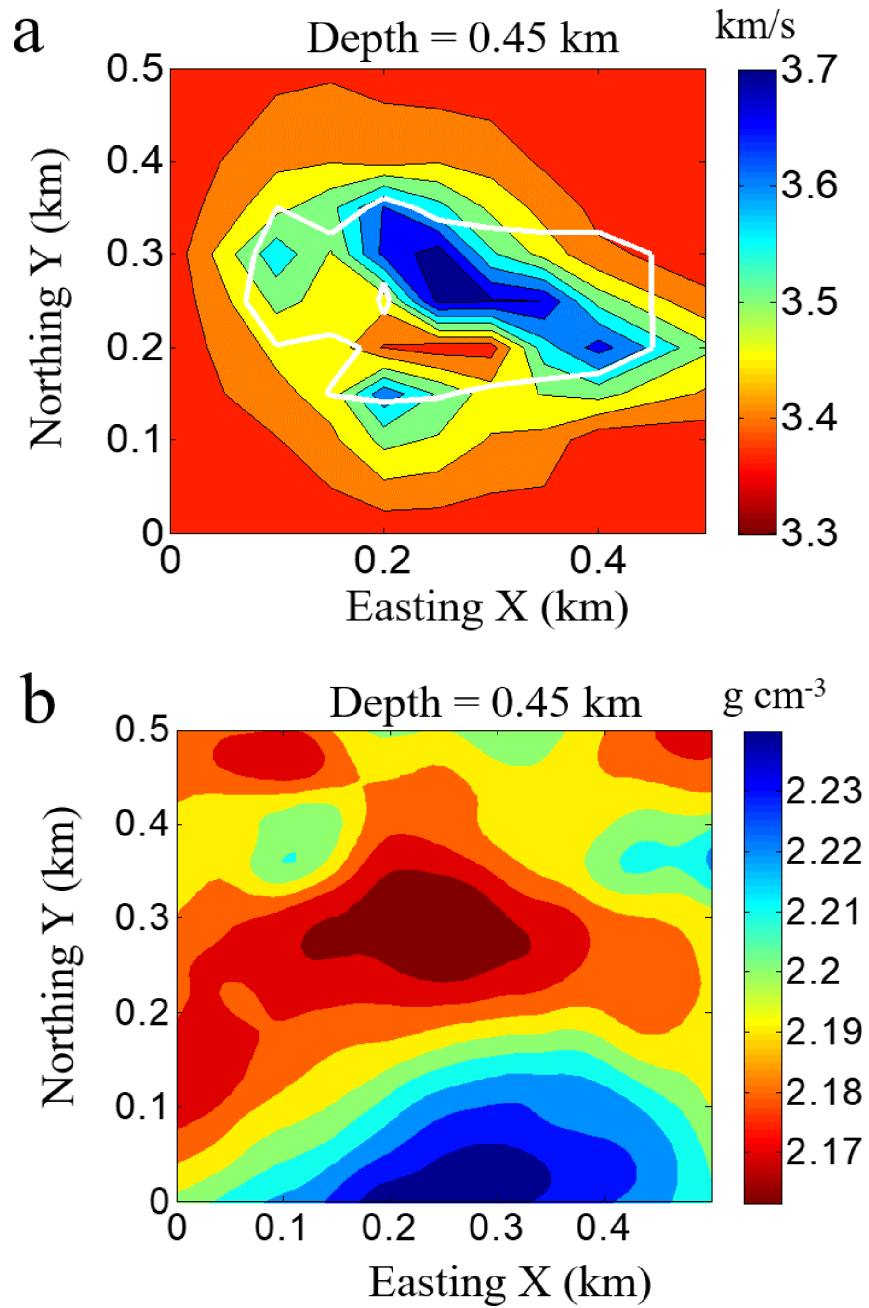


Figure 3.9: Map view at a depth of 0.45 km through (a) the inverted 3D velocity model obtained from double difference tomography, and (b) the 3D density model.

cross-sections at  $X=0.2$  km and  $X=0.25$  km respectively. The velocity cross-sections in Figures 3.10a and 3.10b show significant lateral velocity contrasts. The North-South velocity cross-section at  $X=0.25$  km shows sharp contact between the high and low velocities between depths of 0.45 km and 0.5 km, and  $Y=0.2$  km and  $Y=0.25$  km. The velocities between depths of 0.4 to 0.5 km and 0.2 to 0.3 km along East and North are considered reliable as suggested by the synthetic characteristic tests. The North-South velocity cross-section at  $X=0.25$  km (Figure 3.10b) shows a higher velocity region between depths of 0.45 km and 0.5 km, and  $Y=0.2$  km and  $Y=0.35$  km. Thus, the velocity model indicates two possible scenarios (1) either the unconformity contact around 0.45 km depth is not flat due to localized uplift of the high-velocity basement rock along faults cutting through the unconformity or (2) the sharp lateral velocity contrasts around 0.45 km depth are due to the alteration of the basement rock due to fluid circulation along faults and subsequent ore deposition. The various drill holes in this region suggest significant displacements of the unconformity surface ranging from 16 m up to 36 m (Bruneton, 1993). However as seen in Figures 3.10a and 3.10b, there are many fault traces which are closely spaced together (some faults delineating the lateral velocity contrasts) and the faults themselves have small areal extent. The velocity model lacks the resolution to show the velocity variations across each of these faults. Therefore, we investigate the second scenario by looking at the possible correlations between the inverted velocity images and the known geotechnical zones.

In Figures 3.10a and 3.10b, Zone IV shown on the top of the velocity images corresponds to regolith with  $RMR < 40$  (Table 2.1). Therefore it is characterized by a low-velocity region as seen in the N-S velocity cross-sections. Below zone IV, we can see higher velocities in the cross-section corresponding to zones V and VI with  $RMR > 40$ . In Figure 3.10d the low velocity at the center corresponds to zone IV (regolith with  $RMR < 40$ ) which is also identified in the N-S cross-sections in Figures 3.10a and 3.10b. The zone IV pinches out towards the south (Figures 3.10a and 3.10b) and hence we get relatively higher velocity on the map (Figure 3.10d) around  $X=0.2$  and  $Y=0.15$  km. We project the outline of the higher velocity (top right in Figure 3.10d) on top of the geotechnical map (Figure 3.10c). This high-velocity outline incorporates all three geotechnical

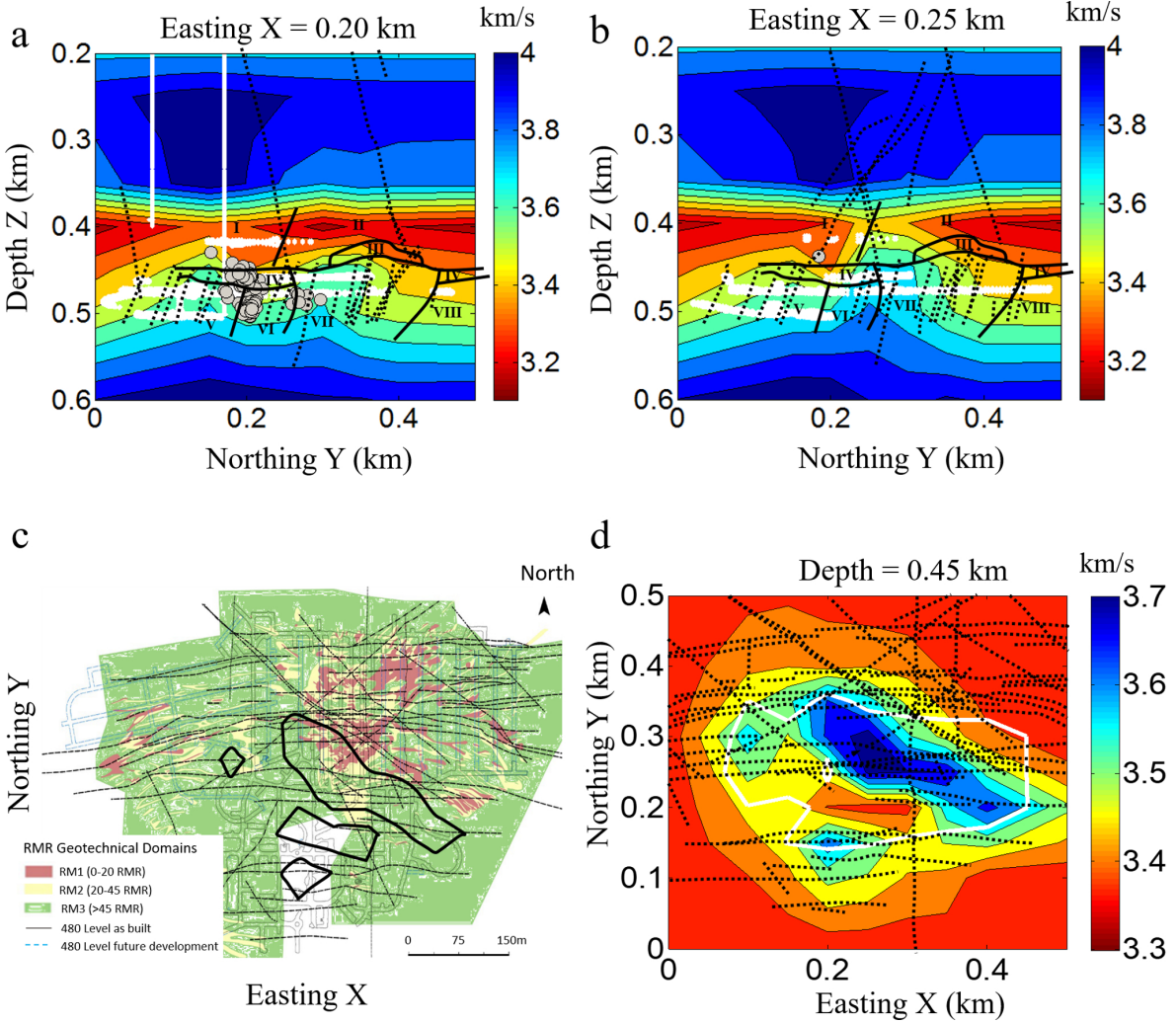


Figure 3.10: (a,b) Vertical cross-sections through the 3D velocity model obtained from double-difference tomography of the field data overlain with the shafts and tunnel network (white dots) and the inverted event locations of multiplet group 1 (gray dots). North-South cross-sections at (a)  $X=0.20$  km, and (b)  $X=0.25$  km. North-South cross-sections in (a) and (b) are superimposed with the geotechnical zone limits (solid black lines) and faults (dotted black lines) from Figures 2.6a and 2.6b respectively, and the known geotechnical zones are annotated from I to VIII. (c) Map view of the geotechnical domains classified based on RMR values superimposed with the known fault traces (from Figure 2.6c). (d) Map view of the velocity model at a depth of 0.45 km overlain with the fault traces shown in Figure 2.6d. The outlines of the low and high-velocity regions identified in figure 3.10d are projected on Figure 3.10c (solid black lines).

domains namely RM1, RM2, and RM3 as seen in Figure 3.10c. The rock quality is good towards the center (near shaft 1 as shown by RM3 domain) and deteriorates towards the ore body due to a higher degree of alteration (domain RM2 and RM1). Since the events are clustered towards the center (near  $X=0.2$  km,  $Y=0.2$  km), the seismic rays mainly sample the high-quality rocks mass (RM3 domain) and hence we get higher velocities in this zone. In the cross-sections (Figures 3.10a and 3.10b), this higher velocity region corresponds to zone VII which varies from extremely poor to good with RMR in the range of 5-50 (which is equivalent to zones contained in the higher velocity outline in the map view in Figure 3.10c as discussed in Chapter 2). Thus, the geotechnical zones correlate well with the velocities obtained from the tomographic inversion.

We have projected the mapped fault traces shown in Figure 2.6d on top of the velocity map at 0.45 km depth (Figure 3.10d). Even though the velocity model lacks the resolution to analyze velocity contrasts across individual faults which are very closely spaced, we can draw some general inferences from Figure 3.10d on a bigger scale. For example, the various faults seem to delineate the low-velocity region in the center (around  $X=0.2$  km,  $Y=0.2$  km). The NW-SE striking faults appear to show the edges of the high-velocity body in the upper right corner in Figure 3.10d. This correlation of the boundaries of high and low-velocity regions with the mapped faults and geotechnical zones suggests that faulting and subsequent motion (eg, uplift of the basement rock) may have some control over the observed geotechnical zones. Since the Uranium deposition is attributed to the fluids flowing along basement faults cutting into the overlying sediments (Fayek, 2013), a close association of rock alteration and faults is geologically plausible.

In this study, we use microseismic data to obtain a 3D velocity model with the application of double-difference tomography. More conventional use of the microseismic monitoring is to study the excavation damaged zones around underground openings based on the event locations (Cai *et al.*, 2001; Young *et al.*, 2004). Thus, we obtain medium velocities beyond the seismically active region. Since the lithological variations have a dominant effect on seismic velocity in regions where other factors like in situ stresses, temperature, fluid contents etc do not vary significantly, the velocity models can be correlated with lithological variations. Furthermore, the different geotechnical

zones are characterized by different lithologies or different degree of alteration within a particular rock type. Therefore, the 3D velocity models can be used to delineate various geotechnical zones as shown in this study. Thus, the passive seismic tomography using microseismic records can act as an effective tool to complement the geotechnical evaluations which often require direct access to the rock samples.

### **3.5 Conclusions**

Microseismic data contain information about the surrounding medium through which the seismic waves have traveled, yet the low signal-to-noise ratio makes it difficult to extract this information. However waveform similarity of microseismic events especially in exploration setting like mine development, hydraulic fracturing stimulations etc allows computation of high-quality differential arrival times using cross-correlation techniques. These reliable differential arrival times can be incorporated in double-difference tomography to obtain very accurate event locations and high-resolution velocity models. In the present study, the relocated microseismic events tightly cluster around the 480 m tunnel network which is the main working level and shaft no 1 which acts as the main service and access shaft. The close association of event locations with mining activities suggests that the microseismic events are induced due to mining activity. Furthermore, the events appear to originate along planar surfaces, thus event occurrence due to fault reactivation remains a plausible hypothesis.

The high-resolution velocity model obtained from double-difference tomography shows lateral velocity contrasts. The lateral velocity contrasts appear to be delineated by numerous faults. Furthermore, the 3D velocity model shows good correlation with the various known geotechnical zones in the mine. This suggests a close association of the faults and the geotechnical zones which in this case can be due to the alteration of the host rocks caused by the fluids flowing along the faults leading to Uranium deposition. Thus, passive seismic tomography provides information beyond the seismically active region like excavation damaged zones and can be of great aid in

geological and geotechnical interpretations.

# Chapter 4

## Induced seismicity during underground mine development: Causes and mechanisms<sup>1</sup>

### Summary

We try to understand the origin of the microseismic events recorded during an underground mine development. The events are located near the main horizontal working level at 480 m depth close to a vertical access shaft. Based on the waveform characteristics and temporal comparisons, we rule out the possibility of these events to be man-made seismic signals/vibrations due to the construction activities like drilling and blasting. Since the events are located far from the actual construction sites at the 480 m level, the stress perturbations due to the excavation of newly created cavity are not responsible for triggering seismicity. The geometry of the microseismic event clusters suggests their occurrence on planar surfaces such as geological faults. We, therefore, present a hypothesis that the microseismic events occur due to reactivation along unmapped faults caused by mining

---

<sup>1</sup>A manuscript including a version of this chapter is in preparation for submission to *Geomechanics for Energy and the Environment*.

development. This raises a question why only faults with specific orientations have associated microseismicity when various other faults with different orientations are known to exist in the area. In order to investigate the likelihood of fault reactivation based on their orientations and spatial locations with respect to the mine layout, we compute changes in the regional stresses due to the horizontal tunnel network and vertical shafts. Using the Coulomb stress change, we identify faults which are most favorably oriented for shear slippage. Results show that the faults inferred from the microseismic event locations near the 480 m tunnel network and the main shaft are well oriented for reactivation. However, the static stress changes due to the tunnels and shafts are insufficient to cause shear slippage. An additional stress perturbation is required for fault reactivation to occur due to frictional failure. The daily patterns in microseismicity show some correlation with the daily rock removal, hoisted out via shaft 1, close to the main event cluster. We show that the peak dynamic stresses due to the vibrations caused by blasting are insufficient to cause frictional failure of fault. However, the vibrations caused by a large rock crusher placed in the 480 m level near shaft 1 are likely responsible for triggering microseismicity along the faults. Thus, modeling of the static and dynamic stresses and integrating them with a suitable failure criterion can produce pertinent insights into the likelihood of anthropogenic processes to yield induced seismicity.

## **4.1 Introduction**

Underground mining operations are known to cause earthquakes in the form of low magnitude microseismic events and sometimes rock-bursts. These events are examples of induced seismicity which refers to triggering of brittle rock failure due to anthropogenic activities. Induced seismicity has also been observed during hydraulic fracturing of unconventional hydrocarbon reservoirs like tight sands and shales, and associated wastewater disposal (Frohlich, 2012; Ellsworth, 2013; Atkinson *et al.*, 2016), Enhanced geothermal systems (Moeck *et al.*, 2009), carbon dioxide sequestration (Verdon *et al.*, 2013; Goertz-Allmann *et al.*, 2014) and reservoir impoundment (Gupta, 2002). Since the induced seismicity is closely associated with the industrial activities, it may pose

a significant risk to the engineering project and the general public living in the neighboring regions if of sufficient magnitude. Therefore it is important to study the possible causes inducing these events and understand their mechanisms in order to mitigate the potential hazard.

In order to establish the main cause of induced seismicity, it is important to continuously monitor the operational parameters used during the industrial activity. In the case of underground mining, the volume of rock removed, the mining technique and the spatial location and geometry of excavation front should be recorded. McGarr (1976) shows that the maximum magnitude of an induced event is limited by the total volume of rock removed during mining assuming that the change in volume is accommodated only by seismic failure. Mining techniques also affect the rate and magnitude of induced events. For example, room and pillar mining is associated with large magnitude events (McGarr *et al.*, 2002). This is due to the fact that if one of the unmined pillars (which are intended to inhibit stope collapse) fails, many others can fail in a cascade causing a large magnitude event. On the other hand, if pillars are not left, the stope collapse and associated seismicity, localized near the advancing face, occurs steadily. Thus maximum magnitudes are smaller even though the rate of seismicity is higher than the room and pillar mining technique. A temporal correlation of these operational parameters with the recorded seismicity can help in identifying the root cause of seismicity.

The event mechanism can be studied by modeling the changes in stresses and pore pressures due to the anthropogenic activity. Seismicity can be triggered by both static and dynamic changes in the in situ stresses due to natural geologic processes or anthropogenic activities (Freed, 2005). Whereas static stress perturbations leave a permanent imprint on the stress field, the dynamic stress perturbations are generally due to transient waves propagating through the medium. Both static and dynamic stress changes have been invoked to explain the aftershock sequences following major events (King *et al.*, 1994; Stein, 1999; Kilb *et al.*, 2000). In underground mine development, the occurrence of the microseismic events is often attributed to the excavation of new cavity (Martin, 1997; Cai *et al.*, 2001) which can be regarded as a static stress change scenario. However Talebi and Young (1992) have shown an increase in the microseismic event occurrence rate immediately

following blasting which may suggest dynamic stress triggering due to the passage of vibrations.

In this Chapter, we study the microseismic data recorded during an underground mine development. Their amplitudes are less than those of the recorded blasts and are thus thought to have negative magnitudes. The details of the microseismic data, acquisition setup, mining operations, and geological settings are provided in Chapter 2. We perform double-difference tomography on this data which is described in Chapter 3. In this Chapter, we focus on the possible cause and mechanism of these microseismic events by analyzing the spatiotemporal distribution of the microseismic events and performing quantitative modeling to compute the stress changes due to the vertical shafts and the horizontal tunnel network.

## **4.2 Potential causes of microseismicity**

### **4.2.1 Man made seismic signals due to mining activity**

Underground mining developments involve the use of drill and blast technique and/or boring machines for construction of access tunnels. The blasts in underground mines can cause significant vibrations with peak ground velocity (*PGV*) (same as peak particle velocity) of up to 1 m/s near the source region (McCreath *et al.*, 1994; Ahmed and Ansell, 2014). The rock debris resulting from drilling is removed from the mines with trucks and/or lifts. A rock crusher is generally used in the main working level to reduce the size of the rock debris so that they can be easily transported to the surface via the vertical access shafts. The operation of machinery such as trucks and rock crushers generates low amplitude vibrations as compared to blasting with a maximum reported *PGV* of up to 0.08 m/s near the source region (Krell, 1979; Ahmed, 2015). These vibrations can be recorded by the geophones. Thus, there is a possibility that the identified events in the recorded data assumed to be microseismic events are simply the mine blasts and the vibrations due to machinery like trucks, lift engines, and rock crusher. However, the waveform characteristics such as amplitudes, frequency content and time duration of the recorded signal should be different in

the case of the man-made seismic signals due to blasting and/or machinery, and the actual microseismic events. Moreover, if the recorded events are such man-made seismic signals, there is likely to be a one-to-one correspondence between the time of occurrence of the events and the timing of the mining activity.

First, we look at the waveform characteristics of our recorded data acquired during an underground mining development. Figure 4.1 shows the waveforms of a mine blast, a microseismic event, and a noisy waveform possibly representing vibrations due to a rock crusher at a common receiver along with their respective time-frequency representation. The amplitude of the blast (Figure 4.1a) is at least three orders of magnitude larger than that of the microseismic event (Figure 4.1c). The blast has a high energy P-wave arrival and has a broader bandwidth (Figure 4.1b) as compared to the microseismic event (Figure 4.1d) with frequencies varying over a wide range from 5-250 Hz. Moreover, the blast waveforms are recorded shortly after the blasting is performed in the mine. Thus, it is easy to identify the recorded blasts and separate them from the recorded events assumed to be microseismic events. Moreover, the recorded events are transient in nature, ie, they typically have a time duration of nearly 200 ms. Figure 4.1e shows a waveform containing a number of repetitive wavelets over the entire recording duration. The time domain signal resembles the vibration signals generated by machines having rotational elements (Randall and Antoni, 2011). Since the rock crusher has a rotating shaft which is driven by a motor, the recorded waveform in Figure 4.1e most possibly represents the vibrations due to the rock crusher. The time-frequency representation in 4.1f shows a number of resonances recorded at high frequencies of  $\sim 100$  Hz and between 150-250 Hz. Kwiatek *et al.* (2008) have reported resonances (with frequencies observed over wide ranges of 30-40 Hz, 110-130 Hz, 200-230 Hz and 300-320 Hz) due to the operation of the water pumps used for injection of fluid in the treatment well during hydraulic fracturing stimulation of geothermal reservoirs. Thus the waveform characteristics and the spectral content allow us to separate the recorded microseismic events from the mine blasts and the vibrations due to the rock crusher.

Figure 4.2 shows the temporal distribution of blasting, the daily rate of rock removal and the

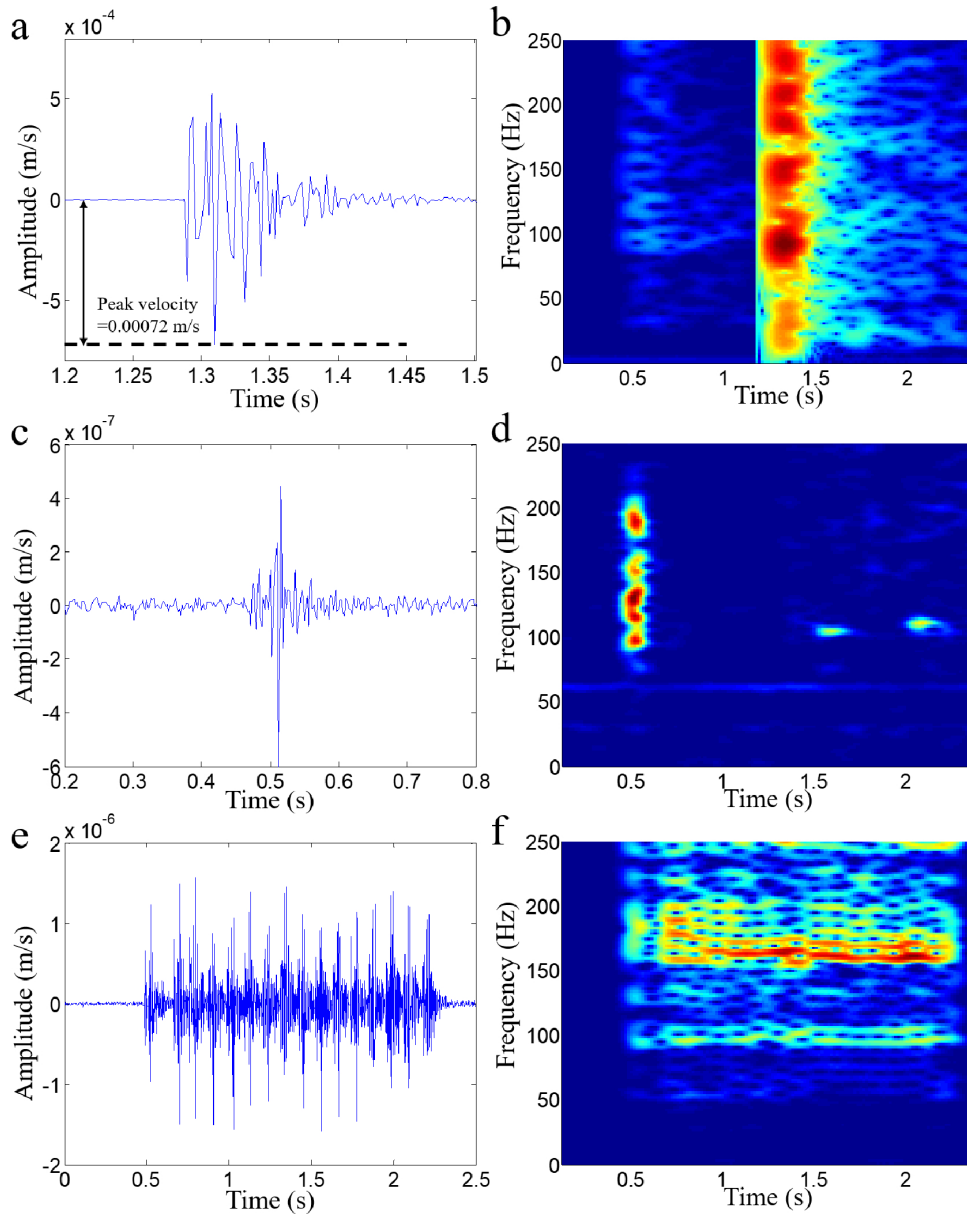


Figure 4.1: (a) Waveform of the mine blast in time with the peak ground velocity (*PGV*) highlighted. (b) Time-frequency representation of the blast signal shown in (a). (c) Waveform of the microseismic event in time. (d) Time-frequency representation of the microseismic events shown in (c). (e) Waveform of the vibrations due to the rock crusher. (f) Time-frequency representation of rock crusher vibrations shown in (e). Different axis limits are used for the time scale for proper visualization.

recorded seismic events (modified from Castellanos and Van der Baan (2015a)). The volume of the removed material has been estimated from the company reports and are thought to be representative but with some uncertainty. On the 8<sup>th</sup> and 9<sup>th</sup> of January, there is no blasting or rock removal, but we see a considerable number of microseismic events during this period. A similar observation can be made on 15 and 17 January. Due to the lack of one-to-one correspondence with mining activities and the differences in the waveform characteristics, we interpret the identified events as microseismic events thereby ruling out the possibility that they are man-made vibrations due to mine blasts and/or the machinery like trucks, lift engines and rock crusher.

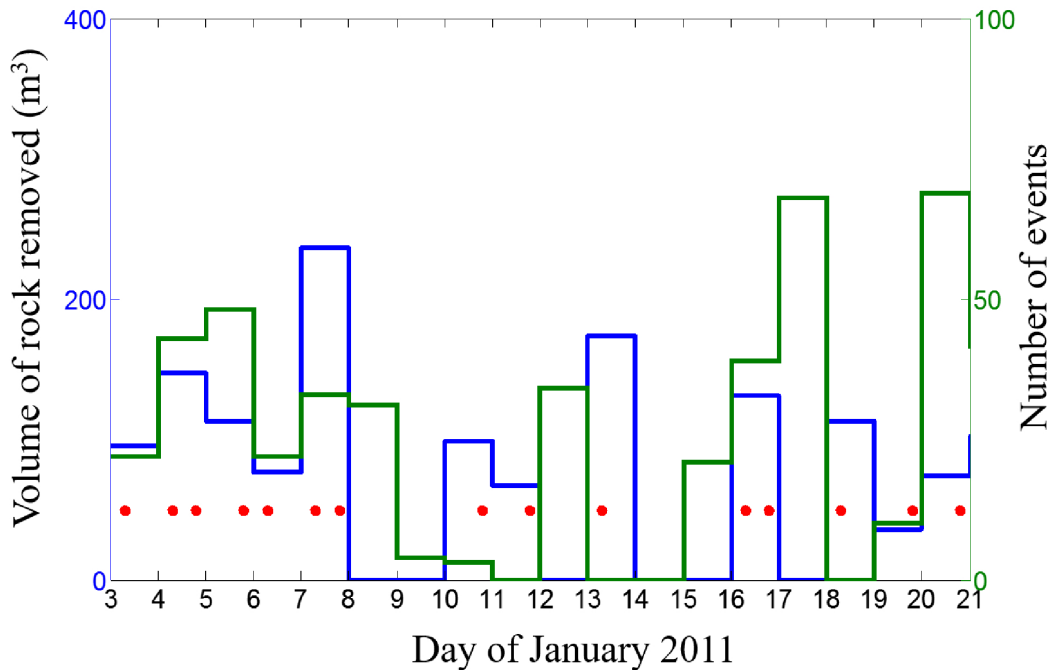


Figure 4.2: Temporal distribution of blasting (red filled circles), volume of rock removed per day (blue line), and the microseismic event count per day (green line) during January 2011 (modified from Castellanos and Van der Baan (2015a)).

#### 4.2.2 Dynamic triggering due to blasting or vibrations from rock crusher

As noted in the previous section, the mining activities like blasting and the operation of the rock crusher can create significant vibrations (Figure 4.1). These transient vibrations can trigger seis-

micity in a critically stressed rock mass similar to the dynamic triggering observed due to the passage of seismic waves generated by large earthquakes (Hill *et al.*, 1993; Kilb *et al.*, 2000; Brodsky and Prejean, 2005; Hill and Prejean, 2007). Therefore, triggering of seismicity due to the vibrations caused by these mining activities can be termed as dynamic triggering.

Talebi and Young (1992) show that the microseismic event count increases immediately following the blasts carried out to construct a shaft in the Underground Research Laboratory in Canada. The event count decreases 2 hours after blasting and follows a decay similar to that observed in the case of aftershocks of a large earthquake. Thus the blasts provide the dynamic stresses needed to trigger seismicity. Castellanos and Van der Baan (2015a) used the same data as we used in this study and compared the temporal distribution of all triggered files recorded by the acquisition system with the blasting activity. Figure 4.3 is reproduced from Castellanos and Van der Baan (2015a). Figure 4.3a shows the distribution on 4 January 2011. There are no recorded seismograms for up to 2-3 hr following the blasts at 7 am and 7 pm. Figures 4.3b-4.3d show that this observation is common for all the detonated blasts throughout the month. This suggests that the blasting is most unlikely to trigger the microseismic events. Therefore dynamic triggering due to blasting can be ruled out.

Castellanos and Van der Baan (2015a) note some correlation between the volume of rock removed and the time of daily rate of occurrence of microseismicity leading them to conclude that dynamic triggering due to debris transportation may be responsible for the observed microseismicity. This correlation can be seen in Figure 4.2 even though the correspondence is not one-to-one and there are some time periods when the volume of rock removed is zero but still microseismicity is observed. We examine this possibility by computing the dynamic stresses generated near the event locations due to the vibrations caused by the mine blasts and the rock crusher.

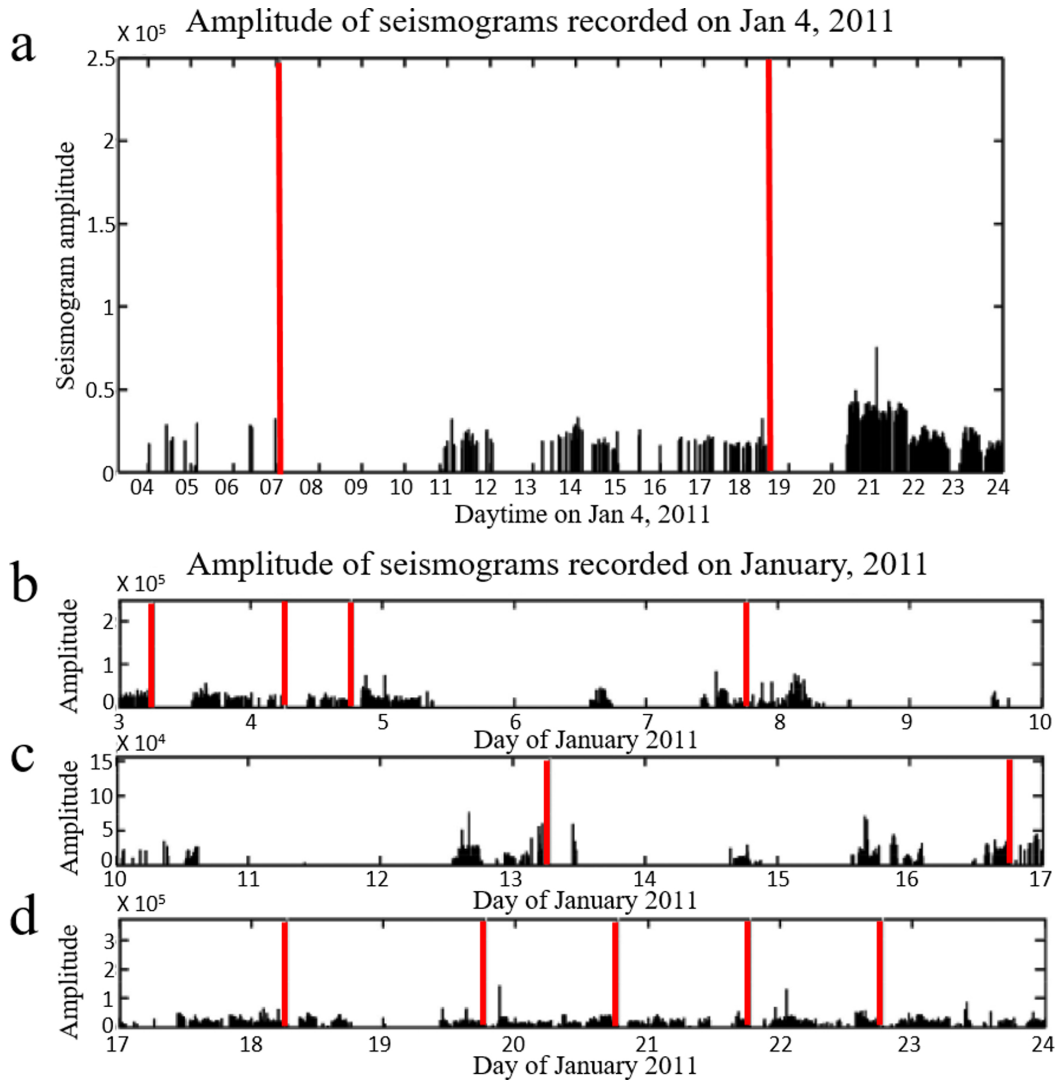


Figure 4.3: Temporal distribution of recorded seismograms and blasting activity on daily basis during January 2011 (from Castellanos and Van der Baan (2015a) and reproduced with permission of Oxford University Press). Amplitude versus time plots of recorded seismograms (black vertical lines) and blasts (red vertical lines) during (a) January 4, 2011, (b) January 3-10, (c) January 10-17, and (d) January 17-24.

### 4.2.3 Microseismicity due to local stress concentrations around newly excavated cavities

Excavation of underground cavities leads to large stress concentration near the walls of the cavities causing brittle failure of the surrounding rock. In the case of cylindrical cavities like vertical shafts or horizontal tunnels, there is a large stress redistribution ahead of the advancing tunnel face as well as near the sidewalls (Martin, 1997). The large deviatoric stresses ahead of the tunnel face initiate cracking causing microseismic events (Martin, 1997). As the tunnel face advances, these cracks begin to further develop due to the large tangential stresses near tunnel sidewalls leading to the development of the excavation damaged zone in the form of notches (Martin, 1997; Cai *et al.*, 2001). Such brittle failures are the most common cause of induced seismicity observed during the excavation of tunnels in underground mines. Thus, microseismicity initiates ahead of the advancing tunnel face and then continue around the sidewalls of the freshly excavated region. Common examples of the damage near the sidewalls of the cylindrical excavation include the borehole breakouts observed in the case of oil and gas wells.

Gibowicz *et al.* (1991) have shown that microseismic events are induced by drilling of the vertical shaft to greater depths due to the large stress concentrations around the shaft walls. Similarly, Martin (1997) and Cai *et al.* (2001) show the development of the excavation damaged zones and associated microseismicity around the horizontal tunnel drilled in the Underground Research Laboratory in Canada. Martin (1997) perform numerical modeling to show the region ahead of the advancing face of the horizontal cylindrical tunnel where the deviatoric stress exceeds the rock strength and cracking initiates leading to microseismicity. This region is limited up to 1 diameter ahead of the tunnel face. Similarly, near the sidewalls of the cavity, the zone of large stress concentrations is limited up to 1 radius away from the sidewalls. Therefore, the easiest way to isolate these failure processes causing microseismicity is to correlate the spatial location of the microseismic events with the construction sites.

Figure 4.4 shows the spatial position in the access tunnels at 480 m depth where construction

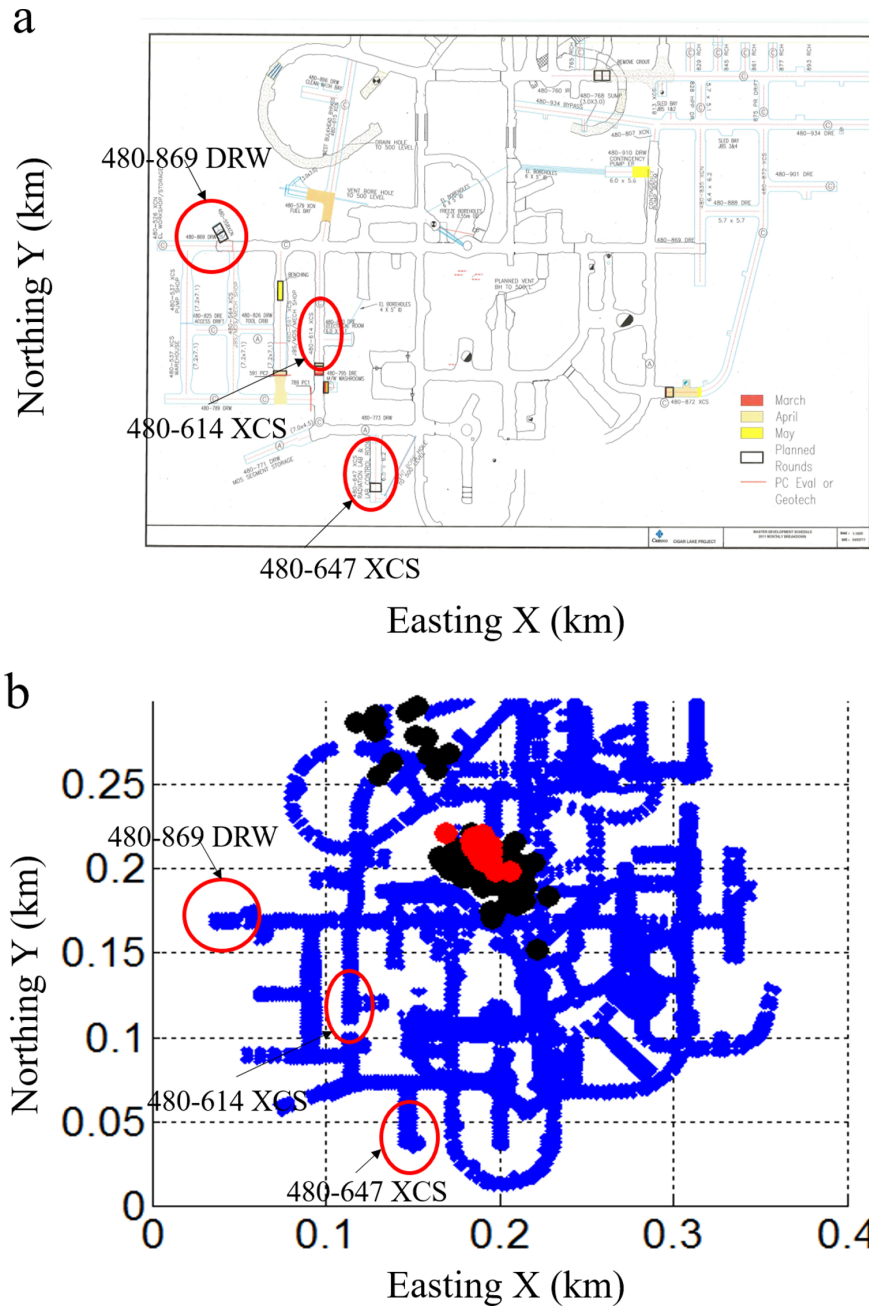


Figure 4.4: (a) Map view of the horizontal tunnel network at 480 m depth showing the construction sites where drill and blast technique was used during January 2011 marked by red closed curves. (b) Map view of the horizontal tunnel network at 480 m depth overlain with the microseismic event locations and the spatial location of the construction sites is shown by red closed curves.

was being carried out in the month of January 2011. The microseismic events cluster near shaft 1 and 480 m level but are separated by at least 100 m from the construction sites at 480 m level. The large stress concentrations which induce microseismicity ahead of the tunnel face and around the sidewalls are restricted up to 1 to 2 radius away, which in this case would be up to a maximum distance of 5 m from the tunnel face and sidewalls (radius of horizontal tunnels is approx. 2.5 m). Therefore we can rule out the possibility that these events are induced due to the large stress concentrations near the tunnel walls.

#### **4.2.4 Microseismicity caused by stress perturbations due to the horizontal tunnel network and the vertical shafts**

The 480 m level has a very complex and irregular access tunnel layout with most of the tunnels oriented along either N-S or E-W directions. The superposition of stress changes due to individual tunnels can considerably perturb the regional stresses up to a large distance from the tunnel network. The construction of the extensive tunnel network at 480 m level has resulted in the removal of a large volume of rock from this depth. A simple model can be used to compute stress changes due to the entire 480 m level by assuming it resembles an oblate spheroidal heterogeneity placed in a homogeneous host rock (Figure 4.5). Such a model geometry has been used to explain the stress perturbations, induced seismicity by fault reactivation and observed ground subsidence in the case of fluid extraction from producing hydrocarbon reservoirs (Segall and Fitzgerald, 1998; Rudnicki, 1999). Here we consider the tunnel network at 480 m depth only and neglect the tunnel networks at 420 m, 460 m, and 500 m. This is because the tunnel network at 420 and 460 m have already been backfilled before the start of the recorded data used in this study. Moreover, these levels and the one at 500 m are much less extensive as compared to the 480 m level (Figure 4.5). Hence the stress perturbations due to the 420 m, 460 m and 500 m near the locations of the recorded microseismic events (which cluster above and below the 480 m level) are limited.

In our mining case, we consider pure elastic stresses only unlike in the case of producing

hydrocarbon reservoirs where poroelastic coupling has been invoked (Segall and Fitzgerald, 1998). This is due to the fact that the access tunnels are being constructed in the basement rocks away from known groundwater sources and hence changes in pore pressure can be neglected. We perform quantitative modeling for computing stress changes due to our oblate spheroidal heterogeneity model and its role in inducing microseismicity. Furthermore, the events occur near vertical shaft 1. Even though this shaft was already completed prior to the recording period, yet we model the stress changes due to the vertical shaft to understand their role in inducing microseismicity.

### **4.3 Stress modeling**

We model perturbations in regional stresses due to the mining infrastructure (vertical shafts and horizontal tunnel network) in order to understand their role in triggering of observed microseismicity. Hence, we first compute the stress changes due to tunnels and shafts and then the resulting Coulomb failure criterion to assess the likelihood of shear failure on pre-existing faults. We use the Eshelby's equivalent inclusion method (Eshelby, 1957; Ju and Sun, 2001) to compute the stress perturbations caused by the horizontal tunnel network. Eshelby's solutions have previously been used to compute induced stress changes in hydrocarbon and geothermal reservoirs (Segall and Fitzgerald, 1998; Rudnicki, 1999), modeling of the compaction bands (Meng and Pollard, 2014), and brittle shear fracturing (Healy *et al.*, 2006). In the next subsections, we describe the model setup, the Eshelby's equivalent inclusion method, the stress concentrations around the vertical cylindrical cavity and the Coulomb failure criterion.

#### **4.3.1 Model geometry and parameters**

In the uranium mine under study, we have two vertical shafts and a network of horizontal tunnels at different depths (Figures 2.1b and 4.5). We assume that the shafts and tunnel network are situated in a homogeneous and isotropic medium of infinite extent. Thus we neglect the effect of

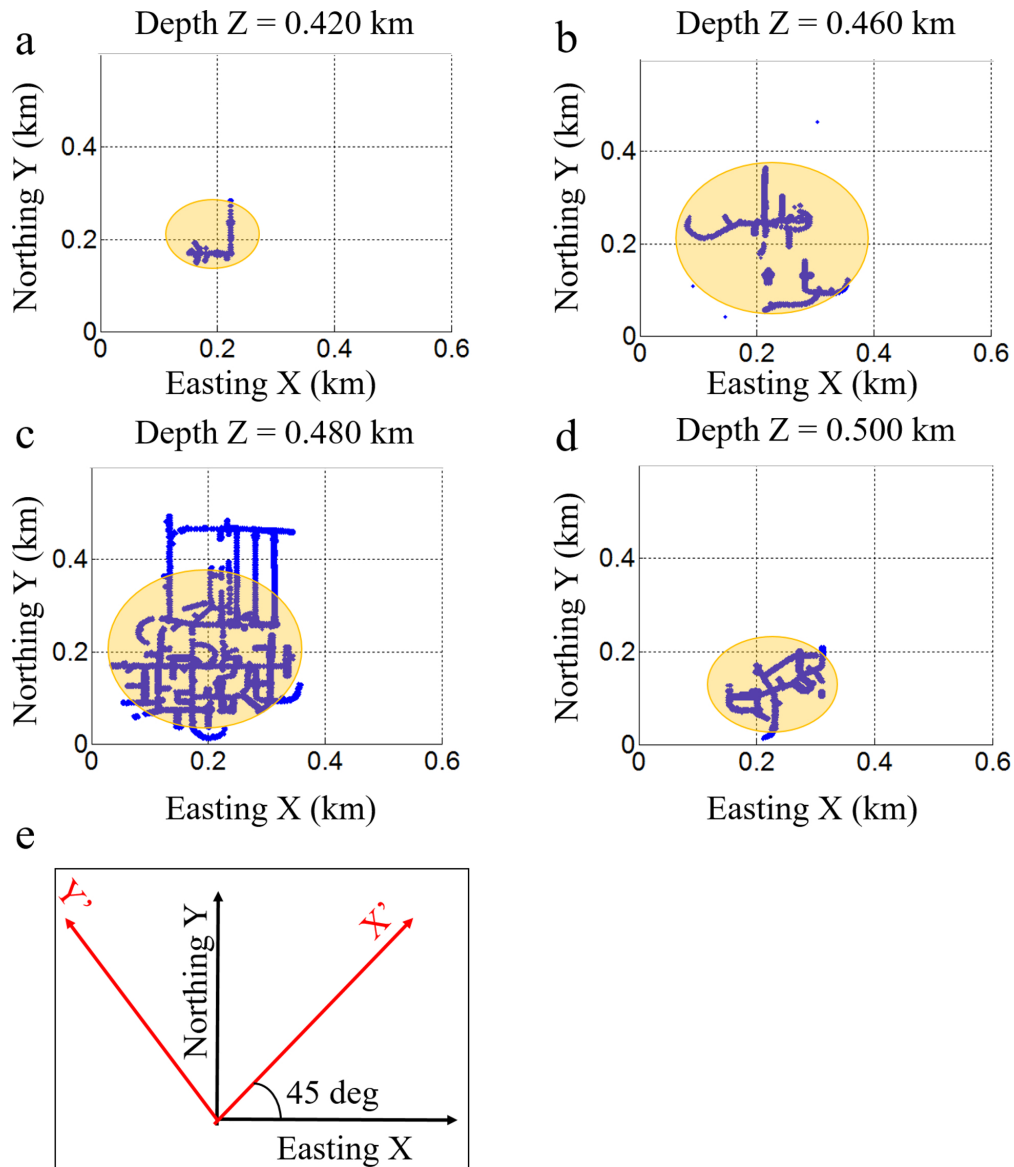


Figure 4.5: Map view of the tunnel layout (blue filled circles) at (a) 0.420 km depth, (b) 0.460 km depth, (c) 0.480 km depth, and (d) 0.500 km depth. The circle encompassing the tunnel network at each depth is the top view of the oblate spheroid used for replacing actual tunnel network. The tunnel network at 480 m depth is most extensive and is modeled as an oblate spheroid with center at  $X=0.2$  km,  $Y=0.2$  km and major axes  $a_o = b_o = 150m$ . The minor axis  $c_o$  (not visible in this map view) is taken to be 2 m since the diameter of the tunnel is approx. 4 m to 5 m. (e) The two Cartesian coordinate systems:  $X$ ,  $Y$ , and  $Z$  along Easting, Northing and Vertical, and  $X'$ ,  $Y'$ , and  $Z'$  along maximum horizontal, minimum horizontal and vertical stresses.

Table 4.1: Parameters for computing stress perturbations around the cylindrical cavity and the oblate spheroidal inclusion

Parameter	Value and Unit
Material properties	
Lamé parameter, $\lambda$	17.5 GPa
Shear modulus, $G$	26.25 GPa
Poisson ratio, $\nu$	0.2
Density, $\rho$	2500 kg/m <sup>3</sup>
Cylindrical cavity	
Radius, $a_c$	2.5 m
Oblate spheroidal inclusion	
Semi-major axis, $a_o$	150 m
Semi-major axis, $b_o$	150 m
Semi-minor axis, $c_o$	2 m
Principal stresses	
Depth, $h$	475 m
Vertical stress, $\sigma_{zz}$	$\rho gh = 11.6$ MPa
Maximum horizontal stress, $\sigma_{xx}$	$1.15 \times \sigma_{zz} = 13.4$ MPa
Minimum horizontal stress, $\sigma_{yy}$	$0.87 \times \sigma_{zz} = 10.1$ MPa
Pore pressure, $p_0$	0.107 MPa

the earth's free surface on stress perturbations due to the shafts and tunnels. The elastic constants of this medium are taken to be equal to the representative values of the basement rock Gneiss (listed in Table 4.1). The vertical shafts are modeled as vertical cylindrical borehole-like cavities for computing resulting stress perturbations. The radius of the cylindrical cavity  $a_c$  is 2.5 m.

The horizontal tunnel networks have complex geometry as shown in Figure 4.5. The diameter of the tunnels is approx. 4 to 5 m. Since the tunnel network at 480 m has extensive areal coverage, we model it as an oblate spheroidal inhomogeneity with semi-major axes  $a_o$ ,  $b_o$  and  $c_o$  along the Easting (X), Northing (Y) and Vertical (Z) axes respectively such that  $a_o = b_o \gg c_o$ . The elastic constants of the inhomogeneity are estimated by assuming it as a composite made up of homogeneous rock and void space. The two end members of this inclusion are a cavity (volume fraction: rock=0; void space=1) and an inclusion (volume fraction: rock=0.9; void space=0.1). Depending upon the volume fraction of the void space, we compute the effective elastic moduli using the Voigt bound (Mavko *et al.*, 2009). We use this upper bound instead of the Reuss or Hill

averages (Mavko *et al.*, 2009) so that the contrast in elastic properties of the spheroidal inhomogeneity and the surrounding matrix is the minimum for any given volume fraction so that our stress concentration estimates are conservative (not overestimated for a given volume fraction).

### 4.3.2 Boundary conditions

We take estimates of regional stresses as boundary conditions for our stress modeling. In the absence of any cavity, we assume a homogeneous stress field throughout the medium. When we introduce the shafts and tunnel network the stress pattern changes around these cavities but returns to the regional stresses as we move away from the mine. At infinity, the stresses are always equal to the regional stresses. The regional stress pattern for Saskatchewan is very homogeneous (Reiter *et al.*, 2014). The direction of regional maximum horizontal stress is NE-SW for Saskatchewan and the minimum horizontal stress is oriented in NW-SE direction. The third principal stress is in the vertical direction. We assume this far-field stress pattern to be representative of the regional stress field around the mine.

According to technical data from the mine operating company, borehole hydrofracture tests were performed for in situ stress measurements. These tests suggest that the minimum principal horizontal stress is 0.87 of the vertical stress and the maximum principal horizontal stress is 1.15 of the vertical stress for a rock mass with a saturated density of 2,500 kg/m<sup>3</sup>. However, the exact depth and methodology of the hydrofracture tests are not available. We take these stress magnitudes as representative values for the far-field stresses. Thus the in situ stresses point to a strike-slip faulting regime as seen from the stress magnitudes in Table 4.1. Since the tunnels are drilled in the basement rock (gneiss) away from known groundwater sources, the pore pressure can be assumed to be equal to the atmospheric pressure at the depth (= 480 m) of the horizontal tunnel network that is being modeled as an oblate spheroidal heterogeneity. This pore pressure is calculated as the sum of the atmospheric pressure at the earth's surface and the pressure of the 480 m long air column. Taking atmospheric pressure ( $p_e$ ) at the earth's surface to be equal to 101325

Pa and air density ( $\rho_a$ ) to be equal to  $1.225 \text{ kg/m}^3$ , the pore pressure at the 480 m level equals to,  $p_0 = p_e + \rho_a gh$ , where  $g=9.8 \text{ ms}^{-2}$  is the acceleration due to gravity and  $h=480 \text{ m}$  is the height of the air column. We further assume this pore pressure to be uniform and unchanged as there is no intentional fluid injection or extraction during the construction of the access tunnels. Table 4.1 lists the pore pressure and the regional stress magnitudes used as boundary conditions in our stress modeling. We assume that each individual cavity is present in the uniform far-field stresses  $\sigma_0$  and the presence of a neighboring cavity does not distort the far-field stresses. We have defined two Cartesian coordinate systems as shown in Figure 4.5e: (i) X, Y, and Z along Easting, Northing and Vertical, and (ii) X', Y', and Z' along the three principal stresses namely the maximum horizontal, the minimum horizontal and the vertical stresses respectively. Since the maximum horizontal stress is along NE-SW, we can transform any vector from the coordinate system (X, Y, Z) to coordinate system (X', Y', Z') by a rotation of +45 deg about the Z axis.

### 4.3.3 Eshelby's equivalent inclusion method

Eshelby (1957) provided solutions for the stress perturbations caused by a spontaneous change in form of a region within an isotropic elastic solid. The region which undergoes a change in form is called inclusion and the surrounding region is called the matrix. When the inclusion undergoes a change in form, both matrix and inclusion attain new stress/strain states. Eshelby (1957) defines stress-free strain or eigenstrain  $\epsilon_{ij}^*$  as the strain state acquired by the inclusion when it is removed from the constraint of the matrix. Eshelby (1957) showed that the stress and strain field developed inside an ellipsoidal inclusion are uniform. Eshelby (1957) also solved the inhomogeneity problem where the ellipsoidal region has different elastic properties from the surrounding matrix. In this case, there is no induced stress field unless an external load is applied. When a remote uniform stress field is applied, the stress perturbations due to the inhomogeneity can be determined by the inclusion problem when the fictitious eigenstrain  $\epsilon_{ij}^*$  is chosen properly.

Suppose the elastic moduli of the ellipsoidal inhomogeneity and the matrix are  $C_{ijkl}^*$  and  $C_{ijkl}$

respectively. The eigenstrain  $\epsilon_{ij}^*$  can be computed as

$$\epsilon_{ij}^* = -(A_{ijkl} + G_{ijkl}^{int})^{-1} \epsilon_{0kl} , \quad (4.1)$$

where  $A_{ijkl}$  is defined as

$$A_{ijkl} = (C_{ijkl}^* - C_{ijkl})^{-1} C_{ijkl} , \quad (4.2)$$

$\epsilon_{0kl}$  is the uniform strain due to uniform far-field stresses  $\sigma_{0kl}$ , and  $G_{ijkl}^{int}$  is the interior point Eshelby's tensor for the ellipsoidal inclusion. The explicit expressions for the components of the interior point Eshelby's tensor  $G_{ijkl}^{int}$  for a spheroidal inclusion are given in Ju and Sun (2001).

Then the stress perturbations outside a spheroidal inhomogeneity centered at  $\mathbf{x}^0$  is given by

$$\sigma'_{ij} = C_{ijkl} G_{klmn}(\mathbf{x} - \mathbf{x}^0) \epsilon_{mn}^* , \quad (4.3)$$

where  $G_{ijkl}(\mathbf{x} - \mathbf{x}^0)$  is the exterior point Eshelby's tensor. The explicit mathematical expressions for  $G_{ijkl}(\mathbf{x} - \mathbf{x}^0)$  are given in Ju and Sun (2001). For an isotropic medium, the linear elasticity tensor  $\mathbf{C}$  contains only two independent elastic constants, namely the shear modulus  $G$  and Lamé parameter  $\lambda$ .

#### 4.3.4 Stress concentration around vertical cylindrical cavities

The stresses around a vertical cylindrical cavity of radius  $a_c$  at a point  $(r, \theta, \tau)$  in cylindrical coordinates can be computed as (Schmitt *et al.*, 2012)

$$\begin{aligned} \sigma_{\theta\theta} = & \frac{\sigma_{xx} + \sigma_{yy}}{2} \left(1 + \frac{a_c^2}{r^2}\right) - \frac{\sigma_{xx} - \sigma_{yy}}{2} \left(1 + \frac{3a_c^4}{r^4}\right) \cos(2\theta) \\ & - \tau_{xy} \left(1 + \frac{3a_c^4}{r^4}\right) \sin(2\theta) , \end{aligned} \quad (4.4)$$

$$\begin{aligned}
\sigma_{rr} = & \frac{\sigma_{xx} + \sigma_{yy}}{2} \left(1 - \frac{a_c^2}{r^2}\right) \\
& + \frac{\sigma_{xx} - \sigma_{yy}}{2} \left(1 + \frac{3a_c^4}{r^4} - \frac{4a_c^2}{r^2}\right) \cos(2\theta) \\
& + \tau_{xy} \left(1 + \frac{3a_c^4}{r^4} - \frac{4a_c^2}{r^2}\right) \sin(2\theta),
\end{aligned} \tag{4.5}$$

$$\sigma_{\tau\tau} = \sigma_{zz} - \nu \left(2(\sigma_{xx} - \sigma_{yy}) \left(\frac{a_c^2}{r^2}\right) \cos(2\theta) + 4\tau_{xy} \left(\frac{a_c^2}{r^2}\right) \sin(2\theta)\right), \tag{4.6}$$

$$\sigma_{r\tau} = (\tau_{xz} \cos(\theta) + \tau_{yz} \sin(\theta)) \left(1 - \frac{a_c^2}{r^2}\right), \tag{4.7}$$

$$\begin{aligned}
\sigma_{r\theta} = & \tau_{xy} \left(1 + \frac{2a_c^2}{r^2} - \frac{3a_c^4}{r^4}\right) \cos(2\theta) \\
& - \frac{\sigma_{xx} - \sigma_{yy}}{2} \left(1 + \frac{2a_c^2}{r^2} - \frac{3a_c^4}{r^4}\right) \sin(2\theta),
\end{aligned} \tag{4.8}$$

$$\sigma_{\theta\tau} = (-\tau_{xz} \sin(\theta) + \tau_{yz} \cos(\theta)) \left(1 + \frac{a_c^2}{r^2}\right), \tag{4.9}$$

where  $\sigma_{\theta\theta}$  is the azimuthal normal stress called hoop stress,  $\sigma_{rr}$  is the radial normal stress,  $\sigma_{\tau\tau}$  is the vertical normal stress and  $\sigma_{r\tau}$ ,  $\sigma_{r\theta}$  and  $\sigma_{\theta\tau}$  are the shear stresses.  $\sigma_{xx}$ ,  $\sigma_{yy}$ ,  $\sigma_{zz}$ ,  $\tau_{xz}$ ,  $\tau_{yz}$ , and  $\tau_{xy}$  are the components of the homogeneous far-field stress.

These near-field stresses in cylindrical coordinates  $(r, \theta, \tau)$  can be converted into a Cartesian coordinate system by

$$\sigma_{xxnf} = \sigma_{rr} \cos^2(\theta) + \sigma_{\theta\theta} \sin^2(\theta) - \sigma_{r\theta} \sin(2\theta), \tag{4.10}$$

$$\sigma_{yynf} = \sigma_{rr} \sin^2(\theta) + \sigma_{\theta\theta} \cos^2(\theta) + \sigma_{r\theta} \sin(2\theta), \tag{4.11}$$

$$\sigma_{zznf} = \sigma_{\tau\tau} , \quad (4.12)$$

where  $\sigma_{xxnf}$ ,  $\sigma_{yynf}$  and  $\sigma_{zznf}$  are the near-field stresses in the Cartesian coordinate system along the X', Y' and Z' axes respectively.

### 4.3.5 Coulomb failure function

The Coulomb failure function ( $CFF$ ) is often used to assess the potential of shear slippage under in situ stresses.  $CFF$  is computed as

$$CFF = \tau - \mu(\sigma_n - p_0) , \quad (4.13)$$

where  $\tau$  is the shear stress and  $\sigma_n$  is the normal stress (compression positive) acting on any weakness plane with a given orientation,  $p_0$  is the pore pressure and  $\mu$  is the coefficient of friction. We assume zero cohesive strength and take  $\mu = 0.6$  owing to the presence of pre-existing fractures. In the case of pre-existing fractures/faults i.e. when cohesive strength is zero,  $CFF > 0$  represents the regions which are most likely to undergo shear slippages under the prescribed stresses (Zoback, 2007). Note that this approach is similar to computing the slip tendency (Morris *et al.*, 1996; Moeck *et al.*, 2009), where the ratio between the shear ( $\tau$ ) and effective normal stress ( $\sigma_n - p_0$ ) is used. In this approach failure occurs if  $\tau/(\sigma_n - p_0) > \mu$ .

Since the cylindrical and spheroidal cavities lead to differential stress concentrations in the surrounding rock mass, there are some regions which are more likely to fail as compared to others. To isolate the effect of these inhomogeneities from the background uniform stress, we use the change in Coulomb stress defined as

$$\Delta CFF = \Delta\tau - \mu(\Delta\sigma_n - \Delta p_0) , \quad (4.14)$$

where  $\Delta\tau$  and  $\Delta\sigma_n$  are the changes in shear and normal stresses respectively resolved on the

weakness plane with a given orientation (Freed, 2005).  $\Delta p_0$  is the change in pore pressure. Shear failure is encouraged if  $\Delta CFF$  is positive and vice versa. We compute the Coulomb stress change around the shafts and tunnel network to identify regions where shear failure is promoted by these structures.

The normal and shear stresses required for  $CFF$  and  $\Delta CFF$  computations (equations 4.13 and 4.14) can be resolved on an arbitrary plane whose normal  $\hat{\mathbf{n}}$  has components  $\hat{n}_1$ ,  $\hat{n}_2$ , and  $\hat{n}_3$  as

$$\sigma_n = \hat{n}_1^2 \sigma_1 + \hat{n}_2^2 \sigma_2 + \hat{n}_3^2 \sigma_3, \quad (4.15)$$

$$\tau = [\hat{n}_1^2 \sigma_1^2 + \hat{n}_2^2 \sigma_2^2 + \hat{n}_3^2 \sigma_3^2 - \sigma_n^2]^{(1/2)}, \quad (4.16)$$

where  $\sigma_1$ ,  $\sigma_2$  and  $\sigma_3$  are the near-field stresses resulting from the sum of the uniform far-field stresses  $\sigma_0$  and the stresses concentrated around the spheroidal inclusion computed using Eshelby's equivalent inclusion method (equation 4.3) or a cylindrical shaft. In the latter case, the stresses  $\sigma_1$ ,  $\sigma_2$  and  $\sigma_3$  are identical to  $\sigma_{xxnf}$ ,  $\sigma_{yyf}$  and  $\sigma_{zznf}$  (equations 4.10, 4.11 and 4.12).

## 4.4 Results

### 4.4.1 Static stress changes due to shaft and tunnel network

The stress perturbations due to the horizontal tunnel network are computed using Eshelby's equivalent inclusion method (Eshelby, 1957; Ju and Sun, 2001) by representing it as an oblate spheroidal inclusion. Figure 4.6 shows the stress perturbations caused by the spheroidal inclusion along line AA' (normal to the inclusion along its centerline) and BB' (ahead of the inclusion tip along its centerline) for different volume fractions of the rock and void space computed using equation 4.3. In the left panel, the stress profile is along line AA' whereas in the right panel it is along BB'. Figures 4.6(b), 4.6(c) and 4.6(d) show the stress perturbations due to the inclusion for volume fraction of

rock=0, 0.5, and 0.9 respectively. Positive values show increase in compressive stresses (the stress perturbation is compressional) whereas negative values represent decrease in compressive stresses (the stress perturbation is tensile). Along AA' the vertical stress perturbation is always tensile and larger in magnitude as compared to the two horizontal stress perturbations. The magnitude of the stress perturbation decreases with increasing volume fraction of the rock. The two horizontal stress perturbations are tensional when the volume fraction of rock is zero but they become compressional as the volume fraction of rock increases. The stress perturbations slowly decay with increasing distance normal to the inclusion. Along BB' the vertical stress perturbations have large compressional values at the tip of the inclusion whereas the horizontal stress perturbation along the X' axis is tensile. Unlike AA', the stress perturbations along BB' are limited at the tip and rapidly decay as we move slightly away from the tip.

Figures 4.7(a) and 4.7(b) show the hoop and radial stresses around the vertical shafts normalized with respect to the maximum principal stress  $\sigma_{xx}$  computed using equations 4.4 and 4.5. The hoop stress is smaller than  $\sigma_{xx}$  at points on the shaft wall in the direction of  $\sigma_{xx}$  ( $\theta = 0^\circ$  and  $180^\circ$ ) whereas it is much greater than  $\sigma_{xx}$  at points perpendicular to  $\sigma_{xx}$  ( $\theta = 90^\circ$  and  $270^\circ$ ). The radial stress pattern is almost symmetrical around the shaft. Radial stresses increase from zero at the shaft wall to the far field stresses at nearly one radius away from the wall. The near-field stresses along the X', Y' and Z' axes in the Cartesian coordinate system normalized with respect to their corresponding far-field stress values are shown in Figures 4.7(d), 4.7(e) and 4.7(f) (equations 4.10, 4.11 and 4.12). The stress perturbations in the principal stresses  $\sigma_{xx}$  and  $\sigma_{zz}$  are tensile at points on the shaft wall along the X' axis ( $\theta = 0^\circ$  and  $180^\circ$ ) whereas they are compressive at points along the Y' axis ( $\theta = 90^\circ$  and  $270^\circ$ ) (Figures 4.7(d) and 4.7(f)). However the stress perturbations in the principal stress  $\sigma_{yy}$  are compressive at points on the shaft wall along the X' axis ( $\theta = 0^\circ$  and  $180^\circ$ ) whereas they are tensile at points along the Y' axis ( $\theta = 90^\circ$  and  $270^\circ$ ) (Figure 4.7(e)). The region of stress perturbations is restricted only up to one radius away from the shaft wall as concluded also by Martin (1997) and Cai *et al.* (2001).

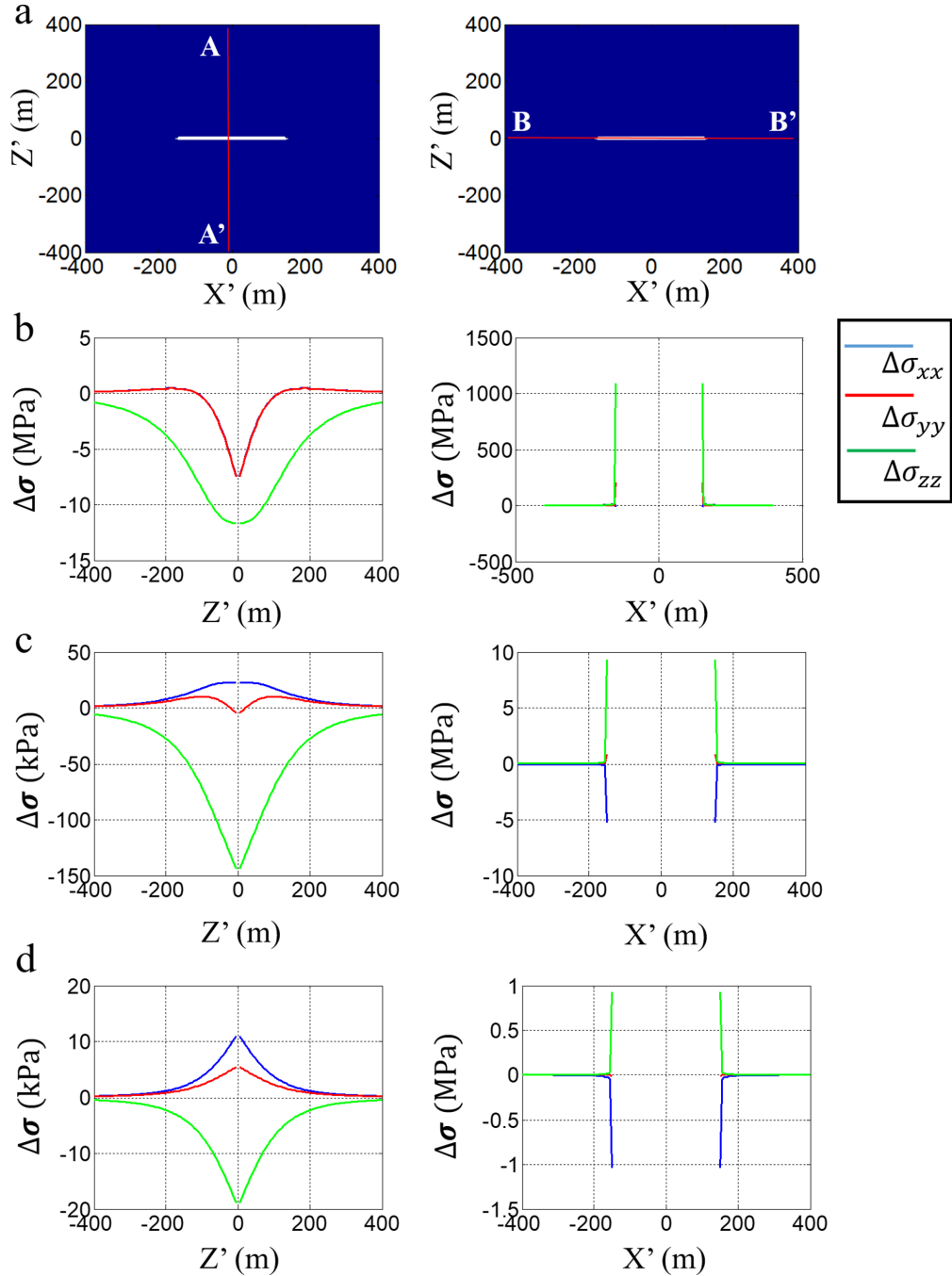


Figure 4.6: Stress perturbations due to the oblate spheroidal inclusion along AA' (left) and BB' (right) shown in (a) for different volume fractions of (b) rock=0, void space=1, (c) rock=0.5, void space=0.5, and (d) rock=0.9, void space=0.1.

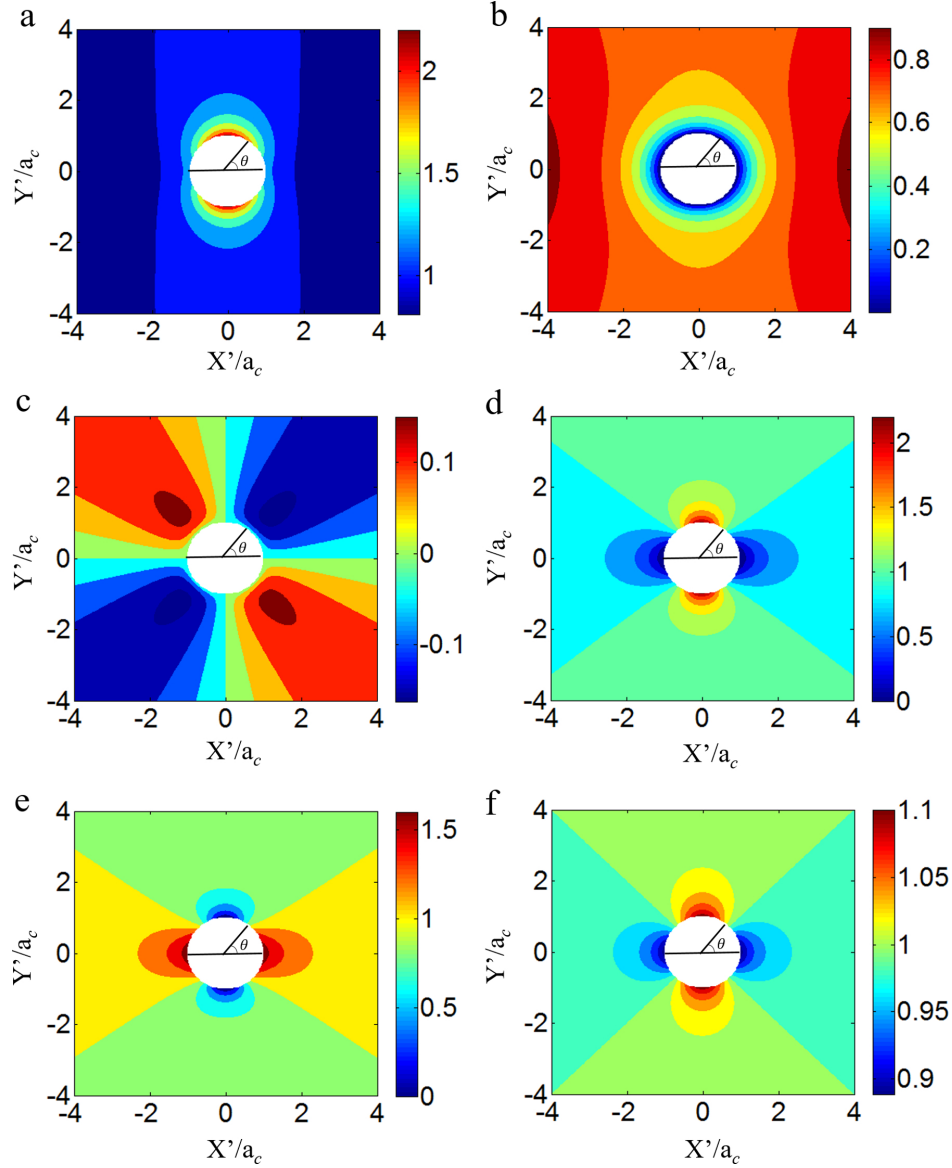


Figure 4.7: Map view of stress distribution around the vertical cylindrical cavity of radius  $a_c$  computed with parameters given in Table 4.1. Angle  $\theta$  is measured with respect to  $X'$ -axis and is positive counterclockwise. (a) Normalized hoop stress  $\frac{\sigma_{\theta\theta}}{\sigma_{xx}}$ . (b) Normalized radial stress  $\frac{\sigma_{rr}}{\sigma_{xx}}$ . (c) Normalized shear stress  $\frac{\sigma_{r\theta}}{\sigma_{xx}}$ . (d) Normalized near-field stress along X-axis  $\frac{\sigma_{xx}^{nf}}{\sigma_{xx}}$ . (e) Normalized near-field stress along Y-axis  $\frac{\sigma_{yy}^{nf}}{\sigma_{yy}}$ . (f) Normalized near-field stress along Z-axis  $\frac{\sigma_{zz}^{nf}}{\sigma_{zz}}$ . The stress perturbations and the resulting potential shear-slippage zone is limited to a few radii away from the shaft wall.

#### 4.4.2 Coulomb stress change

We compute the Coulomb failure function ( $CFF$ ) (equation 4.13) to assess the likelihood of shear slippages along pre-existing fault planes. Figure 4.8a shows the  $CFF$  for fault planes of all orientations in 3D in the uniform far-field stresses on an equal area stereonet plot (lower hemisphere projection). The strike of the fault plane is measured with respect to the geographical North which is marked at the top of the stereonet. Since the regional maximum horizontal stress is oriented NE-SW,  $\sigma_{xx}$  is marked at 45 deg N azimuthal angle,  $\sigma_{yy}$  is marked at 135 degrees N azimuthal angle while  $\sigma_{zz}$  is marked at the center of the plot as it is vertical.  $CFF$  has large negative values for all fault planes suggesting that they will not slip under in situ stresses within the existing far-field regional stress field (in the absence of tunnels or shafts).

The map view of the fault traces at 480 m (Figure 2.4) and 450 m (Figure 2.6d) depths show faults with five major strike directions: (1) E-W, (2) NE-SW, (3) N-S, (4) NNW-SSE, and (5) NW-SE. The faults striking E-W are most frequently occurring followed by faults with strikes in the NW-SE and NE-SW respectively in that order. The faults striking N-S and NNW-SSE are least frequently occurring (Figure 2.6d). The N-S faults are sub-vertical with dips of 80 deg towards East. The faults striking NNW-SSE have similar orientations to the best fitting planes obtained from the relocated microseismic events. Therefore we use the best fitting plane,  $164.7^\circ/55^\circ$  W in place of the NNW-SSE faults for computing the Coulomb stresses. All other faults are steeply dipping (dips  $> 60$  deg), so we take a dip magnitude of 60 deg for these faults in computing the Coulomb stresses. We plot the poles of these faults on top of Figure 4.8a and surround them with colored circles. All these faults are stable under the in situ stresses as shown by the large negative values of  $CFF$ . The fault striking NW-SE (surrounded by a gray circle) has a large negative value of  $CFF$  (around -7 MPa) whereas other fault orientations (surrounded by colored circles) have smaller negative values of  $CFF$  ( $> -6.2$  MPa). Thus the faults striking NW-SE are most unfavorably oriented for reactivation under the far-field regional stresses in the absence of tunnels and shafts.

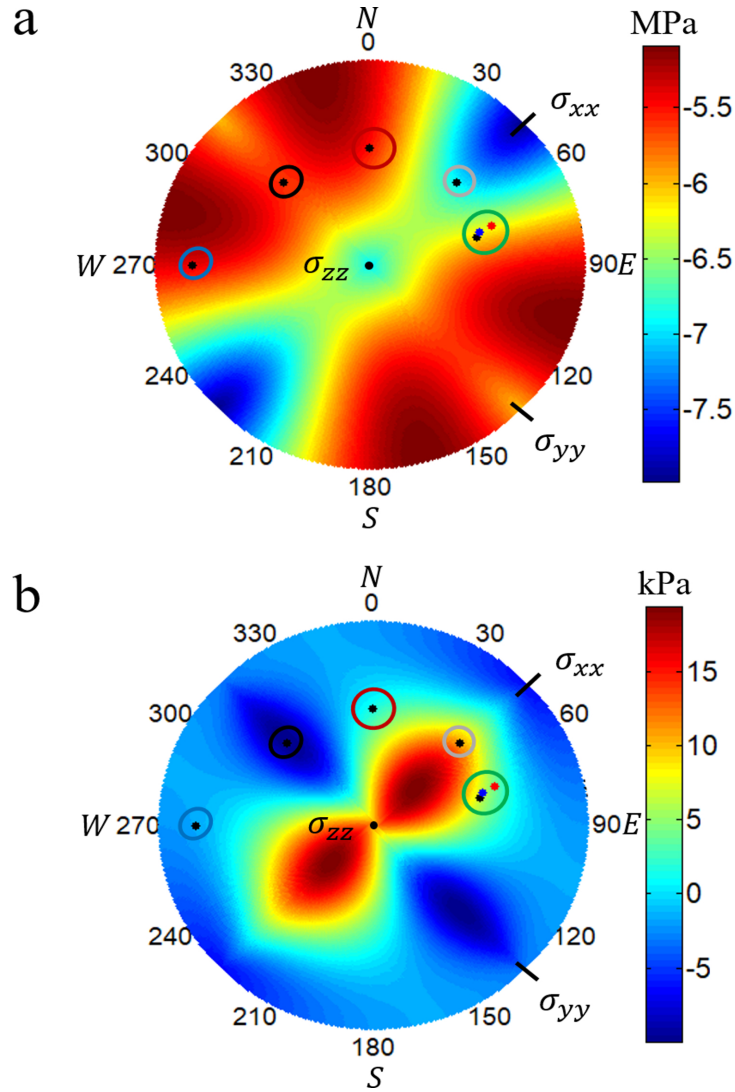


Figure 4.8: (a) Equal area stereonet plot of Coulomb failure function (in  $MPa$ ) for all fault planes in 3D computed in the uniform far-field stresses. (b) Equal area stereonet plot for Coulomb stress changes (in  $kPa$ ) for all fault planes in 3D computed at a point on the roof of the spheroidal inclusion (volume fraction: rock=0.9, void space=0.1) directly above its center. Slip is promoted for hot colors and for cold colors, the slip is restricted. The black circle contains the pole of the NE-SW trending fault dipping at 60 degrees towards SE. The green circle contains the poles of the best-fitting fault planes obtained from the relocated multiplet groups. The blue circle contains the pole of the N-S trending fault dipping at 80 deg towards East. The gray and red circles contain respectively the poles of the NW-SE and E-W trending faults dipping at 60 degrees towards SW and South respectively.

Next we compute the Coulomb stress changes  $\Delta CFF$  (equation 4.14) for all planes in 3D due to the stress concentration around the spheroidal inclusion (volume fraction: rock=0.9, void space=0.1). Since the microseismic events are located near the center of the tunnel network close to shaft 1 which is near the center of our spheroidal inclusion model, we compute the  $\Delta CFF$  at a point on the roof of the inclusion directly above its center. Figure 4.8b shows the plot of  $\Delta CFF$  on equal area stereonet which helps in identifying the orientation of fault planes with positive Coulomb stress change. The faults striking NW-SE has maximum positive Coulomb stress change (surrounded by the gray circle), however, they are most unfavorably oriented in the far-field regional stresses ( $CFF=-7$  MPa). The poles of the best-fitting fault planes obtained from the relocated multiplet groups also have relatively large positive values of  $\Delta CFF$  (surrounded by the green circle). For the faults striking E-W and dipping at 60 deg South, the Coulomb stress change has a very small positive value approaching to zero (surrounded by the red circle). Similarly for the faults striking N-S with dips of 80 deg towards East (surrounded by the blue circle), the Coulomb stress change is nearly zero. The faults striking NE-SW and dipping at 60 deg towards SE have negative values of  $\Delta CFF$  (surrounded by the black circle). This implies that for a point on the roof of the spheroidal inclusion slip is promoted for some fault orientations (namely the fault planes inferred from microseismic event locations) but restricted for others (the faults striking NE-SW). The  $\Delta CFF$  values are small compared with absolute  $CFF$  due to the regional stress field which has large negative values (Figure 4.8a), therefore the static stress field due to the tunnel network is insufficient to cause slippage on pre-existing faults. However, the  $\Delta CFF$  values shown in Figure 4.8b are the most conservative estimates computed using Voigt bound when the volume fraction of the void space is just 0.1. If the volume fraction of void space increases to 0.2, the  $\Delta CFF$  values are higher. Therefore, the  $\Delta CFF$  values shown in Figure 4.8b should be used mainly to identify the faults which move closer to failure as compared to others due to the stress perturbations caused by the horizontal tunnel network.

In order to understand the effect of the stress changes due to the horizontal tunnel network on the reactivation potential of a specific fault based on its spatial location, we compute the Coulomb

stress changes  $\Delta CFF$  as a function of its location. The NW-SE striking fault has maximum Coulomb stress change at a point on the roof of the oblate spheroidal directly above its center (Figure 4.8b). However, this fault is most unfavorably oriented in the regional stress field (Figure 4.8a) and so most unlikely to reactivate as compared to other faults. The Coulomb stress changes for the E-W and N-S trending faults are very small approaching to zero. Since the fault,  $164.7^\circ/55^\circ$  W and  $045^\circ/60^\circ$  SE have relatively large Coulomb stress changes (Figure 4.8b) with opposing trend, we only show the Coulomb stress changes for these two faults as a function of their spatial location in Figure 4.9. Here again we use conservative estimates of stress perturbations by considering the spheroidal inclusion with the volume fraction of rock=0.9 and void space=0.1. Figures 4.9a and 4.9c show the map view in a horizontal plane tangent to the inclusion at its roof. In Figure 4.9a, the Coulomb stress change is positive over a large area in the center and negative near the equator of the inclusion. Thus the inclusion has a positive role in promoting microseismicity along the fault plane  $164.7^\circ/55^\circ$  W towards the central region above the roof. We get similar results at the base of the inclusion. This situation is reversed in Figure 4.9c where the fault is striking NE-SW and the inclusion stabilizes the fault resulting in a lesser likelihood of microseismicity towards central region above the roof. Figures 4.9b and 4.9d show the Coulomb stress change for the vertical cross-section passing through the center of the inclusion parallel to the maximum horizontal stress. The Coulomb stress changes are symmetric above and below the center of the cavity. The stress changes are positive above roof and base of the inclusion and negative very close to the tip region in Figure 4.9b and vice versa in Figure 4.9d.

Figure 4.10 shows the projection of the inverted event locations for the two largest multiplet groups (group 1 and 3) on top of the computed Coulomb stress changes for the fault plane inferred from the relocated multiplet groups ( $164.7^\circ/55^\circ$  W). In Figures 4.10a and 4.10b-4.10c the origin has been shifted to the center of the vertical shaft ( $X=0.207$  km,  $Y=0.170$  km,  $Z=0.480$  km) and the spheroidal inclusion ( $X=0.200$  km,  $Y=0.200$  km,  $Z=0.480$  km) respectively. The event locations have been adjusted with respect to the new origin before projection so as to analyze their positions relative to these structures. In Figure 4.10a, the two relocated multiplet clusters are shifted towards

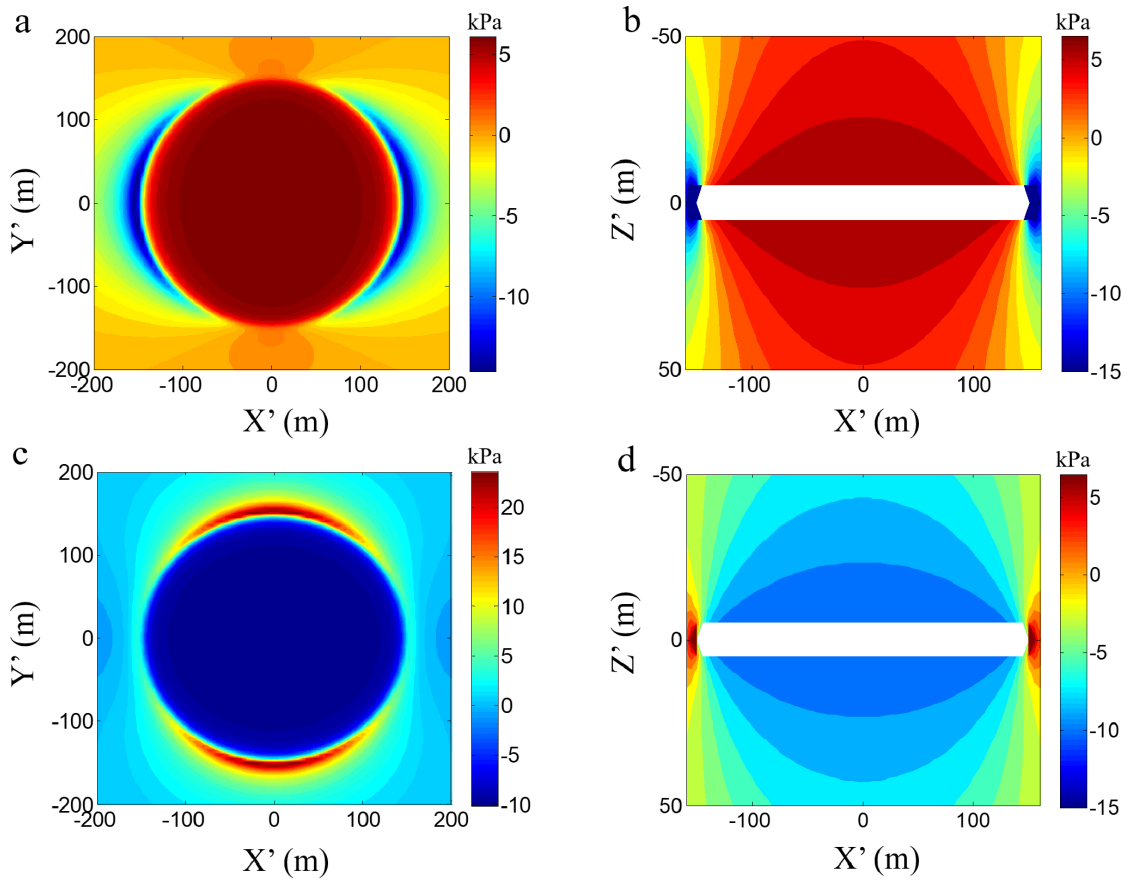


Figure 4.9: Coulomb stress changes (in  $kPa$ ) computed for two fault planes, (a) and (b)  $164.7^\circ/55.0^\circ$  W and (c) and (d)  $045^\circ/60.0^\circ$  SE as a function of their spatial position. (a) and (c) Map view in a horizontal plane tangent to the inclusion (volume fraction: rock=0.9, void space=0.1) at its roof. (b) and (d) Vertical cross-section passing through the center of the inclusion (volume fraction: rock=0.9, void space=0.1) parallel to the maximum horizontal stress. Slip is promoted for hot colors while for cold colors, slip is restricted.

North to NW of the main shaft where the Coulomb stress changes due to the shaft are negligible. Further, from our inverted event locations, we observe that the seismicity is clustered only around the main shaft and it is completely absent around the second shaft. Thus the vertical shafts have a negligible role in inducing static stress transfer at the location of the observed seismicity. However, the static stress field generated by the tunnel network has a much larger spatial extent as compared to the stress field caused by the vertical shafts (Figures 4.10b and 4.10c). Furthermore, the events occur above and below the tunnel network at 480 m depth towards its center where the Coulomb stress change for the fault  $164.7^\circ/55^\circ$  W is positive as shown in Figures 4.10b and 4.10c. Therefore, the tunnel network at 480 m depth has a major role in affecting the initial static stress state which facilitates microseismicity but has insufficient strength to trigger events by itself (Figure 4.8).

## 4.5 Discussion

### 4.5.1 Static stress transfer due to the horizontal tunnel network: Modeling assumptions and role in triggering microseismicity

We first test the validity of the oblate spheroidal inhomogeneity model for computing the stress perturbations due to the complex tunnel network. As shown in Figure 4.5c most of the tunnels at 480 m depth level are aligned either along the N-S direction or E-W direction. The tunnels have circular cross-sections with a maximum diameter of 5 m. We model the stress perturbations due to an individual tunnel oriented along either N-S or E-W directions (I and II respectively in Figure 4.11a) in the homogeneous regional stress field representing it as a horizontal cylindrical cavity using the formulation given in Schmitt *et al.* (2012), equations 11-13. The stress perturbation patterns are identical for both N-S and E-W oriented tunnels and are shown in Figures 4.11b-4.11f. Figure 4.11b shows that the normalized vertical stress is smaller than its far-field magnitude ( $<1$ ) and greater than its far-field magnitude ( $>1$ ) around the tunnel near the horizontal plane. Therefore the vertical stress perturbations due to the horizontal tunnel are

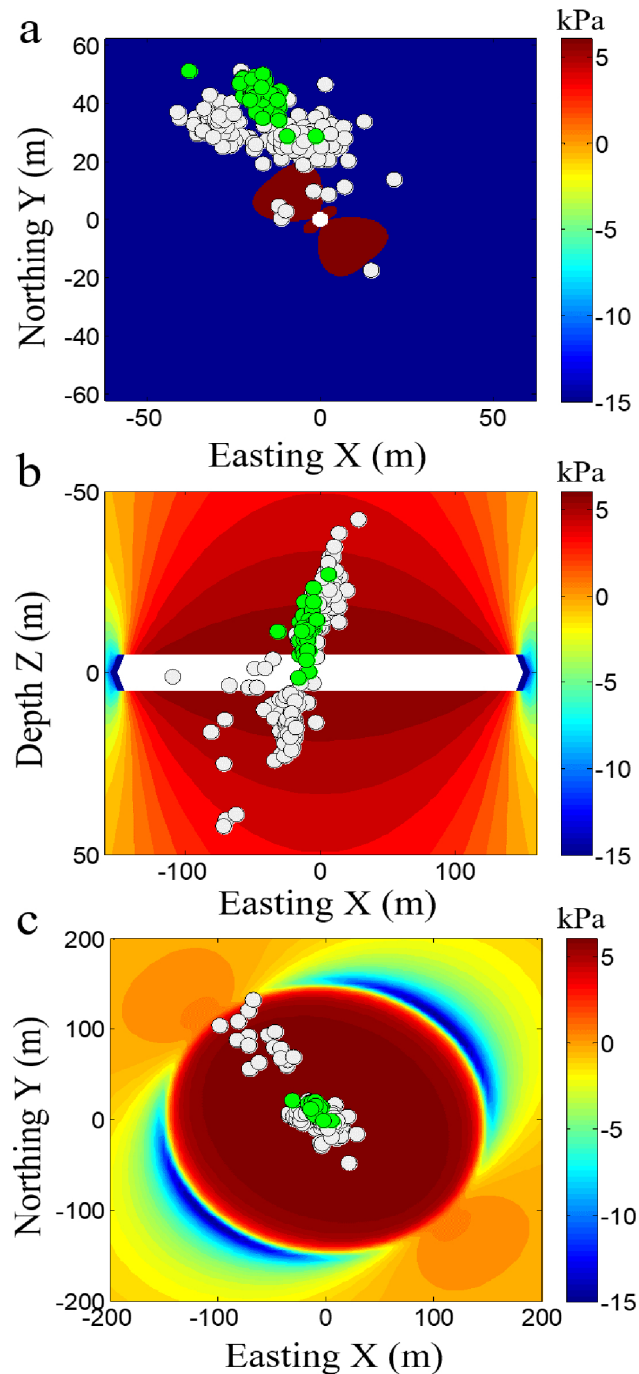


Figure 4.10: Event locations for the two largest multiplet groups, Group 1 (gray circles) and Group 3 (green circles) projected on top of the computed Coulomb stress changes (in  $kPa$ ). (a) Map view for the vertical shaft. (b) Vertical cross-section passing through the center of the inclusion parallel to the maximum horizontal stress. (c) Map view in a horizontal plane tangent to the spheroidal inclusion (volume fraction: rock=0.9, void space=0.1) at its roof. Slip is promoted for hot colors while for cold colors, slip is restricted.

tensile above and below the tunnel and compressive near its horizontal plane as evident from the green curves in Figures 4.11e and 4.11f. Figures 4.11c and 4.11d show that the horizontal stress perturbations have a reversed trend around the tunnel from the vertical stress perturbations.

The large stress perturbations around the tunnel are mainly limited to up to 1 radius from the walls of the tunnels (here up to 2.5 m from tunnel walls) as shown in Figures 4.11b-4.11f. Since the distance between parallel tunnels is much greater than 5 m, their complex stress interactions may be neglected. Moreover, the N-S and E-W trending tunnels intersect each other at an angle of 90 degrees which is known to be most stable with minimum roof settlement (Hsiao *et al.*, 2009). Therefore the overall stress pattern can be obtained by linear superposition of stress perturbations due to individual tunnels.

Comparing Figures 4.11e and 4.11f with Figure 4.6d reveal that the patterns of stress perturbations obtained using the spheroidal inhomogeneity model closely match with the stress change patterns due to an individual tunnel forming the complex network at 480 m depth level. However, the magnitudes of stress perturbations are lower for the inhomogeneity model (Figure 4.6d) as compared to the individual cylindrical tunnels (Figures 4.11e and 4.11f) especially close to the walls due to the smaller stiffness contrast assumed between the inhomogeneity model and the surrounding rock. But these large stress perturbations for the cylindrical tunnels (cavities) quickly decay on moving away from the walls. Thus the oblate spheroidal inhomogeneity with a lower stiffness than the surrounding rock correctly approximates the stress change patterns expected from the linear superposition of the stress changes due to individual tunnels forming the extensive horizontal tunnel network at the 480 m depth level.

We use the Coulomb failure criterion for computing the reactivation potential of pre-existing faults. We inherently assume a shear slip source mechanism for the microseismic events. Ideally, moment tensor inversion could provide more insight into microseismic source mechanism. Unfortunately, the P-wave coda overlaps with the first-arrival S-waves, rendering a moment tensor inversion challenging (Eyre and Van der Baan, 2015), since only P-wave amplitudes can be used. The study of microseismic source mechanism is thus beyond the scope of this study. However, the

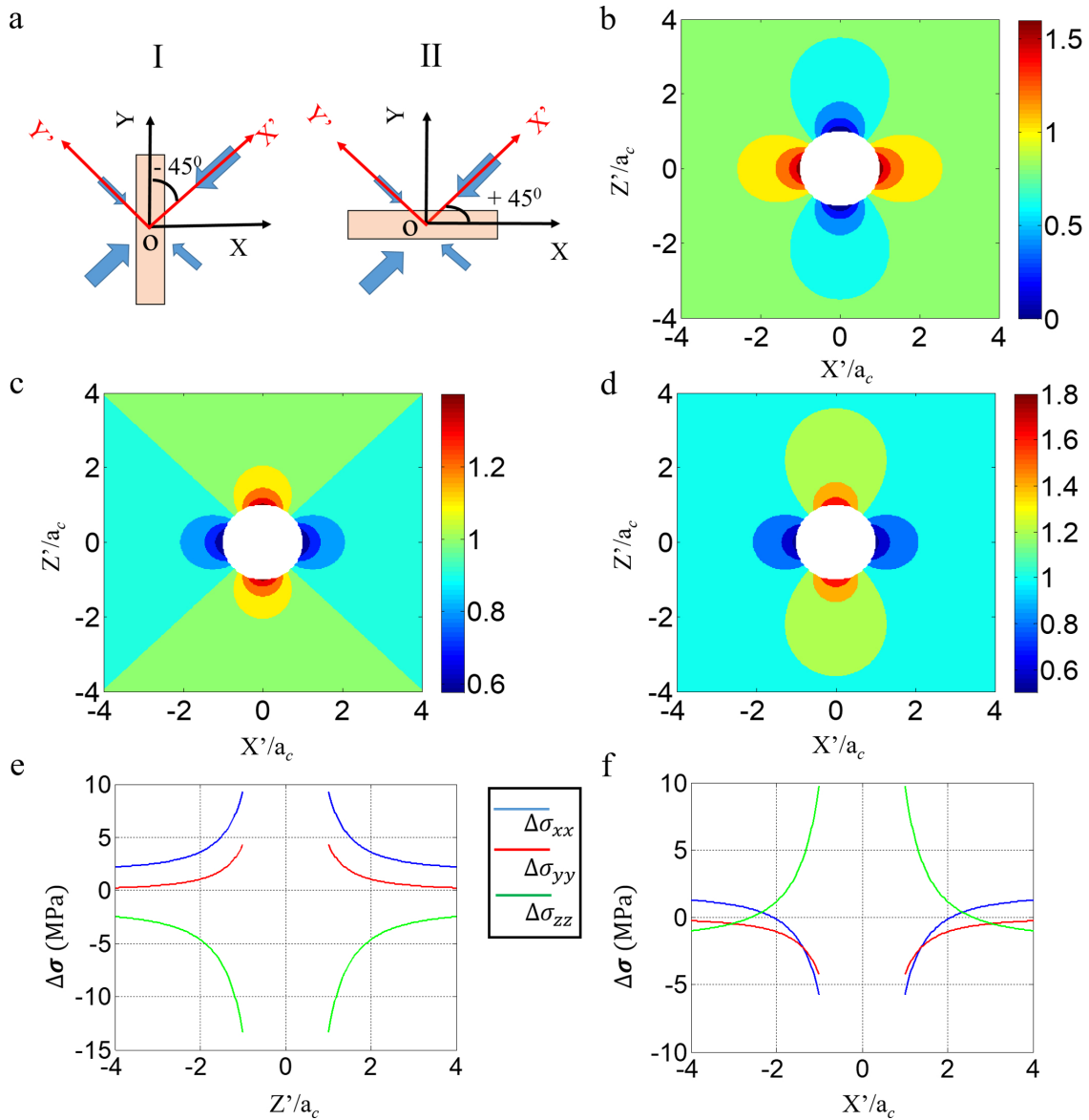


Figure 4.11: Stress perturbations due to a single tunnel modeled as a horizontal cylindrical cavity of radius  $a_c=2.5$  m. (a) Map view of horizontal tunnel (I) oriented along the N-S direction (Y-axis) at an angle of  $-45$  degree to the direction of maximum compressive stress ( $X'$ -axis). Horizontal tunnel (II) along E-W direction (X-axis) makes an angle of  $+45$  degree with the  $X'$ -axis. The maximum and minimum horizontal stresses are shown by thick and thin blue arrows respectively. (b) Normalized near-field stress along  $Z'$ -axis  $\frac{\sigma_{zznf}}{\sigma_{zz}}$ . (c) Normalized near-field stress along  $Y'$ -axis  $\frac{\sigma_{yynf}}{\sigma_{yy}}$ . (d) Normalized near-field stress along  $X'$ -axis  $\frac{\sigma_{xxnf}}{\sigma_{xx}}$ . (e) Stress perturbations along a vertical line aligned along  $Z'$ -axis passing through the center (origin 'o') of the horizontal tunnel. (f) Stress perturbations along a horizontal line aligned along  $X'$ -axis passing through the center (origin 'o') of the horizontal tunnel.

microseismic events belonging to each multiplet group exhibit high degrees of waveform similarity so we expect them to have similar source mechanisms (Castellanos and Van der Baan, 2015b). Also, the microseismic events have significant shear wave components visible in their waveforms recorded at different monitoring wells. Only S-wave/P-wave amplitude ratios less than 5 are indicative of tensile failure (Eaton *et al.*, 2014) for instance due to fluid injection. Furthermore, the preferential alignment of the multiplet groups along postulated faults suggests repeated slips due to mining activity. Therefore it is reasonable to assume a shear slip source mechanism for the microseismic events.

We assume that the shaft and tunnel network are situated in homogeneous far-field stresses. Since we are modeling the stress perturbations in the basement rock with negligible lithology changes, a laterally uniform far-field stress pattern can be expected. In the absence of detailed stress measurements in the study region, this assumption is reasonable as the regional stress pattern for Saskatchewan is very homogeneous (Reiter *et al.*, 2014). Moreover, we model the in situ stresses as the linear superposition of the far-field stresses and the local stress perturbations due to the shaft and tunnel network. Therefore the Coulomb stress changes computed as the difference between the in situ stresses and far-field stresses are insensitive to the changes in far-field stress magnitudes. Thus our results hold for small changes in the far-field stress magnitudes due to measurement errors. However, the Coulomb stress change patterns are most sensitive to the fault orientation with respect to the far-field stress directions (Figure 4.8). Thus the reactivation potential strongly depends upon fault orientation with respect to the regional stresses (Morris *et al.*, 1996).

In our stress modeling, we use representative values of the material properties (elastic constants and density given in Table 4.1) of the host medium containing the shafts and tunnel network. Using a different density value will change the vertical stress thereby changing the magnitudes of the regional stresses because of the set fixed ratio between the minimum horizontal, vertical and maximum horizontal stresses of 0.87:1:1.15. But this does not affect the orientation of the regional stresses because we assume a homogeneous medium. Moreover different elastic constants affect the magnitudes of stress perturbations due to the tunnel network which depends upon elastic

contrasts between the tunnel network (modeled as inhomogeneity) and the host rock (shown in Figure 4.6). Since the Coulomb stress change patterns are not much affected by changes in stress magnitudes our results hold in general for a range of elastic properties, around those in Table 4.1, as long as the host medium is homogeneous. Conversely, material heterogeneity leads to stress heterogeneity, which can change the likelihood of failure substantially, in particular, if some formations become load bearing (Roche *et al.*, 2015b). In this study, we focus on the base scenario of a homogeneous host rock, yet we can model Coulomb stress changes due to the shaft and tunnel network on the postulated faults and analyze the role of static stress changes on observed microseismicity.

The Coulomb stress changes shown in Figures 4.8b and 4.10 have been computed using the coefficient of friction ( $\mu$ ) equal to 0.6. We varied the coefficient of friction from 0 to 0.9 to understand its effect on the Coulomb failure pattern, analogous as done in slip tendency analysis (Morris *et al.*, 1996; Moeck *et al.*, 2009). Failure patterns remain identical to that shown in Figures 4.8b and 4.10, but the magnitude changes with the exact value of the coefficient of friction. Slip tendency analysis (Morris *et al.*, 1996; Moeck *et al.*, 2009) shows that the failure patterns depend upon the ratio of shear to effective normal stress and coefficient of friction determines the failure threshold. Since the shear and normal stress changes are independent of the coefficient of friction, the failure patterns are insensitive to different values of the coefficient of friction.

Based on the geometry of the relocated event clusters and a comparison with the 3D distribution of mapped faults presented in chapter 3, we put forward a hypothesis that the microseismic events originate due to reactivation along an unmapped fault  $164.7^\circ/55^\circ$  W obtained as a best fitting plane to the event cluster in the least squares sense. The 3D velocity model and the geological cross-section show presence of many faults near the unconformity contact; yet the microseismic events align along planes of a specific orientation ( $164.7^\circ/55^\circ$  W). In order to answer why only a fault with a specific orientation is reactivated, we model the static stress transfer due to the vertical shafts and the horizontal tunnel network. Results show that the seismicity is promoted along the postulated fault from the relocated microseismic events ( $164.7^\circ/55^\circ$  W) due to positive Coulomb

stress transfer by the horizontal tunnel network. Moreover the computed Coulomb stress changes for the faults,  $164.7^\circ/55^\circ$  W are conservative as shown by their small positive values in Figures 4.10b and 4.10c since they are computed by assuming volume fraction of the void space to be 0.1. However, in reality, the volume fraction may be larger leading to a larger positive Coulomb stress change. Therefore the role of the horizontal tunnel network in moving the fault closer to failure may be more pronounced than actually inferred from Figures 4.10b and 4.10c.

What triggers the microseismicity? Earthquake activity can be promoted even by small static stress increase of 0.01 MPa on pre-existing faults provided they are critically stressed i.e. they are close to failure under in situ stresses (Stein, 1999). In our study region, the computed  $CFF$  has large negative values for all the fault planes in 3D indicating that they are stable under in situ stresses (Figure 4.8a). The  $\Delta CFF$  due to the tunnel network is at least two orders of magnitudes smaller than the  $CFF$  (Figure 4.8b). We also computed the  $CFF$  and  $\Delta CFF$  assuming that the spheroidal inclusion has a volume fraction of the rock equal to 0.1 and that of void space equal to 0.9. This situation is highly unlikely for our tunnel network at 480 m depth but it allows us to put an upper limit on the Coulomb stress changes due to the tunnel network. Still the resulting  $\Delta CFF$  is an order of magnitude smaller than the computed  $CFF$  for all the fault planes in 3D. Therefore, the changes in static stresses due to the tunnel network alone are not sufficient to cause microseismicity.

The influence of the tunnel network on the reactivated fault  $164.7^\circ/55^\circ$  W near Shaft 1 can be explained using the Mohr circle as shown in Figure 4.12. All three principal stresses are taken into account and the positions of the faults on the Mohr circle are established by computing the normal and shear stresses using equations 4.15 and 4.16. Figure 4.12 is a schematic figure which is exaggerated to show the effect of the stress changes due to the horizontal tunnel network at 480 m depth on the faults of different orientations present near the actual event locations. The initial stress state is shown by the blue semi-circles. Due to the tunnel network the stress state changes such that there is an increase in the normal stress but the increase in the shear stress is much larger as shown by the larger radius of the red semi-circle. The fault  $164.7^\circ/55^\circ$  W (shown by green crosses) moves

closer to the failure criterion. The perpendicular distance of the fault from the failure criterion (O'A' and OA) quantifies the proximity of the stress state to the failure envelope and plays a similar role as the factor of safety in engineering applications. Since O'A' is smaller than OA the fault moves closer to failure due to the influence of the horizontal tunnel network. However, the other fault,  $045^{\circ}/60^{\circ}$  SE near shaft 1 shown by the black crosses moves away from failure. Therefore the tunnel network favors slip along the fault inferred from the relocated microseismic events ( $164.7^{\circ}/55^{\circ}$  W) but to trigger microseismic events we need an additional stress perturbation (equal to the factor of safety O'A'). Note that some points (that is, fault orientations such as NW-SE shown by brown crosses) have also moved closer to the failure envelope, however, these faults are unfavorably oriented for reactivation as compared to other orientations (such as  $164.7^{\circ}/55^{\circ}$  W) under far-field stresses as shown by the large negative value of the Coulomb failure function (pole surrounded by the gray circle) in Figure 4.8a. Hence, reactivation potential strongly depends on both the stress perturbations and the fault orientation (Morris *et al.*, 1996).

#### **4.5.2 Dynamic triggering due to the vibrations generated by the rock crusher**

The dynamic triggering of smaller earthquakes due to the passage of seismic waves generated by a large magnitude earthquake is a well-observed phenomenon documented by many studies (Hill *et al.*, 1993; Kilb *et al.*, 2000; Brodsky and Prejean, 2005; Hill and Prejean, 2007). The underlying mechanisms of dynamic triggering are relatively poorly understood (Brodsky and Van der Elst, 2014). The proposed models fall under two broad categories (Hill and Prejean, 2007), (1) triggering due to frictional failure, and (2) triggering by excitation of the crustal fluids. In the first category, the dynamic stresses generated by the passage of the seismic waves should provide the stress perturbations necessary to exceed the frictional strength of the faults. In other words, the peak dynamic stress should be greater than the factor of safety (Figure 4.12) for triggering seismicity. However, Johnson and Jia (2005) show using laboratory experiments that dynamic triggering can occur at relatively small dynamic stresses due to a nonlinear reduction in the frictional strength of

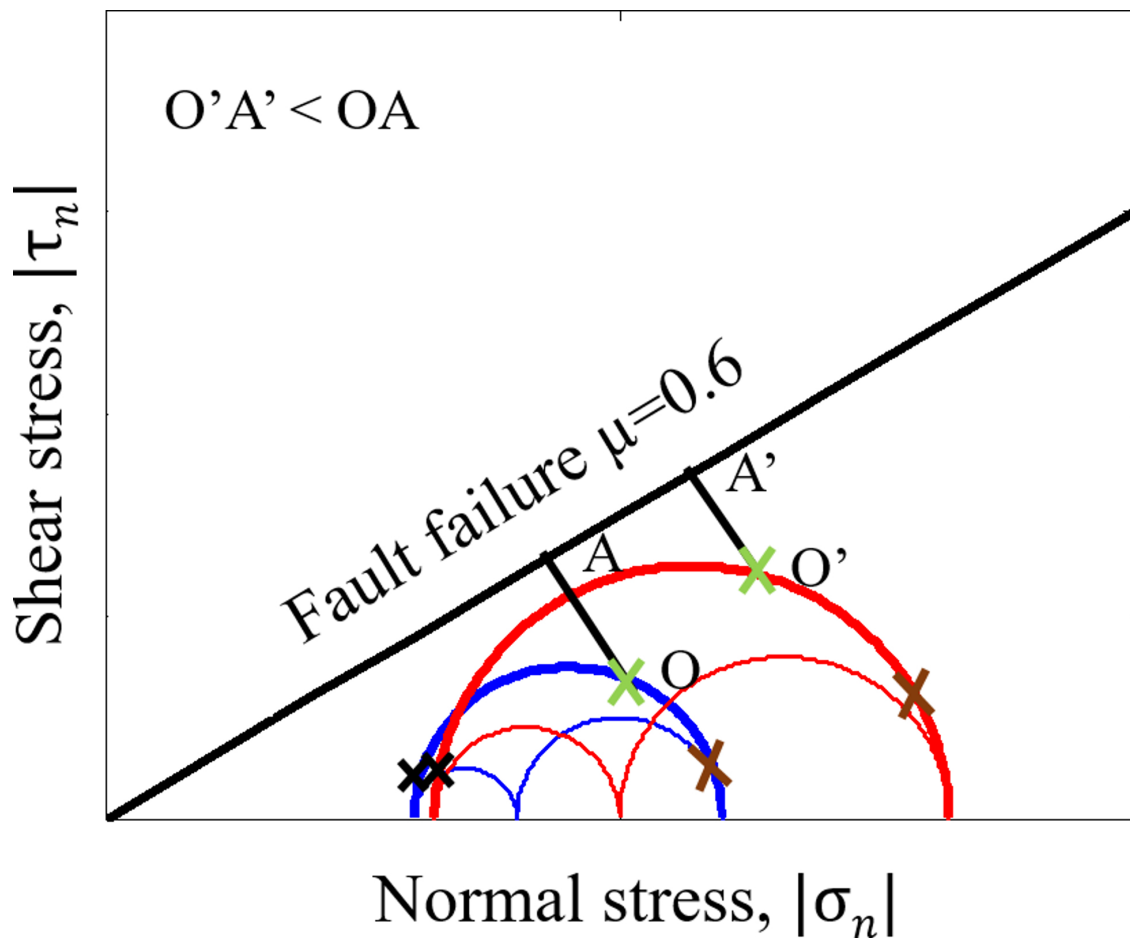


Figure 4.12: Schematic diagram showing Mohr-Coulomb failure criterion. Blue semi-circle shows initial conditions and the red semi-circle shows the new stress conditions at a point above the roof of the inhomogeneity after introducing the tunnel network. The black and green crosses are respectively the fault,  $045^{\circ}/60^{\circ}$  SE, and the fault inferred from the microseismic event locations ( $164.7^{\circ}/55^{\circ}$  W). The brown crosses represent the fault striking in the NW-SE direction and dipping at 60 degrees. OA and O'A' represent the factor of safety which is a measure of the proximity of the stress state at a particular location and fault orientation to the failure envelope.

the faults.

Figure 4.1 shows a peak ground velocity ( $PGV$ ) of 0.00072 m/s for the mine blast at one of the receiver locations. This value is typical for all the blasts in the mine under this study and represents the maximum peak ground velocity obtained from the recorded blast waveforms at all the receiver locations. The peak dynamic stress ( $PDS$ ) induced by the transient seismic waves generated by the blast can be computed as  $PDS = G \times PGV/V$ , where  $G$  is the shear modulus,  $PGV$  is the peak ground velocity and  $V$  is the P-wave velocity (Hill *et al.*, 1993). Taking  $V=3700$  m/s as the average P-wave velocity (as used in Chapter 3),  $G=26.25$  GPa from Table 4.1, we get a peak dynamic stress equal to 5.1 kPa at the receiver location. The peak dynamic stresses decrease with increasing distance from the blasts locations, so the value of 5.1 kPa represents the maximum dynamic stress at the nearest receiver from the blast location. The exact blast locations are not known; however, blasting is performed near the construction sites (Figure 4.4) which are separated from the event locations near shaft 1 by a distance of at least 100 m. Similarly, the nearest receivers from the construction sites are at a distance of around 100 m. Therefore, the peak dynamic stresses due to the blasts at the microseismic event locations will be less than or equal to 5.1 kPa which are at least three orders of magnitude smaller than the magnitude of the  $CFE$  (of the order of few MPa) shown in Figure 4.8a. Thus, the mine blasts are unlikely to dynamically trigger the microseismicity relocated near the working level at 480 m depth and shaft 1.

The main working level at 480 m depth has a rock crusher near shaft 1 at Easting,  $X=0.25$  km and Northing,  $Y=0.16$  km which can generate significant vibrations as shown in Figure 4.1e. Figure 4.13 shows a plot of the peak ground velocity obtained from the vibrations of the rock crusher (as in Figure 4.1e) at each receiver location as a function of the receiver distance from the rock crusher. At each receiver, we take the maximum amplitude among all three components as the magnitude of the peak ground velocity. The peak ground velocity decreases with increasing distance though there is some scatter in the data. We find a similar trend for all other recorded waveforms suspected to be vibrations due to the rock crusher (similar to Figure 4.1e). This decrease in the magnitude of peak ground velocity with distance is due to the combined effect of the geometrical spreading and

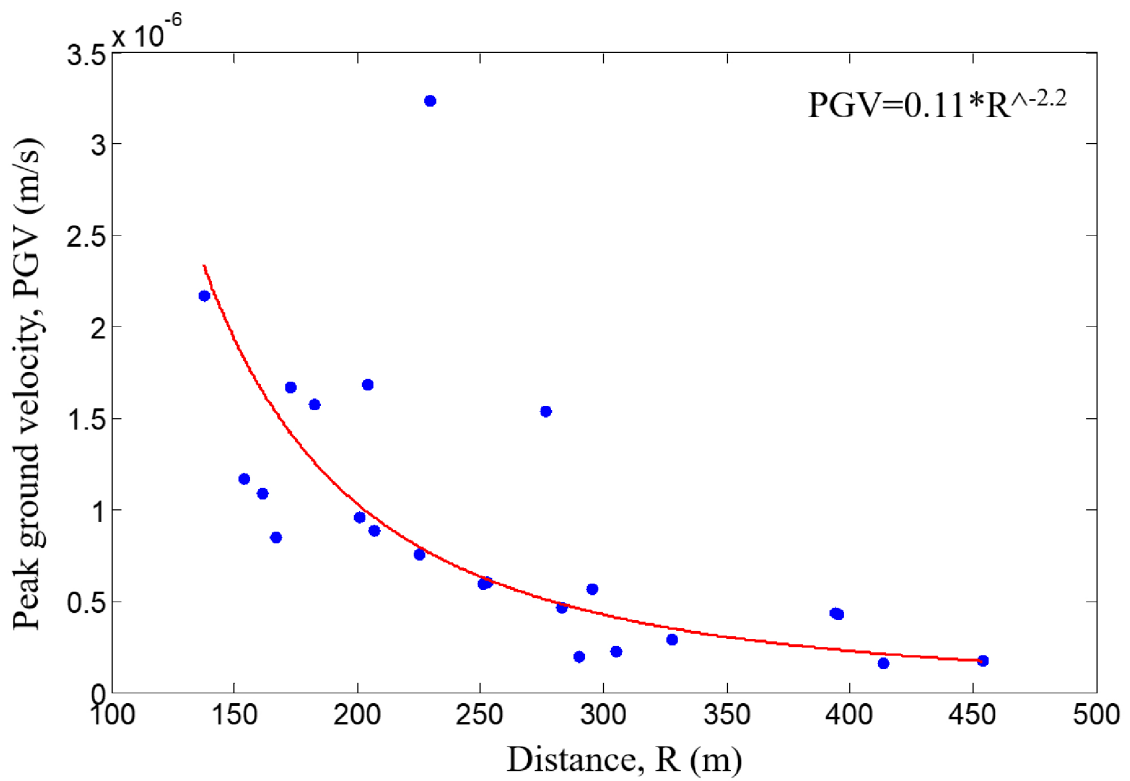


Figure 4.13: Peak ground velocity of the vibrations due to a rock crusher obtained from a single triggered file (similar to Figure 4.1e) as a function of the receiver distance from the rock crusher. The red curve shows the power law fit to the data given by the equation in the upper right corner.

anelastic attenuation. Ahmed (2015) report a power law dependence of the peak ground velocity due to a blast on the distance from the blast location based on in situ measurements in a Swedish mine. We fit a power law to the data in Figure 4.13 (shown by red curve) to get an estimate of the peak ground velocity at a distance of 1 m from the crusher and get a *PGV* of 0.11 m/s. We get similar values by fitting a power law to the other recorded waveforms of the rock crusher vibrations which are close to the maximum reported *PGV* of up to 0.08 m/s due to rock crushers near the source region (Krell, 1979; Ahmed, 2015). Taking the *PGV* near the crusher to be equal to 0.11 m/s, shear modulus  $G=26.25$  GPa from Table 4.1, and phase velocity as P-wave velocity ( $V=3700$  m/s), the peak dynamic stress (*PDS*) near the crusher site can be as large as  $\sim 0.8$  MPa.

The distance between the rock crusher (location  $X=0.25$  km and  $Y=0.16$  km) and the entry of shaft 1 (location  $X=0.207$  km and  $Y=0.17$  km) at 480 m level is  $\sim 44$  m. The output of the rock crusher is converted into a slurry and then pumped to the surface via access shaft 1. Therefore, the large vibrations due to the rock crusher are more efficiently transmitted in the direction of the shaft and the microseismic events locations by the pumping infrastructure. Thus, unlike the blast vibrations, the vibrations due the rock crusher have large magnitudes towards the shaft due to transmission by the pumping infrastructure. Moreover, the rock crusher is operational for most of the time when the rock debris are removed from the mine. Therefore, the large dynamic stresses ( $\sim 0.8$  MPa) approaching the same order of magnitude as required to reactivate the faults are being applied to the unmapped fault near shaft 1 for an extended time duration. Thus, the vibrations due to the rock crusher near the shaft 1 are most likely responsible for the dynamic triggering of microseismicity. This also explains the correlation between the daily rate of microseismicity and the volume of rock removed per day as observed by Castellanos and Van der Baan (2015a) and shown in Figure 4.2.

### 4.5.3 Implications for fluid injection-induced seismicity

There are growing concerns over the increase in seismicity induced by fluid injection during hydraulic fracturing stimulation of unconventional hydrocarbon reservoirs and wastewater disposal (Ellsworth, 2013; Atkinson *et al.*, 2016). The root cause of the induced seismicity due to fluid injection has been attributed to reactivation of pre-existing faults (Frohlich, 2012; Ellsworth, 2013; Atkinson *et al.*, 2016); yet it remains to be understood why felt seismicity occurs in some regions and not others. Modeling the stress perturbations due to these anthropogenic processes and combining them with the in situ stresses to compute reactivation potential of the known faults can help in a better understanding of the likelihood of induced seismicity. Specifically, hydraulic fractures are fluid-filled cracks which are often modeled as penny-shaped cavities containing pressurized fluid. Therefore, Eshelby's equivalent inclusion method can be used to compute the elastic stress perturbations due to the opening of the hydraulic fractures. These elastic stress perturbations can be combined with the pore pressure changes due to fluid diffusion to compute Coulomb stress changes on pre-existing faults to understand their reactivation potential. Dynamic triggering of earthquakes due to the passage of seismic waves generated by large magnitude remote earthquakes has been reported in some fluid-injection sites in the Midwestern United States (Van der Elst *et al.*, 2013). The role of dynamic triggering can be analyzed by modeling the peak dynamic stresses and comparing them with the Coulomb failure function computed from the static stress modeling. A good constraint over the regional stress field and the pre-existing fault distribution combined with the accurate records of injection parameters can greatly enhance the confidence in fault reactivation analysis. Thus our approach can possibly give more insight into why only some faults reactivate, thus creating felt seismicity because of human activities such as hydraulic fracturing or waste-water disposal (Frohlich, 2012; Ellsworth, 2013; Atkinson *et al.*, 2016).

## 4.6 Conclusions

We study the possible causes and mechanisms of the microseismicity induced during an underground mine development. A comparison of the recorded waveform characteristics and the temporal distribution of the events and the mining activities like blasting and rock removal help us to confirm that these events are not man-made seismic signals. The events are located far from the active construction sites thereby ruling out the possibility of their occurrence due to large stress concentrations near the walls of the newly created cavities. This is one of the most common causes of induced seismicity in underground mines, but it does not explain the origin of the microseismic events used in this study. The microseismic cluster geometry suggests that the events align along a planar surface. However, the events do not occur along any mapped faults in the mine. We, therefore, present a hypothesis that the microseismic events originate due to reactivation of an unmapped fault caused by the mining activity.

We model the Coulomb stress change due to the horizontal tunnel network at 480 m depth level for different fault orientations and find that shear slip is promoted on the fault inferred from the relocated multiplet groups ( $164.7^\circ/55^\circ$  W). However, the tunnel network at 480 m has a stabilizing effect on the faults,  $045^\circ/60^\circ$  SE if present near the microseismic event cluster. Thus the tunnel network has a positive role in promoting the observed microseismicity along the postulated fault ( $164.7^\circ/55^\circ$  W). The reactivation potential mainly depends upon (1) fault spatial location relative to the mine layout, and (2) fault orientation with respect to the regional stresses.

The analysis of the Coulomb failure function, or similarly slip tendency, can help in identifying the exact causative mechanism of induced seismicity. In the present study, the horizontal tunnel network moves the fault inferred from the microseismic event locations closer to failure but still the Coulomb failure function has a large negative value. This suggests that additional dynamic stress perturbations from blasting and/or the operation of machinery such as a rock crusher are needed to trigger microseismic events. We find that the peak dynamic stresses due to the vibrations caused by a rock crusher near the event locations can trigger microseismic events along the

favorably oriented fault at that location. Thus stress modeling combined with a suitable failure criterion can help in developing robust models for understanding and predicting the likelihood of induced seismicity due to anthropogenic activities like mine development, hydraulic fracturing, and wastewater disposal.

## Chapter 5

# Dynamics of hydraulic fracturing induced microseismicity: Effect of fracture opening on elastic stresses and pore pressure distribution<sup>1</sup>

### Summary

Hydraulic fracturing induced microseismicity is often attributed to pore pressure changes alone thereby neglecting the role of elastic stress perturbations due to fracture opening. Here we show how fracture opening affects the in situ elastic stresses and the pore pressure diffusion profiles, and subsequently the potential of shear slippages along pre-existing fault planes. We compute the Coulomb failure function for a stationary hydraulic fracture by combining the elastic stress perturbations due to the opening of the fracture and the pore pressure changes due to fluid diffusion in the surrounding rock. Results show that for a fixed length of the hydraulic fracture, the first events in time occur near the crack tip region where the Coulomb stress changes are positive due to

---

<sup>1</sup>A manuscript including a version of this chapter is in preparation for submission to *Geophysics*.

elastic stress perturbations. The pore pressure diffusion subsequently leads to microseismic events near the fracture face where elastic stress perturbations have a stabilizing effect. Furthermore, the shape of the fracture cavity affects the shape of the pore pressure diffusion front. Thus the opening of the hydraulic fracture cavity affects both the in situ elastic stresses and pore pressure distribution thereby influencing the spatiotemporal distributions of microseismicity.

## 5.1 Introduction

Hydraulic fracturing in unconventional hydrocarbon reservoirs like shales and tight sands open cracks and fractures thereby enhancing permeability and subsequent hydrocarbon production. The creation/reactivation of a fracture network perturbs in-situ stresses causing small energy release in the form of microseismic events. Monitoring of these microseismic events helps in spatial mapping of the hydraulic fractures (Rutledge and Phillips, 2003; Maxwell *et al.*, 2002; Cipolla *et al.*, 2011). The fracture dimensions estimated from the microseismic cloud are used to compute the Stimulated Reservoir Volume which is important for estimating subsequent hydrocarbon production. However such interpretation demands a proper understanding of the relation between the microseismic events and the fracture network. This, in turn, requires a deeper understanding of the various physical mechanisms active during hydraulic fracturing and their role in triggering microseismicity.

With the ever-increasing use of hydraulic fracturing in unconventional hydrocarbon reservoirs, there is a growing concern over the risk of inducing large earthquakes due to fluid injection in the subsurface (see Ellsworth (2013) for a recent review). In the Western Canada Sedimentary Basin, Atkinson *et al.* (2016) found good spatial and temporal correlation of moderate-magnitude seismicity (earthquakes with moment magnitudes  $>3$ ) with hydraulic fracturing. Thus it is important to understand the various physical processes active during hydraulic fracturing in order to establish a causal link between hydraulic fracturing treatments and induced seismicity. The spatiotemporal patterns of microseismic clouds around hydraulic fractures can reveal features of these processes.

Most studies of injection-induced seismicity assume that the changes in pore pressure alone are responsible for triggering seismicity (Pearson, 1981; Shapiro *et al.*, 2002; Keranen *et al.*, 2014). Shapiro *et al.* (2002) and Rotherth and Shapiro (2003) used pore pressure perturbations alone to model microseismicity due to hydraulic fracturing and explain the observed triggering front of microseismicity. In fact Shapiro *et al.* (2002) used the triggering front to determine the hydraulic properties of the reservoirs. Shapiro and Dinske (2009) have invoked non-linear diffusion to explain the triggering front of microseismicity observed in unconventional hydrocarbon reservoirs. However, these studies ignore the impact of the opening of a hydraulic fracture on in situ stresses and pore pressure diffusion profile and subsequently on the observed microseismicity.

The elastic stress changes due to major earthquakes are known to trigger aftershocks (King *et al.*, 1994; Stein, 1999). In the case of anthropogenic activities like mine development and reservoir impoundment, the elastic stress changes play an important role in inducing seismicity (Martin, 1997; McGarr *et al.*, 2002). Similarly, in hydraulic fracturing, injection of high-pressure fluids creates new fracture volume which affects the in-situ stresses. Depending upon the opening shape of the hydraulic fracture and the stress field orientation, seismicity may be promoted in some regions and restricted in others. Our objective in this study is to highlight the effect of the hydraulic fracture cavity on the in situ elastic stresses and pore pressure distribution. The stress and pore pressure changes due to the opening of the hydraulic fracture cavity are used to model the microseismic events (which are assumed as shear slip events on pre-existing faults) and explain their spatiotemporal distribution.

In this chapter, we compute the Coulomb failure function on pre-existing faults due to a stationary hydraulic fracture (fixed orientation and dimensions) modeled as a penny-shaped (oblate spheroidal) cavity filled with fluid at a uniform pressure. The elastic stress changes are computed using Eshelby's equivalent inclusion method whereas pore pressure diffusion profiles are generated by considering the fluid-filled cavity as the source. For a stationary fracture, we show that the first events occur close to the crack tip region and these events determine the triggering front in the distance versus time plots. We then model the crack tip propagation using a material balance equa-

Table 5.1: Material and fluid transport properties, geometrical parameters of the hydraulic fracture, and the far-field stresses and pore pressure

Parameter	Value and Unit
Material and Fluid transport properties	
Fracture toughness, $K_{ic}$	10 MPa $\sqrt{\text{m}}$
Young's modulus, $E$	40 GPa
Poisson ratio, $\nu$	0.23
Leak-off coefficient, $C_l$	0.00003 m/s <sup>1/2</sup>
Hydraulic diffusivity, $c$	0.05 m <sup>2</sup> /s
Volume injection rate, $Q_i$	0.15 m <sup>3</sup> /s
Oblate spheroidal cavity	
Semi-minor axis, $a_o$	0.002 m
Semi-major axis, $b_o$	22 m
Semi-major axis, $c_o$	22 m
Stress state	
Vertical stress, $\sigma_{zz}$	67.2 MPa
Maximum horizontal stress, $\sigma_{yy}$	44.6 MPa
Minimum horizontal stress, $\sigma_{xx}$	39.7 MPa
Pore pressure, $p_o$	28.0 MPa
Fracture pressure, $p_f$	41.0 MPa

tion. Using published data examples from Shapiro and Dinske (2009), we show that the triggering front can be explained by assuming the crack tip propagation serves as a proxy for the triggering front.

## 5.2 Methods

### 5.2.1 Model geometry and boundary conditions

We model a stationary hydraulic fracture (having a fixed orientation and dimensions) as an oblate spheroidal cavity whose major axes  $b_o$  and  $c_o$  are equal and much greater than the minor axis  $a_o$  (given in Table 5.1). The cavity is situated in a homogeneous and isotropic medium of infinite extent. The material properties of the rock are typical of Barnett shale reservoir (Vermylen, 2011) and listed in Table 5.1.

We assume homogeneous stresses acting at the boundary of the model at infinity such that the

maximum principal stress is vertical (taken to be the Z-axis), the minimum horizontal stress is shown along the X-axis, and the maximum horizontal stress is taken to be along the Y-axis. The X, Y and Z axes form a Cartesian coordinate system. Since hydraulic fractures open against the minimum principal stress, the minor axis  $a_o$  of the cavity is along the X-axis and the major axes are along the Y and Z axes. The cavity contains water at uniform pressure  $p_f$  (given in Table 5.1). Before hydraulic fracturing, the rock is saturated with water and has a uniform pore pressure  $p_o$ . The magnitudes of the principal stresses and pore pressure  $p_o$  are given in Table 5.1 and represent typical values for a Barnett shale reservoir (Vermylen, 2011) at a depth of 2.7 km.

### 5.2.2 Eshelby's equivalent inclusion method

Eshelby's equivalent inclusion method has been used to model induced stress changes in hydrocarbon and geothermal reservoirs (Segall and Fitzgerald, 1998; Rudnicki, 1999). In chapter 4, we use this method to compute the elastic stress perturbations due to a horizontal tunnel network modeled as an oblate spheroidal inhomogeneity. Here we use it to compute elastic stress perturbations due to a pressurized spheroidal cavity. Our formulation is similar to that of Healy *et al.* (2006) except that we consider all three principal compressive stresses together with uniform pressure at the fracture boundary. The mathematical formulation of the method is given in Chapter 4. We superimpose the uniform pressure on the compressive stresses and compute the corresponding uniform strain  $\epsilon_{0_{kl}}$  (to be used in equation 4.1). The stress perturbations outside the pressurized spheroidal cavity are given by equation 4.3.

### 5.2.3 Pore pressure diffusion

We ignore poroelastic effects thereby neglecting coupling of elastic stresses and pore pressure changes. Therefore the spatiotemporal distribution of pore pressure for a medium with homogeneous and isotropic hydraulic diffusivity can be computed using the diffusion equation given as

$$\frac{\partial p}{\partial t} = c \left( \frac{\partial^2 p}{\partial x^2} + \frac{\partial^2 p}{\partial y^2} + \frac{\partial^2 p}{\partial z^2} \right), \quad (5.1)$$

where  $p$  is the pore pressure at any Cartesian coordinate,  $(x, y, z)$  and time  $t$ , and  $c$  is the homogeneous and isotropic hydraulic diffusivity. The diffusivity  $c$  is given as (Rice and Cleary, 1976; Segall, 1985)

$$c = \frac{k}{\eta \Phi \beta}, \quad (5.2)$$

where  $k$  is the permeability,  $\eta$  is the fluid viscosity,  $\Phi$  is the porosity and  $\beta$  is the fluid compressibility.

Instead of a point injector, we consider an oblate spheroidal cavity at uniform pressure  $p_f$  as our source (with minor axis  $a_o$  and major axes  $b_o=c_o$ ). We assume that the medium has uniform pore pressure  $p_o$  at the start of injection. Thus we have a constant pore pressure boundary condition at infinity at all times. Norminton and Blackwell (1964) give solutions for transient heat flow from constant temperature oblate spheroids which are valid for large time calculations. These are essentially solutions for the diffusion equation (similar to equation 5.1) and can be used for computing pore pressure distributions at large times. We replace the temperature and thermal diffusivity in the Norminton and Blackwell (1964) solutions with pore pressure and hydraulic diffusivity so that the pore pressure at any point  $(\zeta, \xi, \phi)$  in oblate spheroidal coordinates is given by

$$\begin{aligned} p(\zeta, \xi, t) = p_o + (p_f - p_o) \frac{Q_0(i\zeta)}{Q_0(i\zeta_0)} & \left[ \operatorname{erfc} \left( \frac{\zeta - \zeta_0}{2} T^{-1/2} \right) \right. \\ & + A_0(i\zeta, i\zeta_0) (\zeta - \zeta_0) (\pi T)^{-1/2} \exp \left( \frac{-(\zeta - \zeta_0)^2}{4T} \right) \\ & + [B_0(i\zeta, i\zeta_0) + 5P_2(\xi)B_2(i\zeta, i\zeta_0)] \frac{(\zeta - \zeta_0)^3}{2} \\ & \left. (\pi T^3)^{-1/2} \exp \left( \frac{-(\zeta - \zeta_0)^2}{4T} \right) \right], \end{aligned} \quad (5.3)$$

where

$$A_0(i\zeta, i\zeta_0) = 1 + \frac{Q_0(i\zeta) - Q_0(i\zeta_0)}{i(\zeta - \zeta_0)Q_0(i\zeta)Q_0(i\zeta_0)}, \quad (5.4)$$

$$\begin{aligned} B_0(i\zeta, i\zeta_0) &= \frac{2\zeta - \zeta_0}{3(\zeta - \zeta_0)} + \frac{3\zeta - 4\zeta_0}{3i(\zeta - \zeta_0)^2 Q_0(i\zeta)} \\ &\quad - \frac{1}{(\zeta - \zeta_0)^2 Q_0(i\zeta_0)^2} + \frac{3\zeta_0 - 2\zeta}{3i(\zeta - \zeta_0)^2 Q_0(i\zeta)} \\ &\quad + \frac{1}{(\zeta - \zeta_0)^2 Q_0(i\zeta)Q_0(i\zeta_0)}, \end{aligned} \quad (5.5)$$

$$\begin{aligned} B_2(i\zeta, i\zeta_0) &= \frac{-1}{30Q_2(i\zeta_0)} \left[ \frac{\zeta + \zeta_0}{\zeta - \zeta_0} Q_0(i\zeta_0) \right. \\ &\quad \left. + \frac{\zeta_0 Q_0(\zeta) - \zeta Q_0(i\zeta_0)}{i(\zeta - \zeta_0)^2 Q_0(i\zeta)} \right], \end{aligned} \quad (5.6)$$

and

$$T = \frac{ct}{a_f^2}, \quad (5.7)$$

where  $a_f$  is the focal length given by

$$a_f = \sqrt{(b_o^2 - a_o^2)}. \quad (5.8)$$

For a real number  $m$ ,

$$Q_0(im) = -i \cot^{-1} m, \quad (5.9)$$

and

$$Q_2(im) = \frac{i}{2} ((3m^2 + 1) \cot^{-1} m - 3m), \quad (5.10)$$

where  $i$  is the unit imaginary number.

The Cartesian coordinates  $(x, y, z)$  can be obtained from the oblate spheroidal coordinates  $(\zeta, \xi, \phi)$  as

$$\begin{aligned} x &= a_f \sqrt{(1 + \zeta^2)(1 - \xi^2)} \cos \phi , \\ y &= a_f \sqrt{(1 + \zeta^2)(1 - \xi^2)} \sin \phi , \\ z &= a_f \zeta \xi . \end{aligned} \tag{5.11}$$

$T$  in equation 5.7 is the dimensionless time. Norminton and Blackwell (1964) point that for  $T/\zeta^2 \sim 1$ , the error is less than 10% which rapidly decreases as  $T/\zeta^2$  increases. For  $T/\zeta^2 \sim 14$ , the error is less than 0.1%.

#### 5.2.4 Reactivation potential of faults/fractures

Microseismic events are generally considered to be shear slip events (Pearson, 1981; Rutledge and Phillips, 2003), so event triggering can be modeled based on the reactivation potential of pre-existing faults/fractures. The reactivation potential can be quantified using the Coulomb failure function ( $CFF$ ) which is computed as

$$CFF = \tau - \mu(\sigma_n - p) , \tag{5.12}$$

where  $\tau$  is the shear stress and  $\sigma_n$  is the normal stress (compression positive) acting on any weakness plane with a given orientation,  $p$  is the pore pressure and  $\mu$  is the coefficient of friction. We assume zero cohesive strength and take  $\mu = 0.6$  owing to the presence of pre-existing fractures. In the case of pre-existing fractures/faults i.e. when cohesive strength is zero,  $CFF > 0$  represents the regions which are most likely to undergo shear slippages under the prescribed stresses (Zoback, 2007). Note that this approach is similar to computing the slip tendency (Morris *et al.*, 1996; Moeck *et al.*, 2009), where the ratio between the shear ( $\tau$ ) and effective normal stress ( $\sigma_n - p$ ) is used. In this approach failure occurs if  $\tau/(\sigma_n - p) > \mu$ . More details about the changes in

Coulomb failure function and the computation of normal and shear stresses on the plane of arbitrary orientation are given in chapter 4.

### 5.2.5 Crack tip propagation

We use a material balance equation to model crack tip evolution over time. Assuming an incompressible injection fluid (like water), the material balance equation implies that the volume of fluid injected during pumping is equal to the sum of hydraulic fracture volume and the volume of fluid lost to the formation. Thus according to the material balance equation, we have (Economides and Nolte, 2003)

$$Q_i t = \frac{4}{3} \pi a b c + 4 b h_f C_l \sqrt{2t} , \quad (5.13)$$

where  $Q_i$  is the average injection rate of treatment fluid,  $h_f$  is the fracture height,  $a$ ,  $b$ , and  $c$  are the semi-axes of our oblate spheroidal model,  $t$  is injection time, and  $C_l$  is the fluid leak-off coefficient. In equation 5.13, the term on the left-hand side is the volume of treatment fluid injected during time  $t$ , the first term on the right-hand side is the fracture volume, and the last term on the right-hand side is the volume of fluid lost to the formation. For the oblate spheroidal model,  $b=c=L$  where  $L$  is the half length of the hydraulic fracture, and so the fracture height  $h_f=2L$ . The maximum fracture aperture is equal to  $2a$ .

Fracture aperture-to-length scaling has been suggested as linear (Pollard and Segall, 1987; Renshaw and Park, 1997) as well as sublinear (Olson, 2003). The linear scaling (Pollard and Segall, 1987; Renshaw and Park, 1997) assumes constant driving stress conditions. However a constant driving stress condition will cause an unstable dynamic crack propagation. Geologic evidence suggests that during hydraulic fracturing, crack propagation is episodic (Van der Baan *et al.*, 2016) or quasi-static (Olson, 2003). Therefore Olson (2003) suggests that fracture propagation under constant stress intensity factor conditions is more reasonable than the constant driving stress conditions thereby deriving a sublinear relationship between fracture aperture versus length. The

maximum fracture aperture is thus given as (Olson, 2003)

$$2a = K_{ic} \frac{(1 - \nu^2)}{E \sqrt{\pi/8}} \sqrt{2L}, \quad (5.14)$$

where  $K_{ic}$  is the fracture toughness,  $E$  is the Young's modulus, and  $\nu$  is the Poisson's ratio. Substituting equation 5.14 into equation 5.13 and using  $b=c=L$  and  $h_f=2L$  we obtain an expression purely determined by the fracture length  $L$  given by

$$\begin{aligned} \left[ \frac{8\sqrt{\pi}K_{ic}}{3E'} \right]^2 L^5 - [8C_l\sqrt{2t}]^2 L^4 \\ + [16\sqrt{2}C_lQ_it^{3/2}]L^2 - [Q_it]^2 = 0, \end{aligned} \quad (5.15)$$

where

$$E' = \frac{E}{1 - \nu^2}. \quad (5.16)$$

The smallest real root of equation 5.15 gives the half-length of the fracture as a function of time.

## 5.3 Results

We compute the perturbations in the regional stresses due to a stationary hydraulic fracture modeled as an oblate spheroidal cavity (with dimensions given in Table 5.1) using Eshelby's equivalent inclusion method (equation 4.3). Figure 5.1 shows the elastic stress perturbations in the minimum horizontal stress and the vertical stress in a vertical cross-section normal to the maximum horizontal stress. The stress perturbations near the crack tip are tensile (decrease in the compressive stresses shown by hot colors) whereas those around the fracture face are compressive (increase in the compressive stresses). Figure 5.1 can be regarded as the snapshot of elastic stress perturbations around the growing hydraulic fracture at any given time.

The pore pressure perturbations around the stationary hydraulic fracture are computed as a function of time by solving the diffusion equation (equation 5.1) with the hydraulic diffusivity  $c$

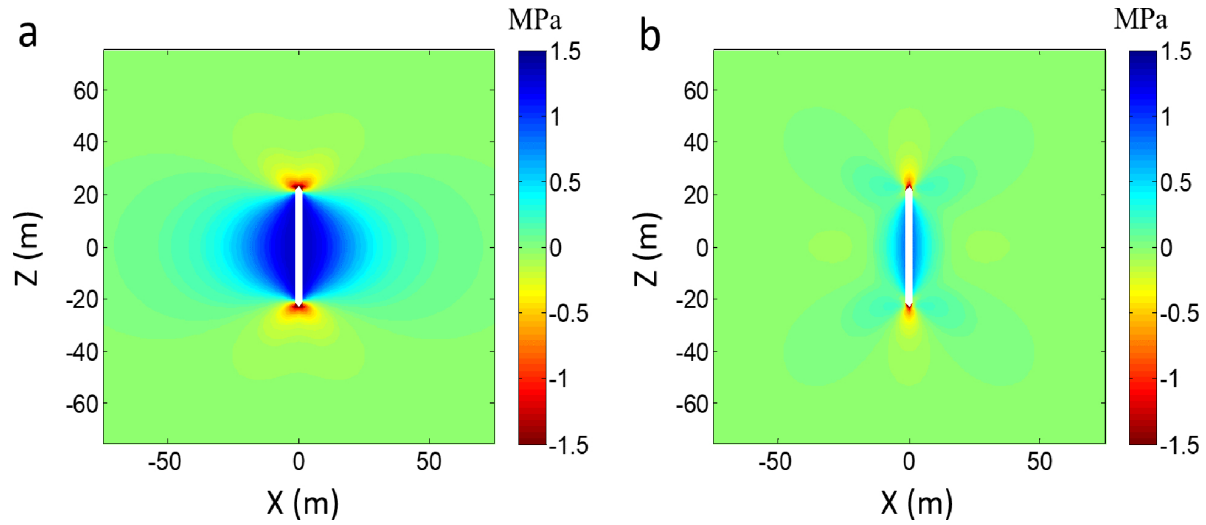


Figure 5.1: Elastic stress perturbations (in MPa) induced by the penny-shaped hydraulic fracture computed with parameters given in Table 5.1. (a) Vertical cross section showing perturbations in the minimum horizontal stress. (b) Vertical cross section showing perturbations in the vertical stress. Hot colors show tensile stress perturbations while cold colors represent compressional stress perturbations.

given by equation 5.2. The solution of the diffusion equation in oblate spheroidal coordinates is given by equation 5.3 with the various terms computed using equations 5.3-5.10. The pore pressure distribution is then transformed from oblate spheroidal coordinates to the Cartesian coordinates using equation 5.11 and is shown in Figure 5.2. Note that the time starts from the instant the hydraulic fracture acquires its current shape and size, and the fracture is assumed stationary as time progresses. The shape of the pore pressure diffusion front is elliptical near the fracture but becomes circular on moving away from the fracture (as seen in Figure 5.2). We have used an isotropic hydraulic diffusivity for computation of the pore pressure perturbations, yet the elliptical shape of the diffusion front suggests that the pore pressure diffusion depends upon the actual shape of the hydraulic fracture.

Next, we compute the Coulomb failure function by combining the elastic stress perturbations and the pore pressure changes using equation 5.12. The magnitude of the Coulomb failure function depends upon the fault orientation with respect to the in-situ stress field making some orientations more favorable for slip than others. However we find that the spatial patterns of the Coulomb

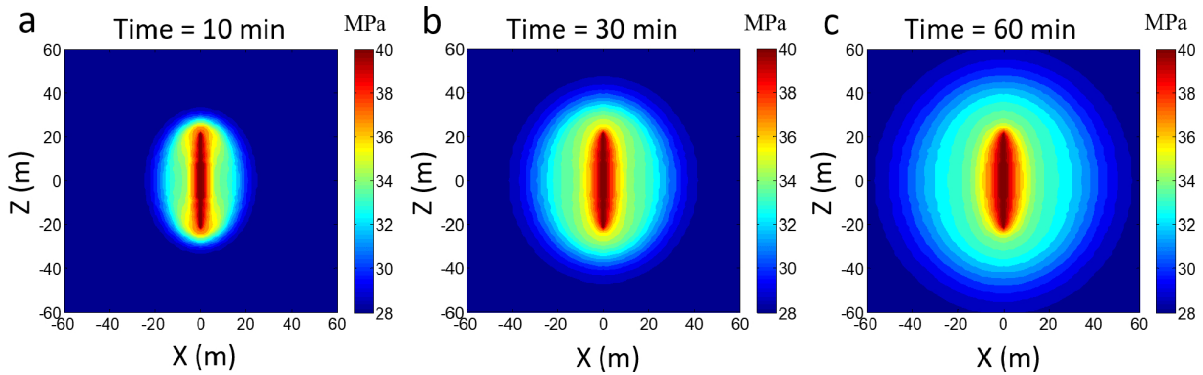


Figure 5.2: Evolution of pore pressure distribution (in MPa) with time due to a uniformly pressurized penny shaped crack. Vertical cross section showing pore pressure perturbations at (a)  $t = 10$  min, (b)  $t = 30$  min, and (c)  $t = 60$  min.

stress changes around the hydraulic fracture are similar for all fault orientations despite the actual magnitude being different, so without loss of generality we show the results for a fault dipping at 45 deg and striking at 45 deg from X-axis. Since we assume a stationary fracture, the elastic stress perturbations are static but the pore pressure changes vary with time. A synthetic microseismic event is triggered at a point in space if the Coulomb failure function at that point is greater than zero. Generating the synthetic microseismic events helps in understanding where the first events (in time) occur around the fracture for any fixed dimensions of the hydraulic fracture (Figure 5.3) thereby highlighting the roles of fracture opening and pore pressure diffusion in triggering microseismicity. The density of the modeled microseismic events is determined by the spatial grid on which the Coulomb failure function is computed.

Figures 5.3a and 5.3b show that as soon as the fracture opens (time  $t=0$ ), shearing-type microseismic events can occur near the crack tip region due to a positive Coulomb failure function. The Coulomb failure function near the fracture face is negative at time  $t=0$  implying that the elastic stress perturbations restrict events near the fracture face. As time progresses, the increase in pore pressure makes the Coulomb failure function positive around the fracture (Figure 5.3c). Thus events near the fracture face can be observed due to pore pressure diffusion (Figure 5.3d). Even though this reactivation potential analysis is static with respect to fracture propagation (as it is for

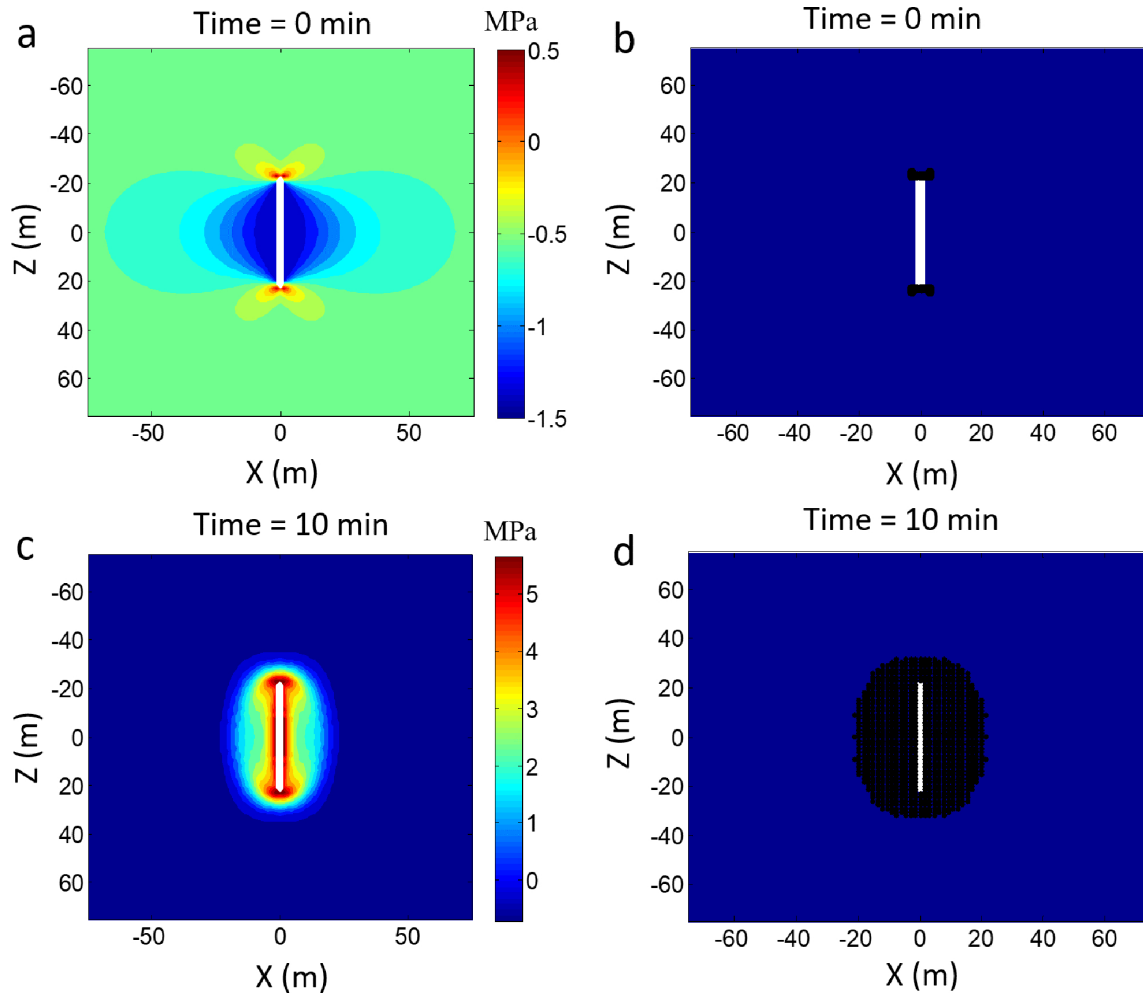


Figure 5.3: Evolution of Coulomb failure function (in MPa) with time and triggering of the microseismic events due to a uniformly pressurized penny-shaped crack. Vertical cross section showing Coulomb failure function at (a)  $t = 0$  min, and corresponding cloud of potentially triggered microseismic events (shown by black dots) at (b)  $t = 0$  min. Vertical cross section showing Coulomb failure function at (c)  $t = 10$  min, and corresponding cloud of potentially triggered microseismic events (shown by black dots) at (d)  $t = 10$  min. Shear slip microseismic events occur for positive values of Coulomb failure function.

fixed fracture dimensions), it shows that the first events (in time) due to shear slippage around the stationary fracture are most likely to occur near the tip region. This complements the analysis of Roche *et al.* (2015b) who show that elastic stress perturbations due to a developing hydraulic fracture promotes fracturing at the fracture tip but inhibits failure in the fracture walls. Pore-pressure diffusion subsequently promotes failure within its zone of influence.

In order to test if the fracture opening or the pore pressure diffusion are responsible for the triggering front observed in the distance versus time plots of microseismic events, we compare the evolution of fracture tip and pore pressure diffusion fronts over time. The fracture length is computed using equation 5.15 whereas the distance of the pore pressure diffusion front from a point injector is computed using  $L = \sqrt{4\pi ct}$  (Shapiro *et al.*, 2002; Rothert and Shapiro, 2003) where  $c$  is the hydraulic diffusivity. Table 5.2 lists the typical values of compressibility and viscosity for water and gas, porosity and the permeability for shale samples (Vermylen, 2011), and the corresponding diffusivity computed using equation 5.2. The diffusivity depends upon the permeability and porosity of the rock as well as the viscosity and compressibility of the formation fluid (equation 5.2). For example, the diffusivity computed using equation 5.2 and the parameters listed in Table 5.2 is  $5 \cdot 10^{-9} \text{ m}^2/\text{s}$  for gas and  $3.3 \cdot 10^{-6} \text{ m}^2/\text{s}$  for water. Thus even for the same geologic formation, the diffusivity of water is three orders of magnitude higher than that of gas. Hence, we compute the distance of the pore pressure diffusion fronts from the point injector for two separate cases assuming that the formation fluid is water in one case and gas in the second case. Figure 5.4 shows the pore pressure diffusion fronts and the crack tip length as a function of time. The pore pressure diffusion fronts in the case of water and gas for typical values of diffusivity/permeability measured in labs (dashed red and solid green lines) lag the crack tip propagation (solid blue line). Even when the lab measured values of permeability (100 nanodarcy) are increased by  $10^4$  times for water (1 millidarcy) and  $10^6$  times for gas (0.1 darcy), the crack tip propagation (blue curve) is much faster than the pore pressure diffusion (dashed magenta and solid black lines).

The evolution of fracture tip over time as given by equation 5.15 depends upon the average injection rate of treatment fluid ( $Q_i$ ), the fluid leak-off coefficient ( $C_l$ ), the fracture toughness

Table 5.2: Parameters used for modeling the triggering front due to fluid diffusion from a point injector

Parameter	Value and Unit
Porosity, $\Phi$	0.1
Permeability, $k$	100 nanodarcy or $9.9 \cdot 10^{-20} \text{ m}^2$
Compressibility gas, $\beta_g$	$10^{-5} \text{ Pa}^{-1}$
Compressibility water, $\beta_w$	$3 \cdot 10^{-10} \text{ Pa}^{-1}$
Viscosity gas, $\eta_g$	$2 \cdot 10^{-5} \text{ Pas}$
Viscosity water, $\eta_w$	$10^{-3} \text{ Pas}$
Diffusivity gas, $c_g$	$5 \cdot 10^{-9} \text{ m}^2/\text{s}$
Diffusivity water, $c_w$	$3.3 \cdot 10^{-6} \text{ m}^2/\text{s}$

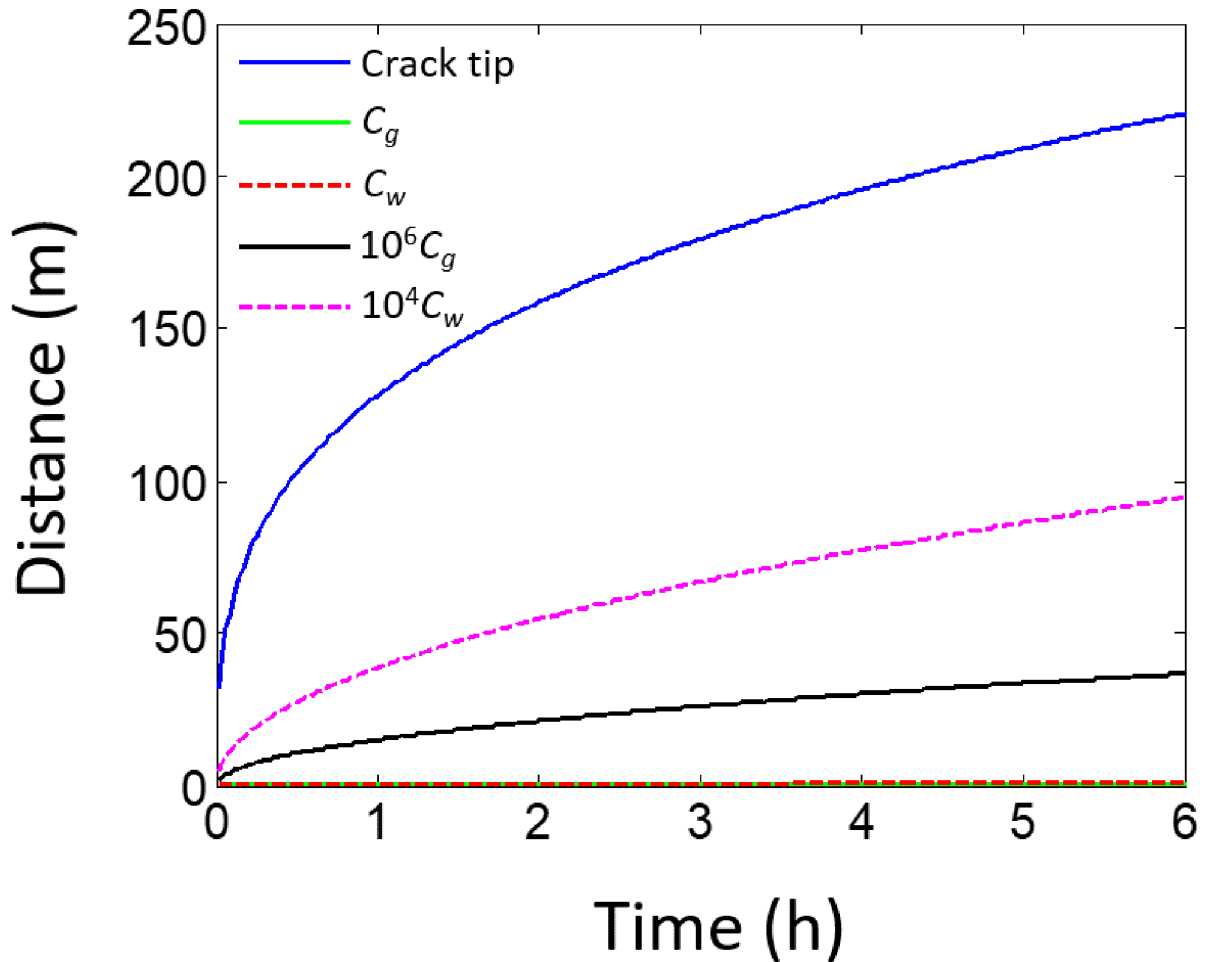


Figure 5.4: Distance of hydraulic fracture tip and pore pressure diffusion front from a point injector as a function of time. Solid blue line shows fracture length. Dashed red and magenta lines show distance of diffusion front in case of water for in situ ( $c_w$  in Table 5.2) and scaled up ( $10^4$  times  $c_w$ ) diffusivity respectively. Solid green and black lines show distance of diffusion front in case of gas for in situ ( $c_g$  in Table 5.2) and scaled up ( $10^6$  times  $c_g$ ) diffusivity respectively.

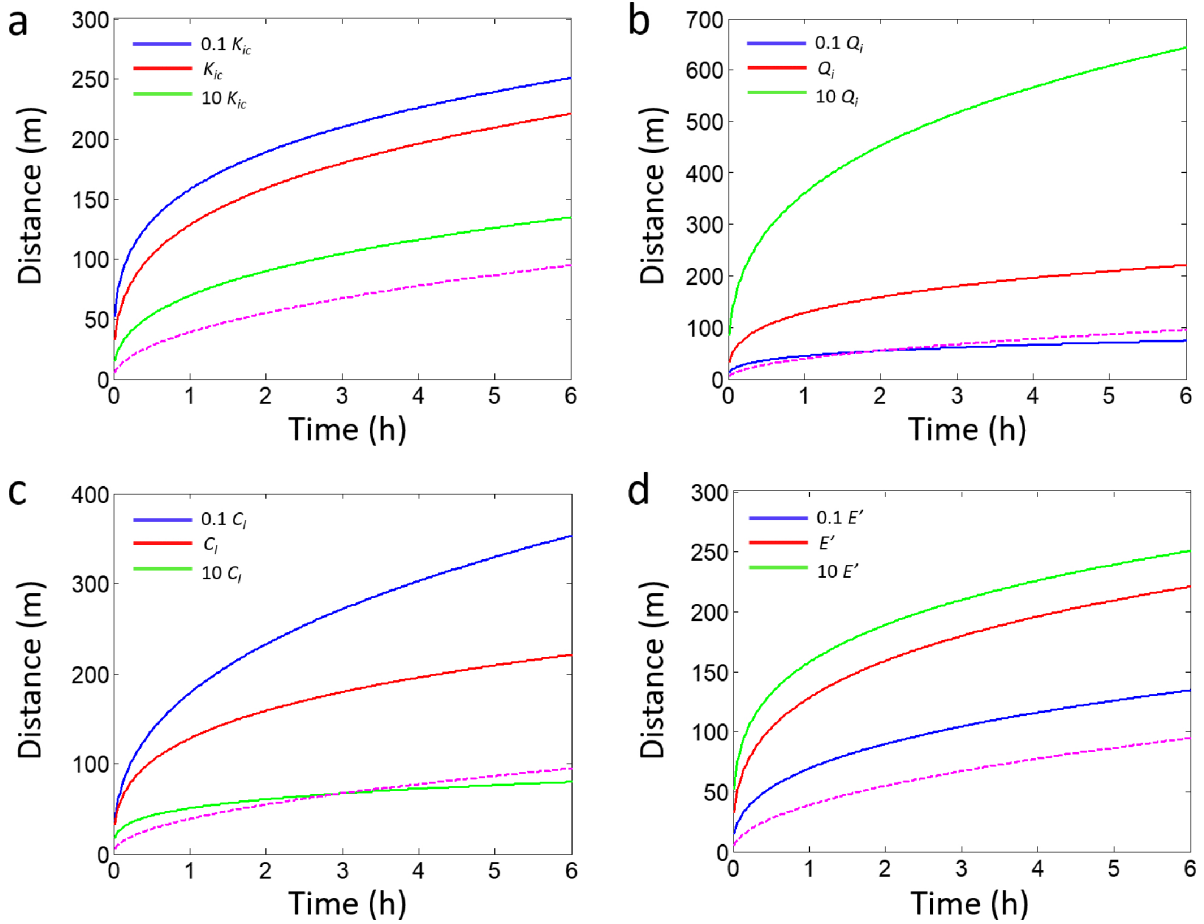


Figure 5.5: Distance of hydraulic fracture tip from the injection point as a function of time for different values of (a) the fracture toughness,  $K_{ic}$ , (b) the volume injection rate,  $Q_i$ , (c) the fluid leak-off coefficient,  $C_l$ , and (d) the plane strain modulus,  $E'$ , given in equation 5.16. Dashed magenta lines show distance of diffusion front in case of water for scaled up ( $10^4$  times  $c_w$ ) diffusivity (same as shown in Figure 5.4).

( $K_{ic}$ ), and the elastic constants of the medium (plane strain modulus,  $E'$  given in equation 5.16). We test the sensitivity of the fracture length growth over time with respect to each of these four parameters by varying them individually while keeping others constants. We vary each parameter around their values given in table 5.1 by increasing and decreasing them by an order of magnitude (multiplying and dividing by 10 respectively). Figure 5.5a shows that the fracture length growth is slower with increasing values of the fracture toughness. The fracture length growth increases with increasing values of the average injection rate as shown in Figure 5.5b. Figure 5.5c shows that with a higher leak-off coefficient ( $C_l$ ), the growth of the fracture length is slower. Higher values of plane strain modulus,  $E'$  results in faster growth of the hydraulic fracture as shown in Figure 5.5d. The dashed magenta lines show the distance of the diffusion front in case of water for scaled up ( $10^4$  times  $c_w$ ) diffusivity. Only the slowest fracture length growth is comparable to the diffusion front growth ( $L = \sqrt{4\pi ct}$ ) for the scaled-up hydraulic diffusivity (Figures 5.5b and 5.5c). These slow fracture length growths are computed either by scaling down the injection rate,  $Q_i$  by a factor of 10 (for  $0.1Q_i$  in Figure 5.5b), or by scaling up the leak-off coefficient,  $C_l$  by a factor of 10 (for  $10C_l$  in Figure 5.5c). However, we assume that the hydraulic fracture is shaped as an oblate spheroidal cavity with equal height and length for computing the length as a function of time using the material balance equation (equation 5.15). In real hydraulic fracturing treatments, the length of fracture is much greater as compared to its height (Fisher and Warpinski, 2011). Therefore, the length of the fracture needs to be scaled up (and the height scaled down to keep the material balance equation (equation 5.15) unchanged) so that actual length growth may be much faster than shown in Figure 5.5 (see details in the discussion section).

Figure 5.6 shows the microseismic data recorded during hydraulic fracturing in Barnett shale. The data are taken from Shapiro and Dinske (2009). The bottom hole pressure and injection rate are shown in Figure 5.6a. The distance of microseismic events from injection domain as a function of time are shown in Figures 5.6b and 5.6c. The black bold lines in the middle 5.6b and bottom 5.6c plots are the triggering fronts modeled based on linear ( $t^{1/2}$ ) and non-linear ( $t^{1/3}$ ) diffusion respectively. The triggering front based on nonlinear diffusion (cubic root temporal distribution)

Table 5.3: Material and fluid transport properties used for the Carthage Cotton Valley gas field

Parameter	Value and Unit
Fracture toughness, $K_{ic}$	10 MPa $\sqrt{\text{m}}$
Young's modulus, $E$	46.84 GPa
Poisson ratio, $\nu$	0.23
Leak-off coefficient, $C_l$	0.00003 m/s <sup>1/2</sup>
Volume injection rate, $Q_i$	0.12 m <sup>3</sup> /s

gives a better fit to the data. The red line in Figure 5.6c is obtained by solving equation 5.15 using the typical parameters for Barnett shale listed in Table 5.1 and scaling up by a constant multiplication factor (of 2.7) so as to get a good fit to the data. The red line modeled using crack tip propagation overlay the black line modeled using non-linear pore pressure diffusion thus giving an identical goodness of fit.

Figure 5.7 shows another example of hydraulic fracturing induced microseismicity at the Carthage Cotton Valley gas field from Shapiro and Dinske (2009). These data correspond to a single stage of the hydraulic fracturing treatment at the Carthage Cotton Valley gas field and are described in detail by Rutledge and Phillips (2003). Figure 5.7a shows the borehole pressure and the fluid flow rate whereas the distance versus time plot of the microseismic events is shown in Figure 5.7b. In Figure 5.7b, Shapiro and Dinske (2009) plot the triggering front as a black dashed line. Here, Shapiro and Dinske (2009) assume that the triggering front is due to the linear growth of the fracture tip during the early times immediately following the start of the fluid injection (see Shapiro *et al.* (2006) for more details). We compute the triggering front (shown by red line in Figure 5.7b) by solving equation 5.15 using the typical parameters for Carthage Cotton Valley gas field listed in Table 5.3 and scaling up by a constant multiplication factor (of 1.9) in order to get a good fit to the data. Our triggering front shown by red line in Figure 5.7b gives a good fit to the data over the entire injection period.

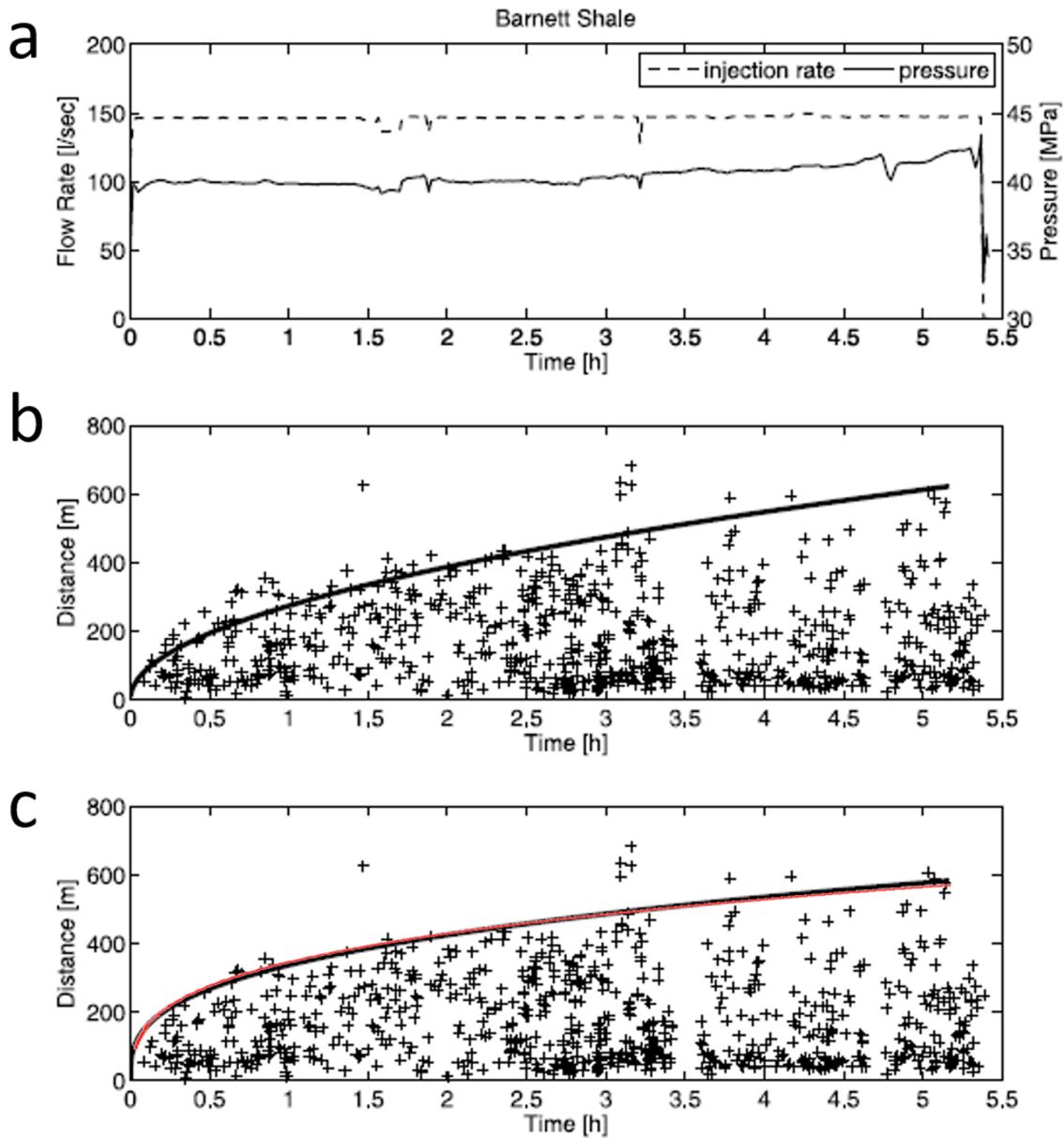


Figure 5.6: Microseismicity induced in Barnett Shale due to hydraulic fracturing (data are taken from Shapiro and Dinske (2009)). (a) Borehole pressure (measured at the injection domain) and fluid flow rate. (b) The time-distance plot of induced microseismic events with the black curve showing scaling of seismicity front as a square root of time (linear diffusion), (c) Time-distance plot with the black curve showing scaling of seismicity front as a cubic root of time. The red curve overlying the black curve is obtained by solving equation 5.15 (taking the smallest real root as the half-length of the propagating crack tip).

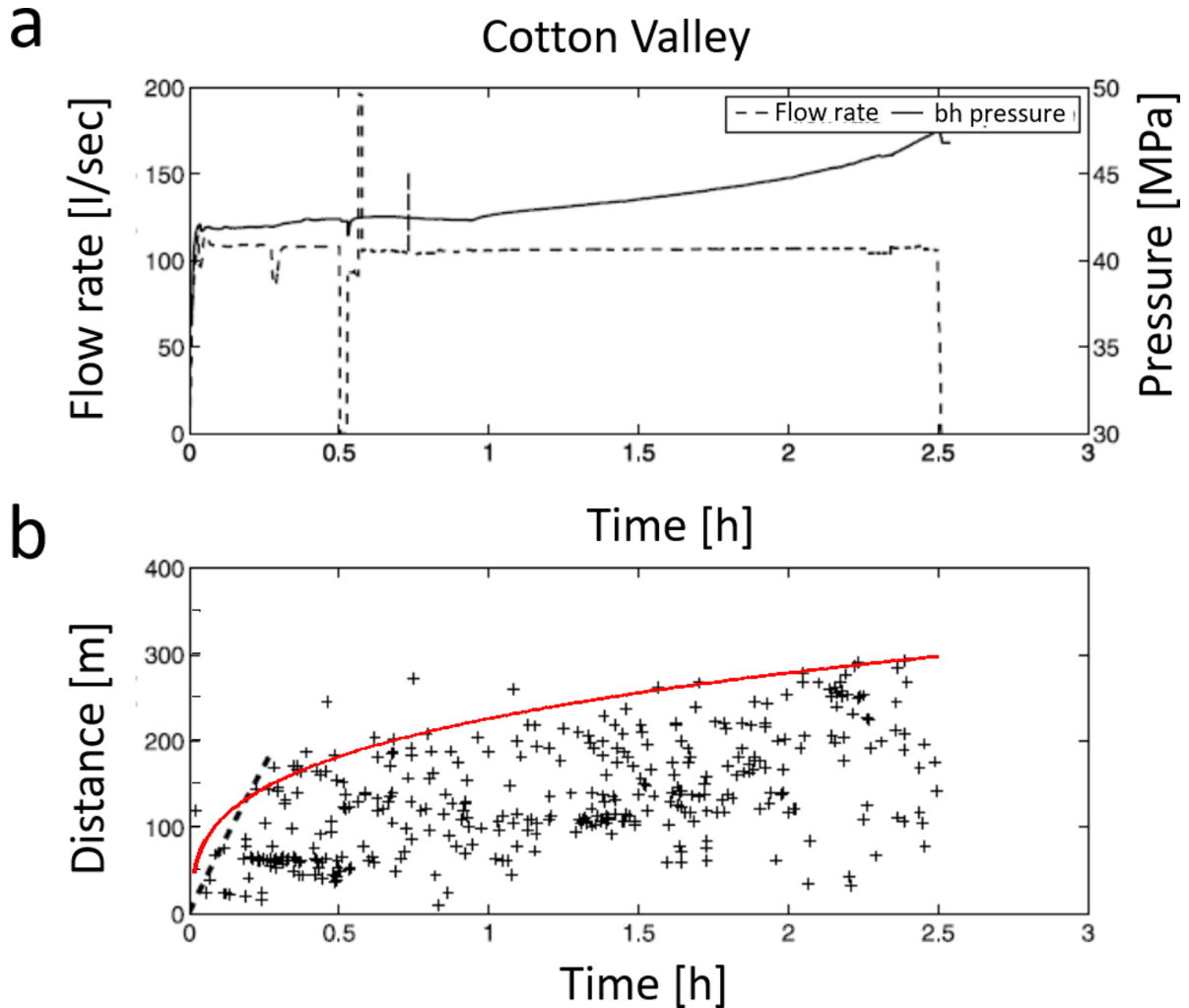


Figure 5.7: Hydraulic fracturing induced microseismicity at the Carthage Cotton valley gas field (data are taken from Shapiro and Dinske (2009)). (a) Borehole pressure (measured at the injection domain) and fluid flow rate. (b) The time-distance plot of induced microseismic events with the black dashed line showing linear scaling of the seismicity front as function of time. The red curve is obtained by solving equation 5.15 (taking the smallest real root as the half-length of the propagating crack tip).

## 5.4 Discussion

We assume a single hydraulic fracture which is shaped as an oblate spheroidal cavity whose length and height are equal and much larger than the width. Such a hydraulic fracture geometry is an idealization and may be possible only in a medium which is homogeneous and isotropic both in its elastic and hydraulic properties, with an anisotropic in situ stress state. In real hydraulic fracturing treatments, the fracture complexity is governed by the medium heterogeneity such as lithological layering, and presence of discontinuities like natural fractures, as well as in-situ stress state. In fact, lithological layering strongly affects the in situ stress field (Roche and Van der Baan, 2015a). Fisher and Warpinski (2011) show using real data that the fracture heights are usually well contained in the stimulated reservoirs due to lithology and stress contrasts across the boundary interfaces within the layered sedimentary strata. In such cases, the hydraulic fractures are much longer as compared to their height and an ellipsoidal shape may be better suited for modeling the hydraulic fracture. In the presence of the natural fracture sets, the fracture network generated by hydraulic fracturing may be very complex rather than being a single fracture cavity. If the in situ stress state is isotropic, and the host medium is elastically homogeneous and isotropic, the fracture network may be approximately spherical rather than being elongated along any specific direction. Such complex fracture network requires numerical modeling to understand the elastic stress perturbations due to opening of individual cavities forming the network. In this study, our goal is to show the significance of the elastic stress perturbations caused by the opening of the hydraulic fracture cavity in triggering of the microseismic events. We show that even for a simple oblate spheroidal cavity model, the elastic stress perturbations near the fracture tip have sufficient magnitude to trigger microseismic events due to shear slippages on pre-existing faults. Moreover, the shape of the pore pressure diffusion fronts depends upon the shape of the hydraulic fracture. Thus this study suggests that the effective stress changes due to the opening of the hydraulic fracture cavity must be taken into account when modeling the microseismic events triggered during hydraulic fracturing.

The Coulomb failure function and the microseismic events shown in Figure 5.3 are modeled by assuming a uniform distribution of faults. If the fault distribution is non-uniform such that the faults are present only near the walls of the cavity and entirely absent near the crack tip, microseismic events will not be observed near the fracture tip. However, our objective in this study is to highlight the role of the elastic stress perturbations and the pore pressure changes caused by the opening of the hydraulic fracture cavity on triggering of the microseismic events rather than on understanding the dependence of the microseismic events on the spatial distribution of the pre-existing faults. Therefore the assumption of a uniform fault distribution is justified for the purpose of this study. The Coulomb failure function shown in Figure 5.3 is computed for faults of a specific orientation. Figure 5.8 shows the Coulomb stress changes for faults of all orientations in 3D at two points A and B located respectively close to the fracture wall directly above its center, and ahead of the fracture tip. The Coulomb stress changes at points A and B are respectively negative and positive for fault planes of all orientations though some faults are more favorably oriented for shear slippage as compared to others. Thus the result that the stress changes due to the opening of the hydraulic fracture cavity inhibit shear slippage close to the walls of the fracture and promote shear slippage near the tip region is general and independent of our choice of fault orientation.

We use the propagating crack tip (equation 5.15) computed using the material balance condition (equation 5.13) as a proxy for the triggering front of microseismicity observed in the distance versus time plots (Figures 5.6 and 5.7). This inference is drawn based on our two results, (1) the elastic stress perturbations near the crack tip trigger microseismic events due to shear slippages (Figure 5.3), and (2) the crack tip propagation is much faster than the pore pressure diffusion (Figure 5.4). We scale up the obtained triggering front by a constant number to get a good fit to the distance versus time plots. This scaling can be understood in the physical sense by realizing that we use an oblate spheroidal cavity model for hydraulic fracturing in the material balance equation (equation 5.13) whereas, in reality, the hydraulic fractures in both data are much longer as compared to their heights. To simulate this, the length can be scaled up by multiplying by a constant number, say,  $n$ . Therefore the aperture scales up by  $\sqrt{n}$  according to equation 5.14. In

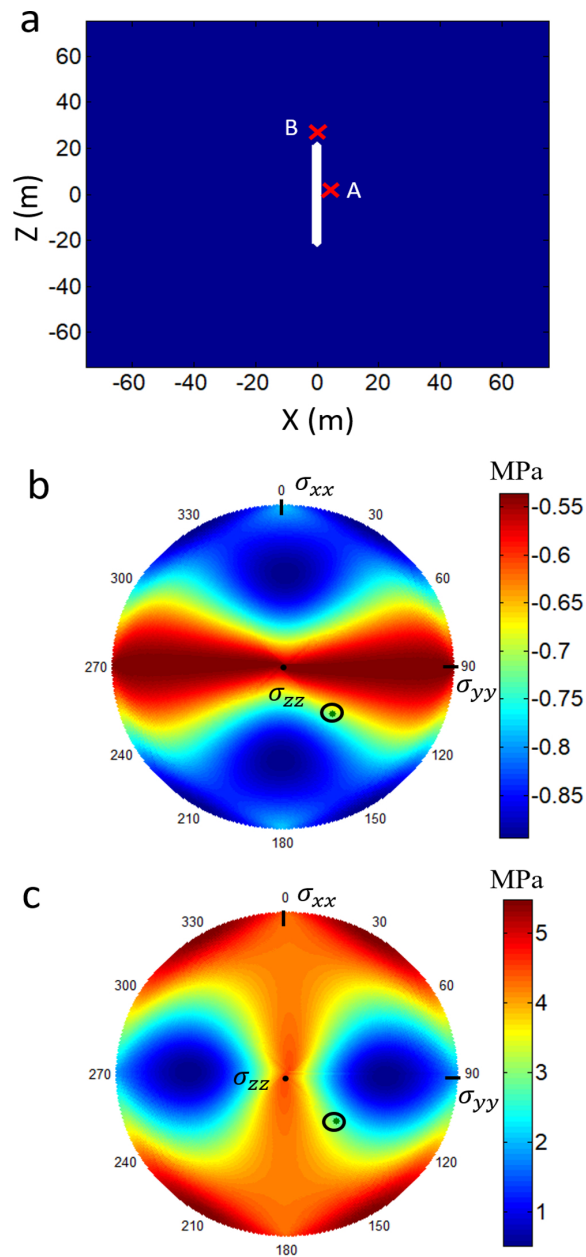


Figure 5.8: (a) Vertical cross-section passing through the center of a hydraulic fracture cavity parallel to the minimum horizontal stress. Points A and B are located respectively close to the wall directly above the center of the fracture, and ahead of the fracture tip. Equal area stereonet plots of Coulomb stress changes (in MPa) for fault planes of all orientations in 3D computed at (b) point A, and (c) point B. The pole of a fault plane with a dip of 45 deg and striking at 45 deg from the X-axis (the minimum horizontal stress,  $\sigma_{xx}$ , direction) is shown as a black dot surrounded by a black circle (b-c).

order to keep the first term in the material balance equation (equation 5.13) unchanged, we scale down the height by  $n\sqrt{n}$  so that the volume of the fracture cavity is the same as that for the oblate spheroidal cavity. However, to keep the second term of the material balance equation unchanged, the leak-off coefficient needs to be scaled up by  $\sqrt{n}$ . This is reasonable since the surface area of the cavity has decreased even though its volume remains unchanged. Therefore the leak-off coefficient should increase for the same leak-off as that for the oblate spheroidal cavity. In the case of Barnett shale (Figure 5.6), we scale up the length by 2.7 to best fit the observed spatiotemporal evolution of microseismicity. Scaling down the height (multiplying with  $1/(2.7 * \sqrt{2.7})$ ) gives us the maximum fracture height of around 95 m at the end of injection which is close to the fracture height of 100 m used by Rozhko (2010) for these data.

To further explore the physical meaning of the scaling of the crack tip propagation (obtained by solving equation 5.13) required to fit the distance versus time plots of the microseismic events and establish the equivalence between our oblate spheroidal cavity model and actual hydraulic fracturing, we reproduce the event locations of the Carthage Cotton valley microseismic data from Rutledge and Phillips (2003). Figure 5.9a shows the map view of the event locations together with the treatment well location (21-10) and the locations of the two monitoring wells namely 21-09 and 22-09 containing the recording geophones array, Array-1, and Array-2 respectively. Only the event locations near and east of the treatment well (21-10) are shown. Rutledge and Phillips (2003) note that this pattern of event locations is most possibly symmetric about the treatment well but due to observational bias most of the low magnitude events towards the West of the treatment well are not recorded. Figure 5.9b shows the projection of the event locations on a vertical cross-section along the strike and passing through the treatment well. The dashed lines show the 80 m completion interval perforated at six discrete intervals ranging from 3 to 6 m. The distance of microseismic events along the strike varies from approximately 420 m for shallow perforation and 240 m for the perforation at depth. Furthermore, the events form distinct bands around the perforation intervals suggesting that they are confined within the target sands and the discrete sand intervals are hydraulically isolated.

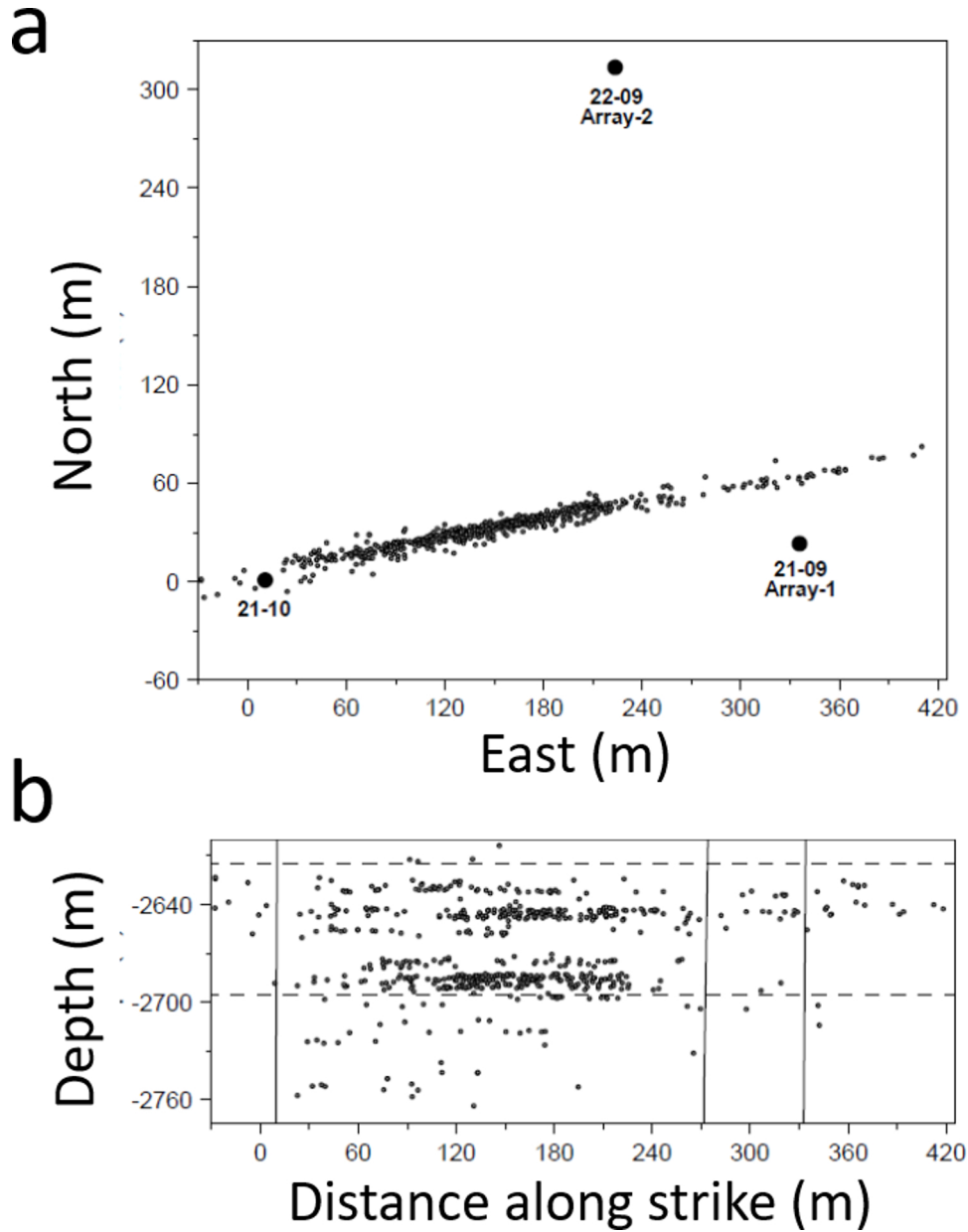


Figure 5.9: Event locations of the Carthage Cotton valley gas field microseismic data taken from Rutledge and Phillips (2003). (a) Map view of the event locations and the treatment well (21-10), and the two monitoring wells (21-09 and 22-09). Only the events near and East of the treatment well (21-10) are shown. (b) The projection of event locations on a vertical cross-section along the strike and passing through the treatment well (21-10). The vertical lines show the projection of the 3 wells and the dashed horizontal lines mark the injection interval.

The distance versus time plot in Figure 5.7b shows the maximum event distance up to approximately 300 m. Shapiro and Dinske (2009) consider only 2.5 hours of injection and hence the maximum distance is less than seen in Figure 5.9a from Rutledge and Phillips (2003). The crack tip propagation front obtained by solving equation 5.15 assuming an oblate spheroidal cavity model gives us a maximum half-length (=half-height) of 150 m. We scaled up this crack tip propagation front by a constant number 1.9 so as to fit the distance versus time plot (Figure 5.7b). Scaling down the height of 300 m by multiplying with  $1/(1.9 * \sqrt{1.9})$  gives us a fracture height of around 115 m which is similar to the height of around 105 m over which the microseismic events are recorded as shown in Figure 5.9b. In Figure 5.9b, we can see events at greater depths beyond the injection interval of 80 m shown by the dashed horizontal lines. This gives an independent validation for using a simple oblate spheroidal cavity model in the material balance equation for computing the triggering front even for complex hydraulic fracture geometries seen during real stimulations. Based on these real data examples we can say that during fluid injection in hydraulic fracturing, the process zone near the propagating crack tip plays an important role in the observed spatiotemporal evolution of microseismicity.

#### **5.4.1 Implications for seismicity based reservoir characterization**

Shapiro *et al.* (2002) and Rothert and Shapiro (2003) show that the triggering front of microseismicity can be used to estimate the hydraulic diffusivity of rocks leading to the seismicity based reservoir characterization (SBRC) approach. The main assumption of SBRC is that the fluid induced microseismicity is triggered in critically stressed rocks solely due to pore pressure diffusion. In a more recent study based on SBRC, Shapiro and Dinske (2009) invoke a non-linear diffusion assuming a large increase in rock permeability due to the creation of new fracture volume in order to explain the triggering front. In this study, we show that an alternative explanation of the triggering front can be obtained in terms of the crack tip propagation alone. SBRC invokes anisotropic diffusivity to explain the elongated shapes of microseismic clouds observed during hydraulic

fracturing. However, the shape of the microseismic cloud depends upon the actual shape of the hydraulic fracture as shown in Figure 5.2. Thus the elongated shape of the microseismic cloud can be obtained even with an isotropic diffusivity provided that the hydraulic fracture has an elongated shape which implicitly assumes an anisotropic stress state.

Shapiro *et al.* (2002), Rotherth and Shapiro (2003), and Shapiro and Dinske (2009) use large values of diffusivity (e.g. as large as  $2.5 \text{ m}^2/\text{s}$  for Barnett shale gas samples) to model the triggering fronts arguing that hydraulic fracturing increases the diffusivity/permeability of the rocks. However Patzek *et al.* (2013) show in a recent study that gas production in Barnett shale obeys a simple scaling theory and obtained permeability values of hydraulically fractured rocks which are 20 to 200 times larger than the values of few nanodarcies measured in the laboratory experiments. Therefore Patzek *et al.* (2013) suggest that the upper limit of permeability values for hydraulically fractured rocks in Barnett shale is typically few microdarcies. Taking a permeability value of 10 microdarcy, and porosity, compressibility and viscosity values from table 5.2, the diffusivities computed using equation 5.2 are  $3.3 \cdot 10^{-4} \text{ m}^2/\text{s}$  and  $5 \cdot 10^{-7} \text{ m}^2/\text{s}$  respectively for water and gas. These values are much smaller than the diffusivity values of  $2.5 \text{ m}^2/\text{s}$  estimated by the SBRC approach. Thus the hydraulic diffusivity obtained using SBRC approach from the time versus distance plots of the microseismic events may be overestimated by many orders of magnitude.

We use the fracture tip growth over time of the oblate spheroidal cavity model to explain the triggering front of microseismicity which we subsequently scaled up to match the actual length and height of the hydraulic fracture. As suggested by Figure 5.3c and 5.3d, the width of the hydraulic fracture (normal to the fracture face) should then be governed by the pore pressure diffusion. Hence the width of the hydraulic fractures can be used to estimate the isotropic permeability. A quick method to get an estimate is to equate the half-width of the microseismic cloud near the injection point with  $L = \sqrt{4\pi ct}$ . The fracture width of the microseismic data of the Carthage Cotton valley gas field (shown in Figure 5.9a) is about 6 m. Taking the injection time of 2.5 hr and half-width of 3 m, we get a diffusivity value of  $7.96 \cdot 10^{-5} \text{ m}^2/\text{s}$ . Using the porosity value of 0.1 and, compressibility and viscosity values for gas from table 5.2, we get a permeability value of 1.6

millidarcy which is an order of magnitude higher than the reported values of in situ permeabilities of less than 0.1 millidarcy for the Carthage Cotton valley tight sands (Bartberger *et al.*, 2002). The obtained permeability value of 1.6 millidarcy is reasonable for the hydraulically fractured tight sands of Carthage Cotton valley as has been pointed out for the Barnett shale by Patzek *et al.* (2013) where permeabilities for hydraulically fractured shales are nearly 20 to 200 times higher than lab measured permeabilities.

#### **5.4.2 Evolution of the microseismic cloud in the case of a planar hydraulic fracture**

Based on our results we present a simplified model for the evolution of the shear-slip microseismic event cloud associated with a single planar fracture. The model implicitly assumes an anisotropic stress state which favors development of a planar hydraulic fracture. Figure 5.10 shows a schematic diagram of the growth of the hydraulic fracture (shown by green color) and the microseismic events (black filled circles and crosses) at different dimensionless times,  $T$ , where  $T=2$  is greater than  $T=1$  and so on. At time  $T=0$ , the fracture initiates and a tensile stress perturbation zone (shown in red) is formed near the crack tip. These elastic stress perturbations near the crack tip trigger microseismic events (black filled circles) at time  $T=0$ . At time  $T=1$ , the fracture length has increased and new microseismic events (black filled circles) are observed farther away from the injection point due to the tensile elastic stress perturbations near the propagating crack tip. At the same time ( $T=1$ ), pore pressure diffusion causes microseismic events around the fracture face which are shown by black crosses. This model of evolution of the fracture cavity and the shear-slip microseismic event cloud is consistent with the inferences drawn from the Coulomb failure function shown around a stationary hydraulic fracture in Figure 5.3.

The hydraulic fracture cavity and associated microseismic cloud continue to grow over time ( $T=2$ ) up to the shut-in time (Figure 5.10) and we get a leading front of microseismicity near the crack tip due to elastic stress changes and a trailing front of microseismic events due to pore pres-

sure diffusion. We have shown in Figures 5.6 and 5.7 that the crack tip propagation can be taken as a proxy for the triggering front observed in the distance versus times plots of the microseismic events. The model presented here suggests that these leading microseismic events are triggered due to the elastic stress perturbations rather than pore pressure changes. Our analysis is restricted only up to the duration of the fluid injection. However, after shut-in when the injection stops, we can expect the microseismic cloud to grow mainly due to the pore pressure diffusion. But the shape of the fracture cavity at the shut-in time should significantly affect the diffusion profile after shut-in.

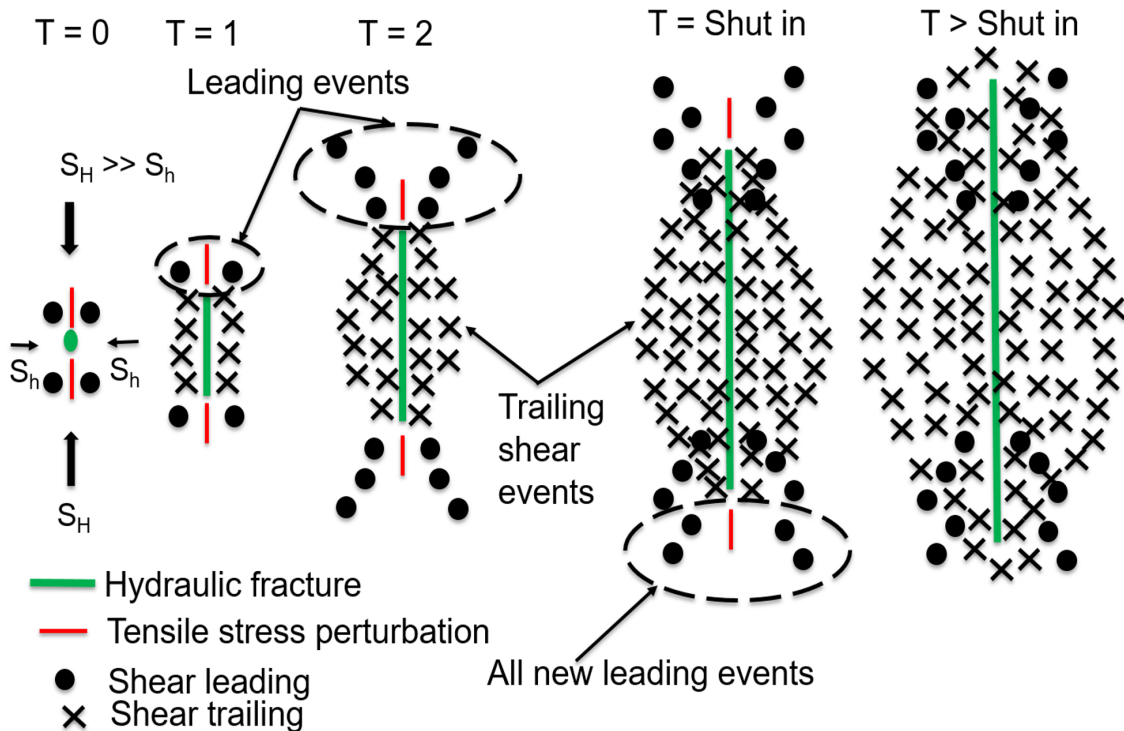


Figure 5.10: Schematic diagram showing the evolution of a planar hydraulic fracture and the associated microseismicity over time.

The growth of microseismic clouds similar to that predicted by our model (Figure 5.10) has been observed in real hydraulic fracturing stimulations. Rutledge and Phillips (2003) show the high-resolution event locations and mark them as early, intermediate and late events based on their time of occurrence with respect to the treatment schedule. The late time events extend farthest from the injection domain in the direction of the maximum horizontal stress. However, there are

late time events which occur near the injection domain. Our model proposes that the events occurring farthest from the injection domain during late times should be triggered by the elastic stress perturbations near the fracture tip while those occurring near the injection domain are triggered due to pore pressure diffusion. Furthermore, Rutledge and Phillips (2003) observe a general migration of events normal to the trend for one of the microseismic clusters which suggests that the fracture zone widens as the treatment progresses. Rutledge and Phillips (2003) attribute this observation to the possible errors in event locations due to temporal changes in velocities over portions of the travel paths affected by the injection. However, our model suggests that this increase in the width of the event cloud over time may be due to triggering of the microseismic events caused by the fluid diffusion near the fracture face. Therefore, the width of the elongated microseismic cloud can be used to estimate the in situ diffusivity/permeability as shown in the last section. However, if the diffusivity estimates are obtained by fitting a diffusion front to the leading microseismic events which are triggered due to the elastic stress perturbations near the propagating crack tip, the obtained diffusivity/permeability may be overestimated by several orders of magnitude.

## **5.5 Conclusions**

Hydraulic fracturing perturbs the in situ stresses due to the opening of cracks/fractures and pore pressure diffusion, yet elastic stress perturbations due to the opening of fractures are often neglected in interpreting the spatiotemporal evolution of observed microseismicity. In this study, we show that the elastic stress perturbations due to the opening of the hydraulic fracture cavity can trigger microseismic events near the crack tip region due to shear slippages on pre-existing faults/fractures. The pore pressure diffusion plays an important role in triggering microseismic events near the fracture face where elastic stress perturbations restrict microseismic events. Furthermore, the shape of the pore pressure diffusion front depends upon the shape of the hydraulic fracture cavity and time. Therefore elongated microseismic clouds can be obtained even with an isotropic diffusivity provided the hydraulic fracture has an elongated shape which implicitly as-

sumes an anisotropic stress state. Unlike the SBRC approach which invokes purely pore pressure diffusion, we use the crack tip propagation to model the observed triggering front of microseismicity. Furthermore, the width of the elongated microseismic cloud may give an idea about the in situ hydraulic diffusivity/permeability. Thus the effect of the opening of the hydraulic fracture cavity on the in situ elastic stresses and the pore pressure diffusion profiles must be taken into account in modeling and interpretation studies of the induced microseismicity.

## **Chapter 6**

### **Modeling shear wave splitting due to stress-induced seismic anisotropy:**

### **Application to hydraulic fracturing induced microseismicity**

#### **Summary**

Hydraulic fracturing induces stress perturbations in the surrounding rocks which can cause brittle failure leading to microseismicity. These stress perturbations may cause preferential closure and alignment of pre-existing cracks resulting in seismic anisotropy. The waveforms of the recorded microseismic events may, therefore, display shear wave splitting due to the stress-induced anisotropy. In this study, we consider the microseismic data recorded during a single stage of a real hydraulic fracturing job in the Cardium formation of the Pembina oil field in Central Alberta. The data show appreciable shear wave splitting with clear separation between the slow and the fast shear waves. We measure the delay times by subtracting the manually picked arrival times of the fast shear waves from the slow shear waves. Next, we model the delay times due to the

stress-induced anisotropy by computing the elastic stress changes during hydraulic fracturing and mapping them into stress-dependent stiffness tensors using the third-order elasticity. The changes in the modeled delay times are negligible for different dimensions of the penny-shaped hydraulic fracture cavity. The measured delay times increase with increasing receiver depth whereas the delay times modeled by assuming stress-induced anisotropy show an opposite trend. Therefore, we interpret that the shear wave splitting observed in our data is due to the intrinsic anisotropy rather than being stress-induced. Thus, the forward modeling of stress-dependent stiffness tensors and delay times can be an important tool for identifying stress-induced anisotropy.

## 6.1 Introduction

Seismic anisotropy is an important geophysical tool to investigate the earth's interior. Seismic anisotropy can originate due to preferred mineral alignment, material heterogeneities in rocks like layering in sedimentary rocks, and the presence of discontinuities like preferential crack orientation. Differential stresses lead to seismic anisotropy due to the closure of aligned cracks and mechanical discontinuity (Nur and Simmons, 1969a). Temporal changes in seismic anisotropy can be used to isolate stress-induced anisotropy from other sources of anisotropy (Teanby *et al.*, 2004a). However, the interpretation of changes in anisotropy in terms of stress changes is complicated due to the spatial variation of seismic sources when using passive seismic data. Therefore forward modeling of the effect of stresses on seismic anisotropy measurements can be a great aid in interpretation of stress-induced anisotropy.

When a shear wave enters an anisotropic medium it splits into fast and slow shear waves which are polarized orthogonally to each other (Crampin, 1981). This phenomenon is called shear wave splitting. The shear wave splitting along a ray path is characterized by two parameters namely the polarization of the fast shear wave ( $\psi$ ), and the time lag ( $\delta t$ ) between the fast and the slow shear waves (Silver and Chan, 1991; Teanby *et al.*, 2004b). The seismic anisotropy of a medium can be characterized by measurements of the shear wave splitting parameters along various ray paths.

The microseismic events recorded during hydraulic fracturing usually contain large shear wave components and can be used for shear wave splitting analysis (Wuestefeld *et al.*, 2011; Verdon *et al.*, 2013). However, most applications of microseismic monitoring are limited to locating them in space and time for understanding the growth of hydraulic fractures. Since hydraulic fracturing is known to induce stress changes in the surrounding rocks, measurements of shear wave splitting parameters and their spatiotemporal variations can reveal the stress evolution in the surrounding rocks. This can be used for characterizing the stimulated reservoir.

In this chapter, we present a quantitative forward model for mapping stresses into seismic anisotropy. We first compute the induced stresses due to hydraulic fracturing using Eshelby's equivalent inclusion method. These induced stresses are then fed into a forward model which uses third-order elasticity to compute stress-dependent elastic stiffness coefficients. The resulting shear wave splitting parameters are computed using the acquisition set up of a real hydraulic fracturing data corresponding to case study 2 described in chapter 2. The details of the microseismic data, acquisition setup, geological and operational settings are given in chapter 2. A comparison of the observed and the modeled shear wave splitting delay times can help in understanding if the anisotropy has a stress-based origin.

## **6.2 Methods**

The forward modeling of stress-induced shear wave splitting parameters involves computation of the stress-dependent elastic stiffness tensors, and modeling of the shear wave splitting parameters at the receivers by tracing the rays from the source to the receivers. We invoke third-order elasticity for modeling the stress-induced stiffness tensors. Nonlinear elasticity has been used for explaining stress-induced anisotropy in laboratory experiments (Johnson and Rasolofosaon, 1996; Winkler *et al.*, 1998) and boreholes (Sinha and Kostek, 1996). Third-order elasticity allows full mapping between stress and stiffness tensors. For modeling the splitting parameters, we use the event locations and the receiver positions of a single stage of a real hydraulic fracturing job. In this study, we

model only the delay times ( $\delta t$ ) between the fast and the slow shear waves.

### 6.2.1 Model set up

In order to model the shear wave splitting parameters, we make a synthetic model based on the acquisition set up of a real hydraulic fracturing job corresponding to case study 2 described in chapter 2. We consider a single stage (stage 7) of the hydraulic fracturing treatment. Figure 6.1 is the treatment plot of stage 7 showing the treatment pressure, slurry rate, proppant concentration and event rates over the injection period. The average treatment pressure can be taken as 42 MPa over the injection period as shown by the red curve in Figure 6.1. After careful processing of the microseismic data acquired during stage 7, we identify 56 and 57 events recorded in the monitoring well 1 and well 2 respectively with high signal-to-noise ratio on which both P- and S-arrival times have been picked. The locations of these events are used to model the splitting delay times at the receiver positions in the two monitoring wells shown in Figure 2.9. We assume that the medium is initially homogeneous and isotropic and the anisotropy arises only due to the application of the anisotropic stresses. We will test this assumption by comparison of the stress-induced modeled splitting delay times with the measured delay times obtained from the microseismic data.

For stress modeling, the hydraulic fracture is represented as a penny-shaped vertical crack. At any point of time during injection, the major axes  $b_o$  and  $c_o$  of the hydraulic fracture shaped as an oblate spheroidal cavity are equal and much greater than the minor axis  $a_o$  (Model 1 given in Table 6.1). The cavity is situated in a medium of infinite extent with homogeneous stresses acting at the boundary of the model at infinity. The maximum horizontal stress in the study region is oriented in the NE-SW direction, the minimum horizontal stress is oriented in the NW-SE direction and the third principal stress is along the vertical direction (Bell and Bachu, 2003; Haug *et al.*, 2007). The average fracture azimuth in our case study is N45°E as reported by the operator (PetroBakken Pembina 14-19-48-10W5 microseismic processing report) which suggests that the maximum horizontal stress is oriented in the NE-SW direction. Since hydraulic fractures open

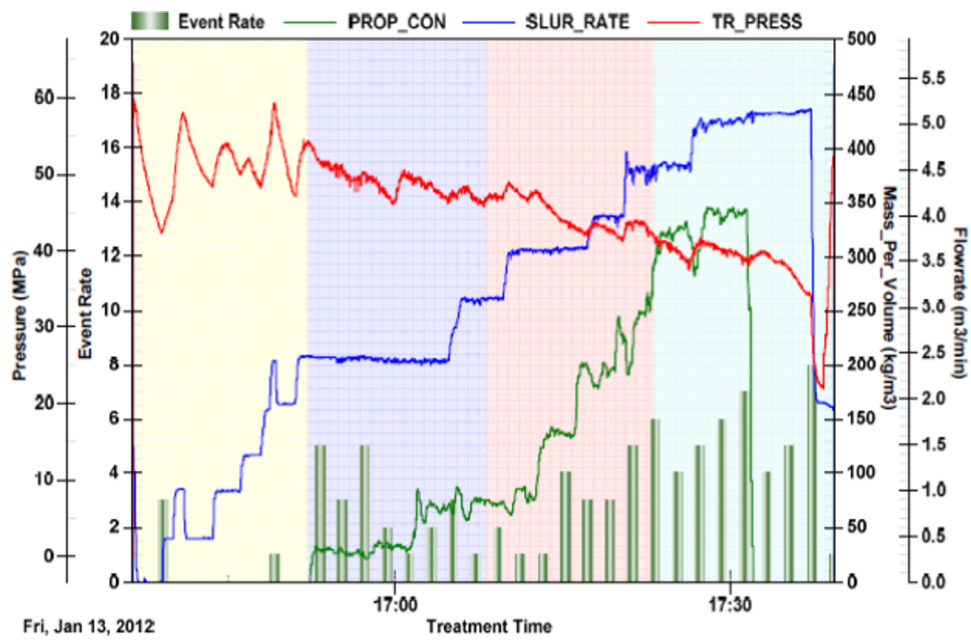


Figure 6.1: Treatment plot for stage 7 (From PetroBakken Pembina 14-19-48-10W5 microseismic processing report). Injection pressure is in red with scale on the left in MPa. The slurry rate is in blue with scale on the right as Flowrate in  $\text{m}^3/\text{min}$ . Proppant concentration is in green with scale on the right in  $\text{kg}/\text{m}^3$ . The event rate is in green bars with scale on the left and refers to events recorded during stage 7 in well 1.

Table 6.1: Material properties, Fracture dimensions, pore pressure, fracture pressure and regional stress state

Parameter	Value and Unit
Material properties	
Young's modulus, $E$	27.6 GPa
Poisson ratio, $\nu$	0.27
Oblate spheroidal cavity (Model 1)	
Semi-minor axis, $a_o$	0.002 m
Semi-major axis, $b_o$	22 m
Semi-major axis, $c_o$	22 m
Stress state	
Vertical stress, $\sigma_{zz}$	43.9 MPa
Maximum horizontal stress, $\sigma_{yy}$	35 MPa
Minimum horizontal stress, $\sigma_{xx}$	25.4 MPa
Pore pressure, $p_o$	17.8 MPa
Fracture pressure, $p_f$	42.0 MPa
Third-order elastic constants (taken from Prioul <i>et al.</i> (2004))	
$c_{111}$	-11300 GPa
$c_{112}$	-4800 GPa
$c_{123}$	5800 GPa

against the minimum principal stress, the minor axis  $a_o$  of the cavity is along the NW-SE direction which is taken to be the X'-axis. The major axes  $b_o$  and  $c_o$  are along the NE-SW direction (taken to be the Y' axis), and the vertical direction (taken as the Z' axes). The cavity contains water at uniform pressure  $p_f$  (given in Table 6.1). We assume that before hydraulic fracturing, the rock is saturated with water and has a uniform hydrostatic pore pressure,  $p_o$ , at the depth of the treatment well (=1815 m below ground level). The magnitudes of principal stresses and pore pressure  $p_o$  are given in Table 6.1. The vertical and minimum horizontal stress magnitudes are estimated from the stress gradients given in Bell and Bachu (2003) and Haug *et al.* (2007) for the study region. Since the vertical stress is known to be the maximum principal stress and the maximum horizontal stress magnitudes are not constrained in Bell and Bachu (2003) and Haug *et al.* (2007), we assume a value of -35 MPa. We later vary these magnitudes to see their effect on our results. The Young's modulus and Poisson ratio estimates (Table 6.1) for the Cardium formation are taken from Haug *et al.* (2007).

Table 6.2: Model 2 and Model 3 with different fracture dimensions used to compute the elastic stress changes

Parameter	Value and Unit	
	Model 2	Model 3
Semi-minor axis, $a_o$	0.003 m	0.004 m
Semi-major axis, $b_o$	76 m	120 m
Semi-major axis, $c_o$	76 m	120 m

### 6.2.2 Event location and seismic ray tracing

We locate events recorded at each monitoring well by using both the P- and S-arrival times combined with the backazimuth information. The high signal-to-noise ratio allows reliable estimation of the backazimuth information using the 3-components waveforms near the P-arrival times. We define a 3D Cartesian grid along the geographical East, North, and vertical with a regular grid spacing of 20 m in all three directions. We then compute the theoretical P and S arrival times and the backazimuth from each grid point to the receiver locations and save them as look up tables. The theoretical P and S arrival times are computed by performing ray tracing through the 1D P- and S-wave velocity models shown in Figure 6.2. Finally, we perform a search over the 3D grid to identify a grid point which simultaneously minimizes the misfit between the theoretical and observed S minus P arrival times, and the theoretical and observed backazimuths. This grid point represents the inverted event location.

Once the events are located, we perform seismic ray tracing from the event locations to the geophone positions using the S-wave velocity model shown in Figure 6.2. We use the pseudo bending ray tracing code of Um and Thurber (1987) for ray tracing. The 1D velocity model (Figure 6.2) is defined on a 3D grid with no lateral velocity variation. The velocity at any point is obtained by linear interpolation from velocities at eight surrounding nodes weighted based on the distance of the point from the surrounding nodes. These ray paths are subsequently used to compute the splitting delay times. However, the ray paths themselves are computed by assuming an isotropic 1D velocity model.

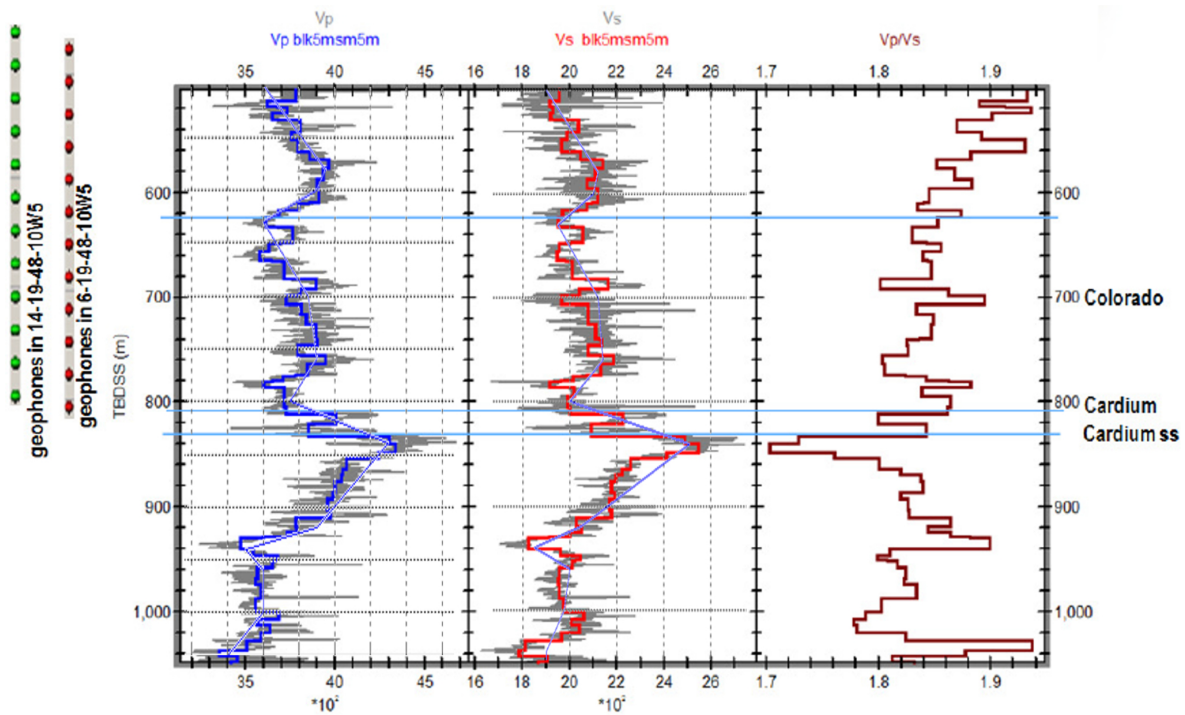


Figure 6.2: P (blue curve) and S (red curve) velocity models obtained by averaging sonic logs (gray curves) using 5 m blocking. (From PetroBakken Pembina 14-19-48-10W5 microseismic processing report). The blocked velocity models are further smoothed as shown by the overlying blue curves. These smoothed velocity models (blue curves) are used for event locations and ray tracing.

### **6.2.3 Elastic Stress changes due to hydraulic fracturing**

The opening of the hydraulic fracture cavity affects the in-situ elastic stresses. The elastic stress changes are computed using the Eshelby's equivalent inclusion method for the oblate spheroidal cavity model of the hydraulic fracture as discussed in Chapter 5. The details of this method and the relevant equations are given in Chapter 4 (equations 4.1-4.3). The material properties, far-field stresses, fracture pressure and fracture cavity dimensions used to compute the elastic stress perturbations are taken from Table 6.1.

The hydraulic fracture cavity also affects the pore pressure distribution in the surrounding rocks as discussed in Chapter 5. However, the spatial extent of the pore pressure diffusion profile depends upon the hydraulic diffusivity of the formation and the time from the start of injection. So, if the hydraulic diffusivity is very low and the injection time is small, the pore pressure changes can be neglected. The stress-induced anisotropy and delay times modeled in this chapter by taking only the elastic stress perturbations can at best be representative of the situation immediately following the start of injection.

The elastic stress changes are computed for a stationary hydraulic fracture with fixed dimensions. Since the hydraulic fracture continues to grow during injection, we model the elastic stress perturbations for three different dimensions of the hydraulic fracture cavity. We name them Model 1, Model 2 and Model 3 and the dimensions for each model are given in Tables 6.1 and 6.2. This gives us a range of possible changes in the elastic stresses during hydraulic fracturing.

### **6.2.4 Anisotropy calculation using third-order elasticity**

The seismic wave propagation in a stressed medium can be modeled using a generalized Hooke's law provided the elastic stiffness tensor is replaced by the stress-dependent effective stiffness tensor. The effective stiffness tensor can be computed using third-order elasticity as a function of stress. In linear elasticity, the potential energy is a quadratic function of strains, whereas, in the case of the third-order elasticity, it includes cubic terms which account for stress-dependent elastic

properties. The strain energy function  $E$  (for arbitrary anisotropy) in a material with third-order elasticity is given as (Mavko *et al.*, 2009)

$$E = \frac{1}{2}c_{ijkl}\epsilon_{ij}\epsilon_{kl} + \frac{1}{6}c_{ijklmn}\epsilon_{ij}\epsilon_{kl}\epsilon_{mn} , \quad (6.1)$$

where  $c_{ijkl}$  and  $c_{ijklmn}$  are respectively the components of second and third-order elastic tensors and the repeated indices imply summation from 1 to 3. The components  $c_{ijkl}$  are the usual elastic constants used in Hooke's law in linear elasticity.  $c_{ijklmn}$  are the third-order elastic constants which can be obtained from lab experiments (Winkler and Liu, 1996; Prioul *et al.*, 2004; Prioul and Lebrat, 2004).

The stress-dependent effective elastic constants depend upon the elastic constants in a reference state (initial state before application of stress), the third-order elastic constants and the finite strains due to applied stresses. They are given by (Mavko *et al.*, 2009)

$$c_{ijkl}^{eff} = c_{ijkl}^0 + c_{ijklmn}\epsilon_{mn} , \quad (6.2)$$

where  $c_{ijkl}^0$  are the elastic constants in the reference state, and  $\epsilon_{mn}$  are the principal strains due to the applied static stresses.

Assuming that the symmetry axes of the medium are aligned along the coordinate axes, the effective elastic constants  $c_{ij}^{eff}$  in Voigt notation can be approximated as (Prioul *et al.*, 2004; Mavko

*et al.*, 2009)

$$\begin{aligned}
c_{11}^{eff} &\approx c_{11}^0 + c_{111}\epsilon_{11} + c_{112}(\epsilon_{22} + \epsilon_{33}) , \\
c_{22}^{eff} &\approx c_{22}^0 + c_{111}\epsilon_{22} + c_{112}(\epsilon_{11} + \epsilon_{33}) , \\
c_{33}^{eff} &\approx c_{33}^0 + c_{111}\epsilon_{33} + c_{112}(\epsilon_{11} + \epsilon_{22}) , \\
c_{12}^{eff} &\approx c_{12}^0 + c_{112}(\epsilon_{11} + \epsilon_{22}) + c_{123}\epsilon_{33} , \\
c_{13}^{eff} &\approx c_{13}^0 + c_{112}(\epsilon_{11} + \epsilon_{33}) + c_{123}\epsilon_{22} , \\
c_{23}^{eff} &\approx c_{23}^0 + c_{112}(\epsilon_{22} + \epsilon_{33}) + c_{123}\epsilon_{11} , \\
c_{44}^{eff} &\approx c_{44}^0 + c_{144}\epsilon_{11} + c_{155}(\epsilon_{22} + \epsilon_{33}) , \\
c_{55}^{eff} &\approx c_{55}^0 + c_{144}\epsilon_{22} + c_{155}(\epsilon_{11} + \epsilon_{33}) , \\
c_{66}^{eff} &\approx c_{66}^0 + c_{144}\epsilon_{33} + c_{155}(\epsilon_{11} + \epsilon_{22}) ,
\end{aligned} \tag{6.3}$$

where  $c_{ij}^0$  are the elastic constants in reference state,  $c_{ijk}$  are the third-order elastic constants, and  $\epsilon_{ij}$  are the strains due to principal stresses  $\sigma_{ij}$ .  $\epsilon_{ij}$  and  $\sigma_{ij}$  are related by the Hooke's law as

$$\sigma_{ij} = c_{ijkl}^0 \epsilon_{kl} . \tag{6.4}$$

Equation 6.3 can be used for computing the stress-dependent effective elastic constants for both an initially isotropic and transverse isotropic medium by substituting the appropriate elastic constants in the reference state ( $c_{ij}^0$ ). It is important to note that in equation 6.3, tension is taken as positive and compression negative (Sinha and Kostek, 1996; Prioul *et al.*, 2004). Therefore, we need to reverse the sign convention of the in situ stresses that we have used in this thesis (tension negative and compression positive) before using equation 6.3.

## 6.2.5 Modeling shear wave splitting delay time

The induced stresses due to hydraulic fractures are inhomogeneous and anisotropic so the stress-induced seismic anisotropy computed using third-order elasticity is also inhomogeneous. We discretize the medium using a regular 3D grid and define the stiffness tensors at each grid point. The stiffness at any spatial point is computed using linear interpolation from the stiffness values at the eight surrounding grid nodes similar to that used for the velocity model. In order to compute shear wave splitting parameters of a ray path at the recording station, the incremental anisotropic effects on each ray path segment need to be computed. This is achieved by using the ray paths obtained from seismic ray tracing and the 3D grid on which the stiffness tensors are defined.

The Christoffel matrix ( $m_{ij}$ ) for each ray segment is defined as (Babuska and Cara, 1991)

$$m_{ik} = \frac{1}{\rho} c_{ijkl} \hat{n}_j \hat{n}_l, \quad (6.5)$$

where  $\rho$  is the density of the medium,  $c_{ijkl}$  is the elastic stiffness tensor, and  $n_i$  and  $n_j$  are the direction cosines of the ray path segment. The Christoffel matrix (equation 6.5) gives three eigenvalues  $\lambda_1 > \lambda_2 > \lambda_3$  such that the velocity of the fast shear wave  $V_f = (\lambda_2)^{1/2}$  and the velocity of the slow shear wave  $V_s = (\lambda_3)^{1/2}$ . The eigenvectors corresponding to eigenvalues  $\lambda_2$  and  $\lambda_3$  give the polarization direction of the fast and slow shear waves respectively (Abt and Fischer, 2008; Shelley *et al.*, 2014). The time lag  $\delta t_n$  between fast and slow shear waves for each ray segment is computed as  $L(V_s^{-1} - V_f^{-1})$  where  $L$  is the length of each ray path segment (Shelley *et al.*, 2014). Summing up the time lag  $\delta t_n$  for all the ray segments from the source to the receiver gives us the delay time  $\delta t$  as

$$\delta t = \sum_{n=1}^N \delta t_n. \quad (6.6)$$

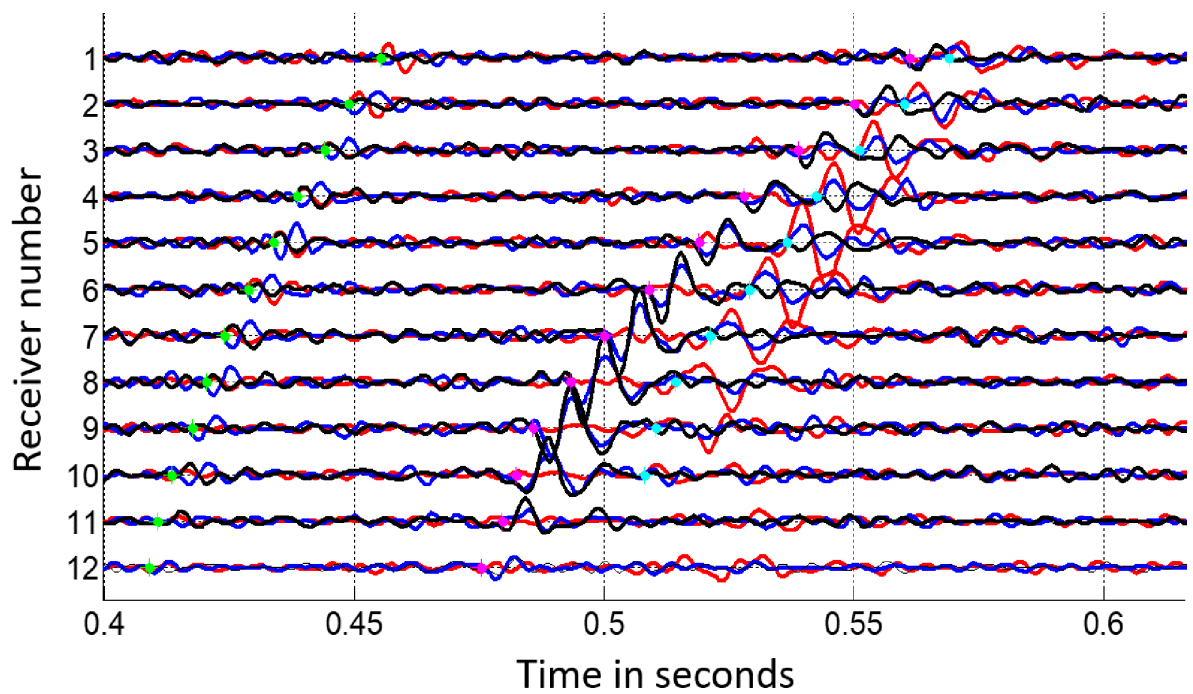


Figure 6.3: A typical microseismic event recorded during stage 7 at well 2 showing manual time picks. For the traces, red=Z, blue=Y, and black=X. Green points: P-arrival times picks. Magenta points: Fast S-arrival times picks. Cyan points: Slow S-arrival times picks

## 6.2.6 Splitting delay time measurements on microseismic data

The recorded microseismic events allow for visual identification of the fast and the slow shear waves as shown in Figure 2.10. We pick both the fast and slow shear wave arrival times. Figure 6.3 shows a microseismic event recorded at well 2 on which both fast and slow shear waves have been picked manually which are displayed respectively as magenta and cyan ticks. We pick the slow shear waves only on those receivers where the arrival is clearly visible. The delay times are then computed simply by subtracting the fast shear wave arrival times from the corresponding slow shear wave arrival times.

## 6.3 Results

Figure 6.4 shows the locations of the events recorded at well 1 (blue circles) and well 2 (red circles) obtained using the grid search approach. The events are elongated approximately NE-SW which is the same as the direction of the maximum horizontal stress in the study region. The mean depth of the events is 821 m and most of the events are confined around this depth. This suggests good containment of the fracture height within the stimulated reservoir.

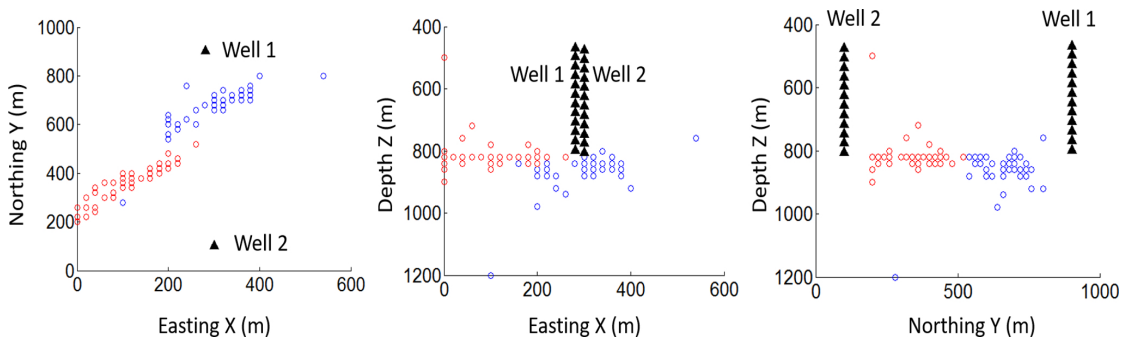


Figure 6.4: Microseismic events of stage 7, blue circles show events detected at monitoring well 1 and red circles show events detected at monitoring well 2. Geophones are shown by black triangles. These events are used for modeling shear wave splitting delay times due to stress-induced anisotropy.

We perform ray tracing from the relocated events to the receiver positions using a 1D velocity

model shown in Figure 6.2. Figure 6.5 shows all the ray paths from the event locations to the receiver positions in the two monitoring wells. Since we assume a penny-shaped crack elongated along the NE-SW direction as suggested by the event locations, the ray paths show a good sampling of the region in the vicinity of the hydraulic fracture on both sides of the fracture walls. These ray paths are later used for computing the shear wave splitting parameters.

Next, we compute the elastic stress perturbations due to a stationary hydraulic fracture using Eshelby's equivalent inclusion method (equation 4.3) and the parameters listed in Table 6.1. Figure 6.6 shows the elastic stress perturbations in the minimum horizontal stress and vertical stress in a vertical cross-section normal to the maximum horizontal stress. The stress perturbations near the crack tip are tensile (shown by hot colors) whereas those around the fracture face are compressive. During injection, the fracture continues to grow, so Figure 6.6 can be regarded as a snapshot of the elastic stress perturbations around the fracture cavity at any instant of time. We also compute the elastic stress perturbations for two other fracture dimensions listed in Table 6.2 which we refer to as Model 2 and Model 3 (Model 1 being the fracture cavity with dimensions listed in Table 6.1).

The induced elastic stresses due to the stationary hydraulic fracture (for Model 1 shown in Figure 6.6) are superimposed on the in-situ effective stresses prior to hydraulic fracturing which are obtained by subtracting the hydrostatic pore pressure from the far-field stresses. These superimposed stresses are then used to compute the effective stiffness tensors using equations 6.3 and 6.4 based on third-order elasticity (equations 6.1-6.2). We assume representative values of the third-order elastic constants for shales (Mavko *et al.*, 2009) listed in Table 6.1. Since the elastic stress perturbations due to the hydraulic fracture are heterogeneous, the effective stiffness tensors computed using equation 6.3 are also heterogeneous. In order to understand this heterogeneity, we compute the velocities of the vertically propagating P and S waves around the hydraulic fracture. Figure 6.7 shows the resulting velocities in a vertical cross-section normal to the maximum horizontal stress. Figure 6.7a shows the velocity of the vertically propagating P-wave, Figure 6.7b shows the velocity of the vertically propagating S wave which is polarized perpendicular to the hydraulic fracture plane, whereas Figure 6.7c shows the velocity of the vertically propagating S

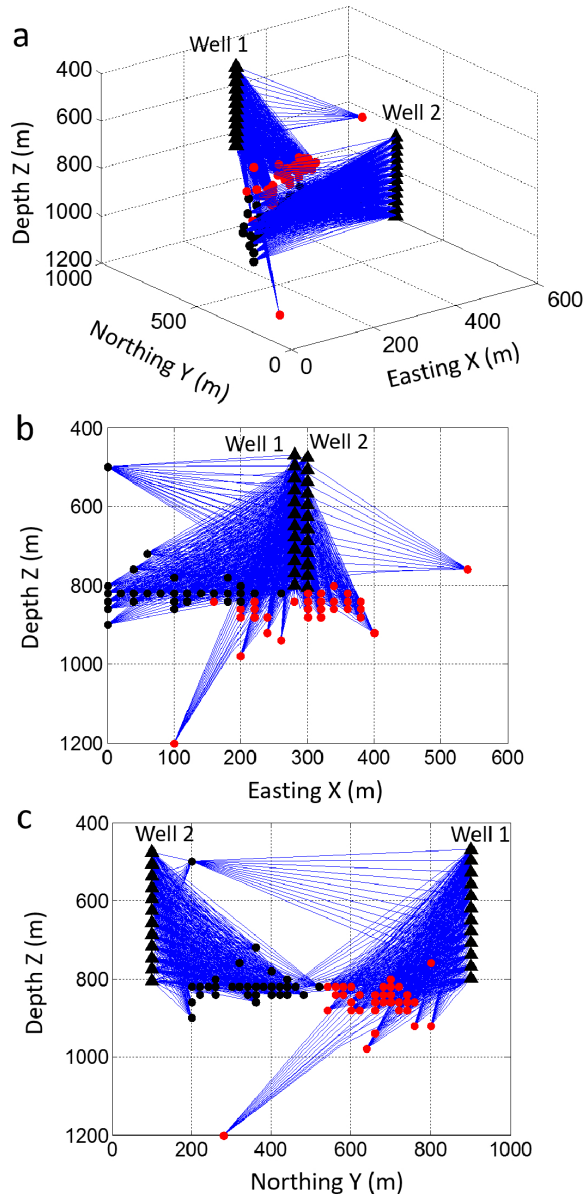


Figure 6.5: Modeled ray paths from microseismic events identified in stage 7 to the receivers in the two monitoring wells. (a) Ray paths in 3D. (b) Ray paths projected on East-West cross-section. (c) Ray paths projected on North-South cross-section. Red filled circles show events detected at well 1 and black filled circles show events identified on well 2. Black triangles are the geophone positions in the two wells.

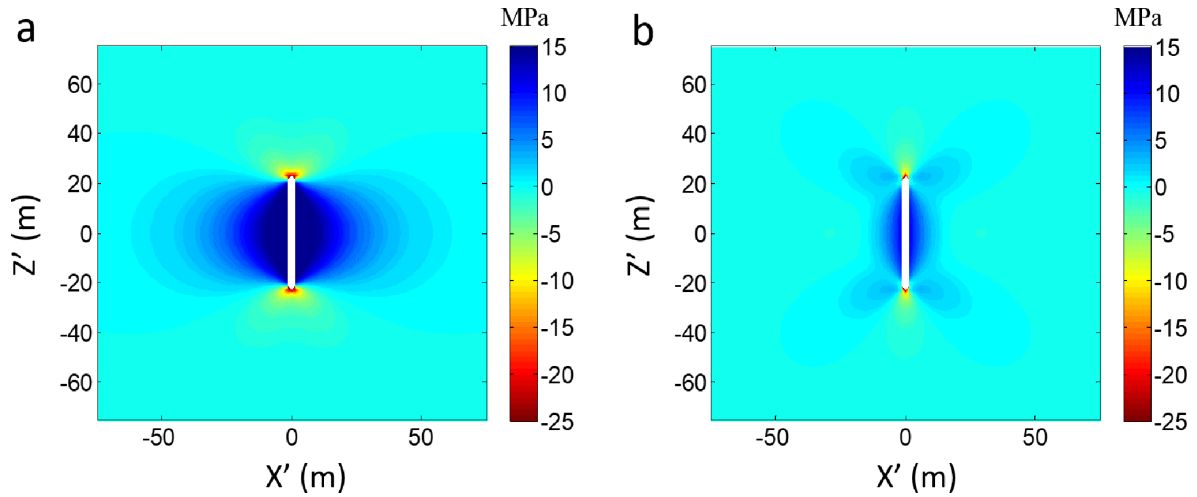


Figure 6.6: Stress perturbations (in MPa) induced by the penny-shaped hydraulic fracture computed with parameters given in Table 6.1. (a) Vertical cross-section showing perturbations in the minimum horizontal stress (b) Vertical cross-section showing perturbations in the vertical stress. Hot colors show tensile stress perturbations whereas cold colors represent compressional stress perturbations.

wave which is polarized parallel to the hydraulic fracture plane. The S wave having a polarization perpendicular to the fracture plane has relatively higher velocities as compared the S wave which is polarized parallel to the fracture plane. The velocities near the fracture face are larger than the background velocities whereas those near the fracture tip are smaller than the background velocities. The magnitude of the velocity change depends upon the assumed material properties, stress state, fracturing fluid pressure inside the cavity and the third-order elastic constants. However, the pattern can be expected to be similar to that shown in Figure 6.7.

Figures 6.8a and 6.8b show the event locations recorded at well 1 (blue circles) and well 2 (red circles). The injection point is shown as a filled black square. The position and the orientation of the hydraulic fracture cavity are shown by a solid black line. The projection of the penny-shaped cavity appears as a line due to a very small aperture of the cavity (2 mm to 4 mm as listed in Tables 6.1 and 6.2). In Figures 6.8c and 6.8d, we show respectively a comparison of the measured (blue circles) and the modeled splitting delay times for the events shown by a filled black circle (in Figures 6.8a and 6.8b) recorded at well 1 and the filled red circle (in Figures 6.8a and 6.8b)

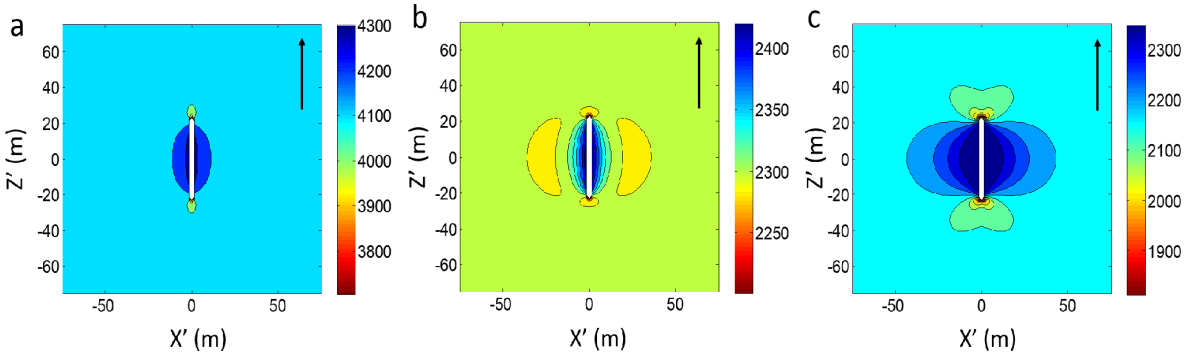


Figure 6.7: Velocities (in  $m/s$ ) around a hydraulic fracture for a vertically propagating wave by superimposing the elastic stress perturbations due to the opening of the fracture on the effective stresses before hydraulic fracturing (far-field stresses minus the hydrostatic pore pressure). (a) Vertical cross-section showing P wave velocity. (b) Vertical cross-section showing S wave velocity with polarization perpendicular to the hydraulic fracture plane. (c) Vertical cross-section showing S wave velocity with polarization parallel to the hydraulic fracture plane. Black arrow points in the direction of propagation of the seismic wave.

recorded at well 2. The modeled delay times are computed for three different dimensions of the fracture cavity namely for Model 1 (green circles), Model 2 (black circles), and Model 3 (magenta circles) by combining the elastic stress changes due to the opening of the fracture cavity with the in-situ effective stress prior to hydraulic fracturing. We also compute the modeled delay times in the absence of the hydraulic fracture cavity (red circles) by considering the in-situ effective stresses prior to the hydraulic fracturing. However, the differences in the modeled delay times for the four scenarios are negligible as shown by the overlapping circles (only magenta circles are visible) in Figures 6.8c and 6.8d. Figures 6.8c and 6.8d show that the measured delay times increase with increasing receiver depth, whereas the modeled delay times decrease with increasing receiver depth. We compare the measured and the modeled delay time for all the recorded events shown in Figure 6.4 and find that the measured and the modeled delay times show opposite trends with increasing receiver depths. This suggests that our modeling assumption that the delay times originate only due to the stress-induced anisotropy is not correct.

Next, we test the sensitivity of the modeled delay times to the horizontal differential stress, the total differential stress and the third-order elastic constants used for mapping stresses into elastic

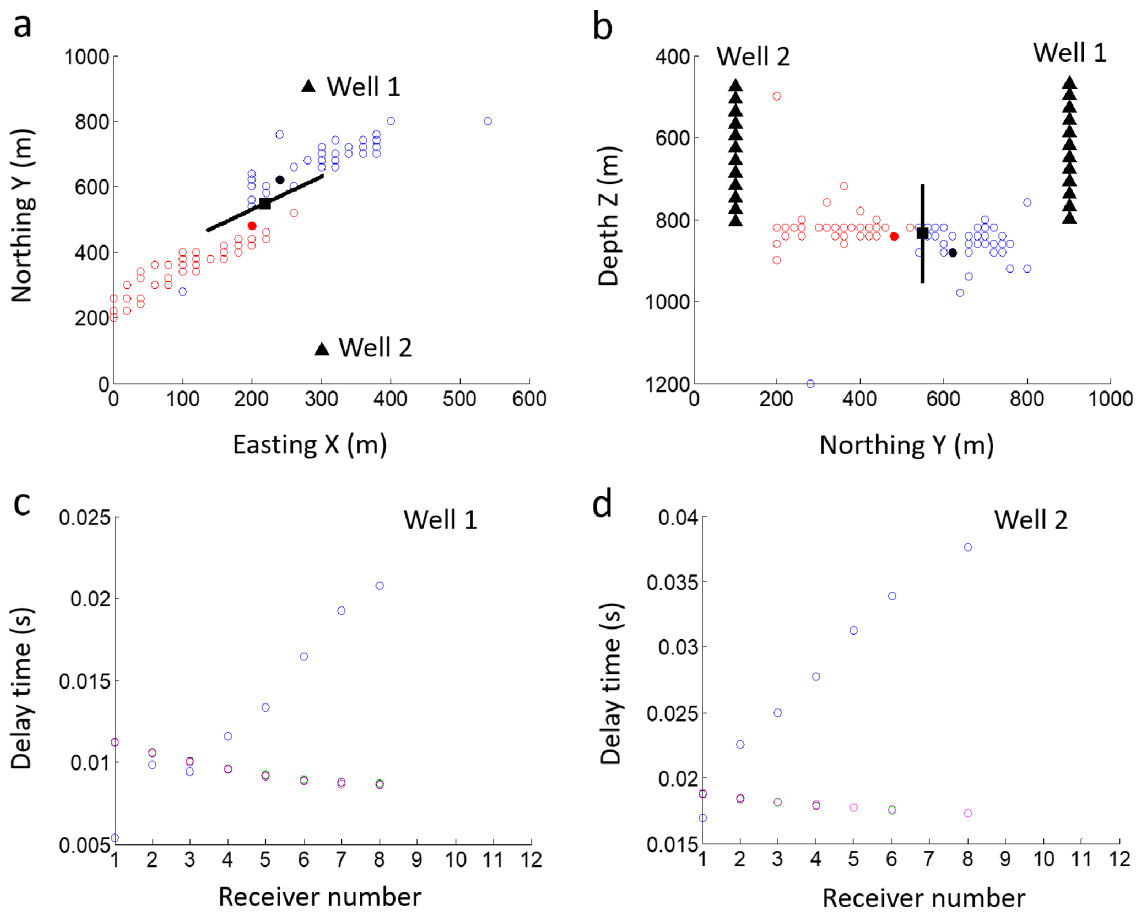


Figure 6.8: (a) Map view and (b) North-South cross-section showing the projections of the event locations recorded at well 1 (blue circles) and well 2 (red circles). The injection point is shown by a filled black square and the modeled fracture cavity is shown by a solid black line with dimensions of Model 3 listed in Table 6.2. A comparison of the measured (blue circles) and the modeled delay times for (c) the event marked as a filled black circle recorded at well 1 and (d) the event marked as a filled red circle recorded at well 2. Modeled delay times are shown by green, black and magenta circles for Model 1, Model 2, and Model 3 respectively (Model dimensions are listed in Tables 6.1 and 6.2). Red circles show the modeled delay times in the absence of the hydraulic fracture cavity by taking only the far-field stresses and the hydrostatic pore pressure. Only magenta circles are visible due to overlap of the red, green and black circles.

Table 6.3: Third-order elastic constants reported for different rocks in the published literature.

Sample	$c_{111}$	$c_{112}$	$c_{123}$	Source
Colton sandstone	-7600 GPa	-1400 GPa	500 GPa	Prioul <i>et al.</i> (2004)
Berea sandstone	-21217 GPa	-3044 GPa	2361 GPa	Sinha and Kostek (1996)

stiffness tensors. Figures 6.9a and 6.9b show the modeled delay times for the two events highlighted in Figure 6.8a by filled black and red circles recorded at well 1 and well 2 respectively for different values of the maximum horizontal stress which is the intermediate stress here (vertical stress is the maximum compressive stress). The vertical and the minimum horizontal stress are kept constant when changing the intermediate stress. Figures 6.9a and 6.9b show that for smaller values of the intermediate stress (smaller horizontal differential stress), the modeled delay times (shown by black circles) show a small increase with increasing receiver depth. Thus, the pattern of changes in the delay times with increasing receiver depth shows some dependence on the selected intermediate stress magnitude. However, the trend never replicates the large increase in the measured delay times with increasing receiver depths for all tested values of the intermediate stresses. In Figures 6.9c and 6.9d, we keep the maximum and minimum horizontal stresses fixed (thereby having constant horizontal differential stress), but vary the vertical stress so that the total differential stress (the difference between the vertical and the minimum horizontal stresses) increases (delay times shown by black circles) or decreases (delay times shown by green circles) by 10%. The pattern of changes in delay times with receiver depth is not affected by the total differential stress. However, the delay times at a particular receiver increase with an increase in the total differential stress magnitude. Figures 6.9e and 6.9f show respectively the modeled delay times at well 1 and well 2 for different values of the third-order constants reported in the literature and listed in Table 6.3. The principal stress magnitudes are taken from Table 6.1. The delay times at a specific receiver vary with the actual third-order constants used but the pattern of the changes in delay times with receiver depth remains unchanged. Thus, the delay times modeled by assuming stress-induced anisotropy never show the trends observed in the measured delay times. Thus, our initial assumption that the anisotropy of the medium is stress induced seems inadequate.

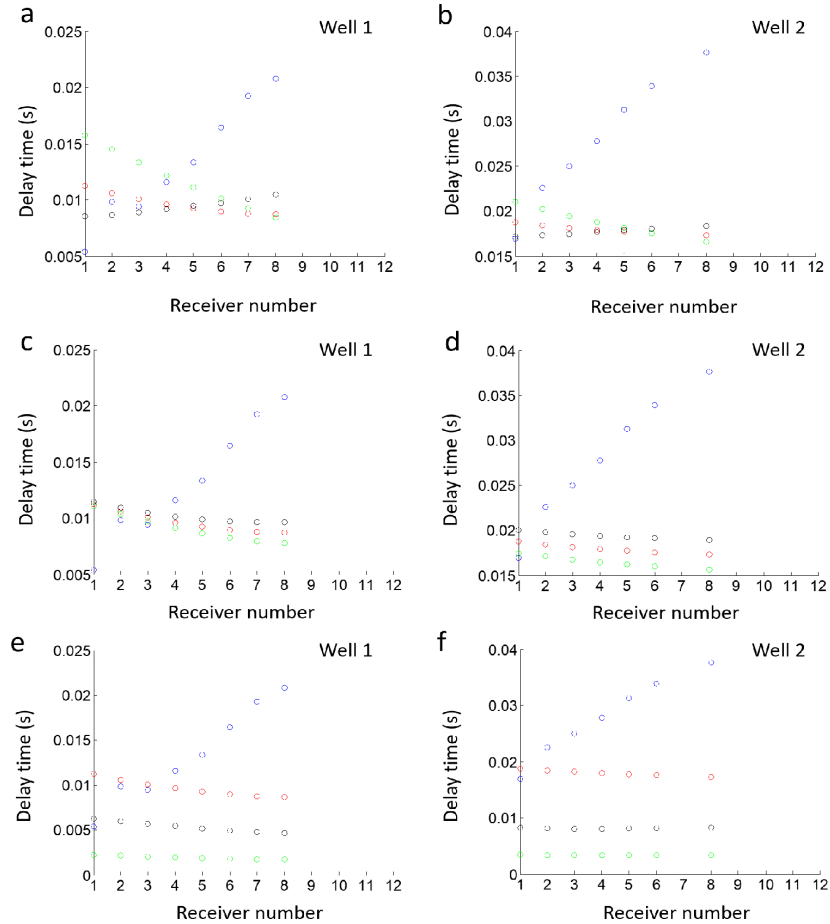


Figure 6.9: A comparison of the measured (blue circles) and the modeled delay times for different values of the intermediate stress magnitude for (a) the event marked as a filled black circle in Figure 6.8a recorded at well 1 and (b) the event marked as a filled red circle in Figure 6.8a recorded at well 2. Modeled delay times are shown by red, green, and black circles for intermediate stress magnitude equal to 35, 40, and 30 MPa respectively. Modeled delay times at (c) well 1 and (d) well 2 for different differential stresses at a constant intermediate stress of 35 MPa. Red circles show the modeled delay times when maximum and minimum principal stresses are given by Table 6.1. Green (Black) circles show the modeled delay times when the maximum principal stress is reduced (increased) so that the differential stress drops (increases) by 10%. Delay times modeled for different third-order elastic constants reported in the literature (listed in Table 6.3) for (e) the event recorded at well 1 and (f) the event recorded at well 2. The principal stress magnitudes are taken from Table 6.1. Red circles are obtained with third-order constants given in Table 6.1. Green circles are obtained with the third-order constants for Colton sandstone whereas black circles are obtained with the third-order constants for Berea sandstone (listed in Table 6.3).

## 6.4 Discussion

Hydraulic fracturing involves the injection of high-pressure fluid in the subsurface leading to the creation/reactivation of new/pre-existing fractures. This process results in elastic stress perturbations and pore pressure changes in the surrounding medium. As shown in Chapter 5, the shape of the pore pressure diffusion fronts depends upon the actual shape of the hydraulic fracture. Since the hydraulic fracture continues to grow during the injection period, the computation of the elastic stress and pore pressure changes as a function of time becomes a complex problem due to the moving boundary of the fracture cavity. Therefore in this chapter, we focus only on the elastic stress changes due to the growing hydraulic fracture cavity thereby neglecting the pore pressure changes. This situation can at best be a representative case for a very low permeability formation at small times after the start of injection. During these times the pore pressure changes can be neglected and the pore pressure can be assumed to have a constant value (same as that before the start of injection which is taken to be hydrostatic in this study).

In Figure 6.8, the delay times computed for different magnitudes of elastic stress perturbations during hydraulic fracture growth are similar as shown for Model 1, 2 and 3 despite different dimensions of the fracture cavity for the three models (Tables 6.1 and 6.2). This may be due to the fact that the large elastic stress perturbations are limited close to the fracture cavity and their magnitudes are usually smaller than the regional stresses as shown in Figure 6.6 (exact magnitudes depend upon the fracture pressure, fracture dimensions, and the material properties). Moreover, a significant portion of the path length of any ray traveling from an event to a receiver is outside the region affected by elastic stress changes due to the fracture cavity. Therefore, delay times are more sensitive to changes in the regional stresses (Figure 6.9) than the elastic stress changes induced by hydraulic fracturing. Shelley *et al.* (2014) show a similar result in the case of Mount Asama volcano, Japan where the splitting delay times are more sensitive to the regional stresses than the stress changes induced by the volcanic eruption modeled as a near-vertical dike inflation.

In this study, we assume that the medium undergoing hydraulic fracturing has homogeneous

and isotropic material properties (as listed in Table 6.1). Any anisotropy in this medium is assumed to be induced solely due to the in-situ stresses which include the regional stresses and the elastic stress perturbations caused by the opening of the fracture cavity. The measured delay times are larger for the horizontal to sub-horizontal propagating waves recorded at the receivers at greater depths as compared to those for the sub-vertically propagating waves recorded at the receivers at shallow depths. This is despite the fact that the distances traveled by the vertically propagating waves are larger as compared to those by the horizontally propagating waves. In general, the horizontal transverse isotropy (HTI) due to aligned vertical fractures is best sensed by vertically propagating waves whereas the horizontally propagating waves best sense the vertically transverse isotropy (VTI) symmetry due to sedimentary layering (Wuestefeld *et al.*, 2011). This suggests that the medium in this study may have VTI symmetry. The reservoir rock in this study belongs to the Cardium formation which contains repeated and stacked coarsening upward successions of silty mudstones through siltstones to very fine to fine-grained sandstones (Duhault, 2012). Therefore, the observed shear wave splitting may be attributed to the VTI symmetry due to the sedimentary layering rather than the in-situ stresses.

## 6.5 Conclusions

Microseismic data contain information about the seismic velocity and anisotropy of the surrounding medium. However, most of the microseismic data acquisition during hydraulic fracturing is carried out using receivers in a single monitoring well which limits their applications to the characterization of the source region based on the event locations. The shear wave splitting parameters extracted from microseismic data offer unique opportunity to constrain the anisotropy system of the medium. In this study, we present a forward model to map the stresses into stiffness tensors using third-order elasticity. We compute the splitting delay times for different dimensions of the hydraulic fracture cavity. The induced stresses during hydraulic fracturing do not appear to affect the modeled delay times significantly. The measured delay times are larger for horizontally to

sub-horizontally traveling seismic waves as compared to those for the sub-vertically propagating seismic waves. However, the modeled delay times show opposite trends to the measured delay times and decrease with increasing receiver depth. This suggests that the observed splitting may originate due to the VTI symmetry caused by sedimentary layering rather than the in-situ stresses. Thus, a comparison of the modeled and measured delay times can be combined with other information such as lithology and well constrained regional stress measurements to infer the source of anisotropy.

# Chapter 7

## Conclusions and suggested directions for future research

### 7.1 Conclusions

Microseismic monitoring is an important tool in real-time imaging of the fracture growth during hydraulic fracturing of unconventional hydrocarbon reservoirs like tight sands and shales. It has also been used in underground mining developments for identifying the excavation damaged zones. These applications are based on the spatial locations of the microseismic events computed using the recorded data. One of our objectives in this thesis was to test the feasibility of the microseismic data for extraction of the medium properties such as seismic velocities and anisotropy beyond the source region. However, the major challenges towards this goal are posed by the poor signal-to-noise ratio of the recorded microseismic data, and/or the poor receiver coverage during acquisition. Most often during hydraulic fracturing of shales and tight sands, the data are recorded with geophone array in a single monitoring well.

We first tested the application of a P-wave passive seismic tomography scheme on a microseismic dataset recorded during an underground mine development. In this case, the monitoring wells provide good azimuthal coverage but the signal-to-noise ratio is low. We obtain highly re-

liable differential arrival times using waveform cross-correlation which are then incorporated in double-difference tomography. The final microseismic event locations are tightly clustered near the main working level and shaft and the cluster geometry suggests the occurrence of microseismic events on a planar surface. The 3D P-wave velocity model correlates well with the various known geotechnical zones within the mine. Thus we show that passive seismic tomography using microseismic data provides information beyond the seismically active region like excavation damaged zones and can complement the geological and geotechnical interpretations. Moreover, higher accuracy in the event locations obtained from double-difference tomography can be of great aid in developing a possible causal mechanism for the observed microseismicity.

We then try to understand the possible causes and mechanisms of the microseismic events recorded during the underground mining development. A comparison of the temporal distribution of the events and the mining activities like blasting and rock removal help us to confirm that these events are not man-made seismic signals. The events are located far from the actual construction sites. Therefore it is unlikely that they are triggered due to the large stress concentrations near the walls of the newly created cavities. Based on the event cluster geometry we hypothesize that the events originate due to fault reactivation caused by the mining activities. We analyze the Coulomb stress changes on faults of different orientations due to the stress changes caused by the horizontal tunnel network. We find that the reactivation potential mainly depends upon (1) fault spatial location relative to the mine layout, and (2) fault orientation with respect to the regional stresses. The horizontal tunnel network moves the fault inferred from microseismic event location closer to failure but still the Coulomb failure function has a large negative value. We estimate the dynamic stresses near the event locations generated by the vibrations due to blasting and the vibrations due to a rock crusher operating in the main working level. We conclude that the vibrations generated by the rock crusher may provide the additional dynamic stress perturbations required to trigger microseismicity due to reactivation of the favorably oriented fault. Thus, the analysis of the Coulomb failure function, or similarly slip tendency, can produce pertinent insights into the likelihood of anthropogenic processes to yield induced seismicity as well as identify the exact causative

mechanism.

We next use the Coulomb failure function to study the processes affecting the shear-slip microseismic events recorded during hydraulic fracturing. We find that the elastic stress perturbations due to the opening of the hydraulic fracture cavity can trigger microseismic events near the crack tip region due to shear slippages on pre-existing faults/fractures. The pore pressure diffusion plays an important role in triggering microseismic events near the fracture face where elastic stress perturbations restrict microseismic events. Furthermore, the shape of the pore pressure diffusion front depends upon the shape of the hydraulic fracture cavity and time. We conclude that the opening of the hydraulic fracture cavity affects both the in-situ elastic stresses and the pore pressure distribution thereby influencing the spatiotemporal distributions of microseismicity. The effect of the opening of the hydraulic fracture cavity must be taken into account in modeling and interpretation studies of the induced microseismicity.

Since microseismic data during hydraulic fracturing are mostly recorded using a geophone array in a single monitoring well, we propose to use shear wave splitting parameters to constrain the seismic anisotropy. We present a forward model to map the in-situ stresses into stiffness tensors based on the third-order elasticity and compute the resulting splitting delay times. We find that the regional stresses can considerably affect the splitting delay times as compared to the induced elastic stresses due to hydraulic fracturing. We can infer the source of anisotropy by combining a comparison of the modeled and the measured shear wave splitting delay times with other information such as lithology and well constrained regional stress measurements. Furthermore, the forward modeling of splitting delay times may be used to interpret if the apparent temporal changes in the measured delay times at a specific receiver are due to changing stress conditions or are simply due to the differences in the event locations.

## 7.2 Suggested directions for future research

1. The passive seismic tomography in Chapter 3 was possible mainly due to a good azimuthal coverage provided by the geophone arrays in 7 monitoring wells. In the case of fewer monitoring wells, the double-difference arrival times may be combined with the polarization information to perform seismic tomography thereby better constraining the event locations and velocity parameters.

2. The microseismic events in Chapter 5 are modeled using a shear-slip failure criterion (Coulomb failure function). The elastic stress perturbations and the pore pressure changes due to the opening of the hydraulic fracture may be incorporated in a tensile failure criterion (Griffith criterion) to look at the potential of tensile microseismic events due to hydraulic fracturing.

3. In Chapter 6, we modeled only the splitting delay times; however, modeling the fast polarization direction can provide more insights into the stress-induced anisotropy. Also, we only consider the elastic stress changes due to the opening of the fracture cavity. The pore pressure changes should be incorporated in the effective stresses to understand their role in affecting the shear wave splitting measurements.

# Bibliography

- Abt, D. L., and K. M. Fischer (2008), Resolving three-dimensional anisotropic structure with shear wave splitting tomography, *Geophys. J. Int.*, 173(3), 859–886.
- Ahmed, L., and A. Ansell, (2014), Vibration vulnerability of shotcrete on tunnel walls during construction blasting, *Tunnelling and Underground Space Technology*, 42, 105–111.
- Ahmed, L. (2015), Models for analysis of young cast and sprayed concrete subjected to impact-type loads. Ph.D. thesis. KTH Royal Institute of Technology, Stockholm.
- Aki, K., A. Christoffersson, and E. S. Husebye (1977), Determination of the three dimensional seismic structure of the lithosphere, *J. Geophys. Res.*, 82, 277–296.
- Aki, K., and W. H. K. Lee (1976), Determination of the three-dimensional velocity anomalies under a seismic array using first P arrival times from local earthquakes 1. A homogeneous initial model, *J. Geophys. Res.*, 81, 4381–4399.
- Arrowsmith, S. J., and L. Eisner (2006), A technique for identifying microseismic multiplets and application to the Valhall field, North Sea, *Geophysics*, 71, V31–V40.
- Atkinson, G. M., D. W. Eaton, H. Ghofrani, D. Walker, B. Cheadle, R. Schultz, R. Shcherbakov, K. Tiampo, J. Gu, R. M. Harrington, Y. Liu, M. Van der Baan, and H. Kao (2016), Hydraulic fracturing and seismicity in the Western Canada sedimentary Basin, *Seismol. Res. Lett.*, 87(3), 631–647.
- Babuska, V., and M. Cara (1991), *Seismic Anisotropy in the Earth*, vol. 10, Springer, Dordrecht, Netherlands.
- Bartberger, C. E., T. S. Dyman, and S. M. Condon (2002), Is There a Basin-Centered Gas Accumu-

- lation in Cotton Valley Group Sandstones, Gulf Coast Basin, U.S.A.? U.S. Geological Survey Bulletin 2184-D. Available at <https://pubs.usgs.gov/bul/b2184-d/>.
- Bell, S. J. and S. Bachu (2003), In situ stress magnitude and orientation estimates for Cretaceous coal-bearing strata beneath the plains area of central and southern Alberta, *Bulletin of Canadian Petroleum Geology*, 51(1), 1–28.
- Brodsky, E. E., and S. Prejean (2005), New constraints on mechanisms of remotely triggered seismicity at Long Valley Caldera, *J. Geophys. Res.*, 110, B04302.
- Brodsky, E. E., and N. J. Van der Elst (2014), The Uses of Dynamic Earthquake Triggering, *Annual Review of Earth and Planetary Sciences*, 42, 317–339.
- Bruneton, P. (1993), Geological environment of the Cigar Lake uranium deposit, *Can. J. Earth Sci.*, 30(4), 653–673.
- Cai, M., P. K. Kaiser, and C. D. Martin (2001), Quantification of rock mass damage in underground excavations from microseismic event monitoring, *Int. J. Rock Mech. Min. Sci.*, 38, 1135–1145.
- Calo, M., C. Dorbath, F. H. Cornet, and N. Cuenot (2011), Large-scale aseismic motion identified through 4-D P-wave tomography, *Geophys. J. Int.*, 186, 1295–1314.
- Castellanos, F., and M. Van der Baan (2013), Microseismic event locations using the double-difference algorithm, *CSEG Recorder*, 38(3), 26–37.
- Castellanos, F., and M. Van der Baan (2015a), Dynamic Triggering of Microseismicity in a mine setting, *Geophys. J. Int.*, 202(2), 728–737.
- Castellanos F., and M. Van der Baan (2015b), Waveform similarity for quality control of event locations, time picking and moment tensor solutions, *Geophysics*, 80(6), WC99–WC106.
- Cipolla, C., S. Maxwell, M. Mack and R. Downie (2011), A practical guide to interpreting microseismic measurements, SPE 144067.
- Crampin, S. (1978), Seismic wave propagation through a cracked solid: Polarization as a possible dilatancy diagnostic, *Geophys. J. Roy. Astr. Soc.*, 53, 467–496.
- Crampin, S. (1981), A review of wave motion in anisotropic and cracked elastic-media, *Wave Motion*, 3, 343–391.

- Davis, S. D., and C. Frohlich (1993), Did (or will) fluid injection cause earthquakes?-Criteria for a rational assessment, *Seismol. Res. Lett.*, 643-4, 207–224.
- De Meersman, K., J-M. Kendall, and M. Van der Baan (2009), The 1998 Valhall microseismicity: An integrated study of relocated sources, *Geophysics*, 74(5), B183–B195.
- Duhault, J. L. J. (2012), Cardium Microseismic West Central Alberta: A Case History, *CSEG Recorder*, 37(08), 48–57.
- Dziewonski, A. M., B. H. Hager, and R. J. O’Connell (1977), Large-scale heterogeneities in the lower mantle, *J. Geophys. Res.*, 82, 239–255.
- Eaton, D. W., M. Van der Baan, B. Birkelo, and J. B. Tary (2014), Scaling relations and spectral characteristics of tensile microseisms: Evidence for opening/closing cracks during hydraulic fracturing, *Geophys. J. Int.*, 196(3), 1844–1857.
- Economides, M. J., and K. G. Nolte (Eds.) (2003), Reservoir Stimulation, 3rd ed.: John Wiley, Hoboken, N. J., 5–1–5–14.
- Ellsworth, W. L. (2013), Injection-induced earthquakes, *Science*, 341(6142), 1225942.
- Eshelby, J. D. (1957), The Determination of the Elastic Field of an Ellipsoidal Inclusion, and Related Problems, Proceedings of the Royal Society of London, Series A, Mathematical and Physical Sciences, 241(1226), 376–396.
- Eyre, T. S., and M. Van der Baan (2015), Overview of moment-tensor inversion of microseismic events. *The Leading Edge*, 34(8), 882–888.
- Fayek, M. (2013), Uranium Ore Deposits: A review. In Uranium: Cradle to Grave, (eds. P.C. Burns and G. Sigmon), *Mineralogical Association of Canada*, 43, 121–147.
- Fischer, K. M., E. Parmentier, A. R. Stine, and E. R. Wolf (2000), Modeling anisotropy and plate-driven flow in the Tonga subduction zone back arc, *J. Geophys. Res.*, 105(B7), 16,181–16,191.
- Fisher, K., and N. Warpinski (2011), Hydraulic Fracture-Height Growth: Real Data, SPE, 145949.
- Freed, A. M. (2005), Earthquake triggering by static, dynamic, and postseismic stress transfer. *Annu. Rev. Earth Planet. Sci.*, 33, 335–367.
- Frohlich C. (2012), Two-year survey comparing earthquake activity and injection-well locations

- in the Barnett shale, Texas, *Proceedings of the National Academy of Sciences*, 109(35), 13934–13938.
- Gibowicz, S. J., R. P. Young, S. Talebi, and D. J. Rawlence (1991), Source parameters of seismic events at the Underground Research Laboratory in Manitoba, Canada: Scaling relations for events with moment magnitude smaller than -2, *Bull. Seismol. Soc. Am.*, 81, 1157–1182.
- Goertz-Allmann, B. P., D. Kuhn, V. Oye, B. Bohloli, and E. Aker (2014), Combining microseismic and geomechanical observations to interpret storage integrity at the In Salah CCS site. *Geophys. J. Int.*, 198, 447–461.
- Got, J.-L., J. Frechet, and F. W. Klein (1994), Deep fault plane geometry inferred from multiplet relative relocation beneath the south flank of Kilauea, *J. geophy. Res.*, 99, 15375–15386.
- Gupta, H. K. (2002), A review of recent studies of triggered earthquakes by artificial water reservoirs with special emphasis on earthquakes in Koyna, India, *Earth Sci. Rev.*, 58, 279–310.
- Gurevich, B., M. Pervukhina, and D. Makarynska (2011), An analytic model for the stress-induced anisotropy of dry rocks, *Geophysics*, 76(3), WA125–WA133.
- Hajnal, Z., I.R. Annesley, D. White, R. B. Matthews, V. Sopuck, R. Koch, M. Leppin, and S. Ahuja (1997), Sedimentary-hosted mineral deposits: a high resolution seismic survey in the Athabasca Basin, in *Proceedings of Exploration'97*, 421–432.
- Haslinger, F., E. Kissling, J. Ansorge, D. Hatzfeld, E. Papadimitriou, V. Karakostas, K. Makropoulos, H. G. Kahle, and Y. Peter (1999), 3D crustal structure from local earthquake tomography around the Gulf of Arta (Ionian region, NW Greece), *Tectonophysics*, 304, 201–218.
- Haug, K. M., C. D. Hawkes, and S. Bachu (2007), Evaluation of Stress And Geomechanical Characteristics of Rocks At Penn West's Pembina CO-Enhanced Oil Recovery Pilot Operation. *Canadian International Petroleum Conference*.
- Healy, D., R. Jones, and R. Holdsworth (2006), Three-dimensional brittle shear fracturing by tensile crack interaction, *Nature*, 439, 64–67.
- Hill, D. P., P. A. Reasenber, A. Michael, W. J. Arabaz, G. Beroza et al., (1993), Seismicity remotely triggered by the magnitude 7.3 Landers, California, earthquake, *Science*, 260, 1617–

1623.

- Hill, D. P., and S. G. Prejean (2007), Dynamic triggering. In *Earthquake Seismology*, ed. H Kanamori, *Treatise Geophys.* 4. Amsterdam: Elsevier. 257–291.
- Hsiao, F. Y., C. L. Wang, and J. C. Chern (2009), Numerical simulation of rock deformation for support design in tunnel intersection area. *Tunnelling and Underground Space Technology*, 24, 14–21.
- Husen, S., E. Kissling, and E. R. Flueh (2000), Local earthquake tomography of shallow subduction in north Chile: A combined onshore and offshore study, *J. geophys. Res.*, 105, 28183–28198.
- Husen, S., S. Wiemer, and R. B. Smith (2004), Remotely triggered seismicity in the Yellowstone National Park region by the 2002 Mw 7.9 Denali Fault earthquake, Alaska, *Bull. seism. Soc. Am.*, 94, S317–S331.
- Johnson, P. A., and P.N. J. Rasolofosaon (1996), Nonlinear elasticity and stress-induced anisotropy in rocks, *J. geophys. Res.*, 101, 3113–3124.
- Johnson, P. A., and X. Jia (2005), Nonlinear dynamic, granular media and dynamic earthquake triggering. *Nature*, 437, 871–874.
- Ju, J. W., and L. Z. Sun (2001), Effective elastoplastic behavior of metal matrix composites containing randomly located aligned spheroidal inhomogeneities. Part I: micromechanics-based formulation, *International Journal of Solids and Structures*, 38, 182–201.
- Kachanov, M. (1993), Elastic solids with many cracks and related problems, in *Advances in Applied Mechanics*, vol. 30, edited by J. W. Hutchinson and T. Wu, Academic Press, New York, 259–445.
- Keranen, K., M. Weingarten, G. Abers, B. Bekins, and S. Ge (2014), Sharp increase in central Oklahoma seismicity since 2008 induced by massive wastewater injection, *Science*, 345(6195), 448–451.
- Kilb, D., J. Gomberg, and P. Bodin (2000), Triggering of earthquake aftershocks by dynamic stresses, *Nature*, 408, 570–574.
- King, G. C. P., R. S. Stein, and J. Lin (1994), Static stress changes and the triggering of earth-

- quakes, *Bull. Seismol. Soc. Am.*, 84, 935–953.
- Kissling, E., W. L. Ellsworth, D. Eberhart-Phillips, and U. Kradolfer (1994), Initial reference models in local earthquake tomography, *J. Geophys. Res.*, 99(B10), 19635–19646.
- Krell, W. C. (1979), The effect of coal mill vibration on fresh concrete, *Concrete International*, 1(12), 31–34.
- Kwiatek, G., M. Bohnhoff, G. Dresen, A. Schulze, T. Schulte, G. Zimmermann, and E. Huenges (2008), Microseismic event analysis in conjunction with stimulation treatments at the geothermal research well Gt GrSk4/05 in Gro Schnebeck/Germany. Proceedings of the Thirty-Third Workshop on Geothermal Reservoir Engineering, Stanford University, Stanford, CA, USA.
- Li, Z., K. M. Bethune, G. Chi, S. A. Bosman, and C. D. Card (2013), Preliminary 3D Modelling and Structural Interpretation of Southeastern Athabasca Basin, Geological Survey of Canada, Open File 7426.
- Lomax, A., J. Virieux, P. Volant, and C. Berge (2000), Probabilistic earthquake location in 3D and layered models: Introduction of a Metropolis- Gibbs method and comparison with linear locations, in C. H. Thurber, and N. Rabinowitz, eds., *Advances in seismic event location*: Kluwer Publishing, 101–134.
- Majer, E., R. Baria, M. Stark, S. Oates, J. Bommer, B. Smith, and H. Asanuma (2007), Induced seismicity associated with enhanced geothermal systems, *Geothermics*, 36, 185–222.
- Martin, C. D. (1997), The effect of cohesion loss and stress path on brittle rock strength, *Can Geotech J*, 34, 698–725.
- Mavko, G., T. Mukerji, and N. Godfrey (1995), Predicting stress-induced velocity anisotropy in rocks, *Geophysics*, 60, 1081–1087.
- Mavko, G., T. Mukerji, and J. Dvorkin (2009), *The Rock Physics Handbook: Tools for Seismic Analysis of Porous Media*. Cambridge, New York: Cambridge University Press.
- Maxwell, S. C., T. I. Urbancic, N. Steinsberger, and R. Zinno (2002), Microseismic Imaging of Hydraulic Fracture Complexity in the Barnett Shale, SPE-77440, SPE Annual Technical Conference and Exhibition, San Antonio, Texas.

- McCreath, D. R., D. D. Tannant, and C. C. Langille (1994), Survivability of shotcrete near blasts. In: Nelson, P. P., Laubach, S. E. (Eds.), *Rock Mechanics*. Balkema, Rotterdam, The Netherlands, 277–284.
- McGarr, A., D. Simpson, and L. Seeber (2002), Case histories of induced and triggered seismicity, *International Handbook of Earthquake and Engineering Seismology* (Academic Press, Waltham, MA), vol. 8, chap. 40.
- McGarr A., S. M. Spottiswoode, and N. Gay (1975), Relationship of mine tremors to induced stresses and to rock properties in the focal region, *Bull. seism. Soc. Am.*, 65(4),81–93
- McGarr, A. (1976), Seismic moments and volume changes, *J. Geophys. Res.*, 81(8), 1487–1494.
- Meng, C., and D. D. Pollard (2014), Eshelby’s solution for ellipsoidal inhomogeneous inclusions with applications to compaction bands, *Journal of Structural Geology*, 67, 1–19.
- Menke, W., and D. Schaff (2004), Absolute Earthquake Locations with Differential Data, *Bull. seism. Soc. Am.*, 94(6), 2254–2264.
- Michelini, A., and T. V. McEvilly (1991), Seismological studies at Parkfield: I. Simultaneous inversion for velocity structure and hypocenters using cubic b-splines parameterization, *Bull. seism. Soc. Am.*, 81, 524–552.
- Moeck, I., G. Kwiatek, and G. Zimmermann (2009), Slip tendency analysis, fault reactivation potential and induced seismicity in a deep geothermal reservoir, *J. Structural Geology*, 31, 1174–1182.
- Monteiller, V., J. L. Got, J. Virieux, and P. Okubo (2005), An efficient algorithm for double-difference tomography and location in heterogeneous media, with an application to the Kilauea volcano, *J. Geophys. Res.*, 110, B12306.
- Morris, A., D. A. Ferrill, and D. B. Henderson (1996), Slip tendency analysis and fault reactivation, *Geology*, 24(3), 275–278.
- Norminton, E. J., and J. H. Blackwell (1964), Transient Heat Flow from Constant Temperature Spheroids and the Thin Circular Disk, *Quarterly Journal of Mechanics and Applied Mathematics*, 17(1), 65–72.

- Norris, A. N., B. K. Sinha, and S. Kostek (1994), Acoustoelasticity of solid/fluid composite systems, *Geophys. J. Int.*, 118(2), 439–446.
- Nur, A. (1976), Origin of velocity changes before earthquakes: The dilatancy diffusion hypothesis and its confirmation, in Aoki, H., and Iizuka, S., Eds., *Volcanoes and Tectonosphere*, Tokai University Press, 173–186.
- Nur, A. (1987), Seismic rock properties for reservoir description and monitoring, in Nolet, G., Ed., *Seismic Tomography*, 203–237.
- Nur, A., and G. Simmons (1969a), Stress-induced velocity anisotropy in rock: An experimental study, *J. Geophys. Res.*, 74(27), 6667–6674.
- Nur, A., and G. Simmons (1969b), The effect of saturation on velocity in low porosity rocks, *Earth Plan. Sci. Lett.*, 7, 183–193.
- Olson, J. E. (2003), Sublinear scaling of fracture aperture versus length: an exception or the rule? *J. Geophys. Res. Solid Earth*, 108(B9).
- Patzek, T. W., F. Male, and M. Marder (2013), Gas production in the Barnett Shale obeys a simple scaling theory, *PNAS*, 110(49), 19731–19736.
- Pearson, C. (1981), The relationship between microseismicity and high pore pressures during hydraulic stimulation experiments in low permeability granitic rocks, *J. geophys. Res.*, 86, 7855–7864.
- Podvin, P., and I. Lecomte (1991), Finite difference computation of travel times in very contrasted velocity models: a massively parallel approach and its associated tools, *Geophys. J. Int.*, 105(1), 271–284.
- Pollard, D. D., and P. Segall (1987), Theoretical displacements and stresses near fractures in rock: With applications to faults, joints, veins, dikes and solution surfaces, in *Fracture Mechanics of Rock*, edited by B. K. Atkinson, Academic, San Diego, Calif, 277–350.
- Poupinet, G., W. L. Ellsworth, and J. Frechet (1984), Monitoring velocity variations in the crust using earthquake doublets: An application to the Calaveras Fault, California, *J. geophys. Res.*, 89, 5719–5713.

- Prioul, R., A. Bakulin, and V. Bakulin (2004), Nonlinear rock physics model for estimation of 3D subsurface stress in anisotropic formations: Theory and laboratory verification, *Geophysics*, 69(2), 415–425.
- Prioul, R., and T. Lebrat (2004), Calibration of velocity-stress relationships under hydrostatic stress for their use under non-hydrostatic stress conditions, SEG Expanded Abstracts 74th International Meeting, October 2004.
- Randall, R. B., and J. Antoni (2011), Rolling element bearing diagnostics-A tutorial. *Mechanical Systems and Signal Processing*, 25(2), 485–520.
- Reiter, K., O. Heidbach, D. Schmitt, K. Haug, M. Ziegler, and I. Moeck (2014), A revised crustal stress orientation database for Canada. *Tectonophysics*, 636, 111–124.
- Renshaw, C. E., and J. C. Park (1997), Effect of mechanical interactions on the scaling of fracture length and aperture. *Nature*, 386, 482–484.
- Roche, V., and M. Van der Baan (2015a), The role of lithological layering and pore pressure on fluid-induced microseismicity, *J. geophy. Res.*, 120 (2), 923–943.
- Roche V., M. Van der Baan and G. Preisig (2015b), 3D modeling of hydraulic fracturing and stress perturbations during fluid injection. 49th US Rock mechanics/Geomechanics Symposium, American Rock Mechanics Association. Paper 15-249. San Francisco.
- Rice, J.R., and M. P. Cleary (1976), Some basic stress diffusion solutions for fluid saturated elastic porous media with compressible constituents, *Reviews of Geophysics and Space Physics*, 14, 227–241.
- Rothert, E., and S. Shapiro (2003), Microseismic monitoring of borehole fluid injections: Data modeling and inversion for hydraulic properties of rocks, *Geophysics*, 68(2), 685–689.
- Rozhko, A. Y. (2010), Role of seepage forces on seismicity triggering, *J. Geophys. Res.*, 115, B11314.
- Rutledge, J. T., and W. S. Phillips (2003), Hydraulic stimulation of natural fractures as revealed by induced microearthquakes, *Geophysics*, 68(2), 441–452.
- Rudnicki, J. W. (1999), Alteration of regional stress by reservoirs and other inhomogeneities: stabi-

- lizing or destabilizing? In: Proceedings of the Ninth International Congress on Rock Mechanics, Paris, 3, 1629–1637.
- Savage, M. (1999), Seismic anisotropy and mantle deformation: What have we learned from shear wave splitting? *Rev. Geophys.*, 37, 65–106.
- Sayers, C. M., and M. Kachanov (1995), Microcrack-induced elastic wave anisotropy of brittle rocks, *J. Geophys. Res.*, 100(B3), 4149–4156.
- Scales, J. A., P. Docherty, and A. Gersztenkorn (1990), Regularisation of nonlinear inverse problems: imaging the near-surface weathering layer, *Inverse Problems*, 6, 115–131.
- Schmitt, D. R., C. A. Currie, and L. Zhang (2012), Crustal stress determination from boreholes and rock cores: Fundamental principles. *Tectonophysics*, 580, 1–26.
- Segall, P. (1985), Stress and subsidence resulting from subsurface fluid withdrawal in the epicentral region of the 1983 Coalinga earthquake, *J. Geophys. Res.*, 90, 6801–6816.
- Segall, P., and S. D. Fitzgerald (1998), A note on induced stress changes in hydrocarbon and geothermal reservoirs, *Tectonophysics*, 289, 117–128.
- Segall, P., and S. Lu (2015), Injection-induced seismicity: Poroelastic and earthquake nucleation effects, *J. Geophys. Res.*, 120(7), 5082–5103.
- Shapiro, S. A., E. Rothert, V. Rath, and J. Rindschwentner (2002), Characterization of fluid transport properties of reservoirs using induced microseismicity, *Geophysics*, 67, 212–220.
- Shapiro, S. A., C. Dinske, and E. Rothert (2006), Hydraulic-fracturing controlled dynamics of microseismic clouds, *Geophys. Res. Lett.*, 33, L14312.
- Shapiro, S. A., and C. Dinske (2009), Scaling of seismicity induced by nonlinear fluid rock interaction, *J. Geophys. Res.*, 114, B09307.
- Shelley, A., M. Savage, C. Williams, Y. Aoki, and B. Gurevich (2014), Modeling shear wave splitting due to stress-induced anisotropy, with an application to Mount Asama Volcano, Japan, *J. Geophys. Res. Solid Earth*, 119, 4269–4286.
- Silver, P. G., and W. W. Chan (1991), Shear wave splitting and subcontinental mantle deformation, *J. Geophys. Res.*, 96, 16429–16454.

- Sinha, B. K. (1982), Elastic waves in crystals under a bias, *Ferroelectrics*, 41(1), 61–73.
- Sinha, B. K., and S. Kostek (1996), Stress-induced azimuthal anisotropy in borehole flexural waves, *Geophysics*, 61, 1899–1907.
- Stein, R. S. (1999), The role of stress transfer in earthquake occurrence, *Nature*, 402(6762), 605–609.
- Talebi, S., and R. P. Young (1992), Microseismic monitoring in highly stressed granite: relation between shaft-wall cracking and in Situ stress, *Int. J. Rock Mech. Min. Sci. & Geomech. Abstr.*, 29(1), 25–34.
- Teanby, N., J.-M. Kendall, R. H. Jones, and O. Barkved (2004a), Stress-induced temporal variations in seismic anisotropy observed in microseismic data, *Geophys. J. Int.*, 156, 459–466.
- Teanby, N., J.-M. Kendall, and M. van der Baan (2004b), Automation of shear-wave splitting measurements using cluster analysis, *Bull. seism. Soc. Am.*, 94(2), 453–463.
- Thurber, C. H. (1983), Earthquake locations and three-dimensional crustal structure in the Coyote Lake area, central California, *J. geophys. Res.*, 88, 8226–8236.
- Thurston, R. (1965), Effective elastic coefficients for wave propagation in crystals under stress, *J. Acoust. Soc. Am.*, 37(2), 348–356.
- Thurston, R., and K. Brugger (1964), Third-order elastic constants and the velocity of small amplitude elastic waves in homogeneously stressed media, *Phys. Rev.*, 133(6A), A1604.
- Um, J., and C. H. Thurber (1987), A fast algorithm for two point seismic ray tracing, *Bull. seism. Soc. Am.*, 77, 972–986.
- Van der Baan, M., D. W. Eaton, and G. Preisig (2016), Stick-split mechanism for anthropogenic fluid-induced tensile rock failure, *Geology*, 44(7), 503–506.
- Van der Elst, N. J., H. M. Savage, K. M. Keranen, and G. A. Abers (2013), Enhanced Remote Earthquake Triggering at Fluid-Injection Sites in the Midwestern United States. *Science*, 341(6142), 164–167.
- Verdon, J. P., and A. Wustefeld (2013), Measurement of the normal/tangential fracture compliance ratio ( $Z_N/Z_T$ ) during hydraulic fracture stimulation using S-wave splitting data, *Geophys.*

- Prospect.*, 61(Suppl. 1), 461–475.
- Verdon, J. P., J.-M. Kendall, A. L. Stork, R. A. Chadwick, D. J. White, and R. C. Bissell (2013), Comparison of geomechanical deformation induced by megatonne-scale CO<sub>2</sub> storage at Sleipner, Weyburn, and In Salah, *PNAS*, 110(30), E2762–E2771.
- Vermilyen, J. P. (2011), Geomechanical studies of the Barnett shale, Texas, USA, PhD Dissertation, Stanford University.
- Waldhauser, F., and W. L. Ellsworth (2000), A double-difference earthquake location algorithm: method and application to the Hayward fault, *Bull. seism. Soc. Am.*, 90, 1353–1368.
- Westman, E., K. Luxbacher, and S. Schafrik (2012), Passive seismic tomography for three-dimensional time-lapse imaging of mining-induced rock mass changes, *The Leading Edge*, 31(3), 338–345.
- Winkler, K., and X. Liu (1996), Measurements of third-order elastic constants in rocks, *J. Acoust. Soc. Am.*, 100, 1392–1398.
- Winkler, K. W., B. K. Sinha, and T. J. Plona (1998), Effects of borehole stress concentrations on dipole anisotropy measurements, *Geophysics*, 63, 11–17.
- Wolfe, C. J. (2002), On the mathematics of using difference operators to relocate earthquakes, *Bull. Seism. Soc. Am.*, 92, 2879–2892.
- Wustefeld, A., J. Verdon, J.-M. Kendall, J. Rutledge, H. Clarke, and J. Wookey (2011), Inferring rock fracture evolution during reservoir stimulation from seismic anisotropy, *Geophysics*, 76, WC157–WC166.
- Young, R. P., D. S. Collins, J. M. Reyes-Montes, and C. Baker (2004), Quantification and interpretation of seismicity, *Int. J. Rock Mech. Min. Sci.*, 41, 1317–1327.
- Zhang, H. (2003), Double-difference seismic tomography method and its applications, Ph.D. thesis, Univ. of Wis.-Madison, Madison.
- Zhang, H., and C. H. Thurber (2003), Double-difference tomography: The method and its application to the Hayward fault, California, *Bull. seism. Soc. Am.*, 93(5), 1875–1889.
- Zhang, H., S. Sarkar, M. N. Toksoz, H. S. Kuleli, and F. Al-Kindy (2009), Passive seismic to-

mography using induced seismicity at a petroleum field in Oman, *Geophysics*, 74(6), WCB57–WCB69.

Zoback, M. D. (2007), Reservoir geomechanics, Cambridge, New York, Cambridge University Press.